Publications of the Astronomy Department of
The Eötvös University

Volume 19

Actual Problems in Celectial Mechanics and Dynamical Astronomy

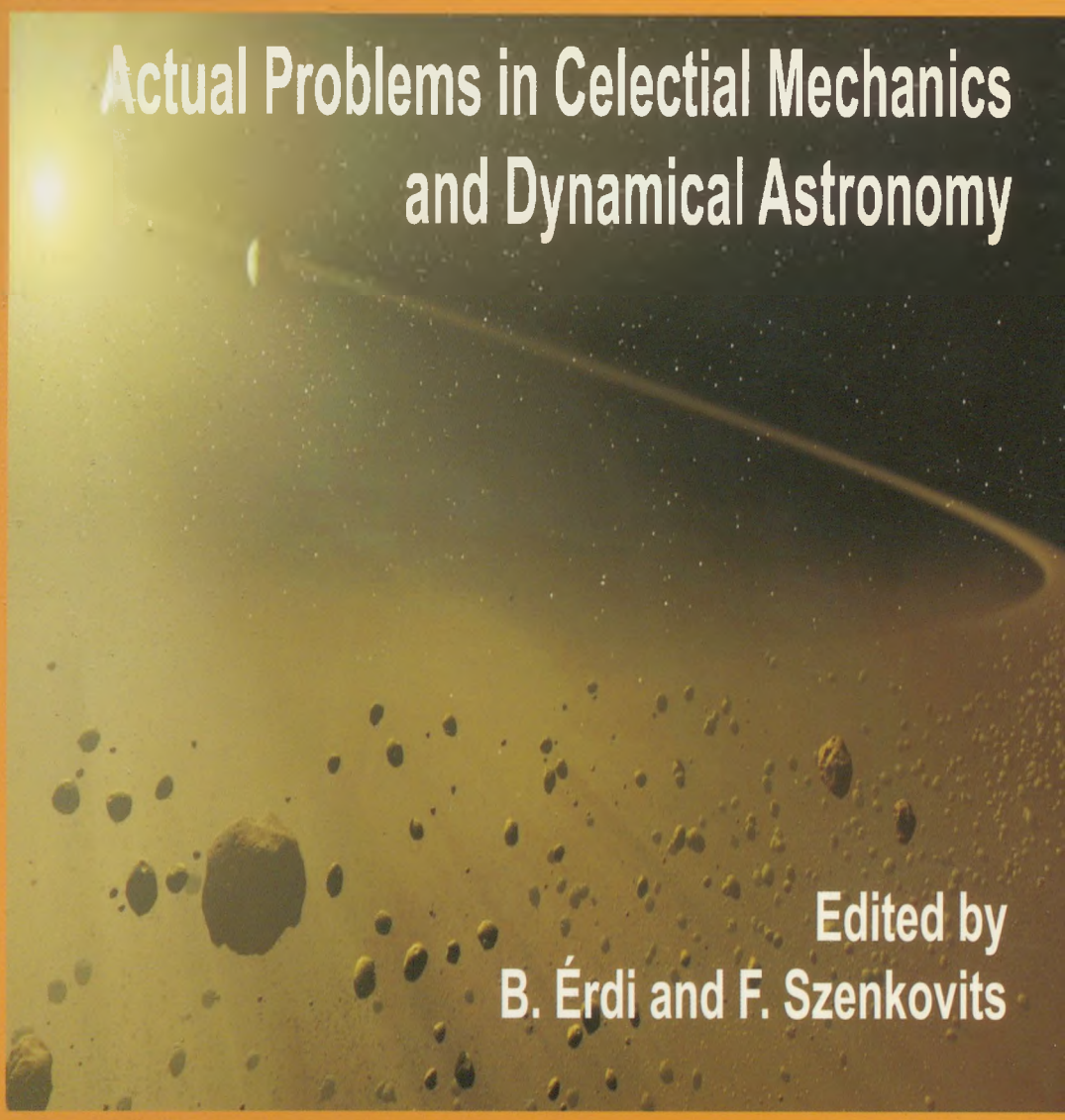

Edited by
B. Érdi and F. Szenkovits

Presa Universitară Clujeană

International Workshop Cluj-Napoca, Romania, May 25-27, 2006

Publications of the Astronomy Department of
the Eötvös University
Vol. 19

INTERNATIONAL CONFERENCE ON ACTUAL PROBLEMS IN CELESTIAL MECHANICS AND DYNAMICAL ASTRONOMY

Cluj-Napoca, Romania, May 25-27, 2006

Edited by

B. Érdi and F. Szenkovits

Published by the Department of Astronomy
of the Eötvös University, Budapest, Hungary
and
Chair of the Mechanics and Astronomy
of the Babeş-Bolyai University, Cluj-Napoca, Romania

PRESA UNIVERSITARĂ CLUJEANĂ / CLUJ UNIVERSITY PRESS
2007

© 2006. All rights reserved. No part of this publication may be reproduced or transmitted in any form or by any means, electronic or mechanical, including photocopy, recording or any information storage and retrieval system, without permission from the authors.

Publication of this volume has been supported by the:

Romanian Ministry of Education and Research and
Hungarian Ministry of Education and Culture.

ISBN 963-463-557 (Department of Astronomy of the Eötvös University)
Responsable publisher: Dr. Bálint Érdi

ISBN 978-973-610-555-5 (Cluj University Press)
"Babeş-Bolyai" University
Cluj University Press
Director: Codruţa Săcelean
Str. Haşdeu nr. 45
400371 Cluj-Napoca, ROMÂNIA
Tel./fax: (+40)-264-597.401
E-mail: presa_universitara@easynet.ro
http://www.editura.ubbcluj.ro/

Contents

Preface

The Chair of Mechanics and Astronomy of the Babeş-Bolyai University, Cluj-Napoca organized a series of three international workshops on celestial mechanics and space dynamics between 1997–1999. Following this tradition, in 25–27 May 2006 an International Conference on Actual Problems in Celestial Mechanics and Dynamical Astronomy was organized at Cluj-Napoca. The Faculty of Mathematics and Computer Science of the Babeş-Bolyai University, the host of this conference, organized this scientific meeting in collaboration with the Loránd Eötvös University (Budapest, Hungary), Sapientia University (Miercuria Ciuc, Romania), Astronomical Institute of the Romanian Academy (Bucharest, Romania) and Institute for Space Science (Bucharest, Romania).

The main topics covered by the meeting were:

- Solar-System dynamics, stability, resonances, chaos;
- Dynamics of populations in the Solar System: NEAs, MBAs, Centaurs, KBOs, TNOs: observations, orbits, theoretical models;
- Galactic and extragalactic dynamics;
- Problems, models, methods and techniques in contemporary celestial mechanics and dynamical astronomy.

The conference was structured into seven sessions of oral presentations, a poster session and a round table discussion. Each of the seven main sessions began with an invited lecture. These lectures reviewed the following fields: the Sitnikov problem (R. Dvorak, Austria); the age of the asteroid families (Z. Knezevic, Serbia and Montenegro); stability of exoplanetary systems (B. Érdi, Hungary); Saari's conjecture (Diacu, Canada); integrability from direct and inverse standpoints (G. Bozis, Greece); stability of exact solutions in restricted many-body problems (E. Grebenicov, Russia); actual Romanian research in post-Newtonian dynamics (V. Mioc, Romania).

Beside the invited lectures, the 21 oral presentations covered the most various domains of celestial mechanics and dynamical astronomy. Chaotic behaviour was a premier topic. It was approached and studied by analytical, geometrical and numerical methods in many astronomical problems: the restricted three-body problem (with examples in the Solar System), the Gylden's model and its generalizations, capture domain, resonances, etc.

Stability and instability were also subjects of discussions. Almost all of the communications held on this topic dealt with exoplanetary systems. But other specific astronomical fields, such as the Solar System or clusters of galaxies were presented too.

Special problems of celestial mechanics were also discussed. We can mention the elliptic restricted three-body problem, photogravitational models, the Hénon-Heiles' model, Maxwell's model for planetary rings, behaviour in the transitory regime, etc. Space dynamics was represented by contributions concerning fly-by trajectories, or EPIRB distress signal via satellite. Finally, numerical techniques and simulations, useful for the investigation of various abstract models and actual problems of celestial mechanics and dynamical astronomy, also occupied a place in the discussions.

In conclusion, the meeting tried to find a common way for the classical mechanics (quantitative, and based on real astronomical situations and models) and the 'abstract' one (qualitative, using geometric tools of the theory of dynamical systems, and often tackling less realistic models, however aimed at the global understanding of astronomical problems).

As to the international participation in this conference, we mention that the contributions belong to authors from ten countries (Austria, Canada, Greece, Hungary, Italy, Poland, Romania, Russia, Saudi Arabia, and Serbia and Montenegro).

The lectures, talks and (especially) the discussions established the bases for an enlarged international cooperation within the framework of this branch of Astronomy.

This volume contains 24 contributions presented at the conference.

The editors:
Bálint Érdi and
Ferenc Szenkovits

Part I

Two-Body Type Problems

PADEU | PADEU **19** (2007), p. 7
ISBN 963 463 557
©Published by the Astron. Dept. of the Eötvös Univ.

Using resonant Earth-flyby trajectories for space exploration

Ştefan Berinde

Babeş-Bolyai University, Cluj-Napoca, Romania

E-mail: sberinde@math.ubbcluj.ro

Abstract

This paper explores the advantages of using gravity assisted trajectories for flyby and rendezvous missions to near-Earth asteroids (NEAs) or other solar system bodies. A special case of such orbits is considered here: resonant Earth-flyby trajectories. On these trajectories the spacecraft acquires a large relative velocity in respect to the Earth by using one deep-space maneuver along the heliocentric orbit. A resonant condition between Earth and the spacecraft is required for a subsequent flyby. This one can send the spacecraft on more inclined orbits, or on orbits with large aphelion distances. In this manner the accessibility region for NEAs is substantially increased and distant bodies in the solar system are reachable with lower costs. The problem is formulated in the frame of Opik's geometric formalism.

Keywords: *Resonant orbits, Earth-flyby trajectories, space missions*

1 Introduction

This is a second paper of the author in a series exploring the advantages of using gravity assisted trajectories for flyby and rendezvous missions to near-Earth asteroids (NEAs) or other solar system bodies. Low-cost transfer orbits from Earth to other celestial bodies are usually based on planetary gravity assistance (ex: Earth flyby), especially for complex missions (as rendezvous or sample return). A low-cost mission implies a low velocity budget, which is of the order of several km/s. This velocity budget is consumed during impulsive

transfers, in order to change the orbit of the spacecraft as needed. The side effect of such carefully designed orbits is the long travel time till completion (several years). Examples of such missions are: NEAR rendezvous mission to asteroid Eros, or StarDust sample-return mission to comet Wild 2.

Some authors already explored direct flight opportunities to NEAs, but the number of accessible objects is rather limited due to high velocity budgets involved (Christou, 2003; Perozzi et al., 2001). Various gravity assisted trajectories can be imagined and explored, like VEGA or VEEGA (Berinde, 2005) or other more complicated ones. But these are target specific with a very limited applicability. In this paper we deal with resonant Earth-flyby trajectories, involving a deep-space maneuver along the transfer orbit. We will analyse the advantages of using such trajectories for space exploration.

2 Opik's geometric formalism

The whole theory is developed in the framework of Opik's geometric formalism for close encounters. This is basically a two "two-body" approximation, with many applications in the field of Celestial Mechanics and Astrodynamics. This approximation is entirely adequate for our purpose and provides simple algebraic formulas for all orbital quantities. We recall some of the principles of this approximation: Earth's orbit is considered circular around the Sun, the spacecraft has a geocentric hyperbolic orbit near the planet and a keplerian heliocentric orbit in interplanetary space, and a planetary encounter is considered an instantaneous event when compared with the interplanetary travel time (Carusi et al., 1990).

Throughout the paper we adopt the following measuring units for distance and time, such that the radius of the Earth's orbit equals 1 and its heliocentric velocity is also 1. It means that the heliocentric gravitational parameter is $\mu_\odot = 1$ and Earth's orbital period is $T_\oplus = 2\pi$.

If a, e, i are the heliocentric orbital elements of the spacecraft before the encounter, the (unperturbed) relative geocentric velocity

$$u^2 = 3 - \frac{1}{a} - 2\sqrt{a(1-e^2)}\cos i \tag{1}$$

is an invariant of the motion during the encounter. The orientation of this

velocity vector is described by the angles (θ, ϕ), given by

$$\begin{cases} \cos\theta = \dfrac{1-u^2-1/a}{2u} \\ \cos\phi = \pm\dfrac{\cos\theta + 1/u}{\sin\theta}\tan i, \end{cases} \tag{2}$$

where $\theta \in [0, \pi]$ and $\phi \in [0, \pi]$ for pre-perihelion motion, respectively, $\phi \in [\pi, 2\pi]$ for post-perihelion motion. The sign of the right term in the second equation dependes on the type of the orbital node: ascending (+) or descending (−). Following we consider only the ascending node, since the descending one is just a mirror case with similar results.

The encounter phase is described by two additional angles, gravitational deflection angle $\gamma \in [0, \gamma_{max}]$ and the inclination of geocentric orbit $\psi \in [0, 2\pi]$ in respect to a given reference plane. We do not enter here into details regarding geometric interpretation of these angles (Carusi et al., 1990), but we give the expression of the maximum deflection angle

$$\sin\frac{\gamma_{max}}{2} = \left[1 + \left(\frac{u}{v_{LEO}}\right)^2\right]^{-1}. \tag{3}$$

This depends on the physical characteristics of the planet, which are hidded in the value of the parameter $v_{LEO} = 0.26$ (7.8 km/s) – the velocity in low-Earth orbit (LEO). For our purpose, we consider LEO a circular orbit at 200 km above the surface of the Earth. This is also the minimum allowed distance for the encounter, that's why the parameter v_{LEO} appears in the formula of maximum deflection angle.

The orientation of the relative geocentric velocity vector after the encounter is given by angles (θ', ϕ'), computed from

$$\begin{cases} \cos\theta' = \cos\theta\cos\gamma + \sin\theta\sin\gamma\cos\psi \\ \sin(\phi - \phi') = \dfrac{\sin\psi\sin\gamma}{\sin\theta'} \\ \cos(\phi - \phi') = \dfrac{\sin\theta\cos\gamma - \cos\theta\sin\gamma\cos\psi}{\sin\theta'}. \end{cases} \tag{4}$$

Finally, the post-encounter orbital elements are given by

$$\begin{cases} \dfrac{1}{a'} = 1 - 2u\cos\theta' - u^2 \\ \tan i' = \dfrac{\sin\theta'\cos\phi'}{\cos\theta' + 1/u} \\ e' = \sqrt{1 - \dfrac{1}{4a'\cos i'}\left(3 - \dfrac{1}{a'} - u^2\right)^2}. \end{cases} \tag{5}$$

In short, the orbit can be propagated analytically as follows

$$(a, e, i) \longrightarrow (u, \theta, \phi) \longrightarrow (u, \theta', \phi') \longrightarrow (a', e', i') \tag{6}$$

The design of our transfer orbits is performed in three stages: insertion on heliocentric orbit, changing encounter geometry with a deep-space maneuver and synchronizing orbital motions for an Earth flyby.

3 Insertion on heliocentric orbit

We consider the initial state of the interplanetary spacecraft its parking LEO orbit around Earth. To escape Earth's gravitational influence with a relative velocity u, it requires an additional velocity in LEO orbit $E(u)$ given by

$$E(u) = \sqrt{u^2 + 2v_{LEO}^2} - v_{LEO}. \tag{7}$$

We notice that $E(0) = 0.11$ (3.3 km/s) and $u \geq E(u)$ only if $u \geq 0.13$ (3.9 km/s), showing the efficiency of heliocentric insertion from LEO orbit.

From now on we denote with u_1 this relative velocity in respect to Earth. In the case of direct transfer orbits, the maximum semimajor axis that can be reached is $a_{max} = [2 - (1 + u_1)^2]^{-1}$ for zero inclined orbits, and the maximum orbital inclination is $\sin i_{max} = u_1$ for almost circular orbits, with $a = (1+u_1^2)^{-1}$ and $e = u_1^2$. We call direct transfer orbits as orbits of type *0-0*.

In the following section we consider an additional velocity impulse u_2 to be applied in heliocentric orbit, in order to change the encounter geometry with the Earth. We will show how this maneuver significantly increases the relative geocentric velocity, which can be used further to obtain a large spectrum of heliocentric orbits. We should note that, without such a maneuver, the

spacecraft will return near the Earth's orbit with the same relative velocity u_1, with no practical benefits.

Let introduce

$$u_{tot} = E(u_1) + u_2 \tag{8}$$

the sum of velocity impulses perfomed by the spacecraft. For low-cost missions we should consider $u_{tot} < 0.35$ ($\approx$10 km/s).

4 Changing encounter geometry with a deep-space maneuver

For reasons concerning optimal transfers, let the velocity impulse u_1 be oriented along the Earth's velocity vector (at point A in figure 1). We obtain a heliocentric orbit with perihelion distance of 1 and aphelion distance

$$Q = \frac{2}{2-(1+u_1)^2} - 1. \tag{9}$$

The velocity of the spacecraft at the aphelion point B is

$$v_Q = \frac{1+u_1}{Q}. \tag{10}$$

Now, let the velocity u_2 be applied at the aphelion (as deep-space maneuver) in order to decrease the heliocentric velocity of the spacecraft to $v_Q - u_2$. In this manner the perihelion distance is lowered, allowing two intersection points with the Earth's orbit, C_1 (first one) and C_2 (second one). The new semimajor axis of the orbit is computed from

$$\frac{1}{a} = \frac{2}{Q} - (v_Q - u_2)^2, \tag{11}$$

and the new relative geocentric velocity at the intersection points is

$$u_3 = \sqrt{3 - \frac{2}{Q} - Q^2 + (Q - v_Q + u_2)^2}. \tag{12}$$

The orientation angles of this velocity in respect to the Earth's velocity vector are given by

$$\cos\theta = \frac{u_1 - Qu_2}{u_3}, \quad \phi = \pi/2. \tag{13}$$

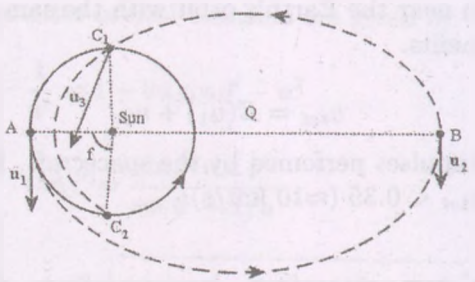

Figure 1: *Geometry of resonant Earth-flyby trajectories*

It can be shown that

$$u_3 \geq u_1 + u_2, \tag{14}$$

with equality only for singular cases $u_1 = 0$ or $u_2 = 0$. Also, in most of the cases we have $E(u_3) \geq u_{tot}$. That is, someone needs a higher velocity impulse in LEO orbit to get the relative velocity u_3, when compared with the combined impulses previously described.

In order to accomplish this scenario we must consider the Earth and the spacecraft arriving at the same time at one of their orbital intersection points. This flyby requirement is analyzed in the next section. Before that, let make the convention that a transfer orbit is of type m-n if the flyby occurs at the intersection point m (1 for first one, 2 for second one) and Earth makes n full revolutions around Sun before the event. Only the following types are of practical interest: *1-1*, *2-1*, *1-2*, *2-2*, *1-3* and *2-3*. We call these orbits *resonant Earth-flyby trajectories*. They have an orbital period less than 4 years (until the flyby) and an aphelion distance less than 4 AU.

5 Synchronizing orbital motions

The true anomaly f of the intesection points is given by

$$\cos f = \frac{Q^2(v_Q - u_2)^2 - 1}{1 - Q(v_Q - u_2)^2}, \tag{15}$$

where we consider $f \in [0, \pi]$ due to the symmetry of the problem. The travel time of the Earth on its orbit is simply

$$t_\oplus(u_1, u_2) = \begin{cases} 2(n+1)\pi - f, & \text{if } m = 1 \\ 2n\pi + f, & \text{if } m = 2, \end{cases} \tag{16}$$

where m decides what intersection point is choosen and n is the number of full revolutions.

The spacecraft travels a time of

$$t_1(u_1) = \pi \left(\frac{Q+1}{2}\right)^{3/2} \tag{17}$$

until deep-space maneuver. From here it takes a time of

$$t_2(u_1, u_2) = \begin{cases} a^{3/2}\left[(\alpha - \sin\alpha) - (\beta - \sin\beta)\right], & \text{if } m = 1 \\ a^{3/2}\left[2\pi - (\alpha - \sin\alpha) + (\beta - \sin\beta)\right], & \text{if } m = 2 \end{cases} \tag{18}$$

until Earth-flyby. The quantities α and β are specific to Lagrange's form of transfer-time equation (Battin, 1987). Their values are, respectively

$$\sin^2\frac{\alpha}{2} = \frac{s}{2a}, \quad \sin^2\frac{\beta}{2} = \frac{s-c}{2a}, \tag{19}$$

where, for our problem, $s = (1 + Q + c)/2$ and $c^2 = 1 + Q^2 + 2Q\cos f$.

In order to synchronize orbital motions of Earth and the spacecraft, we ask for

$$t_\oplus(u_1, u_2) = t_1(u_1) + t_2(u_1, u_2). \tag{20}$$

For each pair of velocities (u_1, u_2) with $u_1 + u_2 = const$, this transcedental equation has at most one solution. In the range $0 < u_1 + u_2 < 0.3$ we numerically obtained a family of solutions for each type of transfer orbits (figure 2 - left panel). For $u_2 = 0$ the orbits are in true resonance. On the right panel of figure 2 we plotted the new relative velocity u_3 versus combined velocity impulses u_{tot}. We see that the gain in velocity is more effective for higher resonant orbits.

With a higher relative velocity in respect to the Earth, the spacecraft can benefit from the flyby in several ways: it can maximize the orbital energy (semimajor axis) to reach large aphelion distances to outer planets, or it can maximize orbital inclination to rendezvous with near-Earth asteroids, or it can enter again on a resonant orbit with the Earth and repeat the steps to get even higher relative velocities. In the next section we discuss the first two opportunities, and we leave the last on just as a remark.

6 Flyby outcomes

The angles (γ, ψ) introduced in section 2 will determine the outcomes of the flyby. We are interested in the extreme values for semimajor axis a' and orbital

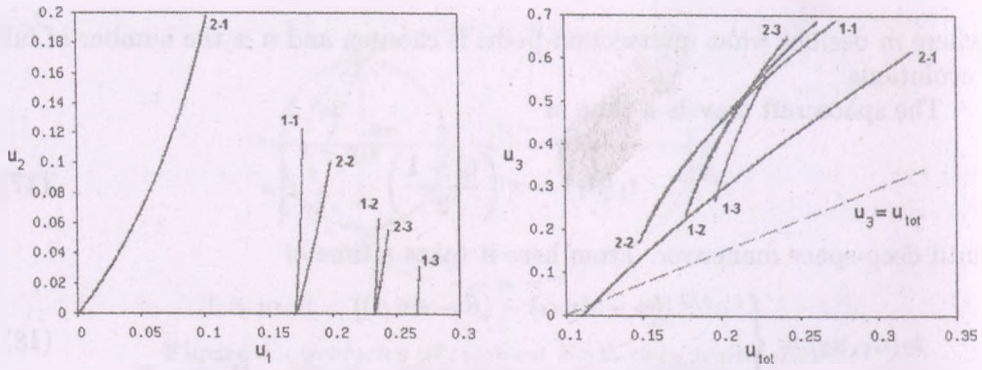

Figure 2: *Families of solutions* (u_1, u_2) *for synchronization equation – left panel; relative velocity* u_3 *function of combined velocity impulses* u_{tot} *– right panel*

inclination i' after the encounter.

6.1 Maximum semimajor axis

We see from first equation in (5) that the semimajor axis a' increases when angle θ' decreases towards zero. In our scenario, the minimum value for this angle is $\theta'_{min} = \max\{0, \theta - \gamma_{max}\}$. Here γ_{max} is computed from (3) using $u = u_3$. For large values of u_3 we have $\theta'_{min} > 0$, since γ_{max} is not sufficiently large to overcome θ.

The maximum values of semimajor axis a'_{max} are plotted on figure 3 (left panel). We surprisingly obtain very large values across the entire planetary system. The maximum aphelion distance is only slightly larger than the value $2a'_{max} - 1$. So, with a velocity budget of about $u_{tot} = 0.17$ (5.1 km/s) we can reach Jupiter's orbit on 1-1 or 2-2 transfer orbits. Even Pluto can be reached with $u_{tot} = 0.22$ (6.6 km/s) on a 1-3 transfer orbit.

6.2 Maximum orbital inclination

Final orbital inclination is also a function of free parameters (γ, ψ). We search for its maximum value i'_{max} by looking at the stationary points of the function

$$\tan i'(\gamma, \psi) = \frac{\sin\gamma \sin\psi}{\cos\theta \cos\gamma + \sin\theta \sin\gamma \cos\psi + 1/u_3}, \tag{21}$$

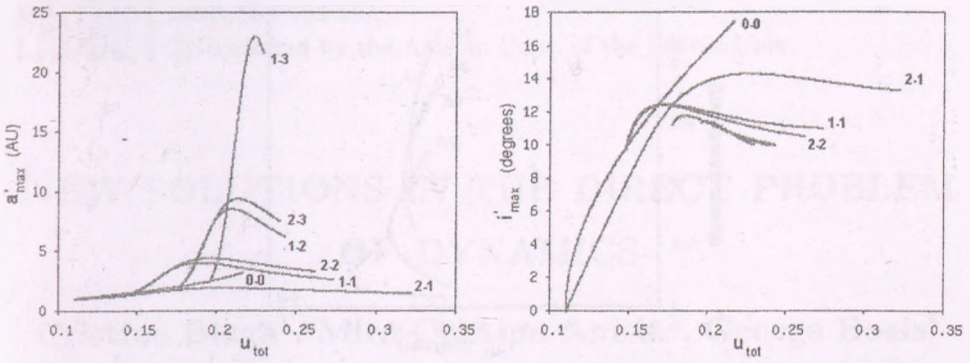

Figure 3: *Maximum values for semimajor axis (left panel) and inclination (right panel) function of combined velocity impulses u_{tot}, for different types of transfer orbits*

computed from (5), using (4), and taking into account that $\phi = \pi/2$. The domain of this function is $[0, \gamma_{max}] \times [0, 2\pi]$. The system of partial derivatives reduces to

$$\begin{cases} \cos\gamma = -u_3 \cos\theta, \\ \cos\psi = -u_3 \dfrac{\sin\theta}{\sin\gamma}. \end{cases} \tag{22}$$

It has always solution, since $u_3 < 1$. But the solution is inside the domain ($\gamma < \gamma_{max}$) if and only if

$$\frac{1}{a} > 3 - u_3^2 - 4\sin^2\frac{\gamma_{max}}{2}. \tag{23}$$

In this case (corresponding to small u_3 values) the maximum inclination is shown to be $\sin i'_{max} = u_3$. These orbits are almost circular (like those studied in section 3). If $u_3 > 0.17$ the inequality (23) is broken. In this case the maximum value is obtained on the boundary of the domain, for $\gamma = \gamma_{max}$. From here we get

$$\cos\psi = -\frac{\sin\theta \sin\gamma_{max}}{\cos\theta\cos\gamma_{max} + 1/u_3} \tag{24}$$

and, finally

$$\tan i'_{max} = -\frac{1}{\sin\theta \tan\psi}. \tag{25}$$

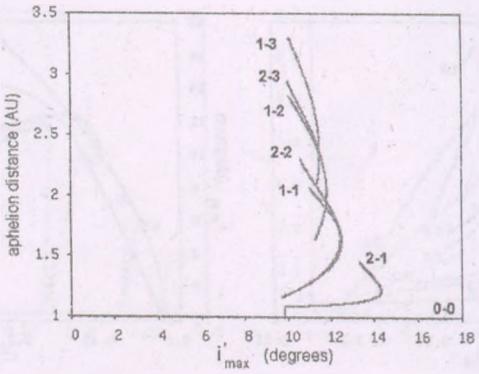

Figure 4: *Values of aphelion distance corresponding to orbits of maximum inclination*

Figure 3 (right panel) plots the curves of maximum values i'_{max}. These values are slightly lower than those from direct orbits (type *0-0*), but the shape of the final orbits is quite different. For example, there are orbits with aphelion distances between 1 and 3 AU even at an inclination greater than 10° (figure 4). This technique of increasing orbital inclination using an Earth-flyby was actually used by the NEAR interplanetary mission (Cheng, 1997).

We conclude that using resonant Earth-flyby trajectories the accessibility region for NEAs substantially increases and outer planets are reachable with lower costs. A next step in this study is to review possible candidates for such missions.

References

Battin, R.H. 1987, An introduction to the mathematics and methods of astrodynamics (AIAA Education Series)

Berinde, S. 2005, in Dynamics of Populations of Planetary Systems (Proceedings of the IAU Colloquium 197), p. 265

Carusi, A., Valsecchi, G.B., Greenberg, R. 1990, Celestial Mechanics and Dynamical Astronomy, 49, 111

Cheng, A. 1997, Space Science Review, 82, 3

Christou, A. 2003, Planetary and Space Science, 51, 221

Perozzi, E., Rossi, A. Valsecchi G.B. 2001, Planetary and Space Science, 49, 3

PADEU | PADEU 19 (2007), p. 17
ISBN 963 463 557
©Published by the Astron. Dept. of the Eötvös Univ.

New solutions in the direct problem of dynamics

Cristina Blaga[1], Mira-Cristina Anisiu[2], George Bozis[3]

[1]Faculty of Mathematics and Computer Science,
"Babeş-Bolyai" University, Cluj-Napoca, Romania
[2]T. Popoviciu Institute of Numerical Analysis, Romanian Academy
P.O. Box 68, 400110 Cluj-Napoca, Romania
[3]Department of Physics, Aristotle University of Thessaloniki GR-54006, Greece
E-mail: [1]cpblaga@math.ubbcluj.ro, [2]mira@math.ubbcluj.ro, [3]gbozis@auth.gr

Abstract
Given a planar potential V, we look for families of orbits $f(x,y) = c$ (determined by their slope function $\gamma = f_y/f_x$), traced by a material point of unit mass under the action of that potential. The second-order equation which relates γ and V is nonlinear in γ; to find special solutions, we consider in addition a linear first-order partial differential equation satisfied by γ. The problem does not admit always solutions; but when solutions do exist, they can be found by algebraic manipulations. Examples are given for homogeneous families γ, and for some special cases which arise in the course of reasoning.
Keywords: *Direct and inverse problem of dynamics, partial differential equations*

1 Introduction

The planar direct problem of Dynamics consists in finding families of orbits $f(x,y) = c$ traced in the xy Cartesian plane by a material point of unit mass, under the action of a given potential V.

Any family of orbits is determined by its 'slope function' $\gamma = f_y/f_x$, the subscripts denoting partial derivatives. There are two equations relating the functions V, γ (and their derivatives):

(i) the first order equation in V, given by Szebehely (1974) (equation (8) below), which is associated with the energy dependence on the family f;

(ii) the energy-free second order linear equation in V, given by Bozis (1984) and written below in the form (6)-(7).

These equations, born in the framework of the inverse problem, are rearranged here in order to face the direct problem, as suggested by Bozis (1995). The difficulty with the second order equation arises from its nonlinearity in the unknown family γ. This is why in several papers additional information on the families of orbits (sometimes on the given potentials also) was used in order to obtain solutions of the direct problem. Homogeneous families produced by homogeneous or inhomogeneous potentials were studied by Bozis and Grigoriadou (1993) and by Bozis et al (1997), as well as families of orbits with $\gamma = \gamma(x)$, corresponding to families $f(x, y) = y + h(x) = c$ (Bozis et al, 2000). Later on (Anisiu et al, 2004), the solutions of equation (6) were looked for in a class of functions verifying a linear PDE

$$r(x, y)\gamma_x + \gamma_y = 0; \tag{1}$$

this class contains the homogeneous functions f, for which γ is homogeneous of zero degree and $r = x/y$. In all these cases γ was found as the common root of certain algebraic equations in γ, with coefficients depending on V and on derivatives of V.

In what follows we consider a given potential V and study the existence and the construction of solutions γ of the direct problem of dynamics, under the hypothesis that γ satisfies an equation of the form

$$a(x, y, \gamma)\gamma_x + b(x, y, \gamma)\gamma_y = c(x, y, \gamma). \tag{2}$$

We may suppose $b \neq 0$ and denote by $r = a/b$ and $s = c/b$.

In the following we replace (2) by the equation

$$r(x, y, \gamma)\gamma_x + \gamma_y = s(x, y, \gamma) \tag{3}$$

with r and s known functions of x, y, γ. We then develop the reasoning to check whether the given potential can be compatible with families $\gamma = \gamma(x, y)$ satisfying the condition (3).

In section 2 we give the basic partial differential equations of the direct problem and add to them two (second order) differential relations derived from (3). Then, in section 3 we obtain the algebraic equations verified by γ_x. In section 4 we obtain three algebraic equations which the required family must

satisfy when γ is a homogeneous function of degree m. The resultants of the two pairs of equations must vanish and this leads to two differential conditions which all adequate potentials must satisfy. In section 5 we present some special cases and examples. A synthesis is presented in section 6.

2 Partial differential equations satisfied by γ

We consider a planar potential V under the action of which a monoparametric family of orbits

$$f(x,y) = c \tag{4}$$

can be described by a material point of unit mass. This family can be represented in a unique way by its *slope function*

$$\gamma = \frac{f_y}{f_x}. \tag{5}$$

To each γ there corresponds a unique family (4).

The nonlinear second order differential equation relating potentials and orbits in the form suitable for the direct problem (Bozis, 1995) is

$$\gamma^2\gamma_{xx} - 2\gamma\gamma_{xy} + \gamma_{yy} = h, \tag{6}$$

where

$$h = \frac{\gamma\gamma_x - \gamma_y}{V_y\gamma + V_x}\left(-\gamma_x V_x + (2\gamma\gamma_x - 3\gamma_y)\,V_y + \gamma\,(V_{xx} - V_{yy}) + (\gamma^2 - 1)V_{xy}\right). \tag{7}$$

Szebehely's equation (1974) involving the total energy $E(f)$ is (Bozis, 1983)

$$V_x + \gamma V_y + \frac{2\Gamma}{1+\gamma^2}\,(E(f) - V) = 0, \tag{8}$$

where

$$\Gamma = \gamma\gamma_x - \gamma_y. \tag{9}$$

In order to solve (8) for $E(f)$, the condition $\Gamma \neq 0$ must be imposed, hence it follows also that $V_x + \gamma V_y \neq 0$. The case $\Gamma = 0$ was studied in detail by Bozis and Anisiu (2001) and will be considered in section 5. If for a given V we can find a solution γ of (6), equation (8) will allow us to find the energy along each member of the family, namely

$$E(f) = V - \frac{(V_x + \gamma V_y)\,(1+\gamma^2)}{2\Gamma}. \tag{10}$$

The real parts of the orbits of the family are lying in the region defined by the inequality (Bozis and Ichtiaroglou, 1994)

$$\frac{V_x + \gamma V_y}{\Gamma} \leq 0. \tag{11}$$

As we have mentioned in the Introduction, the special families of orbits we are going to consider are those for which equation (3) is also satisfied. We differentiate it with respect to x and obtain

$$r\gamma_{xx} + \gamma_{xy} = -r_{001}{\gamma_x}^2 - r_{100}\gamma_x + s_{001}\gamma_x + s_{100}. \tag{12}$$

Then we differentiate (3) with respect to y

$$r\gamma_{xy} + \gamma_{yy} = -r_{001}\gamma_x\gamma_y - r_{010}\gamma_x + s_{001}\gamma_y + s_{010}. \tag{13}$$

For the functions r and s, which depend on the three variables x, y, γ, we adopt the three-subscripts notation, e.g. $\partial^{i+j+k}s/\partial x^i \partial y^j \partial \gamma^k = s_{ijk}$. The system of equations (6), (12) and (13) allows us to obtain the second order derivatives of γ in terms of γ and its first order derivatives.

3 Algebraic equations satisfied by γ_x

We solve the system of equations (6), (12) and (13) with respect to γ_{xx}, γ_{xy} and γ_{yy}. These second order derivatives depend on γ, γ_x, γ_y, on r, s, and their first-order derivatives and, of course, on the first and second order derivatives of V. In fact, considering (3), we can express γ_y in terms of γ_x. We introduce the notations

$$\begin{aligned}
\Pi &= (\gamma + r)^2 (V_y\gamma + V_x) \\
K &= -2(r_{001} - 1)V_y\gamma^2 + [(5r - 2rr_{001})V_y - (2r_{001} + 1)V_x]\gamma + \\
&\quad + r[3rV_y - (1 + 2r_{001})V_x] \\
L &= V_{xy}\gamma^3 + [V_{xx} - V_{yy} + rV_{xy} - 2(r_{100} - s_{001})V_y]\gamma^2 \\
&\quad + [r(V_{xx} - V_{yy}) - V_{xy} + 2(s_{001} - r_{100})V_x + \\
&\quad + (-rr_{100} + r_{010} + sr_{001} - 5s + 2rs_{001})V_y]\gamma \\
&\quad - rV_{xy} + (-rr_{100} + r_{010} + sr_{001} + s + 2rs_{001})V_x - 6rsV_y, \\
M &= (-sV_{xy} + 2s_{100}V_y)\gamma^2 + [s(V_{yy} - V_{xx}) + 2s_{100}V_x + \\
&\quad + (rs_{100} - s_{010} - ss_{001})V_y]\gamma \\
&\quad + sV_{xy} + (rs_{100} - s_{010} - ss_{001})V_x + 3s^2V_y.
\end{aligned} \tag{14}$$

Then, the second-order derivatives of γ can be expressed as

$$\gamma_{xx} = \frac{1}{\Pi}\left(K\gamma_x^2 + L\gamma_x + M\right)$$

$$\gamma_{xy} = -\frac{1}{\Pi}\left\{\left(rK + r_{001}\Pi\right)\gamma_x^2 + \left[rL + \left(r_{100} - s_{001}\right)\Pi\right]\gamma_x + rM - s_{100}\Pi\right\} \quad (15)$$

$$\gamma_{yy} = \frac{1}{\Pi}\left\{\left(r^2K + 2rr_{001}\Pi\right)\gamma_x^2 + \left[r^2L + \left(rr_{100} - r_{010} - sr_{001} - 2rs_{001}\right)\Pi\right]\gamma_x + r^2M - \left(rs_{100} + ss_{001} + s_{010}\right)\Pi\right\}.$$

Remark 1 As we have already mentioned, we have $V_y\gamma + V_x \neq 0$. The case $\gamma + r = 0$ will be studied later. For the moment we suppose that the denominator Π in (15) is different from zero.

Working with (15) we find that the two compatibility conditions $(\gamma_{xx})_y = (\gamma_{xy})_x$ and $(\gamma_{xy})_y = (\gamma_{yy})_x$ produce *one single relation* which, after substituting γ_{xx}, γ_{xy} and γ_{yy} given by (15) and γ_y from (3), reduces to a third-degree algebraic equation in γ_x

$$\Gamma_3\gamma_x^3 + \Gamma_2\gamma_x^2 + \Gamma_1\gamma_x + \Gamma_0 = 0. \quad (16)$$

The coefficient Γ_3 of γ_x^3 in (16) is given by

$$\Gamma_3 = (\gamma + r)^2\left(V_y\gamma + V_x\right)\left[\left(V_y\gamma + V_x\right)(\gamma + r)\,r_{002} - 2\left(V_y\gamma + V_x\right)r_{001}^2 + \left(2V_y\gamma + 3rV_y - V_x\right)r_{001}\right]. \quad (17)$$

In the last factor of Γ_3, all the terms contain the derivatives of r with respect to its third variable γ. It follows that, if r depends merely on x and y, equation (16) is in fact at most of second degree in γ_x. There are significant situations when this condition is fulfilled, as in the case of functions γ homogeneous of order $m \neq 0$, which verify

$$x\gamma_x + y\gamma_y = m\gamma. \quad (18)$$

The coefficient Γ_0 in (16) reads

$$\Gamma_0 = a_1s^3 + a_2s^2 + a_3s - \left(V_y\gamma + V_x\right)\left(a_4s_{200} + a_5s_{110} + a_6s_{020} + a_7s_{100} + a_8s_{010}\right). \quad (19)$$

It follows that the coefficient $\Gamma_0 = 0$ if $s(x, y, \gamma) = 0$. After a factorization by γ_x, equation (16) is again of second degree.

Remark 2 When γ satisfies the condition (1) (case studied by Anisiu et al, 2004), in equation (16) $\Gamma_3 = \Gamma_0 = 0$. Therefore γ_x is the solution of an equation of first degree. This happens, for example, for γ homogeneous of order 0.

In what follows, to ease the algebra, we shall assume that the functions r and/or s are of a form that makes equation (16) of second degree, i.e.

$$G_2\gamma_x^2 + G_1\gamma_x + G_0 = 0. \tag{20}$$

We differentiate (20) with respect to x and substitute the second-order derivatives of γ from (15) and γ_y from (3); the result will be an equation of third order in γ_x

$$H_3\gamma_x^3 + H_2\gamma_x^2 + H_1\gamma_x + H_0 = 0. \tag{21}$$

Our calculations have shown that equation (21) is of second degree if $s = 0$; but it will be of third degree for homogeneous functions of order m. In order that (20) and (21) have a common solution, the necessary and sufficient condition is that their resultant is null. This is a first condition that γ has to fulfil.

Let us suppose that the resultant of (20) and (21) is null. We express γ_x^2 from (20) and substitute it in the first two terms of (21), then again in the result. It follows that γ_x is given by

$$\left(H_3G_1^2 - H_3G_2G_0 - H_2G_2G_1 + H_1G_2^2\right)\gamma_x + H_3G_1G_0 - H_2G_2G_0 + H_0G_2^2 = 0. \tag{22}$$

If the coefficient of γ_x is different from zero, we can express γ_x as a function of γ

$$\gamma_x = -\frac{H_3G_1G_0 - H_2G_2G_0 + H_0G_2^2}{H_3G_1^2 - H_3G_2G_0 - H_2G_2G_1 + H_1G_2^2}, \tag{23}$$

and γ_y from (3) as

$$\gamma_y = s - r\gamma_x. \tag{24}$$

We write the compatibility condition $(\gamma_x)_y = (\gamma_y)_x$, in which we replace γ_x by (23) and γ_y by (24); we obtain a second condition on γ.

From (23) and (24) we can express, after differentiation, $\gamma_{xx}, \gamma_{xy}, \gamma_{yy}$ in terms of γ and derivatives of V up to the fifth order. We insert these values in the basic equation (6), and then the values of γ_x and γ_y from (23) and (24). We obtain a third condition on γ. In order to obtain solutions of the problem under consideration, these three necessary conditions must be satisfied.

If the coefficient of γ_x in (22) is zero and the other term is not zero, we have no solution for our problem. If both coefficients in (22) are null, we are left with equation (20).

As an application to the reasoning developed in this section, we shall study first the case of functions γ which are homogeneous of order m.

4 Functions γ homogeneous of order m

Let us suppose that γ satisfies (18), hence we have $r = x/y$ and $s = m\gamma/y$. As stated above, the first equation in γ_x (20) is of second degree; its coefficients are in this case polynomials in γ. This will happen for the coefficients of the third-degree equation (21) too.

The three conditions on γ are in this case polynomials in γ. For a common solution to exist, a necessary condition is that the resultants of the two pairs of polynomials vanish. The resultants are equal to their Sylvester determinants (Mishina and Proskuryakov, 1965, p. 164). Thus we obtain two necessary conditions to be satisfied by the potential V.

When we start working with a given potential V and a fixed degree of homogeneity for γ, we do not expect the problem to have always a solution. It is advisable to try to factor the first polynomial in γ (the resultant of (20) and (21)) and to check directly if the homogeneous functions γ are compatible with the potential. Proceeding this way we avoid lengthy calculations.

Example 1 *Let us consider $V(x,y) = -x^4 - y^2$ and look for functions γ homogeneous of first order. The polynomials (20) and (21) are of second, respectively third, degree and their resultant is*

$$R_1 = \gamma^5 \left(y\gamma - x^2\right) \left(y\gamma + x^2\right) \left(y\gamma + x\right)^3 \left(y\gamma + 2x^3\right)^4 P_{10}. \tag{25}$$

The index of P denotes in this example the degree of the respective polynomial in γ. The second condition, which follows from the compatibility $(\gamma_x)_y = (\gamma_y)_x$, reads

$$R_2 = \left(y\gamma - x^2\right) \left(y\gamma + x^2\right) \left(y\gamma + x\right) \left(y\gamma + 2x^3\right) P_{12}. \tag{26}$$

Finally, the condition obtained from the basic equation (6) is

$$R_3 = \left(y\gamma - x^2\right) \left(y\gamma + x^2\right) \left(y\gamma + 2x^3\right) P_{22}. \tag{27}$$

The three polynomials in γ have in common two homogeneous solutions of first order, namely $\gamma_1 = x^2/y$ and $\gamma_2 = -x^2/y$, which correspond to the families $f_1 = ye^{-1/x}$, and $f_2 = ye^{1/x}$ and are compatible with the given potential.

5 Special cases and other examples

The case $r = -\gamma$, $s = 0$ ($\Gamma = 0$)

From the equation (8) it follows that

$$\gamma = -\frac{V_x}{V_y} \tag{28}$$

and only potentials $V(x, y)$ satisfying the differential condition

$$V_x V_y (V_{xx} - V_{yy}) = (V_x^2 - V_y^2) V_{xy} \tag{29}$$

are generating families having $\Gamma = 0$ (Bozis and Anisiu, 2001). So then, for our problem, we see immediately if the given potential satisfies or not the condition (29) and, if the potential is admissible, we readily check whether or not the pertinent γ, given by (28), satisfies the pre-assigned condition (3).

As another viewpoint, let us discuss briefly the following two alternatives, possibly leading to an affirmative answer of our problem:

(i) Let us fix the condition (3) but allow the potential $V(x, y)$ to be free. In this case we must inquire whether there exist common solutions for the PDE (29) and the PDE

$$r^* V_y V_{xx} + (V_y - r^* V_x) V_{xy} - V_x V_{yy} + s^* V_y^2 = 0, \tag{30}$$

where

$$r^*(x, y) = r\left(x, y, \gamma = -\frac{V_x}{V_y}\right) \text{ and } s^*(x, y) = s\left(x, y, \gamma = -\frac{V_x}{V_y}\right). \tag{31}$$

The compatibility of these two equations may be checked in a straightforward way.

(ii) Let us consider a potential $V(x, y)$ satisfying the condition (29), i.e. a potential which produces the family (28) of straight lines and let the functions r and s in (3) be at our disposal. In this case we are led to infinitely many choices for r and s for which the condition (30) is satisfied. Indeed, we can take

$$r(x, y, \gamma) = -\gamma + \left(\gamma + \frac{V_x}{V_y}\right) A(x, y, \gamma) \text{ and } s(x, y, \gamma) = \left(\gamma + \frac{V_x}{V_y}\right) B(x, y, \gamma), \tag{32}$$

where A and B are arbitrary functions with the unique provision that the pertinent functions $A^*(x, y)$ and $B^*(x, y)$ (defined as indicated in (31)) do not become

infinite. By choosing the functions r and s as in (32), we have $r^*(x,y) = V_x/V_y$ and $s^*(x,y) = 0$, hence condition (30) is identical to (29).

The case $r = -\gamma$, $s \neq 0$

In this case $\Pi = 0$ in the first of the equations (14) and the formulae (15) are meaningless. Let us suppose that $r(x,y,\gamma) = \gamma$ identically. The condition (3) becomes

$$\gamma\gamma_x - \gamma_y = -s, \tag{33}$$

where s may depend on all three variables x, y and γ. We suppose here that s is not identically null, to avoid that (33) coincides with $\Gamma = 0$ (treated above).

From the derivatives of (33) with respect to x and y, we find

$$\gamma^2\gamma_{xx} - 2\gamma\gamma_{xy} + \gamma_{yy} = s_{010} - \gamma s_{100} + s\gamma_x + ss_{001}. \tag{34}$$

So, in view of (7) and (34), equation (6) may be written as

$$\begin{aligned} &s(V_x + \gamma V_y)s_{001} = (V_x + \gamma V_y)(\gamma s_{100} - s_{010}) \\ &+s\left[\gamma(V_{yy} - V_{xx}) + (1-\gamma^2)V_{xy} + 3sV_y\right]. \end{aligned} \tag{35}$$

The above equation (35) replaces the PDE (6) and its meaning is the following: In order that the given potential $V(x,y)$ supports a family γ, the "given" function $s(x,y,\gamma)$ in (33) must satisfy the PDE (35). In other words, for our problem to admit of an affirmative answer, the required function $\gamma(x,y)$ and the "given" function $s(x,y,\gamma)$ must satisfy both equations (33) and (35). To check if these equations have common solutions γ we proceed as follows: From (35) we can express (by differentiation) γ_x and γ_y in terms of γ and insert them into (33), which then will become an equation of the form

$$F(x,y,\gamma) = 0. \tag{36}$$

Finally we check whether equations (36) and (35) have or do not have common solutions $\gamma(x,y)$.

Example 2 *Let us find solutions of (33) with $s(x,y,\gamma) = -6x/y^2$ which represent families compatible with the potential*

$$V(x,y) = 4x^2 + y^2 + 8x^4 - 2x^2y^2 - y^4 + x^3. \tag{37}$$

Condition (35) is in this case a second-degree polynomial equation in γ, which has the solutions

$$\gamma = \frac{2x}{y} \quad \text{and} \quad \gamma = \frac{2x\left(17x^2 + 7y^2\right)}{y\left(2x^2 - 2y^2 + 1\right)}. \tag{38}$$

The first one is a solution of our problem.

It may happen that $\Pi = 0$ for some particular functions γ. In such a case, we have to check if this particular γ satisfies equation (3). In the affirmative case, we put the values of V and γ in (6)-(7) and, if we obtain an identity, we have a solution of our problem.

Example 3 *Let us look for families γ which are compatible with the Hénon-Heiles potential*

$$V(x,y) = \frac{1}{2}\left(x^2 + 16y^2\right) + x^2 y + \frac{16}{3}y^3 \tag{39}$$

and which satisfy the equation (3) with $r(x,y,\gamma) = x/y + 3\gamma$ and $s(x,y,\gamma) = -3\gamma/(4y)$. The equality $\gamma + r = 0$ holds if and only if $\gamma = -x/(4y)$. This function verifies the equation (3) for the specified values of r and s, and, together with the potential (39), equation (6)-(7), hence it is a solution of our problem. The same family has been found by Bozis et al (1997) as a homogeneous family generated by the inhomogeneous potential (39).

Remark 3 If $V(x,y)$ and $s(x,y,\gamma)$ are left free (to be adequately determined) the possibly existing common solutions $\gamma(x,y)$ of (35) and (36) will be expressed in terms of partial derivatives of the second order in $s(x,y,\gamma)$ and of the third order in $V(x,y)$.

6 General comments

In the framework of the inverse problem of Dynamics, a monoparametric family of orbits is uniquely represented by its slope function γ defined in (5). For a given potential $V(x,y)$, the finding of some or all families generated by V amounts to the solution of the nonlinear in γ second order PDE (6). This is a task more or less impossible.

In this paper, in order to ease and make possible the solution of the problem (even by finding a subset of solutions), we add the restriction on γ expressed by the differential condition (3). In so doing, we come to have to deal with two PDEs, one of the first and one of the second order in the unknown function $\gamma(x,y)$. Therefore the very existence of a solution is not guaranteed. Yet, we showed that, if such a solution does exist, its finding may be accomplished by algebraic manipulation.

We deal basically with the direct problem, i.e. the potential is given and the orbits are to be found. The functions $r(x,y,\gamma)$ and $s(x,y,\gamma)$ are also generally given. One then might suggest to face the problem by solving for γ the first order PDE (3) and then proceed to find, among its solutions, those which are

compatible with the given potential. However, this last task (possible in some of the examples presented in this paper) does not seem to be easier or performable by a straightforward way. Besides that, the finding of the general solution of (3) is not *always* possible.

The above strictly direct problem does not generally have a solution. For this reason, we may profitably deal with the two equations (3) and (6) in various ways. We can e.g. allow tentatively the potential $V(x, y)$ to be free and find compatibility conditions on it so that a solution $\gamma(x, y)$ can be found. Or, keeping $V(x, y)$ fixed, we may allow the functions r and s in (3) to be free and then adjust them properly so that we obtain a solution.

References

[1] Anisiu, M.-C., Blaga, C. and Bozis, G.: 2004, Special families of orbits in the direct problem of dynamics, *Celest. Mech. Dyn. Astron.* **88**, 245-257.

[2] Bǫzis, G.: 1983, Inverse problem with two-parametric families of planar orbits, *Celest. Mech.* **31**, 129-143.

[3] Bozis, G.: 1984, Szebehely's inverse problem for finite symmetrical material concentrations, *Astronom. Astrophys.* **134**(2), 360-364.

[4] Bozis, G. and Ichtiaroglou, S.: 1994, Boundary curves for families of planar orbits, *Celest. Mech. Dyn. Astron.* **58**, 371-385.

[5] Bozis, G.: 1995, The inverse problem of dynamics. Basic facts, *Inverse Problems* **11**, 687-708.

[6] Bozis, G., Anisiu, M.-C. and Blaga, C.: 1997, Inhomogeneous potentials producing homogeneous orbits, *Astron. Nachr.* **318**, 313-318.

[7] Bozis, G. and Grigoriadou, S.: 1993, Families of planar orbits generated by homogeneous potentials, *Celest. Mech. Dyn. Astron.* **57**, 461-472.

[8] Bozis, G., Anisiu, M.-C. and Blaga, C.: 2000, A solvable version of the direct problem of dynamics, *Rom. Astronom. J.* **10**(1), 59-70.

[9] Bozis, G. and Anisiu, M.-C.: 2001, Families of straight lines in planar potentials, *Rom. Astronom. J.* **11**(1), 27-43.

[10] Hénon, M. and Heiles, C.: 1964, The applicability of the third integral of motion: some numerical experiments, *Astron. J.* **69**, 73-79.

[11] Mishina, A. P. and Proskuryakov, I. V.: 1965, *Higher Algebra*, Pergamon Press, Oxford-London.

[12] Szebehely, V.: 1974, On the determination of the potential by satellite observation, in: E. Proverbio (ed.) *Proceedings of the International Meeting on Earth's Rotations by Satellite Observations*, Cagliari, Bologna, 31-35.

PADEU | PADEU **19** (2007), p. 29
ISBN 963 463 557
©Published by the Astron. Dept. of the Eötvös Univ.

Direct and inverse consideration of the question of integrability

George Bozis

Department of Physics,
University of Thessaloniki,
Greece 540 06
E-mail: gbozis@auth.gr

Abstract

The question of the integrability of two-dimensional potentials $V = V(x, y)$ is considered in the light and treated with the tools of the inverse problem of Dynamics. A new equation is proposed to replace the requirement of the vanishing of the Poisson bracket. Both the direct and the inverse problem for 2-D integrable potentials are studied on the basis of this equation. The cases of superintegrability and of conditional integrability are also discussed. Examples and applications are treated in some detail.

Keywords: *Integrability, inverse problem*

1 Introduction

We deal with autonomous two-dimensional potentials $V = V(x, y)$ in Cartesian coordinates, giving rise to families of orbits traced by one material point. Integrability of the potential is meant in the sense of Liouville, i.e. as the possibility of vanishing the pertinent Poisson bracket of the pair of the energy E and the "second integral" of motion (or "invariant") $I(x, y, \dot{x}, \dot{y}) = const.$

The direct-problem viewpoint is: For a given potential, to check analytically its integrable character, i.e. to decide if a dynamical function $I(x, y, \dot{x}, \dot{y})$ does exist in the phase space so that the Poisson bracket $[E, I] = 0$. The great interest in this problem is revealed by the large range of the literature (Lieberman and

Lichtenberg, 1983; Tabor, 1989; Goriely, 2001). An account of relevant literature may be found in Hietarinta's papers (1983, 1986).

The inverse-problem viewpoint is: We are given an expression $I = I(x, y, \dot{x}, \dot{y})$ of the position and the velocity coordinates and we want to know if an autonomous potential $V(x, y)$ does exist so that the Poisson bracket $[E, I]$ vanishes. A first hint on this problem is credited to Bertrand (1852) and is reported by Whittaker (1961, section 151). Developing this idea, Bozis and Ichtiaroglou (1987) established necessary and sufficient conditions which the given expression must satisfy. In fact these conditions were generally given both for velocity independent and velocity dependent force fields. In the present paper the integrability problem is studied in the light of Szebehely's modified PDE (Bozis, 1995). This equation relates potentials $V(x, y)$ and monoparametric families of orbits $f(x, y) = c$, traced with an energy-dependence function $E = \tilde{E}(f(x, y))$, given in advance. The family is uniquely represented by its "slope function" $\gamma(x, y) = f_y/f_x$ (equation (2) below, in section 2). This allows us to express the (possibly existing) second integrals of the motion in the form $\Phi = \Phi(x, y, \gamma, E) = const.$ and present our basic result (equation (15) in section 3). There follow certain comments on the equation (15) and also another derivation of (15). In section 4 we look at the problem from the inverse viewpoint and we offer three necessary and sufficient conditions so that a function of the variables x, y, γ, E given in advance can stand for a second invariant of a potential to be determined. Two examples are commented in some detail. An application of the basic formula (15) is presented in section 5. The role of the other tool of the inverse problem, the pertinent second order PDE, is discussed in section 6, in particular as regards possible superintegrability. In sections 7 and 8, with the aid of formula (15), we discuss the question of conditional integrability from the direct and the inverse point of view. We study configurational invariants, i.e. dynamical quantities which remain constant on the three-dimensional manifold $E = 0$, in the 4-D phase space. Potentials which satisfy the Bateman's second order PDE are studied in section 9 as candidate conditionally integrable or fully integrable, in connection with existing results in the literature. Some remarks are made and some questions for further consideration are put in section 10. The advantages of the new formula (15) and the labor involved in dealing with it compared to other approaches are also discussed in the same section 10.

2 Basic formulae

We consider motion of one massive particle of unit mass in an inertial frame in the xy plane under the action of an autonomous potential $V = V(x, y)$. The energy integral is

$$E = \frac{1}{2}(\dot{x}^2 + \dot{y}^2) + V(x, y) \tag{1}$$

and Szebehely's first order PDE, written for direct problem considerations, reads

$$2(E - V)(\gamma\gamma_x - \gamma_y) = -(1 + \gamma^2)(V_x + \gamma V_y). \tag{2}$$

Dots denote derivatives in the time t and subscripts denote partial differentiation in the pertinent variable. The function

$$\gamma(x, y) = \frac{f_y}{f_x} \tag{3}$$

stands for the "slope function" of any monoparametric family of orbits

$$f(x, y) = c \tag{4}$$

supposedly supported by the potential $V(x, y)$. There is an one-to-one correspondence of families of orbits (4) and slope functions (3). Due to this, we shall refer to each family by its pertinent function $\gamma(x, y)$. Expressed in terms of the velocity components, the slope function is

$$\gamma = -\frac{\dot{x}}{\dot{y}} \tag{5}$$

(so that $f_x\dot{x} + f_y\dot{y} = 0$) and, along any member of any family (4), the velocity components are

$$\dot{x} = -\epsilon\gamma\sqrt{\frac{2(E - V)}{(1 + \gamma^2)}}, \quad \dot{y} = \epsilon\sqrt{\frac{2(E - V)}{(1 + \gamma^2)}}, \quad (\epsilon = \pm 1). \tag{6}$$

The energy E in equations (2) and (6) generally differs from orbit to orbit, i.e.

$$E = \tilde{E}(f(x, y)) \tag{7a}$$

with $f(x, y) = c$ given by (4). Because of (7a) and (3), we have

$$\tilde{E}_y = \gamma\tilde{E}_x \tag{7b}$$

and this leads to the energy-free second order PDE (Bozis, 1995)

$$\gamma^2\gamma_{xx} - 2\gamma\gamma_{xy} + \gamma_{yy} = (\gamma\gamma_x - \gamma_y)H, \tag{8a}$$

where

$$H = \frac{1}{(V_y\gamma + V_x)}\left[2V_y\gamma\gamma_x - V_x\gamma_x - 3V_y\gamma_y + V_{xy}\gamma^2 + (V_{xx} - V_{yy})\gamma - V_{xy}\right]. \tag{8b}$$

If a family $\gamma(x,y)$ and a potential $V(x,y)$ are compatible, in the sense that they satisfy (8), then equation (2), solved for $E = \tilde{E}$, will reveal the energy dependence function (7). Whenever, dealing with a specific pair (V,γ), we want to calculate the velocity components $\dot{x},\dot{y}$ of the orbit at a point (x,y) of the plane, we must use the value $\tilde{E}(c)$ from (7a) for this particular orbit. As far as the variation in time is concerned, the energy E, as given by (1), is constant and is used, together with the function γ given by (5), to replace the velocity components $(\dot{x},\dot{y})$ at a point (x,y) in agreement with formulae (6). Equation (8) will be used as a complement in our analysis, in some detail in section 6, to detect possible superintegrability of the given potential, whereas equation (2) will be our main tool.

3 Basic equation for integrable potentials

Equation (2) cannot be used to face the direct problem (i.e. given the potential to find the monoparametric family $\gamma = \gamma(x,y)$) because the family (4) corresponding to the required γ is not known and $E = \tilde{E}$ cannot be given in advance. Yet, this equation (2) becomes meaningful if E is considered as a parameter. Here we treat the constant E given by (1) as one of the generalized velocity components. So, if, for a given potential $V(x,y)$ and any parameter E, we could obtain a solution of (2) of the form

$$\gamma = \gamma(x,y,E) \tag{9}$$

this would be one particular solution of (2) for any E. Thus, the finding of (9) amounts to the finding of a set of γ's depending on the parameter E, i.e. to a two-parameter set of families $f(x,y,E) = c_0$. These families can actually be established if the general solution of the ODE $dy/dx = -1/\gamma(x,y,E)$ can be found. It is noticeable that in verifying that the PDE (2) is indeed satisfied by (9), it makes no difference if we consider E to be a parameter or to be taken equal to $\tilde{E}$ from (7a) and this, of course, is due to (7b). On the other hand if,

for the same potential, we manage to establish a richer solution of (2), of the form

$$\gamma = \gamma(x, y, E, \bar{\Phi}) \tag{10}$$

where $\bar{\Phi}$ is a new constant, then it is as if we have found what we call an orbital function for this potential (Bozis, 2005). Having an orbital at our disposal, we can assert that the given potential is integrable. This is justified as follows: The equation (10) in principle implies that there exist functions $\bar{\Phi}$ expressed as

$$\bar{\Phi} = \Phi(x, y, \gamma, E). \tag{11}$$

The fact that $\bar{\Phi} = const.$ is interpreted to mean that

$$\bar{\Phi}\left[x, y, \gamma = -\frac{\dot{x}}{\dot{y}}, E = \frac{1}{2}(\dot{x}^2 + \dot{y}^2) + V(x, y)\right] = const. \tag{12}$$

The above equation (12) actually stands for the second integral written in the usual form

$$I(x, y, \dot{x}, \dot{y}) = const. \tag{13}$$

From $d\bar{\Phi}/dt = 0$, in view of (11) and since E is constant in time and $\dot{\gamma} = \gamma_x \dot{x} + \gamma_y \dot{y}$, we obtain

$$\Phi_x \dot{x} + \Phi_y \dot{y} + \Phi_\gamma(\gamma_x \dot{x} + \gamma_y \dot{y}) = 0. \tag{14}$$

Then, in view of equations (2) and (6), equation (14) becomes

$$2(E - V)(\gamma \Phi_x - \Phi_y) = (1 + \gamma^2)(V_x + \gamma V_y)\Phi_\gamma. \tag{15}$$

The above equation (15) is our basic finding. For a given potential $V(x, y)$ and with the (additive to it) constant E treated as a parameter, the finding of any nontrivial particular solution of (15), of the form (11), would prove the integrability of $V(x, y)$ and would provide the pertinent second integral. To establish integrability of the given potential, we need find a solution γ of (2) of the form (10), i.e. a solution broader from the particular solution (9) in the sense that, besides the constant energy E, an additional constant $\bar{\Phi}$ must enter into the scene. On the other hand, the finding of a particular solution $\Phi(x, y, \gamma, E)$ of (15) for any E suffices to imply the existence of the second integral of the potential $V(x, y)$ and actually establishes the invariant itself. Of course, the task is now heavier, in the sense that the required function Φ, now depends on three variables (not two, as the solution of (2) for γ does).The equation (15) substitutes the requirement of the vanishing of the Poisson bracket

$[I, E]$. Indeed, the fact that $[I, E] = 0$, with I and E taken from (13) and (1) respectively, leads to

$$\frac{\partial I}{\partial x}\dot{x} - \frac{\partial I}{\partial \dot{x}}V_x + \frac{\partial I}{\partial y}\dot{y} - \frac{\partial I}{\partial \dot{y}}V_y = 0. \tag{16}$$

Because $I(x, y, \dot{x}, \dot{y}) = \Phi(x, y, \gamma, E)$ and in view of (5), it is

$$\begin{array}{ll} \frac{\partial I}{\partial x} = \Phi_x + \Phi_E V_x, & \frac{\partial I}{\partial y} = \Phi_y + \Phi_E V_y, \\ \frac{\partial I}{\partial \dot{x}} = -\frac{1}{\dot{y}}\Phi_\gamma + \dot{x}\Phi_E, & \frac{\partial I}{\partial \dot{y}} = \frac{\dot{x}}{\dot{y}^2}\Phi_\gamma + \dot{y}\Phi_E. \end{array} \tag{17}$$

Inserting (17) into (16) and taking into account the equations (7), we re-obtain the basic equation (15), which may also be written as

$$(E - V)R = V_x + \gamma V_y, \tag{18}$$

where

$$R(x, y, \gamma, E) = \frac{2(\gamma\Phi_x - \Phi_y)}{(1 + \gamma^2)\Phi_\gamma}. \tag{19}$$

Remarks:

1. As expected and as seen from (15), if $\Phi(x, y, \gamma, E)$ is a solution, then any arbitrary function of Φ is also a solution of (15). Notice also that, on purpose of revealing integrability of a given potential and obtaining the pertinent second integral, certain solutions of the equation (15) are considered trivial. These are:

(i) of the form $\Phi(x, y, E)$ or $\Phi(x, y, \gamma)$. Indeed, in the first case, $\Phi_\gamma = 0$ would imply $\gamma\Phi_x - \Phi_y = 0$ and, ultimately, $\Phi = \Phi(E)$. In the second case, E in (15) would have no partner to balance. In other words, neither γ nor E can be absent from the expression (11).The only exception to the above (apart from the arbitrary function) is the solution

$$\Phi = E \tag{20}$$

which, of course, is valid for any potential $V(x, y)$ but which is not an independent invariant.

(ii) of the form $\Phi(\gamma, E)$, i.e. solutions with both positional coordinates absent. In this case (15) would imply $\Phi_\gamma = 0$ and this would lead again to (20).

2. The denominator in (19) does not vanish unless the numerator also vanishes. This corresponds again to the solution (20). The ratio (19) becomes indeterminate and no other independent integral exists.

3. The solution (9) of the equation (2) may be considered as the obvious zero-solution of (15): $\Phi = \gamma - \gamma(x, y, E) = 0$ (which, of course, does not suffice to ensure integrability). This remark interrelates the two equations (2) and (15). Indeed, for $\Phi_\gamma = 1$, $\Phi_x = -\gamma_x$, $\Phi_y = -\gamma_y$, the equation (15) reduces to (2).

4 The potential expressed in terms of the second integral

We now look at the problem from the inverse viewpoint: A candidate invariant is given and the corresponding potential, if it exists, is required. Specifically we suppose that, somehow, we are given an equation in the form (11) i.e. $\Phi(x,y,\gamma,E) = const.$, together with the information that E stands for the energy and γ for the slope function at the point (x,y) of an orbit traced by a unit mass point (this last piece of information is equivalent to the assertion that $\dot{x},\dot{y}$ in (13) stand for velocity components). We are asked to find the conditions under which this equation $\Phi(x,y,\gamma,E) = const.$, can stand for a second integral for some unknown potential $V(x,y)$, to be determined.We shall see that these conditions are actually put (not directly on the given function $\Phi(x,y,\gamma,E)$ but) on the function $R(x,y,\gamma,E)$, as this is defined by (19). We proceed as follows: We differentiate (18) with respect to the parameter E and we obtain

$$R + (E - V)R_E = 0. \tag{21}$$

From (21), we obtain the potential

$$V(x,y) = E + \frac{R}{R_E}. \tag{22}$$

Formula (22) has been derived under the tacit assumption that an appropriate function R, as defined by (19), does exist (not only in the sense of being determined as a ratio but also) in the sense that it comes from an "appropriate" $\Phi(x,y,\gamma,E)$. (Inappropriate would be functions $\Phi(x,y,\gamma,E)$ for which (22) would not ultimately lead to an autonomous potential). In fact, the left side of (22) must be independent of γ and E, meaning that

$$\left(\frac{R}{R_E}\right)_\gamma = 0 \text{ and } \left(\frac{R}{R_E}\right)_E = -1. \tag{23}$$

A final requirement is that the potential $V(x,y)$, given explicitly by (22), does indeed satisfy the basic equation (15). In taking derivatives in x,y of the ratio R/R_E in (22), we consider E as one of the four independent variables x,y,γ,E. So, we take $E_x = E_y = 0$ and the above requirement leads to the condition

$$\left(\frac{R_x + \gamma R_y}{R} - R\right)_E = 0. \tag{24}$$

In conclusion: The three conditions (23) and (24) are necessary and sufficient for the function R, defined by (19), so that a given expression (11) stands for a second integral of an autonomous potential, which is then given by (22).

Examples

1. For any function $\Lambda = \Lambda(r)$, $r = \sqrt{x^2 + y^2}$, we assert that the function

$$\Phi = \left(\frac{E - \Lambda}{1 + \gamma^2}\right)^{\frac{n}{2}} (x + y\gamma)^n \tag{25}$$

is an admissible function $\Phi(x, y, \gamma, E)$. Indeed, from (25) and (19) we find $R = (x + y\gamma)\Lambda_r/(r(E - \Lambda))$ and we check that the three conditions (23) and (24) are satisfied. The corresponding potential $V(x, y) = \Lambda(r)$ is found from (22). With this function Λ back to (25) we find that $\Phi = (x\dot{y} - \dot{x}y)^n$, i.e. the n-th power of the angular momentum integral $L = x\dot{y} - \dot{x}y$ is constant.

2. It is known that all potentials producing the circles $r = const.$ are of the form

$$V(r, \theta) = g(r) + \frac{1}{r^2} h(\theta) \tag{26}$$

and they are all integrable for any arbitrary functions $g(r)$ and $h(\theta)$. We can verify that to the expression

$$\Phi(x, y, \gamma, E) = \frac{(Exr^2 - y)(x + y\gamma)^2}{(1 + \gamma^2)xr^2} + \frac{y}{x} \tag{27a}$$

there corresponds the function

$$R(x, y, \gamma, E) = \frac{\{\gamma x(x^2 - y^2) - y(3x^2 + y^2)\}}{xr^2(Exr^2 - y)}. \tag{27b}$$

This function R satisfies the integrability conditions (23) and (24) and, according to (22), leads to the potential $V(x, y) = y/(xr^2)$ (which is of the form (26)). According to (12) and (13), the second integral is $I(x, y, \dot{x}, \dot{y}) = (x\dot{y} - \dot{x}y)^2/2 + y/x$. It is noticeable that all homogeneous potentials in x, y of degree of homogeneity -2, can be brought to the form (26) and, as such, they are integrable (the function $g(r)$ must be put equal to zero and the function $h(\theta)$ must be selected appropriately).

5 An application - Integrals homogeneous in the velocity components

Let us consider invariants (13) which are homogeneous in the components of the velocity of degree n, i.e. of the form

$$I(x,y,\dot{x},\dot{y}) = \sum_{p=0}^{n} A_p^n(x,y)\dot{x}^p\dot{y}^{n-p}. \tag{28}$$

In view of (6), the above equation becomes

$$\Phi(x,y,\gamma,E) = \left(\frac{2(E-V)}{(1+\gamma^2)}\right)^{\frac{n}{2}} \epsilon^n \sum_{p=0}^{n}(-1)^p A_p^n(x,y)\gamma^p. \tag{29}$$

We put the question: are there functions $\Phi(x,y,\gamma,E)$ of the form

$$\Phi(x,y,\gamma,E) = \left(\frac{E-\Lambda(x,y)}{(1+\gamma^2)}\right)^{\frac{n}{2}} M(x,y,\gamma) \tag{30}$$

which satisfy the three conditions (23) and (24)? More specifically: can we find an appropriate function $\Lambda(x,y)$ (to be identified with the potential $V(x,y)$) and a function $M(x,y,\gamma)$(to be identified with the series-factor in (29))?

For the function (30), from (19) we find

$$R(x,y,\gamma,E) = \frac{\{2(E-\Lambda)(\gamma M_x - M_y) - n(\gamma\Lambda_x - \Lambda_y)M\}}{(E-\Lambda)\{(1+\gamma^2)M_\gamma - n\gamma M\}}. \tag{31}$$

Inserting (31) into the second of the two conditions (23) , we obtain

$$\gamma M_x - M_y = 0 \tag{32}$$

whose general solution is

$$M = M(\gamma, w),\ w = x + y\gamma. \tag{33}$$

Using (33) and its implications as regards higher derivatives of M (e. g. $M_{y\gamma} = M_w + \gamma M_{\gamma w}$), we find that the first condition (23) is identically satisfied. We now come to the third condition (24). Keeping always in mind that M is given by (33), we come to the result

$$(\Lambda_x + \gamma\Lambda_y)M_\gamma - n\Lambda_y M = 0. \tag{34}$$

From (34) we obtain

$$M(x,y,\gamma) = A(x,y)(\Lambda_x + \gamma\Lambda_y)^n \tag{35}$$

where $A(x,y)$ is arbitrary as far as (34) is concerned. However, the function M, as given by (35), must coincide with M as given by (33). To this end it is necessary that the arbitrary function $A(x,y)$ is selected so that

$$\Lambda_x = xA^{-\frac{1}{n}}, \quad \Lambda_y = yA^{-\frac{1}{n}}. \tag{36}$$

So, we have

$$M(x,y,\gamma) = (x + y\gamma)^n \tag{37}$$

and the expression for Φ in (30) coincides with that in (25). On the other hand, from (36) we obtain $y\Lambda_x = x\Lambda_y$, i.e. $\Lambda = \Lambda(r)$ with $r = \sqrt{x^2+y^2}$ and the restriction $\Lambda_{xy} = \Lambda_{yx}$ leads to $A = A(r)$ also. Clearly, the potential $V(r) = \Lambda(r)$ must be central and the corresponding homogeneous integral must be the n-th power of the angular momentum.

6 Direct problem - The role of the second order PDE (8)- Superintegrability

Let us now suppose that, for a given potential, somehow, we manage to obtain a solution

$$\gamma = \gamma(x,y,c_1,c_2) \tag{38}$$

of the second order PDE (8), depending on two constants c_1, c_2. As the energy is absent from (8), we do not know if and how these constants are related to the energy which, of course, we want to bring into the scene, so that we finally obtain the orbital (10). To this end, we are aided by Szebehely's modified equation (2). Inserting the solution (38) in (2), generally we expect to obtain a relation of the form

$$T(x,y,E,c_1,c_2) = 0. \tag{39}$$

Two cases may arise:

(A) It may be that the positional coordinates x, y do not appear explicitly in (39). This is interpreted to mean that the "three" constants E, c_1, c_2 are not independent. They are related by the relation (39) , so, besides the energy, one additional independent invariant is to be expected. The potential of course is integrable.

Example 1. It can be checked that, for the Newtonian potential

$$V = -\frac{1}{r},\ r = \sqrt{x^2 + y^2} \tag{40}$$

(gravitational constant = 1), all slope functions

$$\gamma(x, y, c_1, c_2) = \frac{c_1 y - x\sqrt{c_1(2r - c_2 r^2 - c_1)}}{c_1 x + y\sqrt{c_1(2r - c_2 r^2 - c_1)}} \tag{41}$$

satisfy the equation (8), for all values of the constants c_1, c_2. Bringing (41) into (2), we find that

$$2E + c_2 = 0. \tag{42}$$

Therefore, in (41), c_2 must be expressed in terms of the energy E before the second integral $c_1 = \Phi(x, y, \gamma, E)$ is found from (41). There results

$$\Phi(x, y, \gamma, E) = \frac{2(1 + Er)(x + y\gamma)^2}{(1 + \gamma^2)r} \tag{43}$$

which, according to (12), leads to $I(x, y, \dot{x}, \dot{y}) = (x\dot{y} - \dot{x}y)^2$, the square of the expected angular momentum constant

$$L = x\dot{y} - \dot{x}y. \tag{44}$$

(B) It may be that the positional coordinates x, y do appear explicitly in (39). This means that there exist indeed three independent invariants c_1, c_2 and E, in other words, the potential at hand is superintegrable.

Example 2. For the same potential (40), all slope functions

$$\gamma(x, y, c_1, c_2) = \frac{y + c_1 r}{x + c_2 r} \tag{45}$$

satisfy the PDE (8). This pair $\{V, \gamma\}$, given by (40) and (45), put back to Szebehely's equation (2), gives

$$2(c_2 x + c_1 y + r)E + 1 - c_1^2 - c_2^2 = 0. \tag{46}$$

This equation, which is of the form (39), with x, y present in it, actually informs us that the three invariants c_1, c_2 and E are independent. From equations (45) and (46) we solve for c_1, c_2 and express them in terms of x, y, γ, E. Renaming c_1, c_2 to Φ_1, Φ_2 respectively, we obtain

$$\Phi_1(x, y, \gamma, E) = \frac{2(x + y\gamma)}{(1 + \gamma^2)}E + \frac{\{(x + y\gamma) + \gamma(y - x\gamma)\}}{r(1 + \gamma^2)}, \tag{47}$$

and

$$\Phi_2(x,y,\gamma,E)=\frac{2\gamma(x+y\gamma)}{(1+\gamma^2)}E+\frac{\{\gamma(x+y\gamma)-(y-x\gamma)\}}{r(1+\gamma^2)}. \tag{48}$$

According to (12) the equation (47) leads to the integral

$$I_1(x,y,\dot{x},\dot{y})=\dot{y}L-\frac{x}{r}, \tag{49}$$

and the equation (48) to the integral

$$I_2(x,y,\dot{x},\dot{y})=\dot{x}L+\frac{y}{r}, \tag{50}$$

where L is given by (44). It can be checked directly that (49) and (50) are indeed integrals of the motion as they are in involution with E, i.e. $[I_1,E]=0$ and $[I_2,E]=0$. However, I_1 is not in involution with I_2. Indeed, from I_1 and I_2, we find the integral

$$[I_1,I_2]=2EL \tag{51}$$

i.e. we "rediscover" the angular momentum integral L. In conclusion: the three independent (but, of course, not all in involution) invariants are E, L and I_1.

7 Fixed energy configurational invariants

The term "configurational invariant" is ascribed to dynamical variables of the form (13) which remain constant not in the entire phase space but on a certain 3-D manifold of it (Hietarinta, 1986). Usually this manifold is taken to be a constant energy manifold, e. g. $E=0$. Our basic equation (15) is of course valid for $E=0$ and it reads

$$2V(\gamma\phi_x-\phi_y)=-(1+\gamma^2)(V_x+\gamma V_y)\phi_\gamma. \tag{52}$$

We define the function

$$\rho(x,y,\gamma)=\frac{2(\gamma\phi_x-\phi_y)}{(1+\gamma^2)\phi_\gamma} \tag{53}$$

(analogously to $R(x,y,\gamma,E)$ in (19)) and we rewrite the equation (52) as

$$\frac{(V_x+\gamma V_y)}{V}=-\rho. \tag{54}$$

Differentiating (54) with respect to γ, we find

$$\frac{V_y}{V} = -\rho_\gamma \tag{55a}$$

and, from (55a) and (54),

$$\frac{V_x}{V} = \gamma\rho_\gamma - \rho. \tag{55b}$$

Equations (55) serve to find (up to a multiplicative constant) the potential $V(x,y)$ when the function $\rho(x,y,\gamma)$ is known, i.e. when the configurational invariant $\phi = \phi(x,y,\gamma)$ on $E = 0$ is known. The equations (55) are analogous to the formula (22). Obviously, the r.h.s. of (55a) and (55b) must be independent of γ. It immediately seen that this requirement leads to one condition (not two) which is

$$\rho_{\gamma\gamma} = 0. \tag{56a}$$

On the other hand, the compatibility condition $V_{yx} = V_{xy}$ leads to the second condition for $\rho(x,y,\gamma)$, which is

$$\rho_{x\gamma} + \gamma\rho_{y\gamma} = \rho_y. \tag{56b}$$

If, on the hypersurface $E = 0$ of the phase space, a configurational invariant $\phi(x,y,\gamma)$ does exist, the corresponding function $\rho(x,y,\gamma)$ must satisfy the two equations (56). However, the existence of a function $\rho(x,y,\gamma)$ satisfying the conditions (56) does not suffice for the actual finding of $\phi(x,y,\gamma)$. This last step still depends on the possibility of solving the PDE (52) for

$$\phi = \phi(x,y,\gamma). \tag{57}$$

If the potential is at our disposal (direct problem), the solution (57) is to be found from (52). As an example, we propose to check that, for the (non-central) potential

$$V(x,y) = -(x^2+y^2+x)^2 - y^2 \tag{58}$$

the equation (52) is satisfied by the following function

$$\phi(x,y,\gamma) = \frac{(x^2-y^2+x)\gamma + y(1+2x)}{(x^2-y^2+x) - y(1+2x)\gamma}. \tag{59}$$

8 An application – Configurational invariants of two variables

In spite of its linearity and its homogeneity in $\phi(x, y, \gamma)$, the above equation (52) is not generally solvable when the potential $V(x, y)$ is given. It is of course much easier to have to deal with (52) rather than with (15). In a work under preparation (Bozis and Meletlidou, 2006) we show that: for potentials $V = V(x, y)$ whose logarithm satisfies Laplace's two-dimensional equation, the equation (52) is solvable for $\phi(x, y, \gamma)$. Actually, the pair (58,59) of potential and configurational invariant was found on this basis. (In section 7, it was presented to serve the inverse problem viewpoint).

In this section, we shall seek solutions of (52) of the more particular form

$$\phi = \Psi(V(x, y), \gamma). \tag{60}$$

The positional coordinates x, y are carried exclusively through the potential $V = V(x, y)$. Calculating $\phi_x, \phi_y, \phi_\gamma$ in view of (60) and inserting them into (52), we obtain

$$\frac{V_x + \gamma V_y}{V_y - \gamma V_x} = \frac{2V}{(1+\gamma^2)} \frac{\Psi_V}{\Psi_\gamma}. \tag{61}$$

If, indeed, such functions $\Psi(V, \gamma)$ do exist, the left-hand side of equation (61) (cannot be any function of x, y, γ but it) must be a function σ of the two variables V and γ , as the right-hand side is, i.e.

$$\frac{V_x + \gamma V_y}{V_y - \gamma V_x} = \sigma(V, \gamma). \tag{62}$$

To this end, the necessary and sufficient condition for (62) to be possible is that

$$\frac{V_y}{V_x} = \frac{\sigma_y}{\sigma_x}. \tag{63}$$

This condition (63), however, is only necessary for the equation (61) to be solvable. Working with (63), (62) and (61), we find, for all γ's, the condition

$$V_y^2 V_{xx} + V_x^2 V_{yy} = 2V_x V_y V_{xy}. \tag{64}$$

The general solution of the PDE (64) (Bateman's equation) as can be verified directly, is

$$y = \lambda(V)x + \mu(V), \tag{65}$$

where λ, μ are arbitrary functions of $V(x,y)$. The pertinent configurational invariant (if it exists) is of the form (60) and is given by the linear homogeneous PDE (61) in the unknown function Ψ of the two variables V and γ. So, now we turn attention to the solution of (61). The subsidiary ODE is

$$\frac{d\gamma}{dV} = -\frac{(1+\gamma^2)}{2V}\sigma(V,\gamma). \tag{66}$$

The potential $V(x,y)$ to be used in (66) must be taken in agreement with (65). Calculating V_x, V_y from (65) and inserting into (62), we find

$$\sigma(V,\gamma) = -\frac{\lambda-\gamma}{1+\lambda\gamma}, \tag{67}$$

where $\lambda = \lambda(V)$. A highly noticeable result is that, as far as the configurational invariant is concerned, the arbitrary function $\mu(V)$ in (65) plays no role, whatsoever. Thus, (66) reads

$$\frac{d\gamma}{dV} = \frac{(1+\gamma^2)(\lambda-\gamma)}{2V(1+\lambda\gamma)}. \tag{68}$$

Remark. Although of the first order, the ODE (68) is hard to solve even for simple functions $\lambda(V)$. For the simplest case $\lambda = \lambda_0 = const.$ one can find the potential $V(x,y) = \tilde{\mu}(y-\lambda_0 x)$, $\tilde{\mu} = arbitrary$, which is fully integrable but trivial. The general solution of (61) (which is good for $E = 0$) is $\Psi = \Psi\left[(\gamma-\lambda_0)^2 V(x,y)/(1+\gamma^2)\right] = const.$, so the square of the momentum $I = (\dot{x}+\lambda_0\dot{y})$ is constant.

9 Bateman's equation as connected to other results

The PDE (64) is known as Bateman's equation and, as reported by Euler et al (1997), it appears (as it stands or, more generally, in higher dimensional form) in testing the Painleve property for PDEs. The same equation (64) appeared also in the study by Bozis and Anisiu (2005) of compatible pairs $\{V(x,y), \gamma(V(x,y))\}$ of potentials and monoparametric families $f(x,y) = c$ with slope function (5) of the specific form $\gamma = \gamma(V(x,y))$. It was found that such pairs do exist e. g. if the family $\gamma(x,y)$ satisfies Bateman's equation (in which case it was shown that the corresponding potential $V(x,y)$ also has to satisfy the same equation).

In the previous section, Bateman's equation appeared as a necessary condition on potentials $V(x,y)$ which possess configurational invariants of the form (60) on the hypersurface $E = 0$ of the phase space. As mentioned already, the integrability of (61) is not ensured although the solution of (61) is reduced to the solution of an ordinary differential equation of the first order. In spite of the above we may conjecture that the Bateman's potentials not only possess configurational invariants but they are good candidate integrable potentials. This statement is also supported by the following facts:

(i) A rich family of integrable two-dimensional potentials (including one arbitrary function of the potential) was established by Giacomini (1990). This family is defined implicitly by the relation

$$A(V) = y + \frac{x}{(\alpha_1 V + \alpha_2)}. \tag{69}$$

One can show by direct calculations that all potentials defined implicitly by the equation (69) satisfy the PDE (64). Clearly this is not something which had to be so by necessity. In other words, the set of Giacomini's potentials needed not belong entirely to the set defined by (64). For $\lambda(V) = -(\alpha_1 V + \alpha_2)^{-1}$, $\mu(V) = A(V)$, equation (65) reduces to Giacomini's (1990) result (69). Giacomini established the second constant of the motion in terms of higher transcendental functions in the momenta.

(ii) The integrable potential $V = x/y$, found earlier by Hietarinta (1984), also satisfies Bateman's equation (64). It is obtainable from (69) for $A = 0$, $\alpha_1 = -1$, $\alpha_2 = 0$ and also from (65) for $\lambda(V) = V^{-1}$, $\mu(V) = 0$. In fact, Hietarinta found, besides the energy integral, two independent integrals and expressed them in terms of parabolic cylinder functions. Of course, only two of the above three independent integrals commute. Finally Hietarinta (1986) comments that "although the potential $V = x/y$ is integrable at any value of the energy, the invariants are best derived using a fixed energy constraint".

10 General remarks and open questions

The present study deals with the question of integrability of a potential $V = V(x,y)$ under the simplest assumptions: one material point is moving in the plane under the action of an autonomous two-dimensional potential and the reference system is inertial. The question is essentially faced both from the direct and from the inverse-problem viewpoint but with the equipment and the pertinent formulae developed in the framework of the inverse problem of

Dynamics. We propose to keep the positional coordinates x, y but express the velocity coordinates $\dot{x}, \dot{y}$ in terms of the energy E, given by (1) and the slope function γ, given by (5). These two functions are present in Szebehely's PDE (1974), as rewritten by Bozis (1995) in the form (2). This equation together with the second order PDE (8) are the basic tools of the inverse problem of Dynamics. In the present study they are completed by the equation (15) and allow us to treat the question of integrability.

From the direct viewpoint we propose the formula (15) for establishing possibly existing second integrals for a given potential $V(x, y)$. We compare the use of (15) to the vanishing of the Poisson bracket $[E(x, y, \dot{x}, \dot{y}), I(x, y, \dot{x}, \dot{y})]$ given in (16) (with E and I taken from (1) and (13) respectively). The main advantage of the formula (15) is that there appear in it only the three partial derivatives of the unknown function $\Phi(x, y, \gamma, E)$ in x, y, γ and this is in agreement with the fact that E is treated as a constant parameter.

For invariants, algebraic in the velocity components $\dot{x}, \dot{y}$, the number of the pertinent position-depending coefficients to be determined is reduced. This becomes evident in the case of the application of section 5. Instead of having to deal with the $(n + 1)$ coefficients $A_p^n(x, y)$ of (28), we have essentially to do with the unique function $M(x, y, \gamma)$ in (30). We have also used formula (15) to fourth degree invariants $I(x, y, \dot{x}, \dot{y})$ (Bozis, 2005).

The formula (15) is also best suited for the study of configurational invariants $\varphi = \phi(x, y, \gamma)$ on the manifold $E = 0$ of the phase space $xy\gamma E$ (section 7). In fact, each solution of (52) leads to a set of functions $\gamma = \gamma(x, y, \phi)$, implying the existence of a two-parametric set of families of orbits (4). In particular in section 8, the possibility of finding potentials possessing configurational invariants of the form (60) is shifted to the possibility of solving a first order homogeneous PDE in an unknown function Ψ of two variables. This, in turn, shifts to the possibility of solving one ordinary differential equation of the first order. We now come to compare each of these approaches to the use of the Hamilton-Jacobi PDE, which, for the case at hand (one massive point of unit mass) reads:

$$S_x^2 + S_y^2 = 2(E - V(x, y)). \tag{70}$$

The problem is to find a complete solution of (70) for the characteristic function S, i.e. a solution $S(x, y, E, \alpha_1, \alpha_2)$, which, in addition to the (already existing in (70) parameter E), includes two constants, one of which must be additive. Disregarding this additive constant, S will include one non-additive constant, say α_2, and also the parameter E which we take as the first constant, i.e. $\alpha_1 = E$. So, the task consists in solving the parameter-dependent PDE (70)

to the extent of bringing into the solution one more non-additive constant α_2. A similar job is to be done with equation (2). However, dealing with (2) is much more preferable because (2) is linear in the unknown function $\gamma(x, y, E)$, whereas (70) is not linear in $S(x, y, E)$. As to the unknown function $\Phi(x, y, \gamma, E)$ in (15), this depends on three variables but (15) is linear and homogeneous.

In dealing with the inverse aspect of the problem, we proved that the tests to be performed on the function $\Phi(x, y, \gamma, E)$ may be replaced by testing the function $R(x, y, \gamma, E)$, as given by (19) through first order derivatives of Φ in x, y, γ. We then wrote down the three criteria (23) and (24) to check the adequateness of the given function $\Phi(x, y, \gamma, E)$ so that the formula (22) is applicable and we find explicitly the pertinent potential. Of a similar nature is the work by Xanthopoulos and Bozis (1983) where the criteria for the adequateness are offered, not for a candidate integral $\Phi = \Phi(x, y, \gamma, E)$ but, for a candidate slope function $\gamma = \gamma(x, y, c_1, c_2)$ depending on two parameters.

The approach to the question of integrability from the inverse problem viewpoint (in particular the existence of formulae like (22)) is also didactic in the following sense: glancing at the PDE (16), which is linear in $I(x, y, \dot{x}, \dot{y})$, one might wonder why it is so rare for this equation (as very often is mentioned in the literature and as common experience is) to offer back to us a solution, once we insert to it a potential (even some very simple potentials $V(x, y)$!). It is now clear that there is a set of "good functions Φ" (satisfying the conditions (23),(24)) and that to this set there corresponds a set of "good functions V" (integrable potentials). No wonder then if a potential, chosen at random, is not integrable and if chaoticity is so frequent even for the motion of one massive particle in the xy plane. This question then deserves more attention.The procedure followed in section 5 is promising to face the study of expressions $I(x, y, \dot{x}, \dot{y})$ which are weighted homogeneous in $\dot{x}, \dot{y}$, e.g. of degrees n and $n - 2$. Instead of having to deal with one function $M(x, y, \gamma)$, one would then have to do with two functions $M_1(x, y, \gamma)$ and $M_2(x, y, \gamma)$. As the available literature in this version of the inverse problem is by now rich enough, the procedure followed in the present study may be extended to cover more general aspects. We mention e.g. the three-dimensional case for one material point (Bozis and Kotoulas, 2005; Anisiu, 2005), the holonomic systems (Borghero, 1987) and the generalized holonomic systems (Borghero and Melis, 1990).

References

[1] Anisiu, M.-C.: 2005, The energy-free equations of the 3D inverse problem of Dynamics, *Inv. Probl. Sci. Eng.* **13**, 545-558.

[2] Bertrand, M. J.: 1852, Sur les integrales communes a plusieurs problèmes de Mécanique, *J. Math. Pures et Appl.* Tome **XVII**, pp.121-174.

[3] Borghero, F.: 1987, Variational determination of the generalised Szebehely's equation, *Rend. Sem. Mat. Univ. Politecn. Torino* **45**, 125-135.

[4] Borghero, F. and Melis, A.: 1990, On Szebehely's problem for holonomic systems involving generalised potential functions, *Celest. Mech. Dyn. Astron.* **49**, 273-284.

[5] Bozis, G. and Ichtiaroglou, S.: 1987, Existence and construction of dynamical systems having a prescribed integral of motion - an inverse problem, *Inverse Problems* **3**, pp.213-227.

[6] Bozis, G.: 1992, Two-dimensional integrable potentials with quartic invariants, *J. Phys. A: Math. Gen.* **25** 3329-3351.

[7] Bozis G.: 1995, The inverse problem of dynamics: basic facts, *Inverse Problems* **11** 687-708.

[8] Bozis, G. and Anisiu, M.-C.: 2005, A solvable version of the inverse problem of Dynamics, *Inverse Problems* **21**, 487-497.

[9] Bozis, G.: 2005, Integrability in the light of the inverse problem, *Rom. Astron. J.* **15** No 1 49-63.

[10] Bozis, G. and Kotoulas, Th.: 2005, Homogeneous two-parametric families of orbits in three-dimensional homogeneous potentials, *Inverse Problems* **21**, 343-356.

[11] Euler, N., Lindblom, O., Euler, M. and Persson, L-E.: 1997, The higher dimensional Bateman equation and Painleve analysis of nonintegrable wave equations, *Symmetry in Nonlinear Mathematical Physics* V 1 185-192.

[12] Giacomini, H. J.: 1990, Integrable Hamiltonians with higher transcendental invariants, *J. Phys. A: Math. Gen.* **23** L587-L590.

[13] Goriely, A.: 2001, *Integrability and nonintegrability of dynamical systems*, World Scientific, New Jersey.

[14] Hietarinta, J.: 1983, A search for integrable two-dimensional Hamiltonian systems with polynomial potential, *Phys. Letters*, **96A**, No.6, pp.273-278.

[15] Hietarinta, J.: 1984, New integrable Hamiltonians with transcendental invariants, *Phys. Rev. Lett.* **52** 1057;

[16] Hietarinta, J.: 1986, Report Series: *Direct methods for the search of the second invariant*, Univ. of Turku (Turku Press).

[17] Lieberman, M. and Lichtenberg, A.: 1983, *Regular and stochastic motion* (Berlin:Springer).

[18] Tabor, M.: 1989, *Chaos and inegrability in Nonlinear Dynamics* (New

York:Wiley).

[19] Whittaker, E. T.: 1961, *Analytical Dynamics of particles and rigid bodies* (Cambridge University Press, fourth edition), pp.331-335.

[20] Xanthopoulos, B. and Bozis, G.: 1983, The planar inverse problem for autonomous systems, in *Dynamical trapping and evolution in the solar system*, pp. 353-367 (eds. V.V. Markellos and Y. Kozai), D. Reidel Publ. Co.

PADEU | PADEU **19** (2007), p. 49
ISBN 963 463 557
©Published by the Astron. Dept. of the Eötvös Univ.

A Closed Form Vectorial Solution to the Relative Orbital Motion

Daniel Condurache[1], Vladimir Martinuşi[2]

Technical University "Gh. Asachi", Department of Theoretical Mechanics, Iaşi, Romania

E-mail: [1]danielcondurache@rdslink.ro, [2]vladmartinus@gmail.com

Abstract

Time-explicit solutions for relative Keplerian dynamics are presented for the general case in which the reference trajectory is elliptic, parabolic or hyperbolic. The non-linear differential equation modeling the motion is solved by means of tensorial and vectorial regularization methods. This regularizing procedure extends the approaches of Levi-Civita and Kustaanheimo-Stiefel in the case of Kepler problem in rotating reference frames. The solution generalizes the approximate results obtained from Hill-Clohessy-Wiltshire, Lawden and Tschauner-Hempel equations. The approximate solutions derived from the liniarized models are in fact the first linear approximation of the exact solution the authors have found.

Keywords: *Orbital relative motion, Kepler's problem*

1 Introduction

The study of the relative orbital motion represents a subject of interest since the 1960's, when Clohessy and Wiltshire published their famous work on satellite motion. The study of the satellite relative motion has applications in present and future space programmes. It is more reliable to launch a single spacecraft (named *Chief*) from Earth, put it on its orbit and launch several other satellites (*Deputies*) from it. Satellite clusters are used improved Earth observations

or may collect more accurate athmospheric data, for example. The satellite formation will also function in the event of a single spacecraft failure.

The fundamental problem in orbital relative dynamics is to determine the motion of the Deputy satellite with respect to the Chief. Consider the Chief orbiting around a Keplerian attraction center (i.e. under the influence of a gravitational force). The inertial orbital elements of the Chief (specific angular momentum $\mathbf{h}_C$, specific energy ξ_C, eccentricity vector $\mathbf{e}_C$ and true anomaly $f_C = f_C(t)$) are considered to be known. At the moment of time $t = t_0$, the Deputy satellite is launched with relative velocity $\Delta\mathbf{v}$ from a position $\Delta\mathbf{r}$ with respect to the Chief. Let $\mathbf{r}$ denote the position vector of the Deputy with respect to the Chief.

The vectorial initial value problem that models the relative motion of the Deputy with respect to a non-inertial reference frame originated in the Chief mass center is:

$$\ddot{\mathbf{r}} + 2\omega \times \dot{\mathbf{r}} + \omega \times (\omega \times \mathbf{r}) + \dot{\omega} \times \mathbf{r} + \frac{\mu}{|\mathbf{r} + \mathbf{r}_C|^3}(\mathbf{r} + \mathbf{r}_C) - \frac{\mu}{r_C^3}\mathbf{r}_C = \mathbf{0}, \quad (1)$$

$$\begin{cases} \mathbf{r}(t_0) = \Delta\mathbf{r}, \\ \dot{\mathbf{r}}(t_0) = \Delta\mathbf{v}, \end{cases}$$

where ω denotes the angular velocity of the rotating reference frame associated with the Chief,

$$\omega = \dot{f}_C \frac{\mathbf{h}_C}{h_C} = \frac{(1 + e_C \cos f_C)^2}{p_C^2}\mathbf{h}_C, \quad (2)$$

$\mathbf{r}_C$ the position vector of the Chief with respect to the attraction center and μ the gravitational parameter. The motion described by eq (1) is studied with respect to a non-inertial reference frame LVLH (Local-Vertical-Local-Horizontal) that translates and rotates with respect to an Earth centered reference frame (ECI). The Cartesian axis of LVLH are chosen as it follows (see **Figure 1**):

- Cx axis in the direction of the position vector of the Chief $\mathbf{r}_C$;
- Cz axis in the direction of the specific angular momentum of the Chief $\mathbf{h}_C$;
- Cy axis completes the positive oriented Cartesian frame $Cxyz$.

Considering the Cartesian coordinates of the Deputy position vector with respect to LVLH $\mathbf{r} = \begin{bmatrix} x & y & z \end{bmatrix}^T$, eq (1) becomes a system of three scalar differential equations.

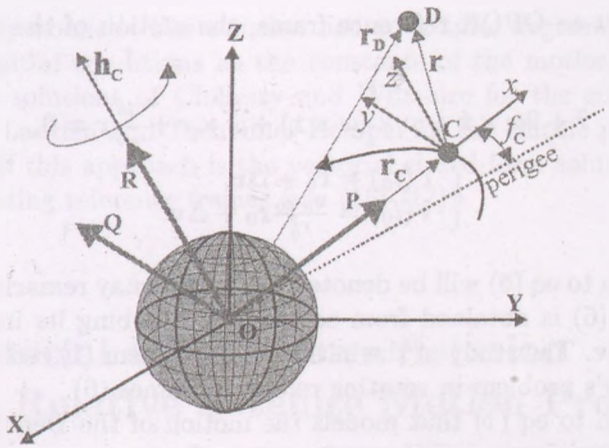

Figure 1: *The relative satellite motion and the reference frames that are used*

Generally, the trajectory of the Chief with respect to ECI reference frame is a conic (ellipse, parabola, hyperbola). The Chief motion in ECI is modeled by the initial value problem:

$$\ddot{\mathbf{r}}+\frac{\mu}{r^3}\mathbf{r}=0, \tag{3}$$
$$\begin{cases} \mathbf{r}(t_0)=\mathbf{r}_0, \\ \dot{\mathbf{r}}(t_0)=\mathbf{v}_0, \end{cases}$$

Let $OPQR$ be an Earth centered rotating reference frame that has the axis parallel with LVLH. The Chief motion with respect to the OPQR reference frame is described by the initial value problem:

$$\ddot{\mathbf{r}}+2\omega\times\dot{\mathbf{r}}+\omega\times(\omega\times\mathbf{r})+\dot{\omega}\times\mathbf{r}+\frac{\mu}{r^3}\mathbf{r}=0, \tag{4}$$
$$\begin{cases} \mathbf{r}(t_0)=\mathbf{r}_0, \\ \dot{\mathbf{r}}(t_0)=\frac{\mathbf{v}_0\cdot\mathbf{r}_0}{r_0^2}\mathbf{r}_0. \end{cases}$$

The solution to eq (4) will be denoted $\mathbf{r}_C^{(rot)}$. One may remark that the motion described by $\mathbf{r}_C^{(rot)}$ is rectilinear:

$$\mathbf{r}_C^{(rot)}=\frac{p_C}{1+e_C\cos f_C}\frac{\mathbf{r}_0}{r_0}. \tag{5}$$

With respect to OPQR reference frame, the motion of the Deputy is then described by:

$$\ddot{\mathbf{r}} + 2\omega \times \dot{\mathbf{r}} + \omega \times (\omega \times \mathbf{r}) + \dot{\omega} \times \mathbf{r} + \frac{\mu}{r^3}\mathbf{r} = \mathbf{0}, \tag{6}$$

$$\begin{cases} \mathbf{r}(t_0) = \mathbf{r}_0 + \Delta\mathbf{r}, \\ \dot{\mathbf{r}}(t_0) = \frac{\mathbf{v}_0 \cdot \mathbf{r}_0}{r_0^2}\mathbf{r}_0 + \Delta\mathbf{v}. \end{cases}$$

The solution to eq (6) will be denoted $\mathbf{r}_D^{(rot)}$. One may remark that the initial value problem (6) is obtained from eq (4) by perturbing its initial conditions with $\Delta\mathbf{r}$ and $\Delta\mathbf{v}$. The study of the initial value problem (1) reduces then to the study of Kepler's problem in rotating reference frames (6).

The solution to eq (1) that models the motion of the Deputy with respect to the non-inertial frame LVLH may be put in the form:

$$\mathbf{r}_D^{(LVLH)} = \mathbf{r}_D^{(rot)} - \mathbf{r}_C^{(rot)}. \tag{7}$$

The first attempts to solve this problem were made by Clohessy and Wiltshire in the early 1960 (see (1)). They offered an approximate solution when the reference trajectory (i.e. the Chief trajectory) is circular. The equations of motion that were deduced are known as the Hill-Clohessy-Wiltshire (HCW) equations because the solution is based on the work oh Hill (see (2)) at the end of the 19th century.

Not very late after the publication of the HCW equations, Lawden (see (3)) gave an approximate solution to the relative satellite motion almost simultaneously with Tschauner and Hempel (see (4), (5)) in case the reference trajectory is elliptic. Their solutions generalize the HCW equations and offer more accurate models for the satellite relative motion.

All these approaches presented above start from a linearization of eq (6). The solutions offer a model with a limited degree of predictability.

The orbital satellite relative motion problem is more intensely studied since the late 1990's, when the satellite flight formations became a quite attractive alternative for space missions. The circular reference trajectory and the elliptic reference trajectory (see (6), (7)) were studied. Time explicit solutions to the relative motion with elliptic reference trajectory were published more recently (see (8), (9)). The models involving different perturbations (like the J_2 oblateness factor or the atmospheric drag) were also studied in recent papers (see (10) - (14)).

The present paper offers an exact vectorial solution to the orbital relative motion problem when the reference trajectory is arbitrary Keplerian (elliptic,

parabolic or hyperbolic). The solution has an infinite degree of predictability and uses the initial conditions as the constants of the motion. The solution generalizes the solutions of Clohessy and Wiltshire for the circular reference trajectory and Lawden and Tschauner-Hempel for the elliptic reference trajectory. The key of this approach is the vectorial closed form solution to Kepler's problem in rotating reference frames (see (15)-(17)).

2 A Vectorial Closed Form Solution to the Relative Satellite Motion Problem

By using the theoretical considerations made in the previous sections of this approach, we present the vectorial closed form solution to the relative satellite motion when the reference trajectory is arbitrary Keplerian (elliptic, parabolic or hyperbolic). The results are given including the case when the specific angular momentum of the Deputy satellite is zero (i.e. its trajectory is rectilinear with respect to the inertial reference frame).

Consider the motion of the Chief satellite with respect to the ECI reference frame modeled by eq (3). Consider $\mathbf{h}_C$ its inertial specific angular momentum, p_C its semilatus rectum, e_C the magnitude of its vectorial eccentricity and f_C its true anomaly. Let $OPQR$ be the rotating reference frame introduced in **Section 1**. With respect to this reference frame, the motion of the Chief satellite is described by eq (5) (see (17), (21)).

The Deputy satellite orbits around the same attraction center. Its motion is described with respect to OPQR reference frame by vector $\mathbf{r}_D^{(rot)}$, that is the solution to eq (6). The motion of the Deputy satellite with respect to the Chief satellite (i.e. the LVLH reference frame) is described by eq (7).

The key to the solution is a representation theorem, as well as a vectorial Sundman-like regularization of Kepler's problem in a rotating reference frame (see (17)). We succinctly present the mentioned results.

The initial value problem that models the motion of the Deputy with respect to the rotating reference frame OPQR is solved, then the result is transported into the non-inertial frame LVLH. This is made by means of a symbolic procedure that uses the inertial reference frame ECI as a cathalyst. The next theorem is fundamental in studying the motion related to a rotating reference frame.

Theorem 2.0.1 *The solution to the initial value problem (6) is obtained by applying the proper orthogonal tensorial function* $\mathbf{R}_{-\omega}$ *to the solution to the initial value problem:*

$$\ddot{\mathbf{r}}+\frac{\mu}{r^3}\mathbf{r}=\mathbf{0}, \tag{8}$$
$$\begin{cases} \mathbf{r}(t_0)=\mathbf{r}_0+\Delta\mathbf{r} \\ \dot{\mathbf{r}}(t_0)=\mathbf{v}_0+\Delta\mathbf{v}+\omega_0\times\Delta\mathbf{r}, \end{cases}$$

where $\omega_0=\omega(t_0)$ *and* $\mathbf{R}_{-\omega}$ *is the solution to the tensorial initial value problem:*

$$\begin{aligned} \dot{\mathbf{Q}}+\widetilde{\omega}\mathbf{Q} &= \mathbf{0}_3, \\ \mathbf{Q}(t_0) &= \mathbf{I}_3, \end{aligned} \tag{9}$$

with $\widetilde{\omega}$ *the skew-symmetric tensor function associated to the continuous vector function* ω.

The previous theorem shows that the vector that models the motion of the Deputy with respect to OPQR, $\mathbf{r}_D^{(rot)}$, is expressed as:

$$\mathbf{r}_D^{(rot)}=\mathbf{R}_{-\omega}\mathbf{r}^{(I)}, \tag{10}$$

where $\mathbf{r}^{(I)}$ is the solution to eq (8).

Remark 2.0.2 *The initial value problem (9) represents the tensorial form of the famous Darboux equation (see (19)): determining the rotation tensor (matrix)* $\mathbf{Q}$ *that models the rotation with a given instantaneous angular velocity* $-\omega$. *This equation is fundamental in attitude kinematics.*

The regularization introduces a new time variable $\tau=\tau(t)$ such as $dt=rd\tau$. By making the substitution:

$$t-t_P=\int_0^\tau r(\sigma)\,d\sigma, \tag{11}$$

with t_P adequately chosen, the initial value problem eq (6) transforms into:

$$\frac{d^2}{d\tau^2}\mathbf{r}-2\xi\mathbf{r}=-\mu\mathbf{e}, \tag{12}$$
$$\begin{cases} \mathbf{r}|_{\tau=0}=\begin{cases} \dfrac{h^2}{\mu(1+e)}\dfrac{\mathbf{e}}{e}, & \mathbf{e}\neq\mathbf{0}, \\ \mathbf{R}_{-\omega}(\mathbf{r}_0+\Delta\mathbf{r}), & \mathbf{e}=\mathbf{0}, \end{cases} \\ \left.\dfrac{d}{d\tau}\mathbf{r}\right|_{\tau=0}=\begin{cases} \dfrac{1}{e}\mathbf{h}\times\mathbf{e}, & \mathbf{e}\neq\mathbf{0}, \\ r_0\mathbf{R}_{-\omega}(\mathbf{v}_0+\Delta\mathbf{v}+\omega_0\times\Delta\mathbf{r}), & \mathbf{e}=\mathbf{0}. \end{cases} \end{cases}$$

where $\mathbf{h}$, ξ, $\mathbf{e}$ are the prime integrals of eq (6) (see (17)):

$$\mathbf{r} \times (\dot{\mathbf{r}} + \omega \times \mathbf{r}) = \mathbf{R}_{-\omega}\mathbf{h}_D^0 \triangleq \mathbf{h}, \tag{13}$$

(analogous to the inertial specific angular momentum conservation)

$$\frac{1}{2}(\dot{\mathbf{r}} + \omega \times \mathbf{r})^2 - \frac{\mu}{r} = \frac{1}{2}[\mathbf{v}_0 + \Delta\mathbf{v} + \omega_0 \times \Delta\mathbf{r}]^2 - \frac{\mu}{|\mathbf{r}_0 + \Delta\mathbf{r}|} \triangleq \xi_D, \tag{14}$$

(analogous to the inertial energy conservation)

$$\frac{(\dot{\mathbf{r}} + \omega \times \mathbf{r}) \times [\mathbf{r} \times (\dot{\mathbf{r}} + \omega \times \mathbf{r})]}{\mu} - \frac{\mathbf{r}}{r} = \mathbf{R}_{-\omega}\mathbf{e}_D^0 \triangleq \mathbf{e}, \tag{15}$$

(analogous to the inertial vectorial eccentricity), where:

$$\begin{cases} \mathbf{h}_D^0 = (\Delta\mathbf{r} + \mathbf{r}_0) \times [\mathbf{v}_0 + \Delta\mathbf{v} + \omega_0 \times \Delta\mathbf{r}] \\ \mathbf{e}_D^0 = \dfrac{[\mathbf{v}_0 + \Delta\mathbf{v} + \omega_0 \times \Delta\mathbf{r}] \times \mathbf{h}_D^0}{\mu} - \dfrac{\Delta\mathbf{r} + \mathbf{r}_0}{|\Delta\mathbf{r} + \mathbf{r}_0|} \end{cases} \tag{16}$$

The following algorithm is applied in order to obtain the closed form vectorial solution to the relative satellite motion in all possible situations that may occur:

1. Eq (12) is solved. The explicit expression for $\mathbf{r}_D^{(rot)}$ is obtained with respect to the independent variable τ.
2. The magnitude of the position vector is computed.
3. The velocity is computed by using:

$$\frac{d}{d\tau}\mathbf{r} = r(\dot{\mathbf{r}} + \omega \times \mathbf{r}) \Rightarrow \dot{\mathbf{r}} = \frac{1}{r}\left(\frac{d}{d\tau}\mathbf{r}\right) - \omega \times \mathbf{r}. \tag{17}$$

4. The motion of the Deputy with respect to the LVLH frame is determined from eq (7) by taking into account that since vector ω has fixed direction,

$$\omega = \frac{(1 + e_C \cos f_C)^2}{p_C^2}\mathbf{h}_C, \tag{18}$$

the tensorial orthogonal map $\mathbf{R}_{-\omega}$ has an explicit expression.

5. The moment of periapsis passage t_P is determined from the initial conditions.

6. An implicit relation between τ and t is given using $t - t_P = \int_0^\tau r(\xi)\, d\xi$. When $\xi \neq 0$, the map $E(\tau(t)) = \sqrt{2|\xi|}\tau(t)$ is implicitly defined. It is analogous to the *eccentric anomaly* from the classic Keplerian motion.

At step 4. in the algorithm above, the expression of $\mathbf{R}_{-\omega}$ is given by a Rodrigues-like formula:

$$\mathbf{R}_{-\omega} = \exp\left(-\int_{t_0}^{t} \widetilde{\omega}(\xi)\, d\xi\right) = \mathbf{I}_3 - \frac{\sin f_C^0(t)}{h_C}\widetilde{\mathbf{h}}_C + \frac{1-\cos f_C^0(t)}{h_C^2}\widetilde{\mathbf{h}}_C^2, \tag{19}$$

with $f_C^0(t) \triangleq \int_{t_0}^{t} \omega(\psi)\, d\psi = f_C(t) - f_C(t_0)$ (eq (18) is taken into account).

The approach is structured starting from the sign of the specific energy of the Deputy ξ_D, each case including the situation of zero specific angular momentum, $\mathbf{h}_D = \mathbf{0}$. In case $\xi_D \neq 0$, the results are expressed with respect to two new vectorial prime integrals and a scalar prime integral, all based on $\mathbf{h}$, ξ_D, $\mathbf{e}$:

$$\mathbf{a} = \begin{cases} \dfrac{\mu}{2e_D|\xi_D|}\mathbf{e}, & \mathbf{e} \neq \mathbf{0} \\ \mathbf{R}_{-\omega}(\mathbf{r}_0 + \Delta\mathbf{r}), & \mathbf{e} = \mathbf{0} \end{cases}; \tag{20}$$

$$\mathbf{b} = \begin{cases} \dfrac{1}{e\sqrt{2|\xi_D|}}\mathbf{h}\times\mathbf{e}, & \mathbf{e} \neq \mathbf{0} \\ \dfrac{1}{n_D}\mathbf{R}_{-\omega}[\mathbf{v}_0 + \Delta\mathbf{v} + \omega_0 \times \Delta\mathbf{r}], & \mathbf{e} = \mathbf{0} \end{cases}; \tag{21}$$

$$n_D = \frac{(2|\xi_D|)^{\frac{3}{2}}}{\mu}. \tag{22}$$

Vectors $\mathbf{a}$ and $\mathbf{b}$ satisfy: $\mathbf{a} = \mathbf{R}_{-\omega}\mathbf{a}_0$ and $\mathbf{b} = \mathbf{R}_{-\omega}\mathbf{b}_0$, where:

$$\mathbf{a}_0 = \begin{cases} \dfrac{\mu}{2e_D|\xi_D|}\mathbf{e}_D^0, & \mathbf{e}_D^0 \neq 0 \\ \mathbf{r}_0 + \Delta\mathbf{r}, & \mathbf{e}_D^0 = 0 \end{cases}; \tag{23}$$

$$\mathbf{b}_0 = \begin{cases} \dfrac{1}{e_D\sqrt{2|\xi_D|}}\mathbf{h}_D^0 \times \mathbf{e}_D^0, & \mathbf{e}_D^0 \neq 0 \\ \dfrac{1}{n_D}[\mathbf{v}_0 + \Delta\mathbf{v} + \omega_0 \times \Delta\mathbf{r}], & \mathbf{e}_D^0 = 0 \end{cases}$$

When $\xi_D \neq 0$, vectors $\mathbf{a}_0$ and $\mathbf{b}_0$ represent the vectorial semimajor and semiminor axis of the inertial trajectory (an ellipse or a hyperbola) of the Deputy and n_D is analogous to the *mean motion* from the classic Keplerian motion.

2.1 Negative Specific Energy: $\xi_D < 0$

2.1.1 Non-Zero Specific Angular Momentum: $\mathbf{h} \neq 0$, Non-Zero Eccentricity: $e_D \neq 0$

The solution to eq (6) is:

$$\begin{aligned}
\mathbf{r}_D^{(rot)}(t) &= [\cos E_D(t) - e_D]\,\mathbf{R}_{-\omega(t)}\mathbf{a}_0 + \sin E_D(t)\,\mathbf{R}_{-\omega(t)}\mathbf{b}_0, \qquad (24)\\
\mathbf{v}_D^{(rot)}(t) &= \frac{n_D}{1 - e_D\cos E_D(t)}[-\sin E_D(t)\,\mathbf{R}_{-\omega(t)}\mathbf{a}_0 \\
&\quad + \cos E_D(t)\,\mathbf{R}_{-\omega(t)}\mathbf{b}_0] \qquad (25)\\
&\quad - [\cos E_D(t) - e]\left[\omega \times \mathbf{R}_{-\omega(t)}\mathbf{a}_0\right] \\
&\quad - \sin E_D(t)\left[\omega \times \mathbf{R}_{-\omega(t)}\mathbf{b}_0\right],
\end{aligned}$$

where $E_D(t) = \sqrt{2|\xi_D|}\tau(t)$, $t \geq t_0$ is deduced from the implicit functional equation:

$$E_D(t) - e_D \sin E_D(t) = n_D(t - t_0) + E_D^0 - e_D \sin E_D^0,\ t \in [t_0, +\infty), \qquad (26)$$

and $E_D^0 \in [0, 2\pi)$ may be computed from:

$$\begin{cases} \cos E_D^0 = \frac{1}{e_D}\left(1 - n_D\frac{|\mathbf{r}_0 + \Delta\mathbf{r}|}{\sqrt{2|\xi_d|}}\right), \\ \sin E_D^0 = n_D\frac{\left(\Delta\mathbf{v} + \frac{\mathbf{v}_0\cdot\mathbf{r}_0}{r_0^2}\mathbf{r}_0\right)\cdot(\mathbf{r}_0 + \Delta\mathbf{r})}{2e_D|\xi_D|}\left[1 - \frac{\omega_0\cdot\mathbf{h}_D^0}{\mu}|\mathbf{r}_0 + \Delta\mathbf{r}|\right]. \end{cases} \qquad (27)$$

Taking eqs (18) and (19) into account, it follows that the motion of the Deputy with respect to the Chief is described by the vectorial expressions:

$$\begin{aligned}
\mathbf{r}(t) &= [\cos E_D(t) - e_D]\left\{\frac{\mathbf{a}_0\cdot\mathbf{h}_C}{h_C^2}\mathbf{h}_C - \frac{\sin f_C^0(t)}{h_C}\tilde{\mathbf{h}}_C\mathbf{a}_0 - \frac{\cos f_C^0(t)}{h_C^2}\tilde{\mathbf{h}}_C^2\mathbf{a}_0\right\} \\
&\quad + \sin E_D(t)\left\{\frac{\mathbf{b}_0\cdot\mathbf{h}_C}{h_C^2}\mathbf{h}_C - \frac{\sin f_C^0(t)}{h_C}\tilde{\mathbf{h}}_C\mathbf{b}_0 - \frac{\cos f_C^0(t)}{h_C^2}\tilde{\mathbf{h}}_C^2\mathbf{b}_0\right\} \qquad (28)\\
&\quad - \frac{p_C}{1 + e_C\cos f_C(t)}\frac{\mathbf{r}_0}{r_0},
\end{aligned}$$

$$
\begin{aligned}
\mathbf{v}(t) \;=\; & \frac{-n_D \sin E_D(t)}{1-e_D\cos E_D(t)}\Big\{\frac{\mathbf{a}_0\cdot\mathbf{h}_C}{h_C^2}\mathbf{h}_C \\
& -\frac{\sin f_C^0(t)}{h_C}\widetilde{\mathbf{h}}_C\mathbf{a}_0-\frac{\cos f_C^0(t)}{h_C^2}\widetilde{\mathbf{h}}_C^2\mathbf{a}_0\Big\} \\
& +\frac{n_D\cos E_D(t)}{1-e_D\cos E_D(t)}\Big\{\frac{\mathbf{b}_0\cdot\mathbf{h}_C}{h_C^2}\mathbf{h}_C-\frac{\sin f_C^0(t)}{h_C}\widetilde{\mathbf{h}}_C\mathbf{b}_0 \\
& -\frac{\cos f_C^0(t)}{h_C^2}\widetilde{\mathbf{h}}_C^2\mathbf{b}_0\Big\} \\
& +\frac{h_C\left[1+e_C\cos f_C(t)\right]^2\left[\cos E_D(t)-e_D\right]}{p_C^2} \\
& \cdot\left\{\frac{\sin f_C^0(t)}{h_C^2}\widetilde{\mathbf{h}}_C^2\mathbf{a}_0-\frac{\cos f_C^0(t)}{h_C}\widetilde{\mathbf{h}}_C\mathbf{a}_0\right\} \\
& +\frac{h_C\left[1+e_C\cos f_C(t)\right]^2\sin E_D(t)}{p_C^2} \\
& \cdot\left\{\frac{\sin f_C^0(t)}{h_C^2}\widetilde{\mathbf{h}}_C^2\mathbf{b}_0-\frac{\cos f_C^0(t)}{h_C}\widetilde{\mathbf{h}}_C\mathbf{b}_0\right\} \\
& -\frac{e_C h_C\sin f_C(t)}{p_C}\frac{\mathbf{r}_0}{r_0},
\end{aligned}
\tag{29}
$$

where

$$
f_C^0(t)=f_C(t)-f_C(t_0)\,. \tag{30}
$$

2.1.2 Non-Zero Specific Angular Momentum: $\mathbf{h}\neq 0$, Zero Eccentricity: $e_D=0$

The solution to eq (6) is:

$$
\mathbf{r}_D^{(rot)}(t) \;=\; \cos\left[n_D(t-t_0)\right]\mathbf{R}_{-\omega}\mathbf{a}_0+\sin\left[n_D(t-t_0)\right]\mathbf{R}_{-\omega}\mathbf{b}_0, \tag{31}
$$

$$
\begin{aligned}
\mathbf{v}_D^{(rot)}(t) \;=\; & -n_D\sin\left[n_D(t-t_0)\right]\mathbf{R}_{-\omega}\mathbf{a}_0+n_D\cos\left[n_D(t-t_0)\right]\mathbf{R}_{-\omega}\mathbf{b}_0 \\
& -\cos\left[n_D(t-t_0)\right]\left[\omega\times\mathbf{R}_{-\omega}\mathbf{a}_0\right]-\sin\left[n_D(t-t_0)\right]\left[\omega\times\mathbf{R}_{-\omega}\mathbf{b}_0\right],
\end{aligned}
\tag{32}
$$

where $t\geq t_0$.and:

$$
\mathbf{a}_0=\mathbf{r}_0+\Delta\mathbf{r};\quad \mathbf{b}_0=\frac{1}{n_D}\left[\mathbf{v}_0+\Delta\mathbf{v}+\omega_0\times\Delta\mathbf{r}\right]. \tag{33}
$$

Taking eqs (18) and (19) into account, it follows that the motion of the Deputy with respect to the Chief is described by the vectorial expressions:

$$\begin{aligned}
\mathbf{r}(t) &= \cos\left[n_D(t-t_0)\right]\left\{\frac{\mathbf{a}_0\cdot\mathbf{h}_C}{h_C^2}\mathbf{h}_C\right. \\
&\quad \left.-\frac{\sin f_C^0(t)}{h_C}\tilde{\mathbf{h}}_C\mathbf{a}_0-\frac{\cos f_C^0(t)}{h_C^2}\tilde{\mathbf{h}}_C^2\mathbf{a}_0\right\} \\
&\quad +\sin\left[n_D(t-t_0)\right]\left\{\frac{\mathbf{b}_0\cdot\mathbf{h}_C}{h_C^2}\mathbf{h}_C\right. \\
&\quad \left.-\frac{\sin f_C^0(t)}{h_C}\tilde{\mathbf{h}}_C\mathbf{b}_0-\frac{\cos f_C^0(t)}{h_C^2}\tilde{\mathbf{h}}_C^2\mathbf{b}_0\right\} \\
&\quad -\frac{p_C}{1+e_C\cos f_C(t)}\frac{\mathbf{r}_0}{r_0},
\end{aligned} \tag{34}$$

$$\begin{aligned}
\mathbf{v}(t) &= -n_D\sin\left[n_D(t-t_0)\right]\left\{\frac{\mathbf{a}_0\cdot\mathbf{h}_C}{h_C^2}\mathbf{h}_C\right. \\
&\quad \left.-\frac{\sin f_C^0(t)}{h_C}\tilde{\mathbf{h}}_C\mathbf{a}_0-\frac{\cos f_C^0(t)}{h_C^2}\tilde{\mathbf{h}}_C^2\mathbf{a}_0\right\} \\
&\quad +n_D\cos\left[n_D(t-t_0)\right]\left\{\frac{\mathbf{b}_0\cdot\mathbf{h}_C}{h_C^2}\mathbf{h}_C\right. \\
&\quad \left.-\frac{\sin f_C^0(t)}{h_C}\tilde{\mathbf{h}}_C\mathbf{b}_0-\frac{\cos f_C^0(t)}{h_C^2}\tilde{\mathbf{h}}_C^2\mathbf{b}_0\right\} \\
&\quad +\frac{h_C\left[1+e_C\cos f_C(t)\right]^2\cos\left[n_D(t-t_0)\right]}{p_C^2} \\
&\quad \cdot\left\{\frac{\sin f_C^0(t)}{h_C^2}\tilde{\mathbf{h}}_C^2\mathbf{a}_0-\frac{\cos f_C^0(t)}{h_C}\tilde{\mathbf{h}}_C\mathbf{a}_0\right\} \\
&\quad +\frac{h_C\left[1+e_C\cos f_C(t)\right]^2\sin\left[n_D(t-t_0)\right]}{p_C^2} \\
&\quad \cdot\left\{\frac{\sin f_C^0(t)}{h_C^2}\tilde{\mathbf{h}}_C^2\mathbf{b}_0-\frac{\cos f_C^0(t)}{h_C}\tilde{\mathbf{h}}_C\mathbf{b}_0\right\} \\
&\quad -\frac{e_C h_C\sin f_C(t)}{p_C}\frac{\mathbf{r}_0}{r_0},
\end{aligned} \tag{35}$$

(notation (30) was used).

Solutions for the zero, respectively the positive specific energy may be deduced exactly in the same way. Parametric equations of the relative motion with respect to LVLH may also be deduced in each particular case that may occur.

2.1.3 The Periodicity Problem (The Orbit Resonance)

In case the Chief trajectory is elliptic and the Deputy trajectory is also elliptic, the motion of the Deputy with respect to the Chief might be periodic. This is accomplished when the ratio between the main periods (of Chief and Deputy) is a rational number, and in this case the trajectory of the Deputy with respect to LVLH is a closed curve. As it follows from the above computations, the two functions involved in the Deputy expressions of motion are f_C (the Chief true anomaly) and E_D (the Deputy eccentric anomaly). Both are periodic functions in the particular situation when the trajectories are elliptic ($\xi_C < 0$, $\xi_D < 0$). The main periods of f_C and E_D are respectively:

$$T_{\text{Chief}} = \frac{2\pi}{n_C} = \frac{2\pi\mu}{\left(\frac{2\mu}{r_0} - v_0^2\right)^{3/2}} \tag{36}$$

$$T_{\text{Deputy}} = \frac{2\pi}{n_D} = \frac{2\pi\mu}{\left(\frac{2\mu}{|\mathbf{r}_0+\Delta\mathbf{r}|} - [\mathbf{v}_0 + \Delta\mathbf{v} + \omega_0 \times \Delta\mathbf{r}]^2\right)^{3/2}}$$

The condition:

$$\frac{T_{\text{Chief}}}{T_{\text{Deputy}}} \in \mathbb{Q}, \tag{37}$$

($\mathbb{Q}$ denotes the set of rational numbers) is necessary and sufficient for the relative motion to be periodic. It follows that the motion of the Deputy with respect to the Chief is periodic (*orbit resonance* case) iff there exists two relative prime natural numbers λ_1 and λ_2 such as:

$$\frac{r_0}{|\mathbf{r}_0 + \Delta\mathbf{r}|} \frac{2\mu - |\mathbf{r}_0 + \Delta\mathbf{r}| \left(\mathbf{v}_0 + \Delta\mathbf{v} + \omega_0 \times \Delta\mathbf{r}\right)^2}{2\mu - r_0 v_0^2} = \left(\frac{\lambda_1}{\lambda_2}\right)^{2/3} \tag{38}$$

The periodicity condition (38) is given using only the initial conditions at $t = t_0$.

2.2 Remarks on the Relative Motion Equations

The non-linear initial value problem (1) that models the motion of the Deputy with respect to the LVLH reference frame has a solution that has the form:

$$\mathbf{r} = \mathbf{r}\left(t, \Delta\mathbf{r}, \Delta\mathbf{v}\right). \tag{39}$$

When $\Delta\mathbf{r} = \mathbf{0}$, $\Delta\mathbf{v} = \mathbf{0}$, then $\mathbf{r} = \mathbf{0}$ is solution to eq (1) or $\mathbf{r} = \mathbf{r}_C$ is solution to eq (6).

In most papers, the solution to the relative orbital motion is obtained from the linearized equations of motion derived from eq (1).

The procedure is like it follows: consider the motion of the Deputy described by eq (1). For $\left(\frac{r}{r_C}\right)^n \simeq 0$, $n \geq 2$, the following approximations are made in eq (1):

$$\begin{aligned} \frac{\mu}{\left|\mathbf{r}_C + \mathbf{r}\right|^3} &= \mu\left(\mathbf{r}_C^2 + 2\mathbf{r}_C \cdot \mathbf{r} + \mathbf{r}^2\right)^{-\frac{3}{2}} \cong \\ &\cong \mu r_C^{-3}\left(1 + \frac{2\mathbf{r}_C \cdot \mathbf{r}}{r_C^2}\right)^{-\frac{3}{2}} \cong \mu r_C^{-3}\left(1 - \frac{3\mathbf{r}_C \cdot \mathbf{r}}{r_C^2}\right) \end{aligned} \tag{40}$$

The vectorial linearized equation that describes the Deputy motion with respect to LVLH becomes:

$$\ddot{\mathbf{r}} + 2\boldsymbol{\omega} \times \dot{\mathbf{r}} + \boldsymbol{\omega} \times (\boldsymbol{\omega} \times \mathbf{r}) + \dot{\boldsymbol{\omega}} \times \mathbf{r} + \omega_*^2 \mathbf{r} = 3\omega_*^2 \frac{3\mathbf{r}_C \cdot \mathbf{r}}{r_C^2}\mathbf{r}_C \tag{41}$$

$$\begin{cases} \mathbf{r}\left(t_0\right) = \Delta\mathbf{r}, \\ \dot{\mathbf{r}}\left(t_0\right) = \Delta\mathbf{v}, \end{cases}$$

where

$$\omega_*^2 = \frac{\mu^4}{h_C^6\left(1 + e_C \cos f_C\right)^2}. \tag{42}$$

Eq (42) represents the vectorial form of Lawden's equations if the reference trajectory is elliptic (see (27)) ($0 < e_C < 1$) or Hill-Clohessy-Wiltshire equations if the reference trajectory is circular ($e_C = 0$) (see (1)). Consider (see (8)):

$$\mathbf{X}_0 = \begin{bmatrix} \Delta\mathbf{r} \\ \Delta\mathbf{v} \end{bmatrix} \tag{43}$$

the state matrix of the Deputy at $t = t_0$ and its state matrix at a moment of time t :

$$\mathbf{X}\left(t\right) = \begin{bmatrix} \mathbf{r} \\ \mathbf{v} \end{bmatrix} = \begin{bmatrix} x_D & y_D & z_D & \dot{x}_D & \dot{y}_D & \dot{z}_D \end{bmatrix}^T. \tag{44}$$

The solution of the linearized equation (41) is presented in the literature (see (8), (27)) via a transformation matrix Φ named state transition matrix that satisfies:

$$\mathbf{X}(t) = \Phi(t, t_0)\,\mathbf{X}_0. \tag{45}$$

Several forms of matrix Φ are used in literature. It is given with respect to the Chief true anomaly as independent variable (see (27)) or with time as independent variable (see (8)). The motion has a low level of predictability when using the model offered by the linearized equations. Some solutions work only for small eccentricities.

The solution presented in the form (45) represents the first linear approximation of the solution introduced in this paper. The state transition matrix based solution offers a finite level of predictability. The solution offered in this papers has an infinite interval of predictability, due to its exact form.

3 Conclusions

A closed form vectorial solution for the orbital relative motion problem was given. The solution has the time as independent variable and does not contain singularities. In the case when both satellites have elliptic orbits, a necessary and sufficient condition for the motion to be periodic was offered. This condition depends only on the initial position and velocity vectors of both satellites. This solution extends the solutions to the linearized equations of relative motion that are widely used in orbital mechanics. The expressions of the relative position vector and velocity are purely vectorial and does not depend on a particular coordinate system that might be used.

Most solutions presented in the literature are the first linear approximation of the solution presented in this paper.

References

[1] Clohessy, W.H., Wiltshire, R.S., "Terminal Guidance System for Satellite Rendezvous", Journal of the Aerospace Sciences, Vol. 27, No. 9, Sept. 1960, pp. 653-658.

[2] Hill, G.W., "Researches in Lunar Theory", American Journal of Mathematics, Vol. 1, 1878, pp. 5-26.

[3] Lawden, D. F., "Optimal Trajectories for Space Navigation", Butterworths, London, 1963, pp. 79–86.

[4] Tschauner, J., Hempel, P., "Optimale Beschleunigeungsprogramme für das Rendezvous-Manover," Acta Astronautica, Vol. 10, 1964, pp. 296–307.

[5] Tschauner, J., "The Elliptic Orbit Rendezvous", AIAA 4th Aerospace Sciences Meeting, Los Angeles, CA, June 27-29, 1966.

[6] Lancaster, E.R., "Relative Motion of Two Particles in Elliptic Orbits", AIAA Journal, Vol.8, No.10, 1970, pp. 1878-1879.

[7] Bereen, T., Svedt, G., "Relative Motion of Particles in Coplanar Elliptic Orbits", Journal of Guidance and Control, Vol. 2, 1979, pp. 443-446.

[8] Melton, R.G., "Time-Explicit Representation of Relative Motion Between Elliptical Orbits", Journal of Guidance, Control, and Dynamics, Vol. 23, No. 4, July-August 2000, pp. 604-610.

[9] Broucke, R.A., "A Solution of the Elliptic Rendezvous Problem with the Time as Independent Variable", AAS/AIAA Space Flight Mechanics Meeting, San Antonio, TX, January, 2002.

[10] Koon, W.S., Marsden, J.E., Masdemont, J., Murray, R.M., "J_2 Dynamics and Formation Flight", AIAA Guidance, Navigation, and Control Conference and Exhibit, Montreal, Canada, 6-9 August, 2001

[11] Schweighart, S.A., Sedwick, R.J., "Development and Analysis of a High-Fidelity Linearized J_2 Models for Satellite Formation Flying", AIAA Space 2001 - Conference and Exposition, Albuquerque, NM, 28-30 August, 2001.

[12] Carter, T., Humi, M., "Clohessy–Wiltshire Equations Modified to Include Quadratic Drag", Journal of Guidance, Control, and Dynamics, Vol. 25, No. 6, November–December 2002, pp.1058-1063.

[13] Roberts, J.A., Roberts, C.E., "The Development of High Fidelity Linearized J_2 Models for Satellite Formation Flying Control", AS/AIAA Space Flight Mechanics Meeting, Maui, Hawaii, February 2004.

[14] Gurfil, P., "Analysis of J_2 Perturbed Motion using Mean Non-Osculating Orbital Elements", AIAA/AAS Astrodynamics Specialist Conference and Exhibit, Providence, Rhode Island, 16 - 19 August 2004.

[15] Condurache, D., "New Symbolic Methods into the Study of Dynamic Systems" (in Romanian), PhD thesis, Technical University "Gh Asachi" Iaşi, 1995.

[16] Condurache, D., Martinuşi, V.,. "The Solution to Kepler's Problem in Non-Inertial Reference Frames", Bul. Inst. Polit. Iaşi, LI(LV), 1-2, Sect. Mathematics, Theoretical Mechanics, Physics, 2005, pp. 43-55.

[17] Condurache, D., Martinuşi, V., "Kepler's Problem in Rotating Reference Frames. Part I: Prime Integrals, Vectorial Regularization", accepted for publication to Journal of Guidance, Control and Dynamics, 2006.

[18] Gantmacher, F.R., *The Theory of Matrices*, chap 15, New York, Chelsea, 1959.

[19] Darboux, G., *Leçons sur la théorie générale des surfaces et les applications*

géométriques du calcul infinitesimal, Tome 1, chap II, Gautiers-Villars, Paris, 1887.

[20] Condurache, D., Martinuşi, V., "Kepler's Problem in Rotating Reference Frames. Part II: Application to Relative Orbital Motion", accepted for publication to Journal of Guidance, Control and Dynamics, 2006.

[21] Goldstein, H., *Classical Mechanics*, chap. 3, Addison-Wesley Publishing Company, Inc. Reading, Massachusets, USA, 1980.

[22] Condurache, D., Martinuşi, V., "About the Rectilinear Keplerian Motion", The 2nd International Symposium of Theoretical and Applied Mechanics "D.I.Mangeron" Conference Proceedings, Bul. Inst. Polit. Iaşi, LI (LIV), 2005, pp. 185-193.

[23] Sundman, K.F., "Mémoire sur le problème des trois corps", Acta Mathematica, Vol. 36, 1912, pp. 105-179.

[24] Levi-Civita., T., "Sur la régularisation du problème des trois corps", Acta Mathematica, **42** 1920, pp. 1-4.

[25] Kustaanheimo, P.E., Tutein, J., "On Spinor Equations of Motion and their Possible Integrals", Astronomische Nachrichten, vol. 303, no. 4, 1982, pp. 221-225.

[26] Kustaanheimo, P.E., "Spinor regularization of Kepler motion", Ann. Univ. Turkuens A, I, **73**, fascl, Publ. Astron. Obs. Helsinki, **102**, 1964, pp. 3-7.

[27] Carter, T.E., "State Transition Matrices for Terminal Rendezvous Studies: Brief Survey and New Example", Journal of Guidance, Control, and Dynamics, Vol. 21, No. 1, January-February 1998, pp. 148-155.

PADEU | PADEU **19** (2007), p. 65
ISBN 963 463 557
©Published by the Astron. Dept. of the Eötvös Univ.

A Novel Hypercomplex Solution to Kepler's Problem

Daniel Condurache[1], Vladimir Martinuşi[2],

Technical University "Gh. Asachi", Department of Theoretical Mechanics, Iaşi, Romania

E-mail: [1]danielcondurache@rdslink.ro, [2]vladmartinus@gmail.com

Abstract
By using a Sundman like regularization, we offer a unified solution to Kepler's problem by using hypercomplex numbers. The fundamental role in this paper is played by the Laplace-Runge-Lenz prime integral and by the hypercomplex numbers algebra. The procedure unifies and generalizes the regularizations offered by Levi-Civita and Kustaanheimo-Stiefel. Closed form hypercomplex expressions for the law of motion and velocity are deduced, together with inedite hypercomplex prime integrals.
Keywords: *Kepler's problem, Sundman transformation, Hypercomplex numbers*

1 Introduction

The classic Kepler problem is described by the initial value problem:

$$\ddot{\mathbf{r}}+\frac{\mu}{r^3}\mathbf{r}=\mathbf{0},\ \mathbf{r}\left(t_0\right)=\mathbf{r}_0,\ \dot{\mathbf{r}}\left(t_0\right)=\mathbf{v}_0. \tag{1}$$

where $\mathbf{r}=\mathbf{r}\left(t\right)$ represents the position vector of the particle with respect to the attraction center and μ the gravitational parameter. The most common regularization procedure used in the literature for Kepler's problem is represented by the introduction of an independent variable $\tau=\tau\left(t\right)$ (called fictitious time) such as:

$$dt=rd\tau, \tag{2}$$

where r represents the magnitude of the solution to eq (1). This was done for the first time by Sundman (see (1)) when studying the restricted three-body problem. Levi-Civita (see (2)) used the time-transformation (2) and complex numbers in order to regularize the planar Kepler's problem. Kustaanheimo and Stieffel (see (3), (4)) used the same procedure and gave a spinor regularization of the spatial Kepler's problem.

The aim of this paper is to provide a closed form unified hypercomplex solution to the classic Kepler problem. By using a vectorial Sundman-like regularization, **Section 2** gives the hypercomplex solution to eq (1) and then particularizes it for the different situations that may occur. The collision case is also studied.

By making the change of variable:

$$t - t^0 = \int_0^\tau r(\alpha)\, d\alpha, \tag{3}$$

the vectorial Sundman like regularization transforms eq (1) into a linear second order initial value problem with constant coefficients:

$$\mathbf{r}'' - 2\xi\mathbf{r} = -\mathbf{L}, \mathbf{r}(0) = \mathbf{r}^0,\ \mathbf{r}'(0) = r^0\mathbf{v}^0, \tag{4}$$

where $(\,)'$ is defined as:

$$(\,)' = r(\dot{\,}),$$

$t^0 \geq 0$ is a constant real number that corresponds to $\tau = 0$, $\tau(t^0) = 0$, $\mathbf{r}^0$, $\mathbf{v}^0$ are the position respectively the velocity vectors at $t = t^0$, ξ is the specific energy and $\mathbf{L}$ is the Laplace-Runge-Lenz vector,

$$\begin{aligned} \xi &= \frac{1}{2}\dot{\mathbf{r}}^2 - \frac{\mu}{r} = \frac{1}{2}\mathbf{v}_0^2 - \frac{\mu}{r_0} \\ \mathbf{e} &= \frac{\dot{\mathbf{r}} \times (\mathbf{r} \times \dot{\mathbf{r}})}{\mu} - \frac{\mathbf{r}}{r} = \frac{\mathbf{v}_0 \times (\mathbf{r}_0 \times \mathbf{v}_0)}{\mu} - \frac{\mathbf{r}_0}{r_0}, \\ \mathbf{L} &= \mu\mathbf{e}, \end{aligned} \tag{5}$$

where $\mathbf{e}$ represents the vectorial eccentricity of the conic when $\mathbf{r}_0 \times \mathbf{v}_0 \neq \mathbf{0}$. The magnitude of the position vector is the solution to:

$$r'' - 2\xi r = \mu,\ r(0) = r^0,\ r'(0) = \mathbf{r}^0 \cdot \mathbf{v}^0. \tag{6}$$

We will also denote:

$$\mathbf{h} = \mathbf{r} \times \dot{\mathbf{r}} = \mathbf{r}_0 \times \mathbf{v}_0$$

the specific angular momentum of the Keplerian motion.

2 A Hypercomplex Solution to Kepler's Problem

Let us consider a hypercomplex number ε such as:

$$\varepsilon^2 = 2\xi, \tag{7}$$

with ξ defined in eq (5). We denote:

$$\begin{cases} \underline{\mathbb{R}} \triangleq \mathbb{R} + \varepsilon\mathbb{R} = \{x + \varepsilon y \mid x, y \in \mathbb{R}\}, \\ \underline{\mathbf{V}_3} \triangleq \mathbf{V}_3 + \varepsilon\mathbf{V}_3 = \{\mathbf{x} + \varepsilon\mathbf{y} \mid \mathbf{x}, \mathbf{y} \in \mathbf{V}_3\}, \end{cases} \tag{8}$$

where $\mathbb{R}$ is the set of real numbers and $\mathbf{V}_3$ is the set of three-dimmensional vectors. It is known that the set of hypercomplex numbers $\underline{\mathbb{R}}$ is a ring and also a $\mathbb{R}-$ second order commutative algebra and $\underline{\mathbf{V}_3}$ is a $\underline{\mathbb{R}}-$ free module. If $\xi < 0$, then the hypercomplex algebra $\underline{\mathbb{R}}$ is isomorphic to the complex numbers algebra $\mathbb{C}$, if $\xi = 0$ it is isomorphic with the dual numbers algebra and if $\xi > 0$ it is isomorphic to the hyperbolic numbers algebra. We introduce a **hypercomplex state vector** $\underline{\mathbf{s}} \in \underline{\mathbf{V}_3}$ like it follows:

$$\underline{\mathbf{s}} \triangleq \mathbf{r}' + \varepsilon\mathbf{r}, \tag{9}$$

where $\mathbf{r}$ is the solution to the regularized eq (4). From eq (4) and (7), it results:

$$\underline{\mathbf{s}}' = \varepsilon\underline{\mathbf{s}} - \mathbf{L};\ \underline{\mathbf{s}}(0) = r^0\mathbf{v}^0 + \varepsilon\mathbf{r}^0 \triangleq \underline{\mathbf{s}}_0. \tag{10}$$

We also introduce the hypercomplex number:

$$\underline{s} \triangleq r' + \varepsilon r, \tag{11}$$

that is related to the radial motion of the particle (it models its radial state). It follows that $\underline{s}$ satisfies:

$$\underline{s}' = \varepsilon\underline{s} + \mu,\ \underline{s}(0) = \mathbf{r}^0 \cdot \mathbf{v}^0 + \varepsilon r^0 \triangleq \underline{s}_0 \tag{12}$$

We also define the *hypercomplex eccentric anomaly* and the exponential of a hypercomplex number:

$$\underline{E}(\tau) \triangleq \varepsilon\tau, \tag{13}$$

$$\exp(\underline{x}) \triangleq \sum_{k=0}^{\infty} \frac{\underline{x}^k}{k!}. \tag{14}$$

Lemma 2.0.1 *There exist two real valued functions $c,\ s:\mathbb{R}\to\mathbb{R}$, indefinitely derivable, such as:*

$$\exp(\underline{E}) = c(\tau) + \varepsilon s(\tau), (\forall)\tau \in \mathbb{R}. \tag{15}$$

Proof. We remark that $\varepsilon^{2k} \in \mathbb{R}$ for any natural number k. Further, we see that:

$$\exp(\underline{E}) = \exp(\varepsilon\tau) = \left[\sum_{k=0}^{\infty} \frac{\varepsilon^{2\kappa}\tau^{2\kappa}}{(2k)!}\right] + \varepsilon\left[\sum_{k=0}^{\infty} \frac{\varepsilon^{2\kappa}\tau^{2\kappa+1}}{(2k+1)!}\right]. \tag{16}$$

The real valued maps:

$$c(\tau) \triangleq \sum_{k=0}^{\infty} \frac{\varepsilon^{2\kappa}\tau^{2\kappa}}{(2k)!}, \qquad s(\tau) \triangleq \sum_{k=0}^{\infty} \frac{\varepsilon^{2\kappa}\tau^{2\kappa+1}}{(2k+1)!} \tag{17}$$

are the ones that satisfy eq (15). The proof is finalized. ■

One may remark that the functions $c(\tau)$ and $s(\tau)$ may be expressed as:

$$c(\tau) = \cosh(\varepsilon\tau); \qquad \varepsilon s(\tau) = \sinh(\varepsilon\tau). \tag{18}$$

If we denote $\underline{\varpi}=\sqrt{2\xi} \in \mathbb{C}$ (the set of complex numbers) then c and s may also be expressed as:

$$c(\tau) = \cosh(\underline{\varpi}\tau); \qquad s(\tau) = \tau\operatorname{sinch}(\underline{\varpi}\tau), \tag{19}$$

where $\operatorname{sinch}(x) \triangleq \begin{cases} \dfrac{\sinh(x)}{x}, & x \neq 0 \\ 1, & x = 0 \end{cases}$.

Notation 2.0.2 *We denote:*

$$\begin{aligned} c_1(\tau) &\triangleq \int_0^{\tau} c(\alpha)\,d\alpha;\ s_1(\tau) \triangleq \int_0^{\tau} s(\alpha)\,d\alpha; \\ c_2(\tau) &\triangleq \int_0^{\tau} c_1(\alpha)\,d\alpha;\ s_2(\tau) \triangleq \int_0^{\tau} s_1(\alpha)\,d\alpha. \end{aligned} \tag{20}$$

The next result offers closed form expressions for the state vector $\underline{\mathbf{s}}$, the radial state $\underline{s}$ and gives a generalized hypercomplex Kepler equation. We denote the imaginary part of a hypercomplex number: $Im(x+\varepsilon y) = y$.

Theorem 2.0.3 *The hypercomplex state vector* $\underline{\mathbf{s}}$ *defined by eq (9) has the vectorial closed form:*

$$\underline{\mathbf{s}} = \underline{\mathbf{s}}_0 + [\varepsilon \underline{\mathbf{s}}_0 - \mathbf{L}]\, \Phi(\tau). \tag{21}$$

The hypercomplex number $\underline{s}$ *has the closed form:*

$$\underline{s} = \underline{s}_0 + [\varepsilon \underline{s}_0 + \mu]\, \Phi(\tau). \tag{22}$$

where $\Phi(\tau)$ *is defined by:*

$$\Phi(\tau) = \int_0^{\tau} \exp(\underline{E}(\alpha))\, d\alpha \tag{23}$$

and the time t *may be deduced from the generalized hypercomplex Kepler equation:*

$$t - t^0 = Im \int_0^{\tau} \underline{s}(\alpha)\, d\alpha. \tag{24}$$

Proof. By differentiating with respect to τ in eq (10), it follows that $\underline{\mathbf{s}}'' = \varepsilon \underline{\mathbf{s}}'$. Then vector $\underline{\mathbf{s}}'$ has the form:

$$\underline{\mathbf{s}}' = \exp(\varepsilon\tau)\, \underline{\mathbf{s}}'(0) = \exp(\varepsilon\tau)\, [\varepsilon \underline{\mathbf{s}}(0) - \mathbf{L}]. \tag{25}$$

By integrating in eq (25) with respect to τ and taking into consideration eq (23), eq (21) is deduced. Eq (22) is deduced similarly.

In order to prove eq (24), consider the dual number:

$$\underline{t} = r + \varepsilon t, \tag{26}$$

where r is the magnitude of the position vector. By differentiating with respect to τ in eq (26), it follows that $\underline{t}' = \underline{s}$. Therefore we may write:

$$\underline{t} = \int_0^{\tau} \underline{s}(\alpha)\, d\alpha + \underline{t}^0 \Rightarrow r - r^0 + \varepsilon\left(t - t^0\right) = \int_0^{\tau} \underline{s}(\alpha)\, d\alpha, \tag{27}$$

that ends the proof. ■

Remark 2.0.4 *By taking into consideration eqs (21), (22), and* ***Lemma 2.0.1****, it results that* $\underline{\mathbf{s}}$ *,* $\underline{s}$ *and* $t - t^0$ *may be written as it follows:*

$$\underline{\mathbf{s}} = [c_1(\tau) + \varepsilon s_1(\tau)]\, [\varepsilon \underline{\mathbf{s}}_0 - \mathbf{L}] + \underline{\mathbf{s}}_0, \tag{28}$$

$$\underline{s} = [c_1(\tau) + \varepsilon s_1(\tau)]\, [\varepsilon \underline{s}_0 + \mu] + \underline{s}_0. \tag{29}$$

$$t - t^0 = r^0 \tau + c_2(\tau)\left(\mathbf{r}^0 \cdot \mathbf{v}^0\right) + s_2(\tau)\left(2\xi r^0 + \mu\right). \tag{30}$$

We present now the main result of this paper. It gives the hypercomplex solution to Kepler's problem.

Theorem 2.0.5 *The following statements hold true:*
The position vector is:

$$\mathbf{r}(\tau) = \mathbf{r}^0 + c_1(\tau)\, r^0 \mathbf{v}^0 + s_1(\tau)\left(2\xi \mathbf{r}^0 - \mathbf{L}\right). \tag{31}$$

The magnitude of the position vector is:

$$r(\tau) = r^0 + c_1(\tau)\left(\mathbf{r}^0 \cdot \mathbf{v}^0\right) + s_1(\tau)\left(2\xi r^0 + \mu\right). \tag{32}$$

The velocity vector is:

$$\begin{aligned} \mathbf{v}(\tau) \;=\; & \left[r^0 + c_1(\tau)\left(\mathbf{r}^0 \cdot \mathbf{v}^0\right) + s_1(\tau)\left(2\xi r^0 + \mu\right)\right]^{-1} \cdot \\ & \left[c(\tau)\, r^0 \mathbf{v}^0 + s(\tau)\left(2\xi \mathbf{r}^0 - \mathbf{L}\right)\right]. \end{aligned} \tag{33}$$

The link between t and τ is given by ***the generalized Kepler equation:***

$$t - t^0 = r^0 \tau + c_2(\tau)\left(\mathbf{r}^0 \cdot \mathbf{v}^0\right) + s_2(\tau)\left(2\xi r^0 + \mu\right). \tag{34}$$

Proof. From eq (21) it follows that:

$$\mathbf{r}' + \varepsilon \mathbf{r} = \left[c_1(\tau) + \varepsilon s_1(\tau)\right]\left(\varepsilon r^0 \mathbf{v}^0 + 2\xi \mathbf{r}^0 - \mathbf{L}\right) + r^0 \mathbf{v}^0 + \varepsilon \mathbf{r}^0. \tag{35}$$

By integrating with respect to τ in eq (35), eq (31) is obtained.
Eq (32) is proven similarly.
Eq (33) results from eq (31) by derivating with respect to τ and taking into account that $\mathbf{r}' = r\mathbf{v}$.
Eq (34) results from eq (32) by direct integration with respect to τ. One may remark that eq (34) represent the generalized Kepler equation. ■

Remark 2.0.6 *The functions c and s defined in this section represent the fundamental trigonometric functions in a space of -2ξ constant curvature associated to the Keplerian motion (see (9; 10; 16)). The following fundamental identities hold true (see (11)):*

$$\begin{aligned} & c^2(\tau) + \varepsilon^2 s^2(\tau) = 1; \qquad c(2\tau) = c^2(\tau) - \varepsilon^2 s^2(\tau); \quad s(2\tau) = 2s(\tau)c \\ & c^2\left(\tfrac{1}{2}\tau\right) = \tfrac{1+c(\tau)}{2}; \qquad \varepsilon^2 s^2\left(\tfrac{1}{2}\tau\right) = \tfrac{1-c(\tau)}{2}; \\ & c(\tau_1 \pm \tau_2) = c(\tau_1)\, c(\tau_2) \mp s(\tau_1)\, s(\tau_2); \\ & s(\tau_1 \pm \tau_2) = s(\tau_1)\, c(\tau_2) \pm c(\tau_1)\, s(\tau_2). \end{aligned} \tag{36}$$

The following approach is splited into two: the situation when $t^0 = t_0$ (the initial moment of time) and $t^0 = t_P$ (the moment of time the particle is situated at the pericenter at the trajectory).

2.1 The Variable $\tau = 0$ at the Initial Moment of Time $t = t_0$

The law of motion and the velocity have the form:

$$\mathbf{r}(\tau) = \mathbf{r}_0 + c_1(\tau)\, r_0 \mathbf{v}_0 + s_1(\tau)\,(2\xi \mathbf{r}_0 - \mathbf{L}). \tag{37}$$

$$\mathbf{v}(\tau) = [r_0 + c_1(\tau)\,(\mathbf{r}_0 \cdot \mathbf{v}_0) + s_1(\tau)\,(2\xi r_0 + \mu)]^{-1} \cdot \cdot [c(\tau)\, r_0 \mathbf{v}_0 + s(\tau)\,(2\xi \mathbf{r}_0 - \mathbf{L})] \tag{38}$$

and the generalized Kepler's equation (34) becomes:

$$t - t_0 = r_0 \tau + c_2(\tau)\,(\mathbf{r}_0 \cdot \mathbf{v}_0) + s_2(\tau)\,(2\xi r_0 + \mu). \tag{39}$$

2.1.1 Negative specific energy $\xi < 0$

The functions c and s defined in eqs (17) have the particular form:

$$c(\tau) = \cos E(\tau), \qquad s(\tau) = \frac{1}{\sqrt{2|\xi|}} \sin E(\tau), \tag{40}$$

where $E(\tau) = \sqrt{2|\xi|}\tau$ represents the eccentric anomaly of the Keplerian motion in case $\mathbf{h} \neq \mathbf{0}$. It results:

$$\mathbf{r}(\tau) = -\frac{\mathbf{L}}{2|\xi|} + \left(\mathbf{r}_0 + \frac{\mathbf{L}}{2|\xi|}\right)\cos E(\tau) + \frac{r_0 \mathbf{v}_0}{\sqrt{2|\xi|}} \sin E(\tau), \tag{41}$$

$$r(\tau) = \frac{\mu}{2|\xi|} + \left(r_0 - \frac{\mu}{2|\xi|}\right)\cos E(\tau) + \frac{\mathbf{r}_0 \cdot \mathbf{v}_0}{\sqrt{2|\xi|}} \sin E(\tau), \tag{42}$$

$$\mathbf{v}(\tau) = [r(\tau)]^{-1} \cdot \left[r_0 \mathbf{v}_0 \cos E(\tau) + \frac{2\xi \mathbf{r}_0 - \mathbf{L}}{\sqrt{2|\xi|}} \sin E(\tau)\right]. \tag{43}$$

The generalized Kepler's equation (39) becomes:

$$t - t_0 = \frac{\mu E(\tau)}{(2|\xi|)^{3/2}} + \frac{\mathbf{r}_0 \cdot \mathbf{v}_0}{2|\xi|}\,[1 - \cos E(\tau)] + \left(r_0 - \frac{\mu}{2|\xi|}\right)\frac{\sin E(\tau)}{\sqrt{2|\xi|}}. \tag{44}$$

Eq. (44) gives the link between the functions t and $E(\tau)$.

One may remark that eq (41) represents the parametric equation of an ellipse (possibly degenerated). Its center has the position vector $-\frac{\mathbf{L}}{2|\xi|}$ with respect to the attraction center. The ellipse conjugate diameters are: $\mathbf{d} = \mathbf{r}_0 + \frac{\mathbf{L}}{2|\xi|}$; $\mathbf{d}^* = \frac{\mathbf{r}_0 \mathbf{v}_0}{\sqrt{2|\xi|}}$. The ellipse is degenerated iff $\mathbf{d} \times \mathbf{d}^* = \mathbf{0}$. This occurs when $\mathbf{h} = \mathbf{r}_0 \times \mathbf{v}_0 = \mathbf{0}$. The equation $r(\tau) = 0$ has a solution $\tau > 0$. From:

$$r(\tau) = \frac{\mu}{2|\xi|} + \sqrt{\left(r_0 - \frac{\mu}{2|\xi|}\right)^2 + \frac{r_0^2 v_0^2}{2|\xi|}} \sin[E(\tau) + \varphi], \tag{45}$$

with φ defined by:

$$\begin{aligned} \cos\varphi &= \frac{\mathbf{r}_0 \cdot \mathbf{v}_0}{\sqrt{2|\xi|}\sqrt{\left(r_0 - \frac{\mu}{2|\xi|}\right)^2 + \frac{r_0^2 v_0^2}{2|\xi|}}}, \\ \sin\varphi &= \frac{2|\xi| r_0 - \mu}{2|\xi|\sqrt{\left(r_0 - \frac{\mu}{2|\xi|}\right)^2 + \frac{r_0^2 v_0^2}{2|\xi|}}}, \end{aligned} \tag{46}$$

it follows that $E(\tau)$ may be computed by solving the trigonometric equation:

$$\sin[E(\tau) + \varphi] = -\frac{\mu}{2|\xi|\sqrt{\left(r_0 - \frac{\mu}{2|\xi|}\right)^2 + \frac{r_0^2 v_0^2}{2|\xi|}}} \tag{47}$$

The value τ_c that satisfies eq (47) represents the collision with the attraction center "moment". The moment of the collision t_c may be computed from eq (44) and it equals to:

$$t_c = t_0 + \frac{\mu E(\tau_c)}{(2|\xi|)^{3/2}} + \frac{\mathbf{r}_0 \cdot \mathbf{v}_0}{2|\xi|}[1 - \cos E(\tau_c)] + \left(r_0 - \frac{\mu}{2|\xi|}\right)\frac{\sin E(\tau_c)}{\sqrt{2|\xi|}} \tag{48}$$

2.1.2 Zero specific energy $\xi = 0$

Functions c and s defined in eqs (17) have the particular form:

$$c(\tau) = 1, \qquad s(\tau) = \tau. \tag{49}$$

It results:

$$\mathbf{r}(\tau) = \mathbf{r}_0 + \tau r_0 \mathbf{v}_0 - \frac{\tau^2}{2}\mathbf{L}. \tag{50}$$

$$r(\tau) = r_0 + \tau(\mathbf{r}_0 \cdot \mathbf{v}_0) + \mu\frac{\tau^2}{2} \tag{51}$$

$$\mathbf{v}(\tau) = [r(\tau)]^{-1}[r_0\mathbf{v}_0 - \tau\mathbf{L}] \tag{52}$$

The generalized Kepler's equation (39) becomes:

$$t - t_0 = r_0\tau + \frac{\tau^2}{2}(\mathbf{r}_0 \cdot \mathbf{v}_0) + \mu\frac{\tau^3}{3} \tag{53}$$

One may remark that eq (50) is the vectorial equation of a parabola (possibly degenerated). The parabola degenerates iff $\mathbf{h} = \mathbf{r}_0 \times \mathbf{v}_0 = \mathbf{0}$. Eq (53) gives the implicit functional equation for determining function τ. In case $\mathbf{r}_0 \times \mathbf{v}_0 = \mathbf{0}$, equation $r(\tau) = 0$ has solution $\tau > 0$ iff $\mathbf{r}_0 \cdot \mathbf{v}_0 < 0$, as it follows from eq (51) and from $\xi = 0 \Leftrightarrow 2\mu = r_0 v_0^2$. The unique solution to eq (51) in case $\mathbf{r}_0 \times \mathbf{v}_0 = \mathbf{0}$, $\mathbf{r}_0 \cdot \mathbf{v}_0 = -r_0 v_0 < 0$ is:

$$\tau_c = \frac{2}{v_0} \tag{54}$$

and it represents the collision with the attraction center "moment". The "real" moment t_c of collision is computed from eqs (53) and (54) and it equals to:

$$t_c = t_0 + \frac{8\mu}{3v_0^3}. \tag{55}$$

2.1.3 Positive specific energy $\xi > 0$

Functions c and s defined in eqs (17) have the particular form:

$$c(\tau) = \cosh E(\tau), \qquad s(\tau) = \frac{1}{\sqrt{2\xi}}\sinh E(\tau). \tag{56}$$

It results:

$$\mathbf{r}(\tau) = \frac{\mathbf{L}}{2\xi} + \left(\mathbf{r}_0 - \frac{\mathbf{L}}{2\xi}\right)\cosh E(\tau) + \frac{r_0\mathbf{v}_0}{\sqrt{2\xi}}\sinh E(\tau), \tag{57}$$

$$r(\tau) = -\frac{\mu}{2\xi} + \frac{\mathbf{r}_0 \cdot \mathbf{v}_0}{\sqrt{2\xi}}\sinh E(\tau) + \left(r_0 + \frac{\mu}{2\xi}\right)\cosh E(\tau), \tag{58}$$

$$\mathbf{v}(\tau) = [r(\tau)]^{-1}\left[r_0\mathbf{v}_0\cosh E(\tau) + \frac{2\xi\mathbf{r}_0 - \mathbf{L}}{\sqrt{2\xi}}\sinh E(\tau)\right]. \tag{59}$$

The generalized Kepler's equation (39) becomes:

$$t - t_0 = -\frac{\mu\tau}{2\xi} + \frac{\mathbf{r}_0 \cdot \mathbf{v}_0}{2\xi}\left[\cosh E(\tau) - 1\right] + \left(r_0 + \frac{\mu}{2\xi}\right)\frac{\sinh E(\tau)}{\sqrt{2\xi}}. \tag{60}$$

One may remark that eq (57) represents the vectorial equation of a hyperbola (possibly degenerated) with the center at the position described by vector $\frac{\mathbf{L}}{2\xi}$. The conjugate diameters of the hyperbola are: $\mathbf{d} = \mathbf{r}_0 - \frac{\mathbf{L}}{2\xi}$; $\mathbf{d}^* = \frac{\mathbf{r}_0\mathbf{v}_0}{\sqrt{2\xi}}$. The hyperbola is degenerated iff $\mathbf{d} \times \mathbf{d}^* = \mathbf{0}$. This occurs when $\mathbf{h} = \mathbf{r}_0 \times \mathbf{v}_0 = \mathbf{0}$. The equation $r(\tau) = 0$ has a solution $\tau > 0$ iff $\mathbf{r}_0 \cdot \mathbf{v}_0 < 0$, as it results from eq (58). The number τ_c that satisfies $r(\tau_c) = 0$ represents the collision "moment". It may be determined by solving the equation:

$$-\frac{\mu}{2\xi} - \frac{r_0 \cdot v_0}{\sqrt{2\xi}}\sinh E(\tau) + \left(r_0 + \frac{\mu}{2\xi}\right)\cosh E(\tau) = 0. \tag{61}$$

The collision moment t_c is computed from eq (60) and it equals to:

$$t_c = t_0 - \frac{\mu\tau_c}{2\xi} + \frac{\mathbf{r}_0 \cdot \mathbf{v}_0}{2\xi}\left[\cosh E(\tau_c) - 1\right] + \left(r_0 + \frac{\mu}{2\xi}\right)\frac{\sinh E(\tau_c)}{\sqrt{2\xi}}. \tag{62}$$

2.2 The Variable $\tau = 0$ at the Periapsis Passage Moment $t = t_P$

The notion of periapsis will be extended to "the point on the trajectory that is nearest to the attraction center". It means that in case of collison, the moment of time t_P will denote the collision moment. In case of no collision, t_P denotes the moment of time when the particle is situated at the periapsis of its trajectory.

One may remark that in this case $\mathbf{r}_P \cdot \mathbf{v}_P = 0$ (at the periapsis the position vector and the velocity vector are orthogonal). The law of motion and the velocity have the form:

$$\mathbf{r}(\tau) = \mathbf{r}_P + c_1(\tau)\, r_P \mathbf{v}_P + s_1(\tau)\left(2\xi\mathbf{r}_P - \mathbf{L}\right), \tag{63}$$

$$\mathbf{v}(\tau) = \left[r_P + s_1(\tau)\left(2\xi r_P + \mu\right)\right]^{-1}\left[c(\tau)\, r_P \mathbf{v}_P + s(\tau)\left(2\xi\mathbf{r}_P - \mathbf{L}\right)\right], \tag{64}$$

and the generalized Kepler's equation (34) becomes:

$$t - t_P = r_P\tau + s_2(\tau)\left(2\xi r_P + \mu\right). \tag{65}$$

Note that if $\mathbf{h} \neq \mathbf{0}$, the following expressions hold true:

$$\mathbf{r}_P = \begin{cases} \frac{h^2}{\mu+L}\frac{\mathbf{L}}{L}, & \mathbf{L} \neq \mathbf{0}, \\ \mathbf{r}_0, & \mathbf{L} = \mathbf{0}, \end{cases} \tag{66}$$

$$r_P = \begin{cases} \frac{h^2}{\mu+L}, & \mathbf{L} \neq \mathbf{0}, \\ r_0, & \mathbf{L} = \mathbf{0}, \end{cases} \tag{67}$$

$$\mathbf{v}_P = \begin{cases} \frac{\mu+L}{h}\frac{\mathbf{h}\times\mathbf{L}}{hL}, & \mathbf{L} \neq \mathbf{0}, \\ v_0, & \mathbf{L} = \mathbf{0}, \end{cases} \tag{68}$$

The situation $\mathbf{L} = \mathbf{0}$ leads to a circular trajectory. The motion is circular and uniform. When $\mathbf{h} = \mathbf{0}$, then: $\mathbf{r}_P = \mathbf{0}$; $r_P v_P = 0$; $v_P = \infty$, and the motion is rectilinear.

We remark that with the hypercomplex number ε defined in eq (7) and the hypercomplex eccentric anomaly $\underline{E}(\tau)$ defined in eq (13), if $\xi \neq 0$ it follows that:

$$c(\tau) = \cosh \underline{E}(\tau) = \begin{cases} \cos\left(\sqrt{2|\xi|}\tau\right) & \text{if } \xi < 0, \\ \cosh\left(\sqrt{2\xi}\tau\right) & \text{if } \xi > 0, \end{cases} \tag{69}$$

$$s(\tau) = \frac{1}{\varepsilon}\sinh \underline{E}(\tau) = \begin{cases} \sin\left(\sqrt{2|\xi|}\tau\right) & \text{if } \xi < 0, \\ \sinh\left(\sqrt{2\xi}\tau\right) & \text{if } \xi > 0. \end{cases}$$

2.2.1 Negative Specific Energy $\xi < 0$

Non-zero Angular Momentum $\mathbf{h} \neq \mathbf{0}$

The law of motion, the position vector magnitude and the velocity are:

$$\begin{aligned} \mathbf{r}(\tau) &= \mathbf{a}[\cos E(\tau) - e] + \mathbf{b}\sin E(\tau), \\ r(\tau) &= a[1 - e\cos E(\tau)], \\ \mathbf{v}(\tau) &= \frac{\sqrt{2|\xi|}}{a[1 - e\cos E(\tau)]}[-\mathbf{a}\sin E(\tau) + \mathbf{b}\cos E(\tau)], \end{aligned} \tag{70}$$

where $\mathbf{a} = \frac{\mu}{2|\xi|}\frac{\mathbf{e}}{e}$, $\mathbf{b} = \frac{2}{e\sqrt{2|\xi|}}\mathbf{h}\times\mathbf{e}$. Eq (70) represents the vectorial parametric equation of an ellipse with the vectorial semiaxis $\mathbf{a}$ and $\mathbf{b}$. In case $a = b$ ($\Leftrightarrow e = 0$), the ellipse becomes a circle with radius r_0.

Eq (34) becomes Kepler's classic equation for the elliptic case:

$$t - t_p = \frac{a}{\sqrt{2|\xi|}}(E(\tau) - e\sin E(\tau)) \tag{71}$$

Zero Angular Momentum $\mathbf{h} = \mathbf{0}$

The law of motion, the position vector magnitude and the velocity are determined by making $\mathbf{b} = \mathbf{0}$, $\mathbf{e} = -\frac{\mathbf{r}_0}{r_0}$ in eqs (70):

$$\begin{aligned} \mathbf{r}(\tau) &= \frac{\mu}{2|\xi|}[\cosh E(\tau) - 1]\frac{\mathbf{r}_0}{r_0}; \\ r(\tau) &= \frac{\mu}{2|\xi|}[1 - \cos E(\tau)]; \\ \mathbf{v}(\tau) &= \frac{\sqrt{2|\xi|}\sinh E(\tau)}{\cosh E(\tau) - 1}\frac{\mathbf{r}_0}{r_0}, \end{aligned} \tag{72}$$

and Kepler's equation is obtained from eq (84) by making $e = 1$:

$$t - t_p = \frac{\mu}{(2|\xi|)^{3/2}}(E(\tau) - \sin E(\tau)). \tag{73}$$

The collision moment is $t_c = t_P$ if $\mathbf{r}_0 \cdot \mathbf{v}_0 \leq 0$ or $t_c = t_P + \dfrac{2\pi(2|\xi|)^{3/2}}{\mu}$ if $\mathbf{r}_0 \cdot \mathbf{v}_0 > 0$.

2.2.2 Zero Specific Energy $\xi = 0$

Non-zero Angular Momentum $\mathbf{h} \neq \mathbf{0}$

The position vector, its magnitude and the velocity vector are:

$$\mathbf{r}(\tau) = \frac{h^2}{2\mu^2}\mathbf{L} + \tau\frac{\mathbf{h}\times\mathbf{L}}{\mu} - \frac{\tau^2}{2}\mathbf{L}, \tag{74}$$

$$r(\tau) = \frac{h^2 + \tau^2\mu^2}{2\mu}, \tag{75}$$

$$\mathbf{v}(\tau) = \frac{2\mu}{h^2 + \tau^2\mu^2}\left[\frac{\mathbf{h}\times\mathbf{L}}{\mu} - \tau\mathbf{L}\right]. \tag{76}$$

Kepler's equation is:

$$t - t_P = \frac{h^2}{2\mu}\tau + \mu\frac{\tau^3}{3}. \tag{77}$$

Zero Angular Momentum $\mathbf{h} = 0$

The law of motion, the position vector magnitude and the velocity are:

$$\mathbf{r}(\tau) = -\frac{\tau^2}{2}\mathbf{L}, \tag{78}$$

$$r(\tau) = \frac{\tau^2 \mu}{2}, \tag{79}$$

$$\mathbf{v}(\tau) = -\frac{2}{\mu\tau}\mathbf{L}. \tag{80}$$

and Kepler's equation is:

$$t - t_P = \mu\frac{\tau^3}{3} \tag{81}$$

The collision occurs iff $\mathbf{r}_0 \cdot \mathbf{v}_0 < 0$, and the collision moment is computed from:

$$t_c = t_0 + \frac{8\mu}{3v_0^3}. \tag{82}$$

2.2.3 Positive Specific Energy $\xi > 0$

Non-zero Angular Momentum $\mathbf{h} \neq \mathbf{0}$

The law of motion, the position vector magnitude and the velocity are:

$$\begin{aligned} \mathbf{r}(\tau) &= \mathbf{a}\left[e - \cosh E(\tau)\right] + \mathbf{b}\sinh E(\tau), \\ r(\tau) &= a\left(e\cosh E(\tau) - 1\right), \\ \mathbf{v}(\tau) &= \frac{\sqrt{2\xi}}{a\left(e\cosh E(\tau) - 1\right)}\left[-\mathbf{a}\sinh E(\tau) + \mathbf{b}\cosh E(\tau)\right], \end{aligned} \tag{83}$$

where $\mathbf{a} = \frac{\mu}{2\xi}\frac{\mathbf{e}}{e}$, $\mathbf{b} = \frac{2}{e\sqrt{2\xi}}\mathbf{h} \times \mathbf{e}$. The first of eqs (83) represents the vectorial parametric equation of a hyperbola with the vectorial semiaxis $\mathbf{a}$ and $\mathbf{b}$. Kepler's equation is::

$$t - t_p = \frac{a}{\sqrt{2\xi}}\left[e\sinh E(\tau) - E(\tau)\right]. \tag{84}$$

Zero Angular Momentum h = 0

The law of motion, the position vector magnitude and the velocity are:

$$\begin{aligned} \mathbf{r}(\tau) &= \frac{\mu}{2\xi}\left[\cosh E(\tau) - 1\right]\frac{\mathbf{r}_0}{r_0}, \\ r(\tau) &= \frac{\mu}{2\xi}\left(\cosh E(\tau) - 1\right), \\ \mathbf{v}(\tau) &= -\frac{(2\xi)^{3/2}\sinh E(\tau)}{\mu\left(\cosh E(\tau) - 1\right)}\frac{\mathbf{r}_0}{r_0}, \end{aligned} \tag{85}$$

and Kepler's equation is:

$$t - t_p = \frac{\mu}{(2|\xi|)^{3/2}}\left[\sinh E(\tau) - E(\tau)\right]. \tag{86}$$

the collision occurs iff $\mathbf{r}_0 \cdot \mathbf{v}_0 < 0$, and the collision moment is computed from:

$$t_c = -\frac{\mathbf{r}_0 \cdot \mathbf{v}_0}{\mu} + \frac{\mu}{(2\xi)^{\frac{3}{2}}}\sinh^{-1}\left[\frac{\sqrt{2\xi}}{\mu}\left(\mathbf{r}_0 \cdot \mathbf{v}_0\right)\right]. \tag{87}$$

2.3 Hypercomplex Prime Integrals

We introduce an inedite hypercomplex prime integral with the help of the considerations made above in this Section.

Proposition 2.3.1 *The hypercomplex vector:*

$$\underline{\mathbf{S}} = \frac{2\xi\mathbf{r} - \mathbf{L}+\varepsilon r\mathbf{v}}{2\xi r + \mu + \varepsilon\left(\mathbf{r}\cdot\mathbf{v}\right)} \tag{88}$$

is constant.

Proof. It results by direct computations noticing that $\underline{\mathbf{S}}' = \mathbf{0}$. ■

Remark 2.3.2 *If we split into particular cases the expression of the constant hypercomplex vector* $\underline{\mathbf{S}}$*, inedite prime integrals ok Kepler's problem may be found.*

2.3.1 Zero Specific Energy $\xi = 0$

Vector $\underline{\mathbf{S}}$ becomes a dual vector, by noticing that $\varepsilon^2 = 0$. It follows that:

$$\underline{\mathbf{S}} = \frac{-\mathbf{L}+\varepsilon r\mathbf{v}}{\mu + \varepsilon\left(\mathbf{r}\cdot\mathbf{v}\right)} \tag{89}$$

and further:

$$\mu r\mathbf{v} + (\mathbf{r}\cdot\mathbf{v})\,\mathbf{L} = \overrightarrow{\text{constant}}. \tag{90}$$

2.3.2 Non-Zero Specific Energy $\xi \neq 0$

By denoting:

$$a = -\frac{\mu}{2\xi}, \tag{91}$$

and taking into account that $\mathbf{L} = \mu\mathbf{e}$, eq (88) becomes:

$$\underline{\mathbf{S}} = \frac{r\mathbf{v} + \varepsilon\,(\mathbf{r} + a\mathbf{e})}{(\mathbf{r}\cdot\mathbf{v}) + \varepsilon\,(r-a)}. \tag{92}$$

From eq (92) it results:

$$\begin{aligned} \frac{r\mathbf{v}\,(\mathbf{r}\cdot\mathbf{v}) - 2\xi\,(r-a)\,(\mathbf{r}+a\mathbf{e})}{(\mathbf{r}\cdot\mathbf{v})^2 - 2\xi\,(r-a)^2} &= \overrightarrow{\text{constant}}, \\ \frac{(\mathbf{r}\cdot\mathbf{v})\,(\mathbf{r}+a\mathbf{e}) - r\,(r-a)\,\mathbf{v}}{(\mathbf{r}\cdot\mathbf{v})^2 - 2\xi\,(r-a)^2} &= \overrightarrow{\text{constant}}. \end{aligned} \tag{93}$$

3 Conclusions

By using a Sundman-like vectorial regularization, the strong non-linear Kepler problem was transformed into a linear differential equation with constant coefficients. Using the hypercomplex numbers algebra related to the specific energy of the Keplerian motion, together with hypercomplex vectors, a hypercomplex unified solution to Kepler's problem was given. By introducing a hypercomplex state vector and a hypercomplex radial state number, vectorial closed form expressions of the solution were obtained. The procedure generalizes the regularization methods introduced by Levi-Civita and Kustaanheimo. The results are expressed depending on the fundamental functions of the trigonometry of a constant curvature space.

References

[1] Sundman, K.F., "Mémoire sur le problème des trois corps", Acta Mathematica, Vol. **36**, 1912, pp. 105-179.

[2] Levi-Civita., T., "Sur la régularisation du problème des trois corps", Acta Mathematica, **42** 1920, pp. 1-4.

[3] Kustaanheimo, P.E., Tutein, J., "On Spinor Equations of Motion and their Possible Integrals", Astronomische Nachrichten, vol. **303**, no. 4, 1982, pp. 221-225.

[4] Kustaanheimo, P.E., "Spinor regularization of Kepler motion", Ann. Univ. Turkuens A, I, **73**, fascl, Publ. Astron. Obs. Helsinki, **102**, 1964, pp. 3-7.

[5] Goldstein, H., *Classical Mechanics*, chap. 3, Addison-Wesley Publishing Company, Inc. Reading, Massachusets, USA, 1980.

[6] Condurache, D., Martinuşi, V.,. "A Vectorial Regularization of the Keplerian Motion", The 2nd International Symposium of Theoretical and Applied Mechanics "D.I.Mangeron" Conf. Proc., Bul. Inst. Polit. Iaşi, **LI (LIV)**, 2005, pp. 185-193.

[7] Condurache, D., Martinuşi, V., "Vectorial Regularization and Temporal Means in Keplerian Motion", Journal of Nonlinear Mathematical Physics, Vol. 13, No. 3, pp. 420-440, 2006.

[8] Berry, M., Healy, L., "The generalized Sundman transformation for propagation of high-eccentricity elliptical orbits", AAS/AIAA Space Flight Mechanics Meeting, San Antonio, Texas, 2002 (paper AAS **02-109**).

[9] Moser, J., Regularization of the Kepler's problem and the averaging method on a manifold. Commun. Pure Appl. Math. 23, 1970, pp. 609-636.

[10] Keane, A.J., Barett R.K., Simmons J.F.L., "The classical Kepler problem and geodesic motion on spaces of constant curvature", Journal of Mathematical Physics, Vol 41, No 12, 2000, pp. 8108-8116.

[11] Herranz, F.J., Ortega, R., Santander, M., "Trigonometry of spacetimes: a new self-dual approach to a curvature/signature (in)dependent trigonometry", J. Phys. A: Math Gen. 33, 2000, pp.4525-4551.

[12] Anosov, D.V., "A note on the Kepler problem", Journal of Dynamical and Control Systems, vol.**8**, no.3, 2002, pp. 413-442 .

[13] Vivarelli, M. D., "The Kepler problem: a unifying view", Celestial Mechanics and Dynamical Astronomy **60**, 1994, pp.291-395.

[14] Vivarelli, M. D., "The Levi-Civita Time Transformation and a Killing Vector for the Kepler Problem", Meccanica, **32**, 1997,pp.135-142.

[15] Vivarelli, M. D., "The Sum Vector S and the Fictious Time s in the Kepler Problem", Meccanica, **35**, 2000, pp.55-67.

[16] Osipov, I.S., "The Kepler problem and geodesic flows in spaces of constant curvature", Celestial Mechanics, vol. **16**, 1977, pp. 191-208.

PADEU | PADEU **19** (2007), p. 81
ISBN 963 463 557
©Published by the Astron. Dept. of the Eötvös Univ.

A Fundamental Model and Numerical Investigations for the Resonances of the Gyldén Problem

Cătălin Cucu-Dumitrescu[1], Dan Şelaru[2], Vasile Mioc[3]

[1,2] Institute for Space Sciences, Str. Atomistilor 406, OP-CP MG-23, RO-077125, Magurele, Romania
[3] Astronomical Institute of the Romanian Academy, Str. Cutitul de Argint 5, RO-040557, Bucharest, Romania

E-mail: [1]cucudumitrescu@yahoo.com, [2]danselaru@yahoo.com, [3]vmioc@aira.astro.ro

Abstract
We tackle the Gyldén-type problem (a two-body problem with time-changing equivalent gravitational parameter). For the most interesting case for astronomy: small-amplitude periodic variation, we study the behavior of the system in the neighborhood of resonances. We adopt the most realistic astronomical situation: only one dominant term of the Hamiltonian. In this case we point out a fundamental model of resonance, common to every resonant situation, and, moreover, identical to the so-called first model of resonance (Breiter 2003). Considering the simplest case of the variation, we perform some numerical experiments. Even in this simplest case, the phase portraits are very complex: a mixture of oscillation zones, circulation zones and chaotic zones.
Keywords: *Gyldén-type problem, nonlinear particle dynamics, resonances*

1 The Gyldén-Type Problem

We study an extension of the *Kepler problem* with time-dependent gravitational parameter that bears the name of the Swedish astronomer *Hugo Gyldén* (Hadjidemetriou, 1963), (Deprit, 1983). The mathematical model can be described in its most general form and in conveniently chosen units, by the Hamiltonian:

$$H(\mathbf{q},\mathbf{p},t)=\frac{|\mathbf{p}|^2}{2}-\frac{1+\varepsilon\mu(t)}{|\mathbf{q}|}. \tag{1}$$

Here $\mathbf{q}=(q_1,q_2)\in\mathbf{R}^2\setminus\{(0,0)\}$ and $\mathbf{p}(=\dot{\mathbf{q}})=(p_1,p_2)\in\mathbf{R}^2$ are the configuration (position) vector and the momentum vector, respectively, whereas $\varepsilon>0$ is a small parameter. Observe that for $\varepsilon=0$ the Hamiltonian $H(\mathbf{q},\mathbf{p})$ corresponds to the standard *Kepler problem*. We have to emphasize that the secular variation of μ (via change of the gravitational constant or/and masses) models concrete astronomical situations; we quote arbitrarily (Dirac, 1938), (Brans, 1961), (Brans & Dicke, 1961), (Hadjidemetriou, 1963) , (Hadjidemetriou, 1966), (Verhulst, 1975).

Since the changes of μ can also be due to nongravitational forces, Şelaru et al. (Selaru et al., 1992) generalized the terminology by introducing the notion of changing *equivalent gravitational parameter*, suggested by the Romanian astronomer *Arpad Pal*. They extended *Gyldén*'s model by including nongravitational, central, inverse-square perturbing forces, absorbed in $\mu(t)$. The source of such a generalization was Saslaw's (Saslaw, 1978) cornerstone paper, which treated the photogravitational (gravitation+radiation) *Gyldén*'s problem.

In this paper we deal with the most interesting case of the equivalent gravitational parameter variation: the periodic one. Here we point out only some astronomical situations approachable in this way: dynamics of particles (from dust to satellites and planets) around pulsating stars, stars with spots, neutron stars, etc.; evolution of a protosolar or protostellar nebula and of planetesimals, planetary nebulae and accretion disks; planetary satellite (artificial or not) dynamics under the influence of the re-emitted solar radiation pressure, and so forth.

From the mathematical standpoint, the *Gyldén*-type problem with periodically changing $\mu(t)$ was approached by us under many aspects: first-order analytical solutions for a periodic variations of $\mu(t)$ (Selaru et al., 1992), (Selaru et al., 1993), refined analytical solutions in the same case (Pal et al., 2006), slowly changing $\mu(t)$ (Cucu & Selaru, 1997), KAM theory applied to this problem (Selaru & Mioc, 1997), chaotic behavior via the exact calculation of *Melnikov*'s integral (Diacu & Selaru, 1998), etc.

In this paper we tackle the *Gyldén*-type problem with periodically changing $\mu(t)$ from a single point of view: resonances.

We shall consider the most interesting case from the standpoint of astronomy: $\mu(t)$ is a zero-average periodic function, *Fourier*-expandable as

$$\mu(t) = \sum_{n=1}^{\infty} C_n \cos(n\omega t + \varphi_n), \tag{2}$$

in which $\omega > 0$ and $\varphi_n \in \mathbf{R}$ stand for frequency and phase, respectively. The fact that the average is zero does not entail loss of generality.

Passing to the *Delaunay*-type variables (L, G, l, g) completed with the canonical pair $(K,\ k = \omega t)$, which makes autonomous the corresponding vector field (see any classical treatise of celestial mechanics), we get the Hamiltonian (Selaru et al., 1992):

$$H(L, G_0, K, l, -, k) = -\frac{1}{2L^2} + \omega K + \varepsilon\mu(k/\omega) R(L, G_0, l), \tag{3}$$

in which

$$R(L, G_0, l) = \frac{1}{r} = \frac{1 + 2\sum_{m=1}^{\infty} J_m(me)\cos(ml)}{2L^2}, \tag{4}$$

where J_m are *Bessel* functions of the first kind, while $e = \sqrt{1 - (G_0/L)^2}$ is the osculating eccentricity. Here, as almost everywhere in this paper, we keep, by abuse, the same notation for the functions of the new variables.

2 Resonances

Let us study the behavior of the system in the neighborhood of a resonance. If there exists a pair $(r, s) \in \mathbf{N}^2$ such that the main frequencies of the system, say, fulfill the condition (Arnold, 1983):

$$|< (\omega_1, \omega_2), (r, -s) >| < \gamma |(r, s)|^{-p} \tag{5}$$

for any choice of the positive parameters γ and p. In this case we say that the system is in the $(r : s)$- resonance.

For the unperturbed system, (5) turns to $|< (\omega_1, \omega_2), (r, -s) >| = 0$. Writing (3) as $H = H_0 + H_1$, we shall have in our case

$$\begin{aligned} \omega_1 &= \frac{\partial H_0}{\partial L} = \frac{1}{L^3}, \\ \omega_2 &= \frac{\partial H_0}{\partial K} = \omega. \end{aligned}$$

3 The Fundamental Model

Let us consider a $(r : s)$-resonance. After one step of *Hori-Deprit* technique (Hori, 1967), (Deprit, 1969) and some linear changes of variables we obtain the Hamiltonian function:

$$H_{res}(L,K,l,k,G_0) = -\frac{1}{2r^2L^2}+\omega(K-sL)+\frac{\varepsilon}{r^2L^2}\sum_{n=1}^{\infty}A_{nsr}(e)\cos(nl-\varphi_n)+O(\varepsilon^2) \tag{6}$$

where (now) $e=\sqrt{1-G_0^2/r^2L^2}$, and we denoted $A_{nsr}(e) := C_{ns}J_{nr}(nre)$.

Let us consider further that the partially averaged Hamiltonian benefits of a dominant term $A^{res}_{msr} := A_{msr}(e_{res}) \neq 0$, where the resonant eccentricity reads $e_{res} := \sqrt{1-G_0^2/r^2L_{res}^2}$ and $(L_{res} = \sqrt[3]{1/r^2s\omega})$. The fact that this term is dominant, mathematically means that there exists $\delta \in \mathbf{R}_+$, $\delta << 1$, such that $A^{res}_{nsr}/A^{res}_{msr} = \delta B^{res}_{nsr}$, $(\forall)\, n \neq m$, where B^{res}_{nsr} is of the order unit or smaller.

In this case we introduce a new couple of conjugate variables (Φ,φ) via the relations $L = \sqrt[3]{1/r^2s\omega} + m\Phi = L_{res} + m\Phi$ (where Φ measures the deviation from the exact resonance) and $l = \varphi/m$.

Neglecting the constants that appear in the expansion of the Hamiltonian, and considering $\Phi = O(\sqrt{\varepsilon})$, we get the new Hamiltonian

$$\begin{aligned} H_{res}(\Phi,\varphi,G_0) &= -\frac{3m^2}{2r^2L_{res}^4}\Phi^2 + \\ &+\frac{\varepsilon}{r^2L_{res}^2}\sum_{n=1}^{\infty}A^{res}_{nsr}\cos(n\varphi/m-\varphi_n)+O(\varepsilon^{3/2}). \end{aligned} \tag{7}$$

Observe that the system ruled by (7) has only one degree of freedom, hence it is, in principle, integrable.

To obtain the main result for this case, we shall estimate the terms that appear in (7). Let us introduce the conjugate variables (Ψ,ψ) via

$$\Psi = m\Phi\sqrt{3/(\varepsilon L_{res}^2|A^{res}_{msr}|)},$$

$\psi = \varphi - \varphi_m + \sigma\pi$, where $\sigma = 0$ for $A^{res}_{msr} < 0$ and $\sigma = 1$ for $A^{res}_{msr} > 0$. Let also introduce the timelike variable τ via

$$t = -sign(A^{res}_{msr})\frac{\sqrt{\varepsilon}m}{r^2L_{res}^3}\sqrt{3|A^{res}_{msr}|}\tau.$$

With these transformations, the new Hamiltonian reads

$$H_{res}(\Psi,\psi,G_0) = \frac{1}{2}\Psi^2+\cos\psi- \\ -\delta\sum_{n=1,n\neq m}^{\infty} B_{nsr}^{res}\cos\left((n/m)\psi+\psi_n\right)+O(\varepsilon^{1/2}), \tag{8}$$

where $\psi_n=(n/m)\left(\varphi_m-\sigma\pi\right)-\varphi_n$.

In this way we got a *fundamental model of resonance* of our problem, namely a formalism common to every resonant situation, no matter which the index of the resonant term is. If δ is of order $\sqrt{\varepsilon}$ or smaller, the contribution of the terms of the series is not significant within the limits of the magnitude order of the approximation. Moreover, in this case our model of resonance becomes identical to the *first fundamental model of resonance* (the perturbed pendulum) (Breiter, 2003). As in *Breiter*'s model, we shall estimate the maximum distance between the $(\Psi=0)$-axis and the separatrix between oscillation and circulation zones in the phase plane (Ψ,ψ). If we come back to our original variables Φ, the corresponding resonance width reads $\Delta_\Phi(m,r,s)=\sqrt{2\varepsilon L_{res}^2\left|A_{msr}^{res}\right|/3m^2}$.

4 Numerical Investigations

To have a deeper insight into the complexity of the problem, we shall concretize the model resorting to the simplest situation: $\mu(t)=\cos\omega t$ (Selaru et al., 1992). The Hamiltonian (3) becomes

$$H=-\frac{1}{L^2}+\omega K+\varepsilon\frac{\cos k+\sum_{m=1}^{\infty}J_m(me)\left[\cos(k+ml)+\cos(k-ml)\right]}{2L^2}, \tag{9}$$

as it is easy to check.

To understand the behavior of the system in the neighborhood of resonances, we performed a series of numerical experiments. The numerical results confirm and corroborate our analytical insights in a more accessible and intuitive form. The departure point is the canonical system associated to the Hamiltonian (9). Consider a $(u:1)$-resonance. Also consider the change of variables $\rho:=\left(u/L^3-\omega\right)/\sqrt{\varepsilon}$, $\gamma:=ul-k$, $\tau:=\sqrt{\varepsilon}t$. The corresponding equations of motion will read

$$\begin{cases} \rho' = -\frac{3u}{L^3}\cos k\left(\sum\limits_{m=1}^{\infty} mJ_m(me)\sin ml\right), \\ \gamma' = \rho - \frac{\sqrt{\varepsilon}u}{L^3}\cos k\left(1+\sum\limits_{m=1}^{\infty}\left[2J_m(me) - L\frac{\partial}{\partial L}(J_m(me))\right]\cos ml\right), \\ k' = \frac{\omega}{\sqrt{\varepsilon}}. \end{cases} \tag{10}$$

For our numerical endeavors, we brought the second equation (10) to an explicit form via the well-known property of the Bessel functions of first kind: $\partial(J_m(me))/\partial L = \left[mG_0^2/(2eL^3)\right][J_{m-1}(me) - J_{m+1}(me)]$. We also used the relation $G_0^2 = L^2(1-e^2)$.

Taking into account the above change of variables and the relation between the constant angular momentum G_0 and L, we get the maximal variation domain of ρ: $\rho \in \left(-\omega/\sqrt{\varepsilon}, \left(u/G_0^3 - \omega\right)/\sqrt{\varepsilon}\right]$. For our numerical investigations we chose G_0^2-values that make possible the transit through resonance; it is easy to calculate that they correspond to $G_0 < \sqrt[3]{u/\omega}$.

Let $\phi : \mathbf{R}\times\mathbf{R}\times\mathbf{T}^2 \longrightarrow \mathbf{R}\times\mathbf{T}^2$ be the global flow of 10, where $\mathbf{T}^2$ stands for the 2D torus. In other words, $\phi(\tau,\rho_0,\gamma_0,k_0)$ is the solution of this system for the initial data (ρ_0,γ_0,k_0) (at $\tau = 0$). Consider the global transversal section in the phase space $S := \left\{(\rho,\gamma,k) \in \mathbf{R}\times\mathbf{T}^2 \mid k = 0\right\}$. On this section we shall consider Poincaré's classical map of the first return $P : S \longrightarrow S$, $P(\rho,\gamma) := \phi(2\pi\sqrt{\varepsilon}/\omega, \rho_0, \gamma_0, 0)$.

It is obvious that, from the numerical standpoint, to get Poincaré's map, it suffices to integrate the first two equations (10) for $\tau \in [0, 2\pi\sqrt{\varepsilon}/\omega]$, considering $k = \tau\omega/\sqrt{\varepsilon}$.

Observe that (10) represents another form of the system ruled by (9), without simplifications or truncations. However, for our numerical endeavors, we truncated the series that appear in the vector field expression, retaining 50 low-order terms. As regards the numerical integration technique, we used a multi-step algorithm of Adam-Bashforth-Moulton-type, of variable order.

A few results of our numerical experiments are illustrated in the next figures. We plotted 300 successive returns for 98 distinct trajectories in Poincaré's section S. We considered a 7x14 rectangular grid of initial data in the region $(\rho,\gamma) \in [-1.5, 1.5]\times[0, 2\pi]$, and 50 terms of the series. The resonant situation taken into consideration are (1:1), (2:1), (3:1) and (4:1), while the value of the small parameter was $\varepsilon = 0.035$ or a double value ($\varepsilon = 0.07$) in some cases. In all the figures we plotted the lines $\rho = \rho_{u:1} = const.$, corresponding to the exact resonances in the zone.

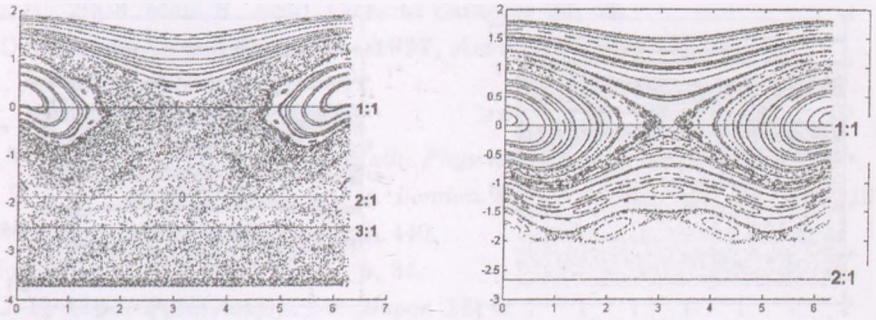

Figure 1: *Resonance 1:1, epsilon = 0,07 (left) and epsilon = 0,035 (right)*

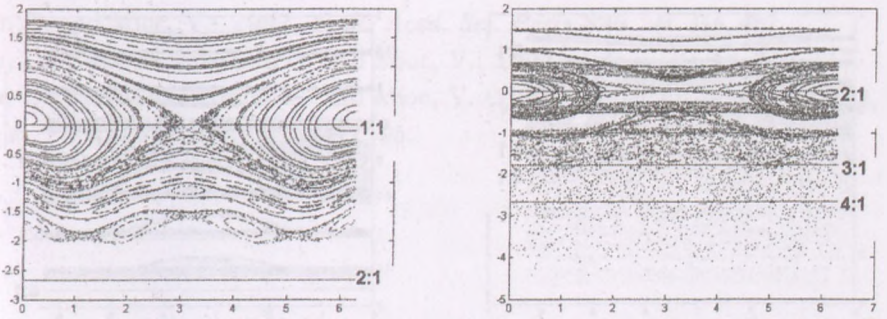

Figure 2: *Resonance 2:1, epsilon = 0,07 (left) and epsilon = 0,035 (right)*

5 Conclusions

We tackled the most interesting case of the *Gyldén*-type problem from the standpoint of astronomy: a zero-average periodic perturbing function, *Fourier*-expandable.

We got a fundamental model of resonance, which, if δ is of order $\sqrt{\varepsilon}$ or smaller, is identical to first fundamental model of resonance.

We tackled the simplest situation $\mu(t) = \cos \omega t$. We showed that only partial averaging is efficient.

The numerical experiments exhibit a very complex behavior of the system, even in the simplest case we considered. The only resonances we show here suffice to show very intricate phase portraits: oscillation, circulation, and chaotic

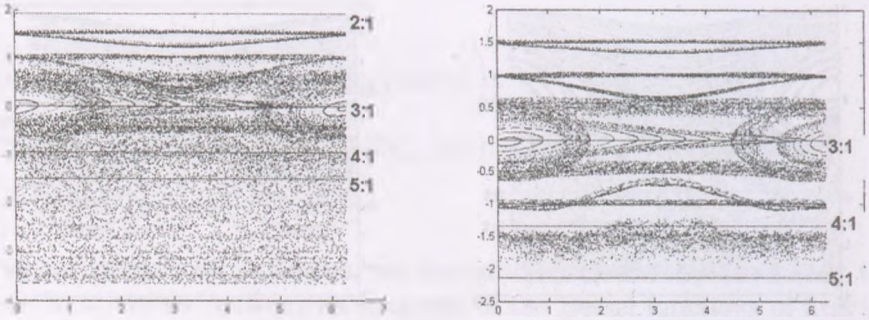

Figure 3: *Resonance 3:1, epsilon = 0,07 (left) and epsilon = 0,035 (right)*

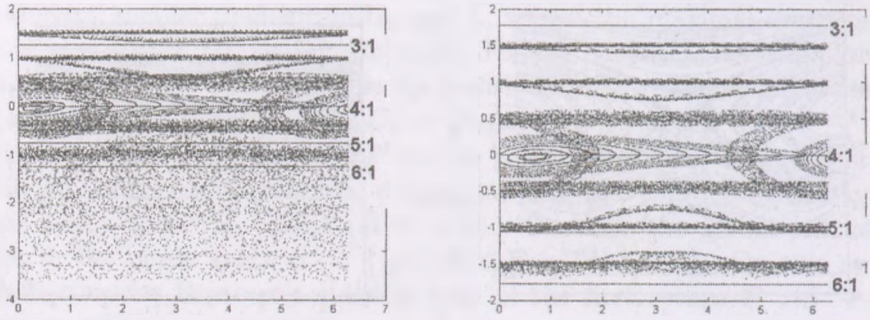

Figure 4: *Resonance 4:1, epsilon = 0,07 (left) and epsilon = 0,035 (right)*

zones.

According to the increase of G_0^2 of and ε, the portraits in the global transversal section (ρ, γ) of the phase space exhibit more and more extended chaotic regions; this is to be expected from the standpoint of celestial mechanics.

References

Arnold, V. I.: **1983**, *Geometrical Methods in the Theory of Ordinary Differential Equations*, Springer, New York.

Brans, C. H.: **1961**, 'Mach's principle and a varying gravitational constant', Ph. D. Thesis, Princeton University, Princeton, NJ.

Brans, C. H. and Dicke, R. H.: **1961**, *Phys. Rev.* **124**, 925.

Breiter, S.: **2003**, Mon. R. Acad. Ciencias Zaragoza **22**, 83.
Cucu-Dumitrescu, C. and Şelaru, D.: **1997**, *Astrophys. Space Sci.* **250**, 93.
Deprit, A.: **1969**, *Celest. Mech.* **1**, 12.
Deprit, A.: **1983**, *Celest. Mech.* **31**, 1.
Diacu, F. and Şelaru, D.: **1998**, *J. Math. Phys.* **39**, 6537.
Dirac, P. A. M.: **1938**, *Proc. Roy. Soc. London*, ser. A: *Math. Phys. Sci.*, **165**, 199.
Hadjidemetriou, J. D.: **1963**, *Icarus* **2**, 440.
Hadjidemetriou, J. D.: **1966**, *Icarus* **5**, 34.
Hori, G.-I.: **1967**, *Publ. Astron. Soc. Japan* **18**, 4.
Pal, A., Şelaru, D., Mioc, V. and Cucu-Dumitrescu, C.: **2005**, *Astron. Nachr.* **327**, 304.
Saslaw, W. C.: **1978**, *Astrophys. J.* **226**, 240.
Şelaru, D. and Mioc, V.: **1997**, *C. R. Acad. Sci. Paris* **325**, sér. II*b*, 487.
Şelaru, D., Cucu-Dumitrescu, C. and Mioc, V.: **1992**, *Astron. Nachr.* **313**, 257.
Şelaru, D., Cucu-Dumitrescu, C. and Mioc, V.: **1993**, *Astrophys. Space Sci.* **202**, 11.
Verhulst, F.: **1975**, *Celest. Mech.* **11**, 95.

PADEU | PADEU **19** (2007), p. 91
ISBN 963 463 557
©Published by the Astron. Dept. of the Eötvös Univ.

Actual Romanian research in post-Newtonian dynamics

Vasile Mioc, Magda Stavinschi,

Astronomical Institute of the Romanian Academy,
Str. Cuţitul de Argint 5, RO-040557 Bucharest, Romania

E-mail: vmioc@aira.astro.ro, magda@aira.astro.ro

Abstract

We survey the recent Romanian results in the study of the two-body problem in post-Newtonian fields. Such a field is characterized, in general, by a potential of the form $U(\mathbf{q}) = |\mathbf{q}|^{-1} +$ something (small, but not compulsorily). We distinguish some classes of post-Newtonian models: relativistic (Schwarzschild, Fock, Einstein PN, Reissner-Nordström, Schwarzschild – de Sitter, etc.) and nonrelativistic (Manev, Mücket-Treder, Seeliger, gravito-elastic, etc.). Generalized models (the zonal-satellite problem, quasihomogeneous fields), as well as special cases (anisotropic Manev-type and Schwarzschild-type models, Popovici or Popovici-Manev photogravitational problem), were also tackled. The methods used in such studies are various: analytical (using mainly the theory of perturbations, but also other theories: functions of complex variable, variational calculus, etc.), geometric (qualitative approach of the theory of dynamical systems), and numerical (especially using the Poincaré-section technique). The areas of interest and the general results obtained focus on: exact or approximate analytical solutions; characteristics of local flows (especially at limit situations: collision and escape); quasiperiodic and periodic orbits; equilibria; symmetries; chaoticity; geometric description of the global flow (and physical interpretation of the phase-space structure). We emphasize some special features, which cannot be met within the Newtonian framework: black-hole effect, oscillatory collisions, radial librations, bounded orbits for nonnegative energy, existence of unstable circular motion (or unstable rest), symmetric periodic orbits within anisotropic models, etc.

Keywords: *Celestial mechanics, post-Newtonian models*

1 Introduction

The study of the two-body problem in other fields than the Newtonian one constitutes a temptation and a challenge at the same time. The goal is obvious: which properties of the Keplerian motion are preserved within a new framework? What non-Keplerian motions are characteristic to such models? Among many models, the post-Newtonian fields constitute a class of choice as regards modelling of concrete astronomical situations.

From a mathematical standpoint, the problem is simple at a first sight. We call post-Newtonian a field characterized by a potential of the form $A/|\mathbf{q}| + f(\mathbf{q}, \mathbf{p}, t)$, where $\mathbf{q}$ is the configuration vector, and $\mathbf{p}$ is the momentum vector. In general, but not always, the terms grouped under the generic name f are much smaller than the Newtonian-type term $A/|\mathbf{q}|$.

From a physical standpoint, f is not necessarily of purely gravitational nature (as in the cases of Schwarzschild, Fock, Einstein PN, Schwarzschild - de Sitter, zonal satellite; see Section 2 below). It can represent supplementary influences as radiation, rotation, electrostatic charge, or combinations of these ones (and gravitation).

In this paper we survey the recent results of the Romanian research in the two-body problem in post-Newtonian fields. Of course, there were many other results obtained in the (restricted and general) three-body problem, five-body problem, n-body problem, but they will be surveyed elsewhere.

Section 2 presents the post-Newtonian fields (in the above acception) considered as a framework for the two-body problem. They are classified from various points of view: physical, mathematical, astronomical.

In Section 3 we point out the goals of such a research and the methods used. The methods can be divided into analytical (quantitative), geometrical (qualitative), and numerical, but their use was in general combined.

Section 4 presents the most important results obtained by the Romanian researchers in this investigation. To mention only few such issues, we quote: problems concerning integrability or nonintegrability (in fact, chaoticity), exact analytical solutions, description of the local flow in the neighbourhood of singularities, description of the global flow (if possible), existence of symmetries, etc.

Section 5 points out some phase curves in the post-Newtonian two-body problem, which cannot be met in the standard Kepler problem. All these phase trajectories are translated in terms of physical orbits.

The final Section 6 puts into evidence the actual usefulness of the study of the so old two-body problem in post-Newtonian fields. We bring arguments,

not only mathematical, but especially from the standpoint of today's astronomy (from ground or from space) and astrodynamics.

2 Post-Newtonian fields

As we have seen in the introductory section, we call post-Newtonian a field characterized by a potential of the form $A/|\mathbf{q}| + f(\mathbf{q}, \mathbf{p}, t)$, or by a Hamiltonian of the form $|\mathbf{p}|^2/2 + A/|\mathbf{q}| + f(\mathbf{q}, \mathbf{p}, t)$, or - in case - by a nonconservative force expressed as $B/|\mathbf{q}|^2 + g(\mathbf{q}, \mathbf{p}, t)$. From the standpoint of their nature, they can be divided into several classes. We shall survey the fields tackled by the recent Romanian research.

2.1 Empirical classical fields

The first creator of a post-Newtonian model was Isaac Newton himself. Unable to explain the observed secular motion of the Moon's perigee, he proposed a potential $A/r + B/r^2$ (with $r = |\mathbf{q}|$ and $A, B > 0$). His model was resumed later by Alexis Clairaut, who eventually abandoned it (e.g. [1]).

Other models, all based on a slightly modified gravitational law, were proposed by Asaph Hall and Simon Newcomb. They considered potentials of the form $A/r^{1+\varepsilon}$, with very small ε.

Many decades later, Mücket and Treder started from a Hall-Newcomb model to propose a logarithmic gravitational potential able to explain quantitatively Mercury's perihelion advance [2, 3].

2.2 Physics-based classical fields

At the end of the 19th century, Hugo von Seeliger proposed an exponential gravitational potential, based on physical principles. After relativity, his model felt into oblivion. But it was reconsidered by many outstanding scientists; it is sufficient to quote Wolfgang Pauli and Edwin Hubble among them.

Maybe the most discussed classical model during the last decade is the one proposed by the Bulgarian physicist Georgi Manev in the 1920s, as a classical alternative to relativity. He resumed Newton's model $A/r + B/r^2$, but with physical arguments. Many Romanian mathematicians, physicists and astronomers tackled Manev's model [1, 4-6]. Their efforts and results attracted many dozens of specialists from all over the world towards this promising domain of research.

During the same 1920s, the Romanian astronomer Constantin Popovici proposed a hybrid post-Newtonian model [7]. It consisted of a combination of a Newtonian gravitational force and a special radiative force (depending on both configuration and momentum).

During the 1990s, Manev's gravitational force and Popovici's radiative force were combined into the so-called Popovici-Manev model. Its study provided many interesting issues [8, 9].

The launch of the artificial Earth satellites raised (even before) another post-Newtonian problem: evolution within the framework of the main problem of space dynamics. It means the evolution of an equatorial satellite in the gravitational field of an oblate planet (potential $A/r + B/r^3$). The problem was generalized as the J_2 problem (with A, B of any sign) [10]. It was further generalized as the zonal-satellite problem (with potential $\sum_{n=1}^{N}(A_n/r^n)$) [11].

A model developed in the 19th century by Hugo Gyldén is characterized by a potential; of the form $A[1 + f(t)]/r$. Many concrete astronomical situations can be modelled in this way [12-15].

2.3 Purely relativistic fields

Relativity answered many tremendous questions in physics and astronomy, even in celestial mechanics. However, no coherent results could be brought in the most celebrated problems of dynamics (the n-body problem) in terms of a classical representation. There were many attempts, but the only widespread approach is the use of the classical formalism that brings the relativity geometry into the realm of classical mechanics. This allows the use of notions as potential or force, and a classical treatment via powerful mathematical tools.

The best known and the most used relativistic model is Schwarzschild's one. Its classical expression reduces to a potential of the form $A/r + B/r^3$ [16, 17]. It is, to some extent, an equivalent to the J_2 problem.

Another well-known relativistic model is the exact solution provided by Fock to Einstein's field equations [18]. Brought into the classical realm, the corresponding potential reads $\sum_{n=1}^{4}(A_n/r^n)$.

Einstein himself created a classical "mirror" to his model: the so-called Einstein's PN field. The Hamiltonian that features this model exhibits a strange term, which mixes configurations and momenta [19].

The Dynamical Theory of Gravity developed - during the recent years - a complex model, whose gravitational potential (translated in classical terms) consists of a modification of Seeliger's potential.

To end this subsection, we mention that the Romanian researchers also approached (but only sporadically) some PPN (post-Newtonian parameterized) relativistic fields [20-22].

2.4 Combined relativistic fields

Many models added different-nature effects to the relativistic gravitation. Two of them were approached by the recent Romanian research:

– the Kerr metric, which models the field generated by a black hole in rotation;

– the Reissner-Nordström metric, which models the field generated by an electrostatically charged black hole.

Of course, mathematical combinations of these situations can also be taken into account, because they are very likely from a physical and astronomical standpoint.

Lastly, we mention a model approached by us: the Schwarzschild - de Sitter model. This one combines the deformation of the spacetime continuum in the neighbourhood of a great mass with the influence of the cosmological background. The equivalent classical potential has the form $A/r + B/r^3 + Cr^2$ [23, 24].

2.5 The gravito-elastic model: a mathematical toy

There is a well-known issue: Newton's theorem about the equivalence of bodies (in certain conditions) with material points with the whole mass concentrated in their centres is exact in only two real situations: gravitational force and elastic force. To mathematically tackle such situations, we approached the so-called gravito-elastic model, associated to the potential $A/r + Br^2$ [25]. It is obvious that it is a particular case of the Schwarzschild - de Sitter model (notice that the equivalence concerns only the mathematical formalism).

2.6 Special models

Other effects were added to post-Newtonian models (especially relativistic), in order to create a more general and realistic framework. One of these effects is anisotropy (with many physical and astronomical connotations), which provided a lot of surprising results as regards dynamics in post-Newtonian fields.

The anisotropic Manev model yielded many new issues as compared to the corresponding isotropic model [26-28]. It is the same as to the anisotropic Schwarzschild model [29, 30].

2.7 General models

A first generalization of the zonal-satellite problem is the two-body problem associated to the so-called quasihomogeneous field. The latter one is mathematically equivalent to the first one, but is much more rich as regards the concrete astronomical situations it models.

A next and higher generalization consisted of a field featured by a potential of the form $\sum_{n=1}^{N}(A_n/r^{\alpha_n})$, with α_n real positive numbers, not necessarily integers.

3 Aims and methods

As it is natural, the goal of all these researches was to unveil the properties of the motion in post-Newtonian fields. The investigations focused on some general subjects:

– transposition of classical results (corresponding to the Newtonian field) into the realm of post-Newtonian fields;
– global properties of the motion;
– local properties of the motion;
– singularities (in our case, collisions): collisional and near-collisional dynamics;
– behaviour at infinity: escape and near-escape dynamics;
– equilibria: nature, stability;
– special orbits: periodic, quasiperiodic, heteroclinic, homoclinic;
– symmetries;
– resonances and chaoticity.

Tackling all these topics, the Romanian researchers obtained many remarkable results (see Section 4).

The first methods used were quantitative (analytical). Series expansions (powers of one or two small parameters) were especially used, within the framework of the theory of perturbations. We obtained first-order, second-order, and even third-order approximate solutions. In few cases the exact integration was possible. We resorted to: canonical transformations, averaging, successive approximations, and several other classical approaches.

But the approximate or even exact analytical solutions are written via lengthy formulae, and never describe clearly the nice properties of the geometrical and physical orbits. That is why we resorted in most cases to qualitative analysis. The powerful tools of the theory of dynamical systems allowed us (in most above mentioned topics) to write the motion equations in a simple and elegant manner. The results consisted of clear local or even global phase-portraits.

Among the tools used within the geometrical tackling of the problems, the McGehee-type transformations (of first and, especially, second kind) have the central place. Due to them we managed to describe many local phase-portraits, especially in the limit cases of collision and escape. Of much help were the fundamental theorems of the KAM theory (concerning the persistence of the invariant tori), or the Melnikov integral.

Of course, quantitative and qualitative methods cannot be clearly separated. They were combined to extract information about the (local or global) flow from the motion equations and first integrals. In addition, "non-orthodox" tools in celestial mechanics were also used. It is sufficient to mention the calculus of variations, the algebraic theory of groups, or the theory of functions of complex variable.

Besides, a tool started half a century ago was used and proved to be efficient: the numerical experiment. Such an approach was very useful in investigating the special situations of resonance and chaoticity.

Analytical, geometrical, and numerical methods - all were used (sometimes separated, but combined in most cases) to provide new and significant results in the post-Newtonian dynamics.

4 General results

We shall present here the most important recent results obtained by the Romanian researchers in the investigation of post-Newtonian two-body problems.

Resorting to quantitative methods, the exact analytic solution of the Manev-type problem was obtained. It was tackled in both classical coordinates (radius vector - polar angle; Keplerian orbital elements) [5] and Sundman-regularized coordinates [4]. We used both the theory of perturbations and the exact analytical integration of an unperturbed problem.

In the same manner, the exact solutions of the Popovici and Popovici-Manev problems were provided [7-9].

First-order (and - in some cases - second-order or even third-order) solutions were got for the two-body problem in many fields. We quote arbitrarily:

Schwarzschild - de Sitter's field, PPN fields, Fock's field, Mücket-Treder's field, etc [e.g., 18, 20-23].

As we have already said, the analytic expressions of all these solutions are very intricate and do not describe clearly the physical evolution of the system. That is why we resorted to qualitative analysis, obtaining in this way much more rich results.

All tackled models present an isolated singularity at the origin, singularity that corresponds to a collision. Using the McGehee-type transformations, we managed to depict the so-called collision manifold for all problems. In all isotropic problems, the collision manifold is homeomorphic to a 2D cylinder or (equivalently) to a 2D torus. In the anisotropic problems studied (Manev and Schwarzschild), this manifold has the shape of a cylinder/torus with "humps", which provides surprising results (as regards collisional orbits).

A first-choice result is the proof of the existence of spiral collisions (the black-hole effect). They are collisions with nonzero angular momentum constant. Surprisingly, they are much more probable (from the standpoint of the Lebesgue measure) than the classical rectilinear collisions [31].

Another surprising result is the proof of the existence of oscillatory collisions (with nonconstant angular momentum, which alternates its sign). This issue was pointed out in the anisotropic Manev-type and Schwarzschild-type problems [26-30].

Even if the escape does not constitute a singularity, this limit situation was also taken into account. The results are the same as in the case of the collision manifold, as regards the look of the infinity manifold. Cylinders/tori without "humps" (in isotropic cases) or with "humps" (in anisotropic cases) are present.

As a natural further step after the investigation of collision and escape, the equilibria were tackled. Interesting results were obtained in the J_2 problem as regards the nonlinear stability of equilibria.

In almost all problems studied, the symmetries occupied a place of choice [32-35]. It was proved that these symmetries form an Abelian group with an idempotent structure. Such groups always own subgroups of order two, isomorphic to Klein's group. The symmetries put into evidence were of much help in proving the existence of families of periodic orbits in both Manev-type and Schwarzschild-type anisotropic two-body problems [26-30].

A very "astronomical" problem, Gyldén's one, benefitted of a special attention. Via the modern tools of the theory of dynamical systems, chaos in this problem was discovered [36]. Moreover, such a kind of chaoticity was pointed out also by numerical experiments.

5 Non-Keplerian orbits

In this section we shall emphasize orbits specific to post-Newtonian problems, which cannot be met in the standard Kepler problem. Every phase curve will be translated in terms of physical trajectories, and conversely.

– *Spiral orbital motion.* This is the most common motion in the two-body problem in post-Newtonian fields. In other words, the motion is performed on precessional conic sections (the Laplace-Ruge-Lenz vector does not exist).

– *Nonrectilinear collisional motion.* Within isotropic models, such trajectories are spiral. Within anisotropic models, besides spiral trajectories, there also are oscillatory orbits (for which the angular momentum alternates its sign).

– *Bounded orbits with nonnegative-energy level.*

– *Unbounded orbits with negative-energy level.*

– *Unstable relative equilibria.* They are unstable rest positions for zero angular momentum, and unstable circular orbits for nonzero angular momentum.

– *Phase curves that connect collision to saddles.* In physical terms, they are orbits that eject asymptotically from collision and tend asymptotically to an unstable circular orbit, or conversely.

– *Phase curves that connect infinity to saddles.* In physical terms, they are orbits that come from infinity and tend asymptotically to an unstable circular orbit, or conversely.

– *Heteroclinic orbits that connect saddle to saddle.* They physically represent motion that starts asymptotically from and unstable circular orbit and tend asymptotically to another unstable circular orbit.

– *Homoclinic orbits that surround a centre.* They physically represent motion that starts asymptotically from and unstable circular orbit and tend asymptotically to the same orbit.

– *Rectilinear librations.* This is the case of heteroclinic saddle-saddle curves with zero angular momentum. The particle goes back and forth between two limit distances it cannot go beyond.

– *Quasiperiodic orbits.* In all tackled cases, quasiperiodic orbits do exist. They are much more probable (from the point of view of the Lebesgue measure) than the periodic orbits.

– *Bi-homoclinic curves.* In the physical space they represent motions that start asymptotically (one inwards, the other outwards) from an unstable orbits, then tend asymptotically to the same orbit.

Of course, more intricate phase-portraits are met, too. There are, for instance, homoclinic or bi-homoclinic loops surrounded by periodic and quasiperiodic orbits. The latter ones can be, in turn, surrounded by a larger homoclinic

orbit, and so forth.

All these issues prove the complexity of the two-body problem associated to post-Newtonian models.

References

[1] F. Diacu, V. Mioc, C. Stoica: 2000, Nonlinear Analysis **41**, 1029

[2] G. Ballinger, F. Diacu: 1993, Rom. Astron. J. **3**, 51

[3] V. Mioc, P. Blaga: 1991, Rom. Astron. J. **1**, 103

[4] V. Mioc, C. Stoica: 1995, C. R. Acad. Sci. Paris, sér.I, **320**, 645; **321**, 961

[5] J. Delgado, F. N. Diacu, E. A. Lacomba, A. Mingarelli, V. Mioc, E. Perez, C. Stoica: 1996, J. Math. Phys. **37**, 2748

[6] F. Szenkovits, C. Stoica, V. Mioc: 1999, Mathematica **41**, 105

[7] M.-C. Anisiu: 1995, Rom. Astron. J. **5**, 49

[8] M.-C. Anisiu: 2003, Rom. Astron. J. **13**, 171

[9] M.-C. Anisiu, V. Mioc: 2004, Rom. Astron. J. **14**, 71

[10] V. Mioc, M. Stavinschi: 2000, Serb. Astron. J. **161**, 9

[11] V. Mioc, M. Stavinschi: 1998, Serb. Astron. J. **158**, 31; 37

[12] D. Şelaru, C. Cucu-Dumitrescu, V. Mioc: 1992, Astron. Nachr. **313**, 257

[13] D. Şelaru, C. Cucu-Dumitrescu, V. Mioc: 1993, Astrophys. Space Sci. **202**, 11

[14] D. Şelaru, V. Mioc: 1997, C. R. Acad. Sci. Paris **325**, sér. IIb, 487

[15] A. Pal, D. Şelaru, V. Mioc, C. Cucu-Dumitrescu: 2006, Astron. Nachr. **327**, 304

[16] C. Stoica, V. Mioc: 1997, Astrophys. Space Sci. **249**, 161

[17] V. Mioc, M. Stavinschi: 1998, Bull. Astron. Belgrade **156**, 21

[18] V. Mioc: 1994, Astron. Nachr. **315**, 175.

[19] D. Şelaru, D. Mihai, V. Mioc: 1998, Bull. Astron. Belgrade **156**, 27

[20] V. Mioc, L. Mircea: 1994, Studia Univ. Babeş-Bolyai, ser. Mathematica, **39**, No.4, 93

[21] V. Mioc, E. Radu: 1995, Rom. Astron. J. **5**, 37

[22] V. Mioc, E. Radu: 1995, Studia Univ. Babeş-Bolyai, ser. Mathematica, **40**, No.2, 101

[23] P. Blaga, V. Mioc: 1992, Europhys. Lett. **17**, 275

[24] V. Mioc, M. Stavinschi: 1998, Rom. Astron. J. **8**, 125

[25] V. Mioc, M. Stavinschi: 1999, Rom. Astron. J. **9**, 19; **29**; 37

[26] F. Diacu: 2000, J. Phys. A **33**, 6573

[27] F. Diacu, M. Santoprete: 2001, Phys. D **156**, 39

[28] F. Diacu, M. Santoprete: 2004, Phys. D **194**, 75

[29] V. Mioc, E. Pérez-Chavela, M. Stavinschi: 2003, Celest. Mech. Dyn. Astron. **86**, 81

[30] V. Mioc, M.-C. Anisiu, M. Barbosu: 2005, Celest. Mech. Dyn. Astron. **91**, 269

[31] F. Diacu, A. Mingarelli, V. Mioc, C. Stoica: 1995, in R. P. Agarwal (ed.), World Sci. Ser. Appl. Analysis, 4, World Scientific, Singapore, 213

[32] V. Mioc: 2002, Phys. Lett. A **301**, 429

[33] V. Mioc: 2002, Baltic Astron. **11**, 393

[34] V. Mioc: 2003, Astron. Nachr. **323**, 271

[35] V. Mioc:2004, Hvar Obs. Bull. **28**, 167

[36] F. Diacu, D. Şelaru: 1998, J. Math. Phys. **39**, 6537

PADEU | PADEU 19 (2007), p. 103
ISBN 963 463 557
©Published by the Astron. Dept. of the Eötvös Univ.

Hénon-Heiles' two-body problem. New features of the global flow

V. Mioc, D. Pricopi

Astronomical Institute of the Romanian Academy, Str. Cutitul de Argint 5, RO-040558 Bucharest, Romania

E-mail: vmioc@aira.astro.ro, dpricopi@aira.astro.ro

Abstract
We tackle the two-body problem associated to Hénon-Heiles' generalized potential. The equilibrium points are found and their nature is discussed. We pointed out the main features of the global flow for some cases of interest.
Keywords: *celestial mechanics, Hénon-Heiles' model, global flow*

1 Introduction

Hénon-Heiles' potential reads $W(q_1, q_2) = (\lambda q_1^2 + q_2^2)/2 + q_1^2 q_2 - C q_2^3/3$, where $(q_1, q_2) \in \mathbb{R}^2$ are the standard Cartesian coordinates and λ and C are real parameters (Hénon and Heiles, 1964). Many authors tackled this model, from the initial numerical experiment via Poincaré sections (Hénon and Heiles, 1964) to quantitative and qualitative approaches (e.g. van der Merwe 1991; Antonov and Timoshkova 1993; Anisiu and Pal 1999; Mioc and Barbosu 2003a,b). For a much larger and deeper insight into the model, see Boccaletti and Pucacco (1996).

In Section 2, the basic equation are written down. In Section 3 we study the existence and the nature of the equilibrium points of Hénon-Heiles' potential. In Section 4, the main features of the global flow are pointed out.

2 Basic equations

Consider the relative motion of a unit-mass particle with respect to the field-generating source. Its dynamics is associated to the planar Hamiltonian

$$H(\mathbf{q},\mathbf{p}) = (p_1^2+p_2^2)/2 - [(\lambda q_1^2+q_2^2)/2 + q_1^2 q_2 - Cq_2^3/3] \tag{1}$$

in which $\mathbf{q}=(q_1,q_2)\in\mathbb{R}^2$, $\mathbf{p}(=\dot{\mathbf{q}})=(p_1,p_2)\in\mathbb{R}^2$ are the configuration vector and the momentum vector of the particle, respectively, and λ and C are real parameters.

The equations of motion generated by (1) explicitly read

$$\begin{aligned} \dot{q}_1 &= p_1, & \dot{q}_2 &= p_2, \\ \dot{p}_1 &= \lambda q_1 + 2q_1q_2, & \dot{p}_2 &= q_1^2 - Cq_2^2 + q_2. \end{aligned} \tag{2}$$

The Hamiltonian (1) is a constant of motion, i.e. $H(\mathbf{q},\mathbf{p})=h$, which provides the first integral of energy (h is the energy constant).

The angular momentum $L(\mathbf{q},\mathbf{p})$ is not a constant of motion (except certain cases that will pointed out in the next sections), hence we do not dispose of the corresponding first integral. This was to be expected, given the anisotropic structure of the potential.

3 Equilibrium points

We find the equilibrium points by putting $\dot{q}_i=\dot{p}_i=0$, $i=\overline{1,2}$ in (2) and solving the resulting set of equations:

$$\begin{aligned} q_1(\lambda+2q_2) &= 0 \\ q_1^2+q_2-Cq_2^2 &= 0 \end{aligned} \tag{3}$$

We find four equilibrium points:

$$(q_1^0,q_2^0)\in\{(0,0),(0,1/C),(\sqrt{\lambda(\lambda C+2)}/2,-\lambda/2),(-\sqrt{\lambda(\lambda C+2)}/2,-\lambda/2)\} \tag{4}$$

The characteristic equation reads:

$$[\sigma^2-2(\lambda/2+q_2^0)][\sigma^2-2(1/2-Cq_2^0)]-4(q_1^0)^2=0 \tag{5}$$

For $(q_1^0, q_2^0) = (0,0)$ the eigenvalues are $\sigma_{1,2} = \pm 1$, $\sigma_{3,4} = \pm\sqrt{\lambda}$ if $\lambda \geq 0$ or $\sigma_{3,4} = \pm i\sqrt{-\lambda}$ if $\lambda < 0$. This equilibrium point is a saddle (the motion in the vicinity of the collision manifold is unpredictable: the test particle can collide or can escape to infinity). For $(q_1^0, q_2^0) = (0, 1/C)$, $C \neq 0$, the eigenvalues are $\sigma_{1,2} = \pm i$ and $\sigma_{3,4} = \pm\sqrt{(\lambda C + 2)/C}$ if $(\lambda C + 2)/C \geq 0$ or $\sigma_{3,4} = \pm i\sqrt{-(\lambda C + 2)/C}$ if $(\lambda C + 2)/C < 0$. So, this is a saddle, too. The equilibrium points $(q_1^0, q_2^0) \in \{(\sqrt{\lambda(\lambda C + 2)}/2, -\lambda/2), (-\sqrt{\lambda(\lambda C + 2)}/2, -\lambda/2)\}$, exists if and only if $\lambda(\lambda C + 2) \geq 0$. The characteristic equation reads $\sigma^4 - (\lambda C + 1)\sigma^2 - \lambda(\lambda C + 2) = 0$. It's easy to show that the eigenvalues are $\sigma_{1,2} = \pm i\sqrt{[-(\lambda C + 1) + \sqrt{\Delta}]/2}$ and $\sigma_{3,4} = \pm\sqrt{[(\lambda C + 1) + \sqrt{\Delta}]/2}$ where $\Delta = (\lambda C + 1)^2 + 4\lambda(\lambda C + 2)$. These equilibrium points are saddle, too.

4 Main features of the global flow

As usual in anisotropic fields, we pass to standard polar coordinates via the real analytic diffeomorphism

$$\begin{aligned} r &= |\mathbf{q}|, \qquad \theta = \arctan(q_2, q_1), \\ u &= \dot{r} = (q_1 p_1 + q_2 p_2)/|\mathbf{q}|, \quad v = r\dot{\theta} = (q_1 p_2 + q_2 p_1)/|\mathbf{q}| \end{aligned} \tag{6}$$

which represents a McGehee-type transformation of the second kind (McGehee 1974). In these coordinates the motion equations read

$$\begin{aligned} \dot{r} &= u, \qquad \dot{\theta} = v/r, \\ \dot{u} &= v^2/r + (\lambda\cos^2\theta + 2\sin^2\theta)r + (3\cos^2\theta - C\sin^2\theta)r^2\sin\theta, \\ \dot{v} &= -uv/r + 2(1-\lambda)r\sin\theta\cos\theta + [1 - (C+3)\sin^2\theta]r^2\cos\theta, \end{aligned} \tag{7}$$

whereas the energy integral acquires the form

$$(u^2 + v^2)/2 - (\lambda\cos^2\theta + 2\sin^2\theta)r^2/2 - [(3\cos^2\theta - C\sin^2\theta)r^3\sin\theta]/3 = h$$

All the orbits are situated on the Hill's surface

$$f(r,\theta) = U(\theta)r^3 + V(\theta)r^2 + h$$

where $f(r,\theta) = (u^2+v^2)/2 \geq 0$ is the kinetic energy of the particle and the functions U and V are defined by

$$\begin{aligned} U(\theta) &= [1-(C/3+1)\sin^2\theta]\sin\theta, \\ V(\theta) &= \lambda/2+(1-\lambda/2)\sin^2\theta. \end{aligned}$$

From a detailed analyses of the Hill's surface we obtained the next results:

5 Case $C \in (-\infty, 0)$ and $\lambda \in (-\infty, 0]$

5.1 Negative energy case ($h < 0$)

On the directions of $\theta \in (0, \pi)$,

- The collisions are not possible;
- There are no equilibrium points;
- The motion is unbounded (the test particle can be captured from infinity or can escape to infinity).

On the directions of $\theta \in (\pi+\theta', 2\pi-\theta')$ where $\theta' = \arcsin\sqrt{\lambda/(\lambda-2)}$ we distinguish the next situations:

1. If $h < -4/3C^2$ the motion is not possible on these directions;
2. If $h = -4/3C^2$ we have an equilibrium point (a saddle, see Section 3) at the distance $r = -2/C$ on the direction $\theta = 3\pi/2$;
3. If $0 > h > -4/3C^2$ the motion is bounded (oscillatory orbits).

On the directions of $\theta \in [\pi, \pi+\theta'] \cup [2\pi-\theta', 2\pi]$, the motion is not possible.

5.2 Zero energy case ($h = 0$)

On the directions of $\theta \in (0, \theta') \cup (\pi-\theta', \pi)$,

- The collisions are not possible;
- There are no equilibrium points;
- The motion is unbounded (the test particle can be captured from infinity or can escape to infinity);

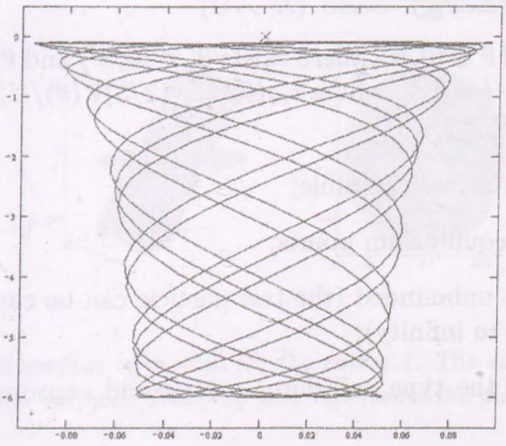

Figure 1: *An example of oscillatory orbit corresponding to case 3 before. The initial conditions as chosen as follow:* $r_0 = 5$, $\theta_0 = 3\pi/2$, $u_0 = 0$ *and* $v_0 = 0.1$.

- The particle cannot leave the collision manifold if, at the initial moment, is situated on it.

On the directions of $\theta \in (\pi + \theta', 2\pi - \theta')$,

- The collisions are possible;
- There are no equilibrium points;
- The motion is bounded (oscillatory orbits).

On the directions of $\theta \in [\theta', \pi + \theta']$,

- The collisions are not possible with zero energy;
- There are no equilibrium points;
- The motion is unbounded (the test particle can be captured from infinity or can escape to infinity).

On the directions of $\theta \in [\pi, \pi + \theta'] \cup [2\pi - \theta', 2\pi]$, only the motion on the collision manifold is possible.

5.3 Positive energy case ($h > 0$)

On the directions of $\theta \in (0, \pi)$, there exists $\theta_1' \in (0, \theta')$ and $\theta_2' \in (\pi - \theta', \pi)$, such that $f(r_{cr}(\theta_i)) = 0$, $i = \overline{1,2}$, where $r_{cr}(\theta) = -(2/3)V(\theta)/U(\theta)$.

If $\theta \in (0, \theta_1') \cup (\theta_2', \pi)$,

- The collisions are not possible;
- There are no equilibrium points;
- The motion is unbounded (the test particle can be captured from infinity or can escape to infinity);
- The orbits of the type collision - escape and capture - collision are not possible.

If $\theta \in [\theta_1', \theta_2']$,

- the following type of orbits are possible: collision - escape, capture - collision, capture - escape, collision - collision;
- There are no equilibrium points;

On the directions of $\theta \in [\pi, 2\pi]$,

- The collisions are possible;
- There are no equilibrium points;
- The motion is bounded (oscillatory orbits).

6 Case $C \in (-\infty, 0)$ and $\lambda \in (0, +\infty)$

6.1 Negative energy case ($h < 0$)

On the directions of $\theta \in [0, \pi]$,

- The collisions are not possible;
- There are no equilibrium points;
- The motion is unbounded (the test particle can be captured from infinity or can escape to infinity);

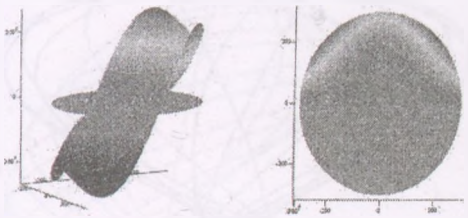

Figure 2: *The Hill surface of motion for the case 4.1. The second panel represents a top-down view of this surface. The gray disk represents the plane* $f = 0$.

On the directions of $\theta \in (\pi, 2\pi)$, we distinguish the next situations:

1. If $-4/\lambda \leq C < 0$,

1.1. If $h < -4/3C^2$ the motion is not possible on these directions;

1.2. If $h = -4/3C^2$ we have an equilibrium point (a saddle, see Section 3) at the distance $r = -2/C$ on the direction $\theta = 3\pi/2$;

1.3. If $-(\lambda^2/24)(\lambda C + 6) > h > -4/3C^2$ the motion is bounded (oscillatory orbits) and there are no equilibrium points.

1.4. If $h = -(\lambda^2/24)(\lambda C + 6)$, there exists two equilibrium points (that are saddle, see Section 3) at the radial distance $r = \sqrt{\lambda(\lambda C + \lambda + 4)}$, on the directions $\theta \in \{\pi + \bar{\theta}, 2\pi - \bar{\theta}\}$, where $\bar{\theta} = \arcsin\sqrt{\lambda(\lambda C + \lambda + 4)}$.

1.5. If $0 > h > -(\lambda^2/24)(\lambda C + 6)$,

- The collisions are possible;
- There are no equilibrium points;
- The motion is bounded (oscillatory orbits).

2. If $C < -4/\lambda$,

2.1. If $h < -4/3C^2$ then exists $\theta_1 \in (\pi, 3\pi/2)$ and $\theta_2 \in (3\pi/2, 2\pi)$, such that $f(r_{cr}(\theta_i)) = 0$, $i = \overline{1,2}$, where $r_{cr}(\theta) = -(2/3)V(\theta)/U(\theta)$.The motion is not possible on the directions of $\theta \in (\theta_1, \theta_2)$; the motion is bounded on $\theta \in (\pi, \theta_1) \cup (\theta_2, 2\pi)$ the collisions are not possible and there is no equilibrium points.

2.2. If $h = -4/3C^2$ we have an equilibrium point (a saddle, see Section 3) at the distance $r = -2/C$ on the direction $\theta = 3\pi/2$;

2.3. If $0 > h > -4/3C^2$ the motion is bounded (oscillatory orbits)

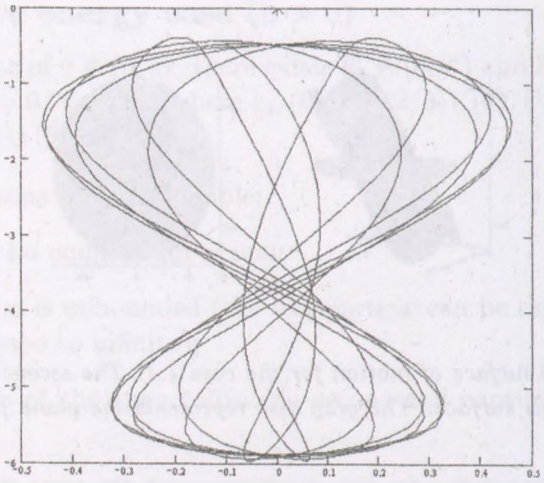

Figure 3: *An example of oscillatory orbit corresponding to case 1.3 before. The initial conditions as chosen as follow:* $r_0 = 5$, $\theta_0 = 3\pi/2$, $u_0 = 2.83$ *and* $v_0 = 0.2$.

6.2 Zero energy case ($h = 0$)

On the directions of $\theta \in [0, \pi]$,

- the following type of orbits are possible: collision - escape, capture - collision, capture - escape, collision - collision;
- there are no equilibrium points;

On the directions of $\theta \in (\pi, 2\pi)$,

- The collisions are possible;
- There are no equilibrium points;
- The motion is bounded (oscillatory orbits).

6.3 Positive energy case ($h > 0$)

On the directions of $\theta \in [0, \pi]$,

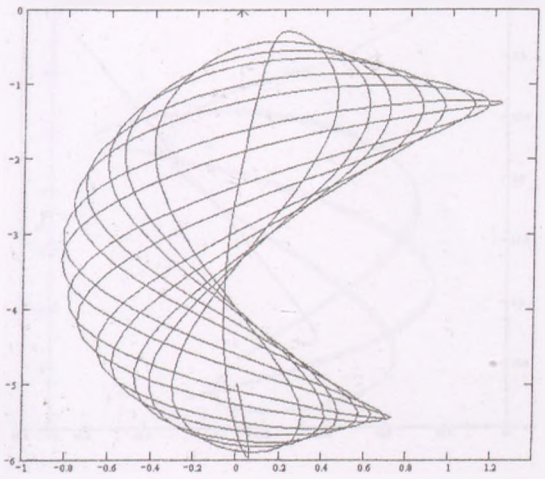

Figure 4: *An example of oscillatory orbit corresponding to case 1.5 before.*

- the following type of orbits are possible: collision - escape, capture - collision, capture - escape, collision - collision;
- there are no equilibrium points;

On the directions of $\theta \in (\pi, 2\pi)$,

- The collisions are possible;
- There are no equilibrium points;
- The motion is bounded (oscillatory orbits).

The remaining cases ($C \in [0, +\infty)$, $\lambda \in (-\infty, 0]$ and $C \in [0, +\infty)$, $\lambda \in (0, +\infty)$) can be treated in a similar manner.

References

Anisiu, M.C., Pal, A. 1999, Rom. Astron. J., 9, 179

Antonov, V.A., Timoshkova, E.I. 1993, Astron. Rep., 37, 138

Boccaletti, D., Pucacco, G. 1996, Theory of Orbits, Springer-Verlag, Berlin, Heidelberg, New-York

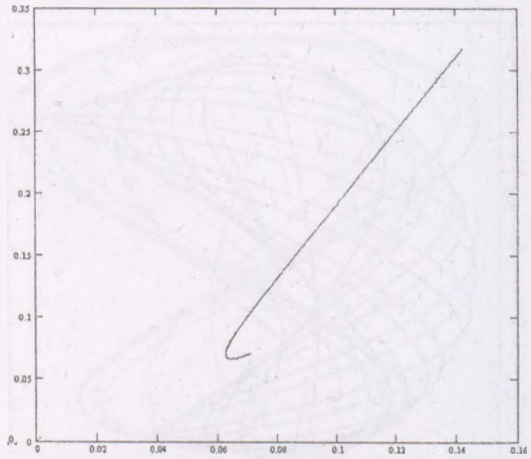

Figure 5: *An example of capture-escape orbit corresponding to case 4.2.3 before.*

Chenciner, A., Montgomery, R., 2000, Ann. Math., 152, 881

Craig, S., Diacu, F.N., Lacomba, E.A., Perez, E. 1999, J. Math. Phys., 40, 1359

Delgado, J., Diacu, F.N., Lacomba, E.A., Mingarelli, E., Mioc, V., Perez, E., Stoica, C. 1996, J. Math. Phys., 37, 2748

Devaney, R.L. 1978, Invent. Math., 45, 221

Diacu, F.N., Mingarelli, A., Mioc, V., Stoica, C. 1995, in R.P. Agarwal (ed.) Dynamical Systems and Aplications, World Science Series in Applicable Analysis, Vol. 4, World Scientific, Singapore, p. 213

Diacu, F.N., Mioc, V., Stoica, C. 2000, Nonlinear Anal., 41, 1029

Gutzwiller, M.C. 1973, J. Math. Phys., 14, 139

Hnon, M., Heiles, C. 1999, ApJ, 69, 73

McGehee, R. 1973, J. Diff. Ec., 14, 70

McGehee, R. 1974, Invent. Math., 27, 191

Mioc, V. 2002, Rom. Astron. J., 12, 193

Mioc, V., Barbosu, M. 2003a, Serb. Astron. J., 167, 47

Mioc, V., Barbosu, M. 2003b, Spacetime Subst., 4, 164

Mioc, V., Pricopi, D. 2005, Rom. Astron. J., 15, 65

Mioc, V., Stavinschi, M. 2000, Rom. Astron. J., 10, 71

Mioc, V., Stavinschi, M. 2001, Phys. Lett. A., 279, 223

Mioc, V., Perez-Chavela, E., Stavinschi, M. 2003, Celest. Mech. Dyn. Astron., 86, 81

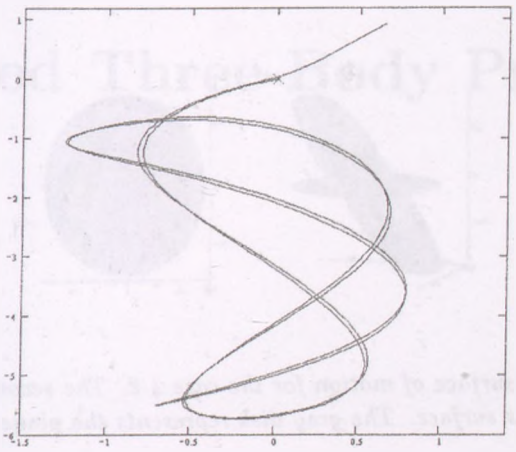

Figure 6: *An example of oscillatory orbit situated on the directions of . The particle will escape on the directions of* $\theta \in [0, \pi]$.

Mioc, V., Anisiu, M.-C., Barbosu, M. 2005, Celest. Mech. Astron., (in press)

Saari, D.G. 1974, Celest. Mech., 9, 55

Santoprete, M. 2002, J. Math. Phys., 43, 2307

Stoica, C., Mioc, V., 1997, Astrophys. Space. Sci., 249, 161

Santoprete, M. 2002, J. Math. Phys., 43, 2307

Van der Merwe, P. du T. 1991, Phys. Lett., 156, 216

Wintner, A. 1941, The Analytical Foundation of Celestial Mechanics, Princeton University Press, Princeton, N.J.

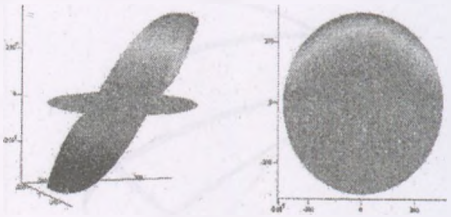

Figure 7: *The Hill surface of motion for the case 4.2. The second panel represents a top-down view of this surface. The gray disk represents the plane* $f = 0$.

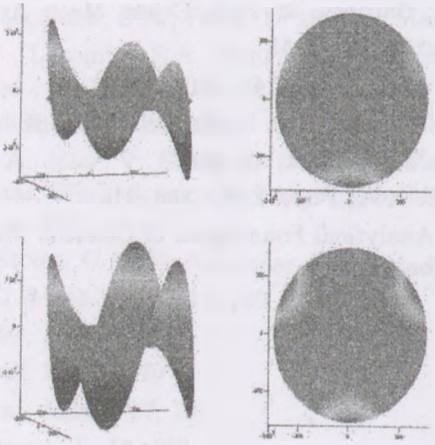

Figure 8: *The Hill surface of motion for the remaining cases* $C \in [0, +\infty)$, $\lambda \in (-\infty, 0]$ *and* $C \in [0, +\infty)$, $\lambda \in (0, +\infty)$, *respectively.*

Part II

Restricted Three-Body Problems

PADEU | PADEU 19 (2007), p. 117
ISBN 963 463 557
©Published by the Astron. Dept. of the Eötvös Univ.

On the Constantin Popovici Photogravitational Model

Ciprian Chiruţă[1], Tiberiu Oproiu[2]

[1]The "Ion Ionescu de la Brad" University of Agricultural Sciences and Veterinary Medicine, 3, M. Sadoveanu Alley, RO-700490, Iasi, Romania
[2]Astronomical Institute of Romanian Academy, Astronomical Observatory Cluj-Napoca, 19, Ciresilor St., RO-400487, Cluj-Napoca, Romania

E-mail: [1]kyru@univagro-iasi.ro, [2]toproiu@yahoo.com

Abstract
The paper deals with the photogravitational model proposed in 1923 by the Romanian astronomer Constantin Popovici for the two-body problem. We show here the relationship between Popovici's model and Poyting-Robertson's effect. The variation of the orbital energy is given for Poynting-Robertson's effect. Popovici's model is extended for the restricted three-body problem. The equations of motion are written in a rotating, barycentric, dimensionless coordinate system and comments on the equilibrium points and the Jacobi-energy are added to our study. Possibilities of applications to the solar system are also discussed.
Keywords: *Photogravitational problem, orbital energy, restricted three-body problem*

1 Introduction

In the first quarter of the 20th century, the Romanian astronomer Constantin Popovici (1878-1956) proposed a modification of the inverse-square law that results from the combination of the Newtonian attraction and the repelling force of radiation. He added a term depending on the radial velocity and on the speed of light (Popovici 1923), which made his law (as he mentioned) applicable

to radial attractive or repulsive forces. The photogravitational force proposed by Popovici has the following form:

$$F = -\frac{A}{r^2} + \frac{R}{r^2} - \frac{R}{r^2}\frac{\dot{r}}{c}, \tag{1}$$

where $-\frac{A}{r^2}$ represents the Newtonian attraction force, A being the attraction of the luminous body (Sun) at the unit distance; $\frac{R}{r^2}$ represents the force due to the light pressure of the central body, R being the light repulsion at unit distance; $\frac{R\dot{r}}{cr^2}$ a corrective term, added by Popovici, representing the force due to the finite speed of light. Here, c denotes the light speed and $\dot{r}$ the component of the speed of the attracted body on the radius vector. Eq. (1) can be written also in the form:

$$F = -\frac{A}{r^2} + \frac{R}{r^2}(1 - \frac{\dot{r}}{c}), \tag{2}$$

Instead of Eq. (1) Popovici used the relation:

$$F = -\frac{k}{r^2}(1 + \varepsilon\dot{r}), \tag{3}$$

where $k = A - B$ and $\varepsilon = R/(ck)$. This was given for the first time in the paper: Popovici, C., 1923: *Sur une modification de la loi de Newton-Coulomb*, Bull. Astron., vol 3, pp. 257-261.

This form has also been used by Giuseppe Armellini (1887-1958) in order to generalize Newton's attraction law. Armellini proposed the expression:

$$F = -\frac{Gmm'}{r^2}(1 + \varepsilon\dot{r}), \tag{4}$$

where m and m' are the masses of the interacting bodies, G is the universal attraction constant, r the distance between the bodies and ε Armellini's constant. The value of this constant was determined through a comparison between theory and observations. For the first time, Armellini's law was published in: Armellini, G., 1937: *I problemi fondamentali della Cosmogonia e la legge di Newton*, Rendiconti, Accad. Naz. Lincei, 26, 209.

Popovici's model has been reconsidered in the last decades by several Romanian researchers: Anisiu (1995a, 1995b, 2003), Anisiu and Mioc (2004), Mioc and Blaga (2001, 2002), Barbosu (2000), Barbosu and Oproiu (2004) etc.

2 Popovici's model and Poynting-Robertson's effect

In 1903 Poynting stated that a particle (small meteors, cosmic dust) is strongly affected both by gravitation and light radiation forces, as it approaches a luminous celestial body. He has also suggested that an infinitesimal body on a solar orbit suffers a gradual loss of the angular momentum and eventually spirals into the Sun. In a system of coordinates where a luminous body (e.g. Sun) is at rest, the radiation scattered by an infinitesimal mass suffers a *blue shift* in the direction of motion and a *red shift* in the opposite direction. This gives rise to a drag force, opposed to the direction of motion. The proper relativistic treatment of this problem was formulated by Robertson (1937). He showed that, to the first order in $\vec{V}/c$, the radiation pressure force is given by (Ragos et all, 1995):

$$\vec{F}_{rad} = \vec{F}_1 + \vec{F}_2 + \vec{F}_2, \tag{5}$$

where

$$\vec{F}_1 = F_p \frac{\vec{r}}{r}, \tag{6}$$

$$\vec{F}_2 = -F_p \frac{\vec{V}\vec{r}}{cr} \frac{\vec{r}}{r}, \tag{7}$$

$$\vec{F}_3 = -F_p \frac{\vec{V}}{c}, \tag{8}$$

where F_p denotes the magnitude of the radiation force, $\vec{r}$ the position vector of the particle with respect to the radiation source, $\vec{V}$ the corresponding velocity vector and c the speed of light. The first term ($\vec{F}_1$), in Eq. (5) is the *radiation pressure*. The second term ($\vec{F}_2$) represents the *Doppler shift* of the incident radiation and the third term ($\vec{F}_3$) is due to the absorption and subsequent re-emission of part of the incident radiation. The last two terms taken together are the *Poynting-Robertson effect*.

Let us use Popovici's notation:

$$F_p = \frac{R}{r^2}, \tag{9}$$

where $R = F_p|_{r=1}$. If we take into account that $\dot{r} = \vec{V}\vec{r}/r$, than Eq. (5) becomes:

$$\begin{aligned} \vec{F}_{rad} &= \frac{R}{r^2}\frac{\vec{r}}{r} - \frac{R}{r^2}\frac{\dot{r}}{c}\frac{\vec{r}}{r} - \frac{R}{r^2}\frac{\vec{V}}{c} \\ &= \frac{R}{r^2}(1-\frac{\dot{r}}{c})\frac{\vec{r}}{r} - \frac{R}{r^2}\frac{\vec{V}}{c} \end{aligned} \tag{10}$$

Let us denote by

$$\vec{F}_{PR} = \frac{R}{r^2}\frac{\dot{r}}{c}\frac{\vec{r}}{r} + \frac{R}{r^2}\frac{\vec{V}}{c}, \tag{11}$$

the Poynting-Robertson (PR) effect, and by

$$\vec{F}_{CP} = \frac{R}{r^2}\frac{\dot{r}}{c}\frac{\vec{r}}{r}, \tag{12}$$

the Popovici's correction term (CP). We observe that:

$$\vec{F}_{CP} = \vec{F}_{PR}|_{\frac{v}{c}=0}. \tag{13}$$

3 Energy relations

We note that for Popovici's model the orbital energy is not conserved. According to Stiefel and Scheifele (1971), the *"Keplerian energy"* (per mass unit), is given by:

$$E_k = \frac{V^2}{2} - \frac{\mu}{r}, \tag{14}$$

where $\mu = G(M+m) \approx GM = A, \quad m \ll M.$

For the perturbed two-body problem, we know the equation:

$$\frac{dE_k}{dt} = (\vec{V}, \vec{P}), \tag{15}$$

where the parenthesis on the right-hand side denote the *scalar product* of the vectors $\vec{V}$ and $\vec{P}$, and $\vec{P}$ represents forces (other than the central attraction) that act on the particle of mass m.

In our case $\vec{P} = \vec{F}_{rad}$, and taking into account Eq. (5), we get:

$$\frac{dE_k}{dt} = (\vec{V}, \vec{F}_{rad}) = (\vec{V}, \vec{F}_1) + (\vec{V}, \vec{F}_2) + (\vec{V}, \vec{F}_3) \tag{16}$$
$$= -\frac{d}{dt}(\frac{R}{r}) - \frac{R}{c}(\frac{\dot{r}}{r})^2 - \frac{R}{r^2}\frac{V^2}{c}.$$

If we denote by

$$E = E_k + \frac{R}{r} = \frac{V^2}{2} - \frac{A-R}{r} = \frac{V^2}{2} - \frac{k}{r}, \tag{17}$$

then, from Eq.(16), we get:

$$\frac{dE}{dt} = -\frac{R}{c}(\frac{\dot{r}}{r})^2 - \frac{R}{r^2}\frac{V^2}{c}. \tag{18}$$

If we consider $V^2/c = 0$ in Eq. (18), we recover Popovici's theorem:

"L'énergie ne se conserve plus. Cette quantité $E = \frac{V^2}{2} - \frac{k}{r}$ *que l'on appelle dans la Mécanique newtonienne l'énergie, varie dans le même sens avec le temps. La relation suivante, qui est en même temps l'équation du mouvement:*

$$\frac{dE}{dt} = -\alpha k(\frac{r'}{r})^2, \quad r' = \frac{dr}{dt};$$

$\frac{dE}{dt} > 0$ *attraction;* $\frac{dE}{dt} < 0$ *répulsion,*
nous fait voir comment l'énergie est dépensée par le mécanisme de la propagation".

Eq. (16) for the variation of keplerian energy is similar to that found by Robertson (Robertson, 1937, Eq (5.10) p.437).

4 Extension to the Circular Restricted Three-body Problem

The repulsive and the gravitational force form the so-called *photogravitational force field*; a few researches studied the motion of celestial bodies in such a field. V.V. Radziewsky formulated for the first time "the photogravitational three-body problem" (1950, 1953a,b, 1966).

In what follows we consider Popovici's model for the restricted three-body problem.

Let us consider the restricted circular three-body problem: P_1 (having the mass M_1), P_2 (having the mass M_2) and a third body P, of mass m, negligible with respect to the mass of the first two. P_1 and P_2, called "primaries", are moving along circular orbits around their center of mass, in the gravitational field. The body with the negligible mass is submitted to the photogravitational force generated by P_1 and the gravitational force generated by P_2. The equations of motion of the third body can be written:

$$m\ddot{\vec{r}} = \vec{F}_1 + \vec{F}_2, \tag{19}$$

where:

$$\vec{F}_1 = \vec{F}_g + \vec{F}_{rad} = -G\frac{mM_1}{r_1^2}\frac{\vec{r}_1}{r_1} + \frac{L_1}{4\pi c r_1^2}a(1 - \frac{\dot{\vec{r}}_1}{c})\frac{\vec{r}_1}{r_1} \tag{20}$$

is the photogravitational force due to P_1, where L_1 – the luminosity of the body P_1 (for example: the Sun), c – the speed of light and a – the area of the section on the P_1P direction, and

$$\vec{F}_2 = -G\frac{mM_2}{r_2^2}\frac{\vec{r}_2}{r_2} \tag{21}$$

is the attraction force of the body P_2 (Fig. 1).

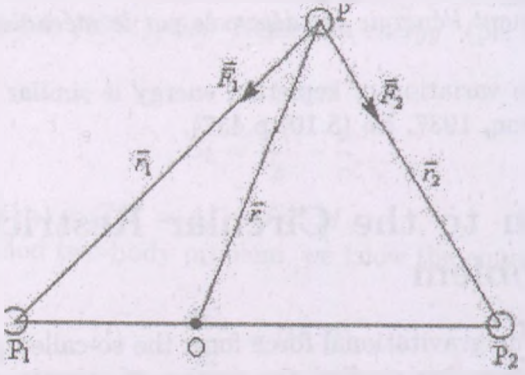

Figure 1: *The restricted three-body problem*

Dividing by m in (19) we get:

$$\ddot{\vec{r}} = -\frac{GM_1}{r_1^3}(1 - \frac{L_1}{4\pi c}\frac{1}{GM_1}\frac{a}{m})\vec{r}_1 - \frac{GM_2}{r_2^3}\vec{r}_2 - \frac{L_1}{4\pi c^2 r_1^2}\frac{\dot{r}_1}{r_1}\frac{a}{m}\vec{r}_1 \tag{22}$$

Let us introduce the notations:

$$A = GM_1, \quad R = \frac{L_1}{4\pi c}, \quad q_1 = 1 - \frac{R}{A}.\frac{1}{\sigma}, \quad \sigma = \frac{m}{a} \tag{23}$$

Then, Eq (22) can be written under the form:

$$\ddot{\vec{r}} = -\frac{A}{r_1^3}q_1\vec{r}_1 - \frac{GM_2}{r_2^3}\vec{r}_2 - \frac{R}{cr_1^2}\frac{\dot{r}_1}{r_1}\frac{1}{\sigma}\vec{r}_1. \tag{24}$$

where the last term was introduced by Constantin Popovici. This has a breaking effect, similar to the motion in a resisting medium (Antonacopoulos, 1970).

The motion is studied in an inertial system $O\xi\eta\zeta$. With respect to this coordinate system, the bodies have the following coordinates (fig. 2): $P_1(\xi_1, \eta_1, \zeta_1)$, $P_2(\xi_2, \eta_2, \zeta_2)$, $P(\xi, \eta, \zeta)$. Let the origin of the inertial coordinate system be taken at the center of mass of the primaries, and let the direction of the axes be chosen such that the $\xi\eta$-plane is the plane of their motion; then $\zeta_1 = \zeta_2 = 0$. The scalar equations of the motion are:

$$\begin{cases} \ddot{\xi} = -\frac{A}{r_1^3}q_1(\xi - \xi_1) - \frac{GM_2}{r_2^3}(\xi - \xi_2) - \frac{R}{cr_1^3}\frac{\dot{r}_1}{\sigma}(\xi - \xi_1), \\ \ddot{\eta} = -\frac{A}{r_1^3}q_1(\eta - \eta_1) - \frac{GM_2}{r_2^3}(\eta - \eta_2) - \frac{R}{cr_1^3}\frac{\dot{r}_1}{\sigma}(\eta - \eta_1), \\ \ddot{\zeta} = -\frac{A}{r_1^3}q_1\,\zeta - \frac{GM_2}{r_2^3}\,\zeta - \frac{R}{cr_1^3}\frac{\dot{r}_1}{\sigma}\,\zeta, \end{cases} \tag{25}$$

Let us introduce a dimensionless, rotating, barycentric coordinate system $Oxyz$ with the same origin, and where the axes Ox and Oy rotate around the Oz axis with an angular velocity equal to the unity. The Oz axis coincides with the $O\zeta$ axis. The Ox axis will be chosen such that P_1 and P_2 will lie on it and the positive direction will be from P_1 to P_2. We will also choose the mass unit to be the sum of the masses of the finite bodies: $M_1 + M_2 = 1$. We denote $\mu = \frac{q}{1+q}$ where $q = \frac{M_2}{M_1}$; we have $1 - \mu$ for the mass of P_1 and μ for the mass of P_2. Let the unit distance be the distance between the two finite bodies (see Fig. 2). Their coordinates will be $P_1(x_1, 0, 0)$ and $P_2(x_2, 0, 0)$, and $x_2 - x_1 = 1$.

The coordinates in the new coordinate system are given by:

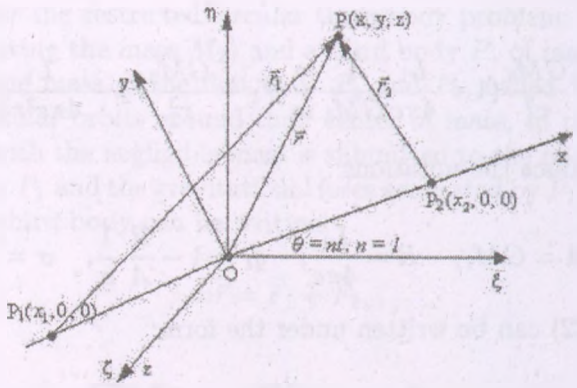

Figure 2: *Reference system*

$$\begin{cases} x = \xi \cos t + \eta \sin t, \\ y = -\xi \sin t + \eta \cos t, \\ z = \zeta \end{cases} \tag{26}$$

and

$$\begin{cases} \xi = x \cos t - y \sin t, \\ \eta = x \sin t + y \cos t, \\ \zeta = z. \end{cases} \tag{27}$$

Computing the second order time derivatives of ξ, η, ζ from equations (27) and replacing them in (25) we find (Moulton, 1923):

$$\begin{cases} \ddot{x} - 2\dot{y} = x - \frac{1-\mu}{r_1^3} q_1 (x - x_1) - \frac{\mu}{r_2^3}(x - x_2) - \frac{R}{c r_1^3} \frac{\dot{r}_1}{\sigma}(x - x_1), \\ \ddot{y} + 2\dot{x} = y - \frac{1-\mu}{r_1^3} q_1 (y - y_1) - \frac{\mu}{r_2^3}(y - y_2) - \frac{R}{c r_1^3} \frac{\dot{r}_1}{\sigma}(y - y_1), \\ \ddot{z} = \frac{1-\mu}{r_1^3} q_1 z - \frac{\mu}{r_2^3} z - \frac{R}{c r_1^3} \frac{\dot{r}_1}{\sigma} z. \end{cases} \tag{28}$$

Remark: If the last terms of the above relations are zero, from (28), we get the Radziewsky case (Radziewsky 1950, 1953a, 1953b). If we denote: $U = \frac{x^2+y^2}{2} + \frac{(1-\mu)q_1}{r_1} + \frac{\mu}{r_2}$, then (28) can be written in the form:

$$\begin{cases} \ddot{x} - 2\dot{y} = \frac{\partial U}{\partial x} - \frac{R}{cr_1^3}\frac{\dot{r}_1}{\sigma}(x - x_1), \\ \ddot{y} + 2\dot{x} = \frac{\partial U}{\partial y} - \frac{R}{cr_1^3}\frac{\dot{r}_1}{\sigma}(y - y_1), \\ \ddot{z} = \frac{\partial U}{\partial z} - \frac{R}{cr_1^3}\frac{\dot{r}_1}{\sigma}z. \end{cases} \tag{29}$$

5 Stationary solutions of motion

The equilibrium points for the relative motion verifies the conditions: $\dot{x} = \dot{y} = \dot{z} = 0$ and $\ddot{x} = \ddot{y} = \ddot{z} = 0$. From (28), taking into account that $\dot{r}_1 = 0$, we have:

$$\begin{cases} x - \frac{1-\mu}{r_1^3}q_1(x - x_1) - \frac{\mu}{r_2^3}(x - x_2) = 0, \\ y - \frac{1-\mu}{r_1^3}q_1(y - y_1) - \frac{\mu}{r_2^3}(y - y_2) = 0, \\ -\frac{1-\mu}{r_1^3}q_1\, z - \frac{\mu}{r_2^3}z = 0. \end{cases} \tag{30}$$

We notice that this system can also be obtained from Eqs. (5) – (7) (Radziewski, 1953, p. 66), where we take $q_2 = 1$, $m_1 = 1 - \mu$, $m_2 = \mu$. Radziewski proved that this system had 7 libration points: three collinear (L_1, L_2, L_3) situated on the Ox axis, two triangular (L_4, L_5) and two in the same plane (L_6, L_7).

The equations that give the coordinates of these points can be found numerically. Their values for the L_4 and L_5 points are determined from:

$$\begin{cases} x_{L_4,L_5} = \frac{1}{2}\, q_1^{2/3} - \mu, \\ y_{L_4,L_5} = \pm q_1^{1/3}(1 - \frac{1}{4}\, q_1^{2/3})^{1/2}. \end{cases} \tag{31}$$

As we know, the motion in the vicinity of these points is stable if (Zagouras, 1991):

$$36\,\mu\,(1 - \mu b) \leq 1 \tag{32}$$

where $b = 1 - \frac{1}{4}q_1^{2/3}$.

Remark: If $q_1 = 1$, we get the classical, restricted three body problem. Denoting $E = \frac{\dot{x}^2+\dot{y}^2}{2} - U$, in (Chiruta & Oproiu, 2005) is established the formula:

$$\dot{E} = -\frac{R}{c}\frac{1}{\sigma}(\frac{\dot{r}_1}{r_1})^2. \tag{33}$$

If $\dot{E} = 0$, we get the relation (2) (Radziewski, 1953, p.55):

$$v^2 = x^2 + y^2 + \frac{2(1-\mu)q_1}{r_1} + \frac{2\mu}{r_2} - C. \tag{34}$$

For $v = 0$ we get the surfaces of zero relative velocity, that separate the regions of real motion ($v^2 \geq 0$) from those of imaginary motions ($v^2 < 0$).

6 Numerical examples

In what follows, let us consider that the third body (of negligible mass – for example a solar sail, heliocentric station, etc.) moves in the Sun–Jupiter system around the libration point L_4. By means of numerical integration of (10) we got various trajectories. The initial conditions (Table I) were taken from the paper (Zagouras, 1991, p.337).

Table 1: $\mu = 0.00095$ $q_1 = 0.1$ $y_0 = 0.451486$.

x_0	$\dot{x}_0$	$\dot{y}_0$
0.293469	0.080198	-0.159920
0.377311	0.101299	-0.418712
0.218806	0.057661	-0.022960

The left-hand trajectories in Figs. 3, 4, 5 have been obtained without Popovici's term (the case considered by Zagouras), while the right-hand trajectories in Figs. 3, 4, 5 have been calculated with Popovici's term. In this case we used the notation $w = \frac{R}{c\sigma}$ ($w = 0$ for the Zagouras's trajectories).

In this particular case, we notice that the introduction of Popovici's term preserves the shape of the trajectories determined by Zagouras, but, generally, not the periodic character as well.

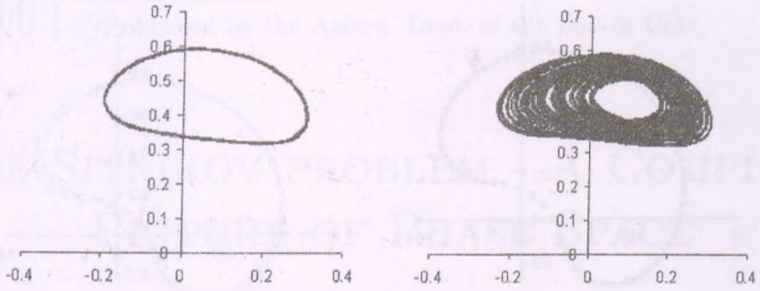

Figure 3: *Left: $w = 0$. Right: $w = 0.001$.*

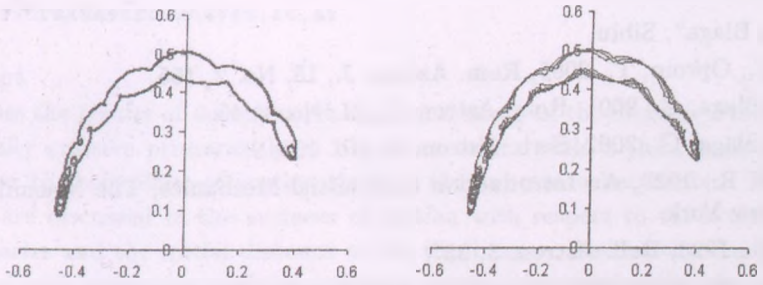

Figure 4: *Left: $w = 0$. Right: $w = 0.0001$.*

References

Anisiu, M.-C., 1995a, Analele stiintifice ale Univ. "Al I. Cuza", 16, 115.

Anisiu, M.-C., 1995b, Rom. Astron. J., 5, No. 1, 49.

Anisiu, M.-C., 2003, Rom. Astron. J., 13, No. 2, 171.

Anisiu, M.-C., Mioc, V., 2004, Rom. Astron. J., 14, No. 1, 71.

Antonacopoulos, G. A., 1970, Astrophysical Space Sci., 9, 482.

Armellini, G., 1937, Rendiconti, Accad. Naz. Lincei, 26, 209.

Barbosu, M., 2000, in M. V. Alania, E. A. Grebenikov (eds), "Mathematica" System in Theaching and Research, Proc. 2nd Int. Workshop on "Mathematica" System in Teaching and Research, January 28-30, 2000, Siedlce, Poland, 16.

Barbosu, M., Oproiu, T., 2004, General Mathematics, vol. 12, No. 2, 19. University

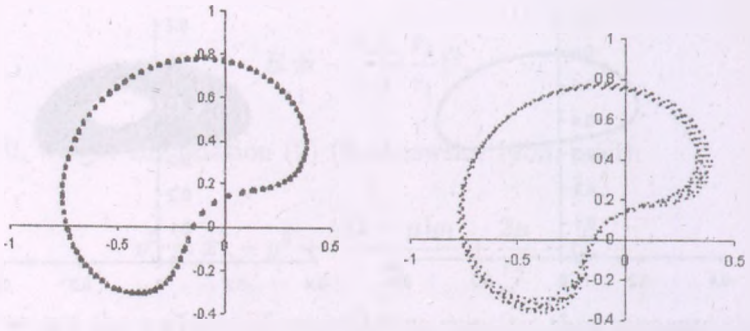

Figure 5: *Left: $w = 0$. Right: $w = 0.00001$.*

"Lucian Blaga", Sibiu.

Chiruţă, C., Oproiu, T., 2005, Rom. Astron. J., 15, No. 2, 165.

Mioc, V., Blaga, C., 2001, Rom. Astron. J., 11, No. 1, 45.

Mioc, V., Blaga, C., 2002, Serb. Astron. J., No. 165, 9.

Moulton F. R., 1923, An Introduction to Celestial Mechanics, The Macmillan Company, New York.

Popovici C., 1923, Bull. Astron. 3, 257.

Poynting, J. H., 1903, Phil. Trans. Roy. Soc., London, 202, 525.

Radzievsky, V. V., 1950, Astron Zh. 27, 4, 250 (in Russian).

Radzievsky, V. V., 1953a, Astron Zh. 30, 3, 265 (in Russian).

Radzievsky, V. V., 1953b, Astron Zh. 30, 4, 378 (in Russian).

Radzievsky, V. V., 1966, Astron Zh. 27, 178 (in Russian).

Ragos, O., Zafiropoulos, F. A., Vrahatis, M. N., 1995, Astron. Astrophys. 300, 579.

Robertson, H. P., 1903, Mon. Not. Roy. Astron. Soc., 97, 423.

Stiefel, E. L., Scheifele, G., 1971, Linear and Regular Celestial Mechanics, Springer Verlag, Berlin.

Zagouras, C.G., 1991, Celest. Mech. Dyn. Astr., 51, 331.

PADEU | PADEU 19 (2007), p. 129
ISBN 963 463 557
©Published by the Astron. Dept. of the Eötvös Univ.

The Sitnikov problem - A Complete Picture of Phase Space

Rudolf Dvorak

University of Vienna, Institute for Astronomy
AstroDynamicsGroup, A-1180 Vienna, AUSTRIA

E-mail: dvorak@astro.univie.ac.at

Abstract
We discuss the results of an extensive numerical study of the Sitnikov Problem, where two equally massive primaries have Keplerian orbits while a third body moves perpendicular to their plane of motion through their common barycenter. The possible motions are discussed in the surfaces of section with respect to the eccentricity e of the primaries and the initial distance of the third mass. Besides the shrinking of the main land with increasing e of the primaries we can observe the dominance of the 2:1 periodic orbit, which disappears (reappears) via pitchfork bifurcation (inverse pitchfork bifurcation). On one hand the presence of sticky regions close to stable islands and sticky fingers far into the chaotic sea is very well visible in the respective plots. On the other hand 'escape channels' showing orbits with very small escape times are also present for any value of the eccentricity.
Keywords: *Sitnikov Problem, Phase Space*

1 Introduction

The Sitnikov Problem (=SP) can be regarded as a special case of the three dimensional restricted three-body problem (Sitnikov, 1960). It is defined in the following way: Two equally massive primary bodies orbit around their common barycenter and a third (massless) body moves perpendicular to the orbital plane of the primaries through the center of mass (see Fig. 1). It is of special interest

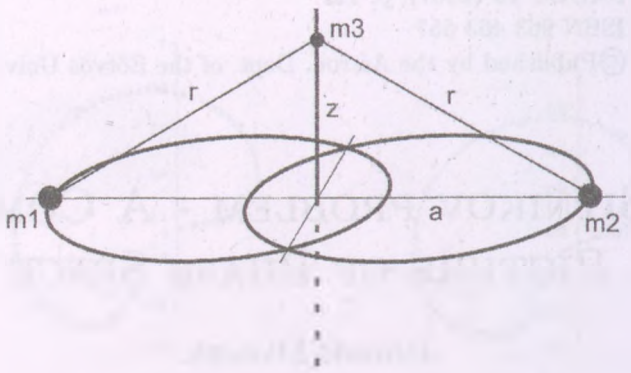

Figure 1: *Schematic view of the Sitnikov Problem; $m_1 = m_2$; the motion of m_3 is confined to the axis perpendicular to the plane of motion of the two primary bodies through the barycenter.*

for nonlinear dynamics because it can be regarded as a perfect example for chaotic motion (Moser, 1973).

2 Analytical Results

2.1 The Circular Case

If the primaries move on circular orbits, the problem is integrable, but if the orbits are eccentric, a general solution cannot be obtained and the dynamical description becomes quite complicated because of the nonlinearity of the respective equations of motion.

L. Euler solved the Sitnikov Problem as a special case of the two fixed center problem, when the two masses involved are equal ($m_1 = m_2$) and the third massless body moves perpendicular to the line of connection of the the two masses. He solved this problem generally for any motion of a massless body moving in the same plane as the primary bodies by means of quadratures. G. Pavanini (1907) expressed the solutions of the circular Sitnikov by means of Weierstrass elliptic functions. MacMillan (1913) gave a solution in terms of elliptic integrals in Legendre's normal form and was able to find a solution in form of a Fourier series expansion where the coefficients are power series depending on the perturbation parameter.

With $m_1 = m_2 = m$, $r^2 = a^2 + z^2$ and $a = constant$ the total energy of the systems reads

$$h = \frac{1}{2}\dot{z}^2 - \frac{2m}{r} \tag{1}$$

from which one finds the equation of motion by differentiating (1) with respect to the time

$$\ddot{z} = -\frac{2mz}{r^3}. \tag{2}$$

From the energy relation it follows furthermore

$$\frac{dz}{dt} = \sqrt{2h + \frac{4m}{r}} \tag{3}$$

which can be separated and prepared for integration

$$dt = \pm \frac{dz}{\sqrt{2h + \frac{4m}{r}}}. \tag{4}$$

Setting $m = \frac{1}{2}$ and $a = 1$ leads to the equation of motion

$$\ddot{z} = -\frac{z}{\left(\sqrt{1+z^2}\right)^3}. \tag{5}$$

Because of the constant distance between the primaries this case is integrable. The purely periodic motion can be represented via formal trigonometric series (e.g. Lhotka, 2004).

2.2 The Elliptic Case

For treating the low energy case Wodnar (1992) introduced a transformation of the independent variable time t to the angle $\zeta = \frac{z}{r(\varphi)}$ which is the tangent of the angle between the barycenter and one primaries' position seen from the mass m_3. The equation of motion in the dependant ζ variable is:

$$\zeta'' + \frac{e\cos\varphi + (0.25 + \zeta^2)^{-1.5}}{1 + e\cos\varphi}\zeta = 0, \tag{6}$$

where the ' stands for the derivation with respect to the true anomaly φ.

Following Hagel (1992) and Hagel and Trenkler (1993) the expression $(0.25+\zeta^2)^{-1.5}$ can be developed into a polynomial differential equation of the form

$$\zeta'' + g_1(\varphi)\zeta + \sum_{k=2}^{M} \zeta^k = 0 \tag{7}$$

with an appropriately chosen M to ensure the sufficiently accurate results for ζ. To achieve this goal one can expand the expression $\Xi(\zeta) = (0.25 + \zeta^2)^{-1.5}$ into a Taylor series or, which turns out to be more efficient, into Chebycheff polynomials which yield

$$\Xi = 8 - 46\zeta^2 + 203\zeta^4 - 616\zeta^6 + 1168\zeta^8 \tag{8}$$

which is valid in the range $-0.8 < \zeta < 0.8$. Thus one is lead to the following equation which describes motions in the vicinity of the barycenter and can be used for further investigations. For the linearized equation

$$\zeta'' + g_1(\varphi)\zeta = 0 \tag{9}$$

using Floquet theory one can derive exact analytical solutions for the frequencies and the amplitudes. This can be used for a subsequent perturbation theory which gives quite good solutions up to large eccentricities of the primaries. In an extension of this study Lhotka (2004) developed the perturbation theory up to very high orders and succeeded to find precise solutions in a wide range of eccentricity and distance of the third body to the barycenter.

3 Numerical Results

When the primaries have eccentric orbits the problem is non-integrable and all features connected with a chaotic system are present. One significant difference between regular orbits (on a torus) and a chaotic orbit is the sensitivity of an orbit with respect to the initial conditions. In Fig. 2 one can see that a slight difference in the initial condition (0.0001 in the position) can lead to completely different orbits. While one orbit escapes to the top, another one to the bottom, a third orbit seems to be stable. In fact also this orbit escapes after several revolutions of the primaries.

To visualize the phase space structure an appropriate tool is the use of the Poincaré surface of section method (SOS) where the whole phase is replaced by a space of lower dimension; in the case of the SP this space is a plane z (the distance to the barycenter) versus $\dot{z}$ (the velocity).

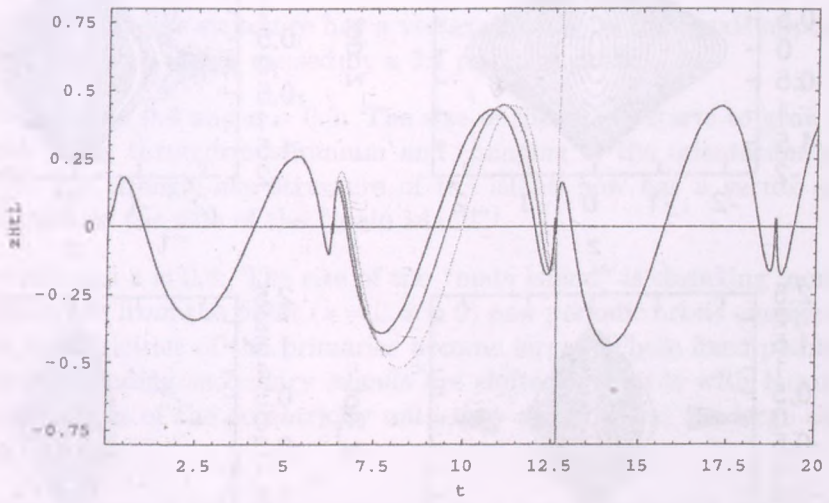

Figure 2: *The sensitivity with respect to the initial condition; three different orbits with slightly different initial positions ($\Delta z = \pm 0.0001$) for $e = 0.3$*

The structure of the phase space for different eccentricities is shown in Fig.3. Any of these orbits in the SOS starts with different initial conditions for z with $\dot{z} = 0$ and $a = a_{\min}$ (= periastron); one can imagine that we "drop" the third mass from this position. Points on this subspace of the three dimensional phase space are plotted for the next crossing of the orbit with the SOS when the primaries are again in their perihelion position.

- $e = 0$: As stated above all initial conditions lead to closed curves, which we can understand as sections of KAM-tori with a plane.
- $e = 0.1$: We see two islands of invariant curves around a stable point, which correspond to the 2:1 resonance (where the primaries make two complete revolutions whereas the third mass finishes exactly one oscillation – two crossings of the barycentre). Inside the "main island" one can also see two other islands, which correspond to different resonant motions.
- $e = 0.2$: The "main island" shrinks towards the point of equilibrium in the center and the 2:1 island is more and more isolated and shrinks also in size.

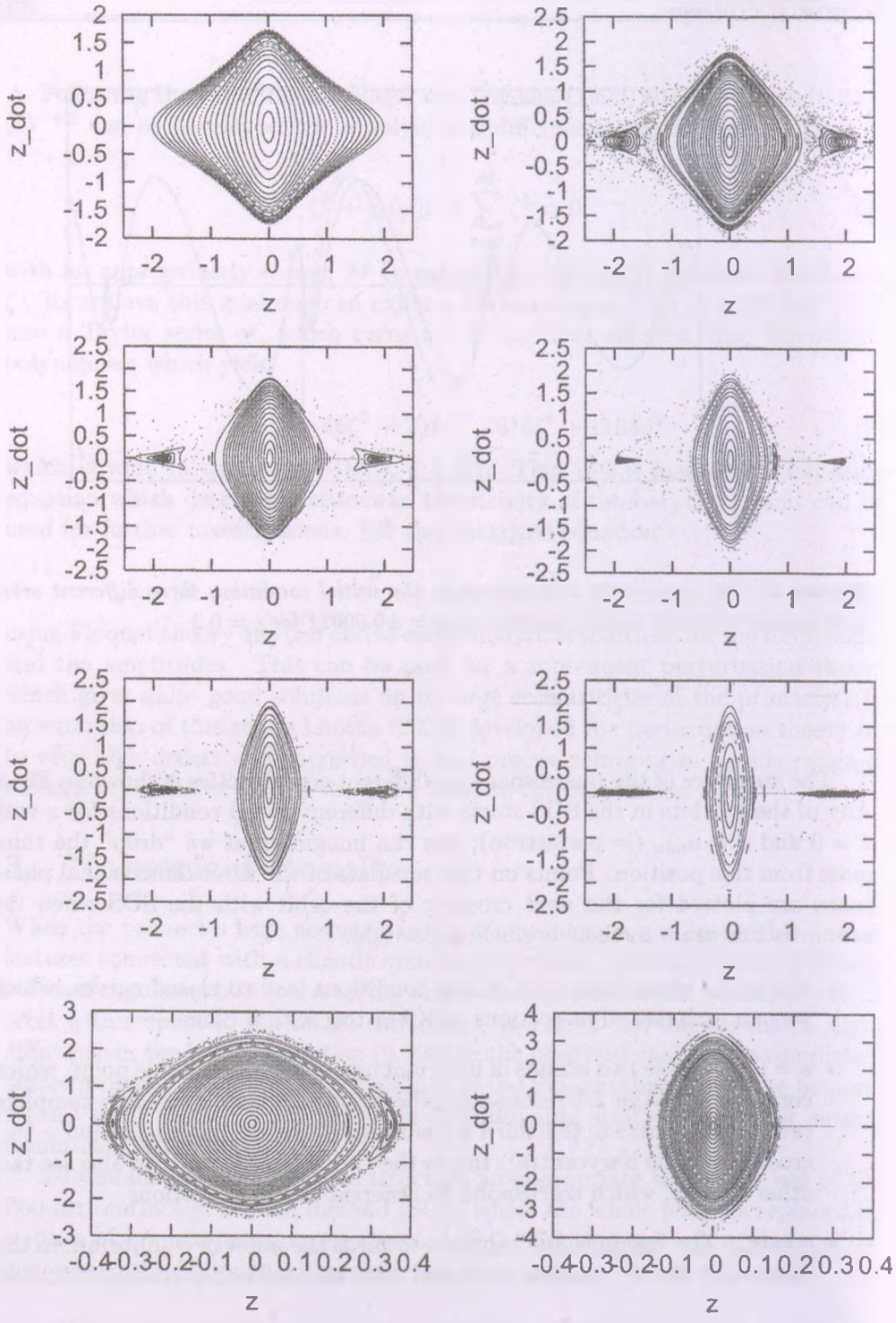

Figure 3: *Surfaces of Sections ($z, \dot{z}$ for 8 different eccentricities of the primaries: e=0, 0.1, 0.2, 0.3, 0.4, 0.5, 0.6, 0.8 (from left to right and top to bottom)*

The triangle-like structure has a vertex directly on the x-axis opposite to the main land and is caused by a 3:1 resonant orbit.

- $e = 0.3$, $e = 0.4$ and $e = 0.5$: The size of the island starts to grow again after going through a minimum and changing of the orientation on the SOS: the triangle-like structure of the island now has a vertex on the abscissa on the side of the "main island"[1].

- $e = 0.6$ and $e = 0.8$: The size of the "main island" is shrinking more and more while from the point $(z = 0, \dot{z} = 0)$ new periodic orbits emerge when the eccentricities of the primaries become larger. These fixed points and the surrounding secondary islands are shifted outwards with larger and larger values of the eccentricity until they disappear in the large chaotic see.

For some values of the eccentricities ($0.58 < e < 0.84$ the 2:1 island disappears because of pitchfork bifurcations. The point itself becomes unstable and two stable islands appear on the axis $z = 0$. In Fig. 4 we show the respective SOS for $e = 0.6$, where the 2:1 PO island is already unstable and computed the stable and unstable manifold through this homoclinic point, where the consecutive crossings of stable and unstable manifolds are well visible.

An interesting feature was unveiled by Alfaro and Chiralt: In their article they established that the center is unstable for specific intervals of e: $0.85586179 < e < 0.85586331$, $0.97752150 < e < 0.97752189$ and for an infinite number of eccentricity intervals when it is more and more increased. Via a numerical integration we visualized this splitting of the central island (which we call mainland) which happens now with respect to the the y-axis (the velocity $\dot{z}$ of the SOS) (Fig. 5).

4 The Phase Space Structure

To establish the complete phase phase structure of the SP we used extended numerical integration of the equations of motion for a fine grid in the eccentricity and of the initial distance z of the third body to the barycenter; its initial velocity $\dot{z}$ was set to 0. Furthermore at the beginning of the integration the primaries were always in their pericenter. The Surface of Section was chosen as the plane z versus $\dot{z}$ for every instant when the primaries are in their pericenter.

[1] this well known effect, the "squeeze effect" in non-integrable Hamiltonian systems is described in details in van der Weele (1988).

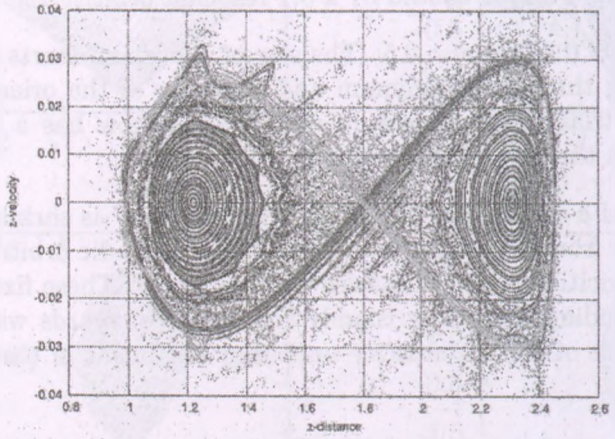

Figure 4: *The stable and unstable manifold through the 2:1 Periodic Orbit.*

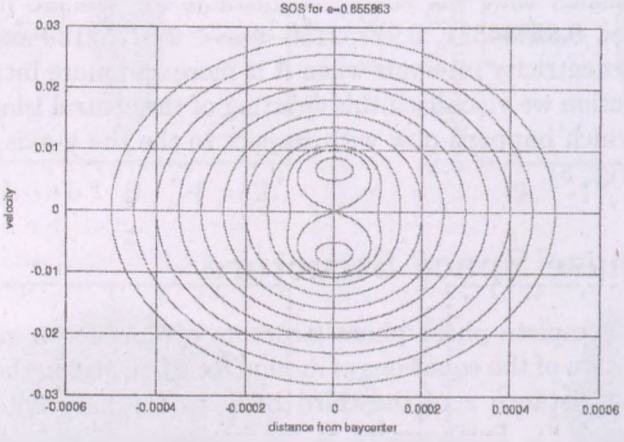

Figure 5: *The unstable center for e=0.855963.*

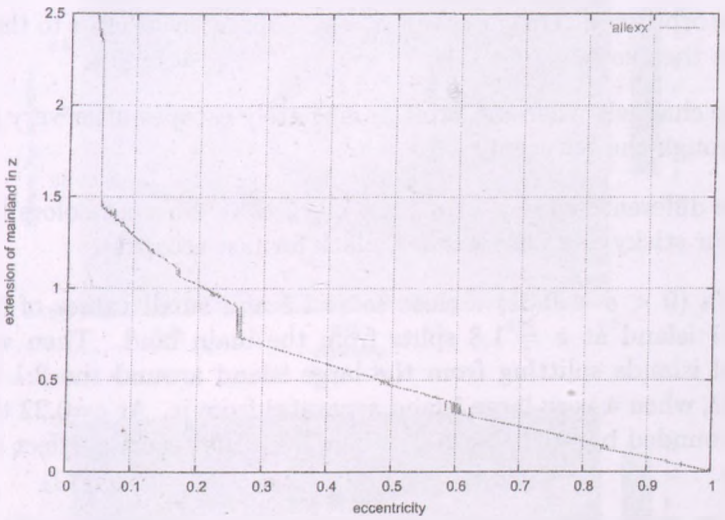

Figure 6: *Extension of the mainland in the Sitnikov Problem.*

We show in Fig. 6 the extension of the mainland depending on the eccentricity of the primaries. Below the line all orbits stay in the vicinity of the barycenter without escaping for the integration time 10^6 time units[2]. The extension of the mainland suddenly drops which is due to the destruction of a KAM-torus which separated the outer chaotic see with an inner layer of chaotic motion. Then, with larger e, the appearance of a cantorus with large holes allows to connect these two chaotic regions.

Using the results of a more detailed investigation covering the whole range of the eccentricity of the primaries we plot the escape time of an orbit on the grid eccentricity versus initial distance z of the 'planet' from the barycenter. To show the details we splitted into 3 different intervals of the eccentricity: $0 < e < 0.3$, $0.33 < e < 0.66$ and $0.66 < e < 0.99$

The following different types of orbits can be classified in the SOS:

1. Periodic orbits (PO) which are fixed points in the SOS,
2. Motion on a torus (quasi PO) which are invariant curves (IC) in the SOS,
3. Sticky orbits close to an invariant torus visible trough a 'fuzzy IC',

[2]we counted in radians thus making the number of points in the SOS to $10^6/2\pi$ for every orbit

4. Escape orbits which may stay for at least some returns close to the barycenter but then escape,

5. Escape channels where an orbit immediately escapes after very few crossings trough the barycenter.

All these different types of orbits are marked by different colors (yellow for stable, red for sticky, blue for escapes, black for fast escapes).

- Fig. 7a ($0 < e < 0.31$) : close to z=1.5 and small values of ($e \sim 0.02$) the 2:1 island at $z = 1.8$ splits from the main land. Then we can see several islands splitting from the large island around the 2:1 PO up to e=0.12, when a very large island separates from it. At e=0.22 the 2:1 PO is surrounded by 3:1 PO which suffers from the sqeezing effect mentioned above.

- Fig. 7b ($0.33 < e < 0.63$): Then up to e=0.58 the 2:1 island steadily increases in size up to the moment when it becomes unstable and splits into two stable islands (pitchfork bifurcation). These two symmetric islands are shifted more and more away from the center (respectively shifted towards the center). Smaller fingers show the splitting of other high order resonant POs which disappear fast and are surrounded by many sticky orbits. The whole domain from the bifurcation on between the two stable islands ($1 < z < 2.5$) is filled with sticky orbits! For small respectively large z distances one can see small escape channels where the orbit escapes very fast to infinity.

- Fig. 7c ($0.63 < e < 0.93$): The continuation of the stable PO shows a crab-like symmetric structure with many splittings of high order POs. Between ($0.75 < e < 0.85$) the area seems to be totally depleted from stable orbits. Then the 2:1 PO island again starts to dominate the phase space structure up to values quite close to $e = 1$.

5 Conclusions

In this article we briefly reported about some of the analytical work for the circular and also the elliptic Sitnikov problem. We emphasized the results of a somewhat time consuming numerical investigation of the whole phase space structure covering the range for the distance from the barycenter of the third body from ($0 < z < 2.5$) and for the eccentricity of the primaries ($0 < e < 0.99$).

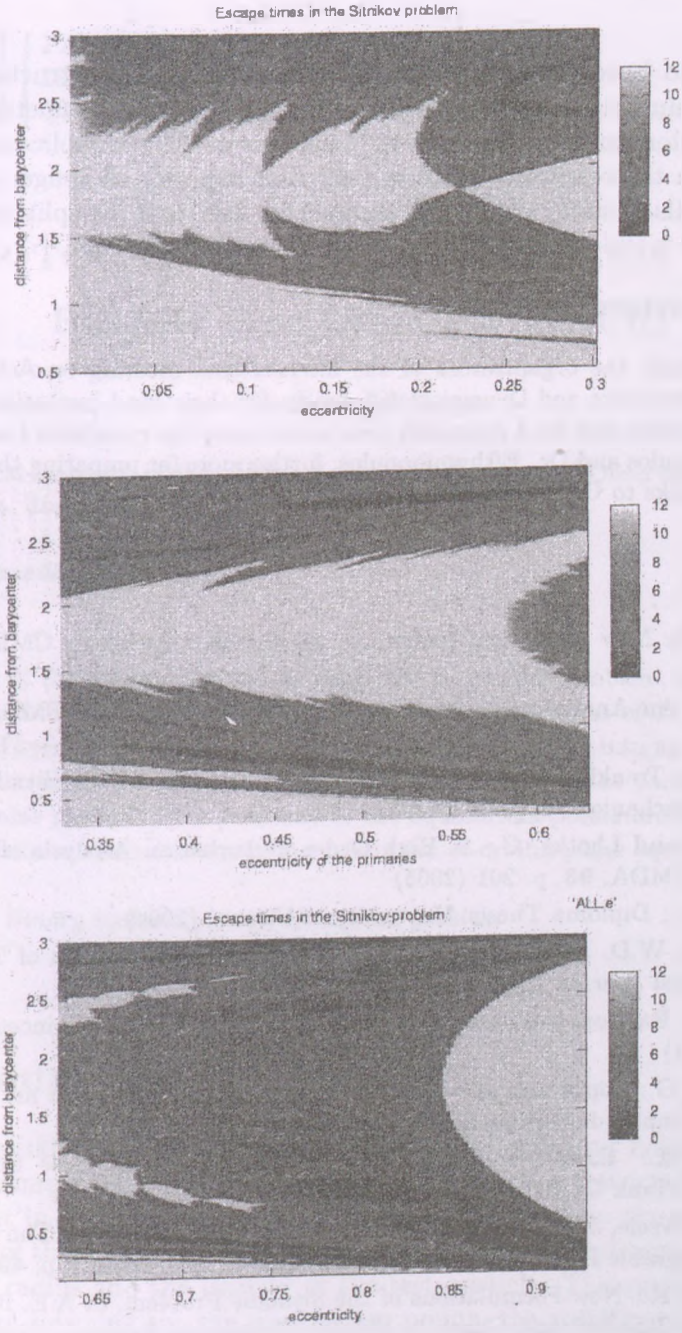

Figure 7: *Phase space structure of the Sitnikov problem: eccentricity versus distance of the third body;* $0 < e < 0.3$ *(top),* $0.33 < e < 0.66$ *(middle) and* $0.66 < e < 0.99$ *(bottom). Yellow marks stable orbits, red sticky ones, blue escapes and black very fast escapes.*

To be able to have a detailed picture of the phase space structure we have undertaken numerical integration for a fine grid in the parameter e and the initial condition on the z-axis for 10^6 time steps. The complicated structure was shown in the respective plots and discussed shortly. A longer paper going into the details of sticky orbits and escape channels, and the splitting of the 2:1 PO from the mainland using also analytical results is in work.

Acknowledgement

I specially thank the organizators of the international meeting on Actual Problems in Celestial Mechanics and Dynamical Astronomy for their kind invitation. For many fruitful discussions and for a computer code to calculate the manifolds I am grateful to Prof. Contopoulos and Dr. Efthymiopoulos; furthermore for preparing the manuscript I give my thanks to C. Lhotka from the ADG in Vienna.

References

[1] Dvorak, R: New Numerical Results to the Sitnikov Problem, CMDA **56**, p. 71 (1993)

[2] Hagel, J. An Analytical Approach to the Sitnikov Problem, CMDA **53**, p. 267 (1992)

[3] Hagel, J.; Trenkler, T.: A Computer-Aided Analysis of the Sitnikov Problem, Celestial Mechanics **56**, p. 81, (1993)

[4] Hagel, J. and Lhotka, C.: A High Order Perturbation Analysis of the Sitnikov Problem, CMDA, **93**, p. 201 (2005)

[5] Lhotka, C.: Diploma Thesis, University of Vienna, (2004)

[6] McMillan, W.D. An Integrable Case in the Restricted Problem of Three Bodies, Astronomical Journal **27**, p. 11 (1913)

[7] Moser, J.: Random and Stable Motion in Dynamical Systems, Princeton University Press (1973)

[8] Pavanini, G.: Sopra una nuova categoria di soluzione periodichi nel problema dei tre corpi, Annali di Mathematica, Serie III, Tomo XIII (1907)

[9] Sitnikov, K.: Existence of Oscillatory Motions for the Three Body Problem, Dokl.Akad.Nauk USSR, 133, p. 303 (1960)

[10] van der Weele, J. P., Capel, H. W., Valkering, T. P., Post, T.: The squeeze effect in non-integrable Hamiltonian systems Physica A, **147**, Issue 3, p. 499 (1988)

[11] Wodnar, K.: New Formulations of the Sitnikov Problem, in A.E. Roy (ed): Predictability, Stability and Chaos in N-Body Dynamical Systems, Plenum Press, p. 457 (1991)

PADEU | PADEU 19 (2007), p. 141
ISBN 963 463 557
©Published by the Astron. Dept. of the Eötvös Univ.

A PHOTOGRAVITATIONAL PROBLEM IN THE BINARY SYSTEM RW TAURI

Rodica Roman

Astronomical Institute of Romanian Academy, Astronomical Observatory of Cluj-Napoca, Romania

E-mail: rroman@math.ubbcluj.ro

Abstract
In the frame of the photogravitational restricted three-body problem, the binary system RW Tauri and a spherical ice test particle with the radius of 13.9 microns are considered. There are established the trajectory of the particle into an inertial frame and into the co-moving frame; the variation of the velocity of the particle (as a time function) is also plotted. The positions of the equilibrium points are calculated and the equipotential surface corresponding to the out-of-orbital-plane equilibrium points is plotted.
Keywords: *Binary system: photogravitational problem*

1 Introduction

From Radzievski (1953), to Simmons (1985) and Ragos and Zagouras (1994), many astronomers have studied the photogravitational restricted three-body problem. But in such a problem there are many parameters: the masses of the components of the binary system, the distance between components, their luminosities, the radius and the density of the test particle. The studies that have been done are referring to: the equilibrium points, the stability of the equilibrium points, the movement of the test particle in the vicinity of the equilibrium points, the existence of the out-of-the-orbital-plane equilibrium points.

In order to be able to study the role of the test particle in the photogravitational restricted three-body problem, in this paper is particularized: the binary system (RW Tauri) and the density of the test particle, by assuming it is an ice particle. So, a very concrete subject is put in discussion.

2 The problem

In the binary system RW Tauri (which is considered having a circular relative orbit) a spherical, ice particle is assumed. The radius of the particle is 13.9 microns. Considering that the only existing forces are the gravitational forces and the radiation pressures which act onto particle, we shall try to determine the following:

- The trajectory of the particle in the inertial reference frame.
- The trajectory of the particle in the co-moving reference frame.
- The length of the trajectory arc of the particle during an half of orbital period.
- The variation of the velocity of the particle in time, in the inertial frame.
- The equilibrium points of the particle.
- The equipotential surfaces corresponding to the equilibrium points.

In Figure 1 are represented the forces which act onto particle S_3; here S_1 and S_2 are the components of the binary system.

This problem can be studied in the frame of the restricted three-body problem, considering m_1 and m_2 the masses of the stellar components of the binary system and adopting an inertial reference frame, originated in the common mass center of m_1 and m_2.

The equations of movement of the test particle in the inertial frame are (Roman, 2003):

$$\frac{d^2X'}{dt^2} = -G\frac{(1-\beta_1)m_1}{r_1^3}(X'-X_1') - G\frac{(1-\beta_2)m_2}{r_2^3}(X'-X_2') \qquad (1)$$

$$\frac{d^2Y'}{dt^2} = -G\frac{(1-\beta_1)m_1}{r_1^3}(Y'-Y_1') - G\frac{(1-\beta_2)m_2}{r_2^3}(Y'-Y_2') \qquad (2)$$

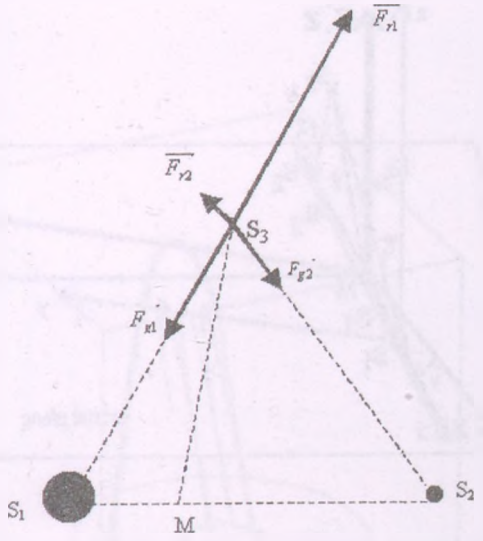

Figure 1: *The forces which act in the problem*

$$\frac{d^2Z'}{dt^2} = -G\frac{(1-\beta_1)m_1}{r_1^3}Z' - G\frac{(1-\beta_2)m_2}{r_2^3}Z' \tag{3}$$

where: $X_1' = -R_1\ cos\ v$, $X_2' = R_2\ cos\ v$,
$Y_1' = -R_1\ sin\ v$, $Y_2' = R_2\ sin\ v$,

and: $v = \omega_k\ t$.

Here G represents the Newtonian gravitational constant and ω_k is the angular keplerian velocity. In Figure 2 are represented the inertial frame $(MX'Y'Z')$ and the co-moving frame $(MXYZ)$ which is assumed to rotate synchronous with the rotation of S_1 and S_2, around the mass center M. The reference system $(Mxyz)$ is the co-moving reference frame used to obtain the equilibrium points. R_1 and R_2 are the distances from S_1 and S_2 to M and $\vec{S_1S_3} = \vec{r_1}$ and $\vec{S_2S_3} = \vec{r_2}$.

In equations (1), (2), (3) for the coefficients β_i we have: $\vec{F}_{ri} = \beta_i\vec{F}_{gi}$, with $i \in \{1,2\}$. Here β_i depends on the radius r_3 of the test particle and on its

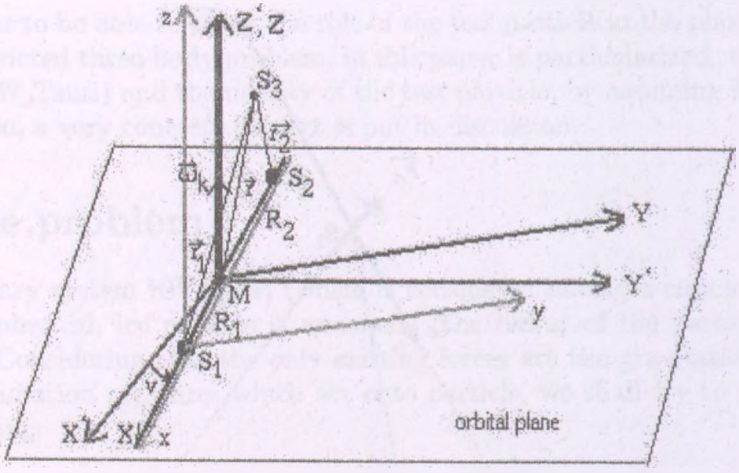

Figure 2: *The forces which act in the problem*

density ρ_3:

$$\beta_i = \frac{3\, l_i}{16\, \pi\, c\, G\, r_3\, \rho_3\, m_i}$$

where l_i, $i \in \{1, 2\}$ are the luminosities of the two components of the binary system and c represents the speed of light. The value $\beta_i = 0$ corresponds to the case when the radiation pressure is neglected. For our problem, considering the radiation pressure, $\beta_1 > 1$ and $\beta_2 < 1$, because the luminosity of S_1 is $l_1 = 66.6\ l_{Sun}$ and $l_2 = 3\ l_{Sun}$.

The trajectory of the particle is represented by using the inertial reference frame (Figure 3) and the co-moving reference frame (Figure 4).

The initial position is taken into the inner of the Roche lobe of the star S_1 and the initial velocity is assumed to be zero.

From equations (1), (2), (3), the length of the trajectory arc of the test particle, during a half of orbital period, is:

- without radiation pressure: $L = 3.000071376 * 10^{10}$ meters and if we consider the radiation pressure the length of the trajectory is: $L = 5.78291769 * 10^{10}$ meters.

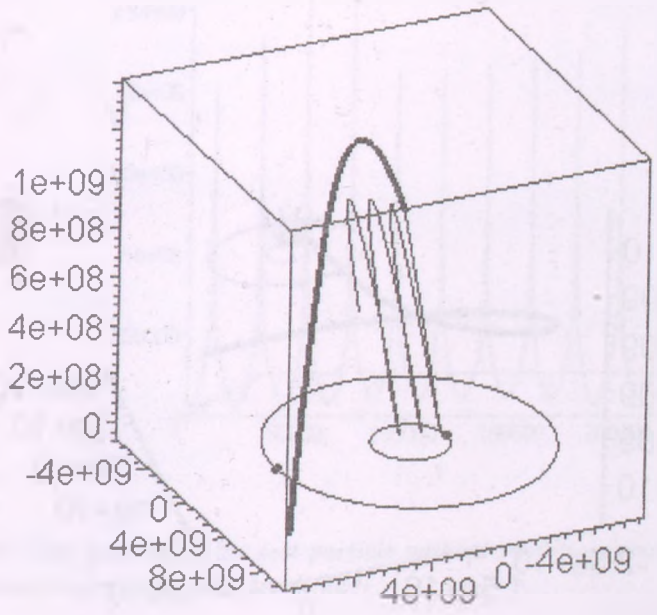

Figure 3: *Trajectories of the test particle into an inertial frame, without radiation pressure (thin line), and with radiation pressure (thick line), during 0.3* $P_{orbital}$

In Figure 5 is represented the variation of the velocity of the particle in time, in the inertial frame, during an orbital period. The curve with low amplitude correspond to the situation when the radiation pressure is considered.

In Figure 6 one can see the variation of the velocity of the test particle, considering the radiation pressure, for different initial positions, all these positions being considered into the Roche lobe of the star S_1.

As it is presented in Figure 7, the radius of the test particle has a very important role if the existence or the non existence of the equilibrium points out-of-the-orbital-plane is discussed. In our problem the radius of the test particle is 13.9 microns; so, in Figure 7 we can see that exists L_2 (into the orbital plane) and exist also equilibrium points out of the orbital plane. Simmons (1985)

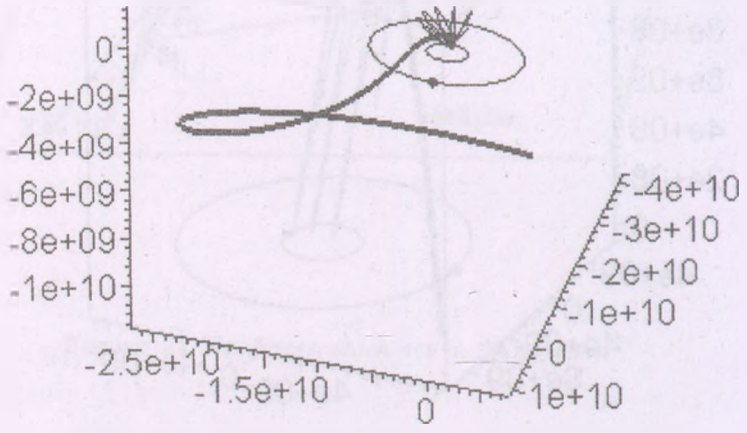

Figure 4: *Trajectories of the test particle into the co-moving frame,without radiation pressure (thin line), and with radiation pressure (thick line), during 0.7* $P_{orbital}$

postulated that if out-of-the-orbital-plan equilibrium points exist, there are 1 or 2 couples. In our problem only one couple of such equilibrium points exist (L_6 and L_7), situated in the vicinity of the Mz axe.

The coordinates of the equilibrium points are:

$$L_2(1.27014\,;\ 0\,;\ 0),\quad L_6(-0.1702\,;\ 0\,;\ -0.3229),\quad L_7(-0.1702\,;\ 0\,;\ +0.3229)$$

and the equilibrium surfaces corresponding to these equilibrium points are represented in Figure 8.

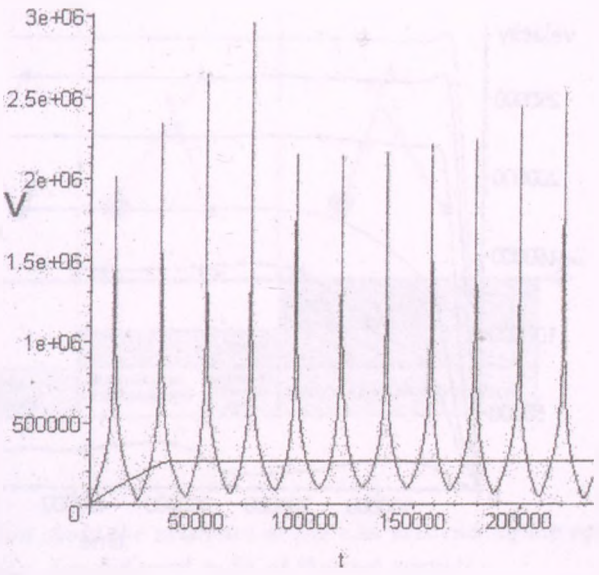

Figure 5: *The velocity of the test particle without radiation pressure and with radiation pressure (curve with low amplitude)*

3 Conclusion

If the radiation pressure is greater than the gravitational pressure, the role of the test particle in the photogravitational restricted three-body problem become very important. Taken a suitable value for the radius of the test particle, we can learn many things about the influence of the radiation pressure on the trajectory of the test particle, on his velocity and on the shape of the equipotential surfaces corresponding to the equilibrium points.

Acknowledgement

The author is grateful to assistant Radu Zapotinschi for his support with computing.

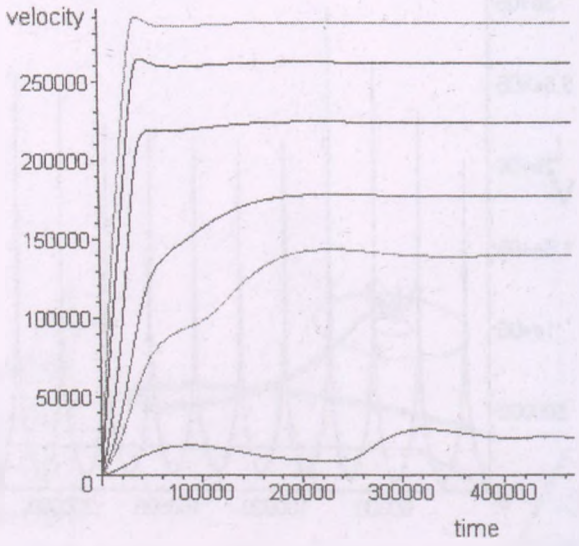

Figure 6: *The variation of the velocity of the test particle considering the radiation pressure, for different initial positions; the closer is the particle from the binary system, the higher is his velocity*

References

Moulton, F.R. 1923, An introduction to celestial mechanics, Second Edition, The Macmillan Company, New York

Radzievsky, V.V., 1953, Astron. J. Soviet Union, 33, 265

Ragos, O., Zagouras, C., 1994, Astrophys Space Sci. 209, 267

Roman, R., 2003, Modelul Roche la stele duble, Ed. Casa Cărţii de Ştiinţă, Cluj

Simon, V., 1997, Astron. Astrophys. 319, 886

Simmons, J.F.L., McDonald, A.J.C., Brown, J.C. 1985, Celestial Mechanics, 35, 145

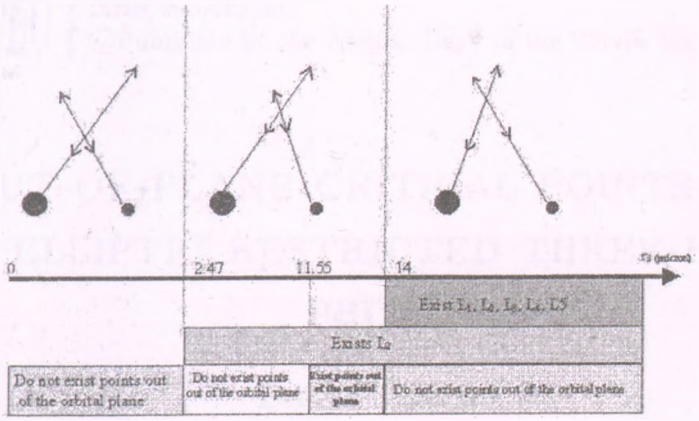

Figure 7: *Discussion about the existence or the non existence of the equilibrium points out of the orbital plan, for different radii of the test particle*

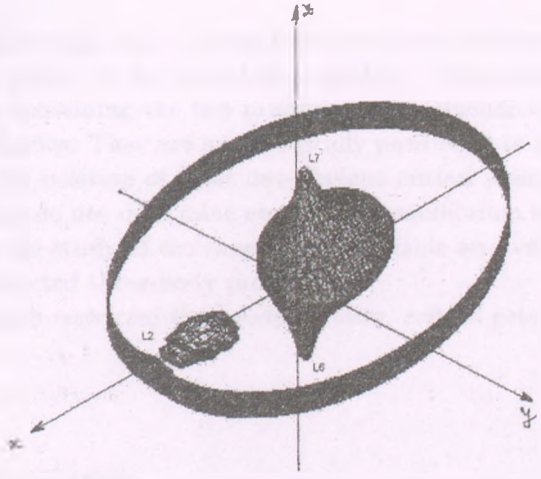

Figure 8: *The equipotential surfaces which correspond to L_2, L_6 and L_7 and the coordinates axes*

PADEU | PADEU **19** (2007), p. 151
ISBN 963 463 557
©Published by the Astron. Dept. of the Eötvös Univ.

Out-of-plane critical points in the elliptic restricted three-body problem

Ferenc Szenkovits

Babeş-Bolyai University, Department of Applied Mathematics, RO-400048 Cluj-Napoca, Kogalniceanu 1, Romania
Eötvös University, Department of Astronomy, Pázmány Péter sétány 1/A, 1117 Budapest, Hungary

E-mail: fszenko@math.ubbcluj.ro

Abstract
In the three-dimensional elliptic restricted three-body problem the existence of out-of-plane critical points of the potential is proved. These critical points lie in the coordinate plane containing the two primaries and perpendicular to the plane of rotation of the primaries. They are symmetrically positioned to the axis containing the two primaries. The position of these out-of-plane critical points depends on the true anomaly, thus they do not determine new relative equilibrium solutions. These points are important in the study of the shape of the variable zero velocity surfaces existing in the elliptic restricted three-body problem.
Keywords: *Elliptic restricted three-body problem, critical points.*

1 Introduction

The elliptic restricted three-body problem (ERTBP) describes the three-dimensional motion of a small particle under the gravitational attraction of two bodies (the primaries), which describe elliptic orbits in a plane around the centre of mass. Szebehely and Giacaglia (1964) obtained in the planar ERTBP a simple

form of the equations of motion – similar to that in the case of the circular restricted three-body problem – by using the true anomaly of the primaries as the independent variable and by introducing a special set of dimensionless variables describing the position of the third body. They also deduced an invariant relation, the generalization of the Jacobi integral, known in the circular restricted three-body problem, and proved the pulsation of the zero velocity curves in the planar case.

In the case of the planar ERTBP five critical points of the potential Ω are known, corresponding to relative equilibrium solutions. They are the same known in the circular restricted three-body problem, the so called Lagrangian points: L_1, L_2, L_3 collinear with the two primaries, and L_4, L_5 the triangular points, which form equilateral triangles with the primaries.

Many authors studied the stability of these relative equilibria and different aspects regarding the motions around these points. The first results concerning this problem are presented in Danby (1964), who computed the linear stability of the orbits around L_4. Györgyey (1984) made investigations regarding the nonlinear stability of motions around L_5. Meire established results relating to the stability regions in the $\mu - e$ plane of the triangular points in the elliptic restricted three-body problem (Meire, 1980, 1981, 1982). Simó (1992) studied stability zones around triangular libration points in the 3D elliptic restricted three-body problems. Evteev (1993) established bifurcation properties of the collinear libration points. In connection with the stability study of the triangular Lagrngian points Lohinger and Dvorak (1993) analysed the extension of the stable regions around these equilibrium points. They determined the stable regions depending on two parameters, the mass ratio μ and the orbital eccentricity e of the primaries.

By using the model of the ERTBP, dynamics of different families of celestial bodies can be studied. Resonant families of periodic orbits were calculated for the Sun-Jupiter-asteroid system and different aspects of these orbits were studied by Dvorak (1992), Hadjidemetriou (1992), Liao and Saari (1998), and Sidorenko (2006). Kotoulas (2005) investigated the planar and the three-dimensional 1:2 resonant motion with Neptune in the framework of the ERTBP. Ollé and Pacha (1999) and Palacián et al. (2006) calculated families of periodic orbits of the spatial ERTBP.

Sándor and Érdi (2003) developed a symplectic mapping for Trojan-type motion in the secularly changing ERTBP. By using this mapping they studied the boundary of the stability region for different values of the initial eccentricities of hypothetical Jupiter's Trojans.

Dvorak (1986), Benest (1988, 1989, 1996, 1998, 2003) and Pilat-Lohinger et

al. (2003) treated the problem of the stability of planetary orbits in double stars with the aid of numerical studies in the model of the ERTBP. Érdi and Sándor (2005) investigated the stability of co-orbital motions in such exoplanetary systems, where the only known giant planet either moves fully in the habitable zone, or leaves it for some part of its orbit. Domingos et al. (2006) studied the stability of hypothetical satellites of extrasolar planets through numerical simulations of the ERTBP. Their results indicate that extrasolar planets in the habitable zone could harbour Earth-like satellites.

Palacián and Yanguas (2006) studied the spatial restricted three-body problem in the case where the small particle is far from the primaries, that is, the so-called comet case.

Many authors have performed qualitative studies in the ERTBP, mainly oriented to find new integrals of the equations of motion. Starting from the integrals of the general three-body problem (expressed in non-uniformly rotating rectangular coordinates), Ovenden and Roy (1961) obtained formal expressions for the Jacobi integral and the angular momentum integrals of the ERTBP in terms of certain auxiliary functions. Using these expressions they concluded that "the Jacobi integral of the CRTBP for long-term predictions in any real case where the two massive bodies' relative orbit has a finite eccentricity (however small) is without justification even if the mass of the third body is infinitesimal". Dvorak (1977) continued these studies considering the existence of the Jacobi integral in the elliptic restricted three-body problem. Pál and Oproiu (1991) starting from Rein's 'semiaveraging' scheme of the elliptic restricted three-body problem (according to Mojseev's classification), determined the slopes of the 'zero relative velocity' curves in the libration point L_1, for different values of the eccentricity e and of the mass ratio μ.

Contopoulos (1967) deduced two integrals of motion in the plane ERTBP for orbits with small eccentricity near the primaries. These integrals, given in the form of formal series, depend periodically on the time, with frequency equal to that of the second body.

Vrcelj et al. (1978) derived an invariant relation – containing also a nonintegrable term – generalizing the Jacobi integral to the ERTBP on the basis of the classical perturbation theory and by making use of the energy and angular momentum integrals. This invariant relation was reduced and applied to calculate the Jacobi constant for asteroids (Vrcelj et al., 1978a; Vrcelj, 1979) .

Makó and Szenkovits (2004) generalized Szebehely's (Szebehely, 1967) result concerning the pulsating Hill's regions to the spatial ERTBP. By using the obtained invariant relation, they deduced necessary conditions of the gravitational capture of small bodies, in case of small eccentricities of the primaries

and bounded motion of the test particle. Some properties of these variable Hill-regions were studied in Szenkovits and Makó (2005).

The problem of gravitational capture was studied by using the model of the ERTBP in case of irregular moons by Astakhov and Farrelly (2004).

As we have seen, in the planar case of the ERTBP the Lagrangian equilibrium points play a central role. The aim of this paper is to clarify the problem of existence of out-of-plane equilibrium points in the case of the spatial ERTBP. The existence of two new critical points of the potential Ω is proved, when the true anomaly satisfies the condition $f \in \left(\frac{\pi}{2}, \frac{3\pi}{2}\right)$. The position of these points depends on the value of the true anomaly f, so these points are no longer (relative) equilibrium points. These critical points play an important role in the study of the topological type of the variable zero velocity surfaces in the ERTBP.

2 The elliptic retricted problem

In the elliptic restricted three-body problem (ERTBP) two massive primaries (planetary objects) P_1 and P_2, with masses m_1 and m_2 revolve on elliptical orbits under their mutual gravitational attraction and the motion of a third, massless body $P_3, (m_3 = 0)$ is studied. The orbit of P_2 around P_1, in an inertial system is

$$\rho = \frac{a\left(1-e^2\right)}{1+e\cos f}, \tag{1}$$

where ρ is the mutual distance, a and e are the semimajor axis and the eccentricity of the elliptical orbit $(e < 1)$, and f is the true anomaly.

In our study a nonuniformly rotating and pulsating coordinate system is used. In this system of reference the origin O is in the center of mass of the two massive primaries, and the $\bar{\xi}$ axis is directed towards m_2. The $\bar{\xi}\bar{\eta}$ coordinate-plane rotates with variable angular velocity, in such a way that the two massive primaries are always on the $\bar{\xi}$ axis, and the period of the rotation is 2π. Besides the rotation, the system also pulsates, to keep the primaries in fixed positions: $\bar{\xi}_1 = -\mu, \bar{\eta}_1 = \bar{\zeta}_1 = 0, \bar{\xi}_2 = 1-\mu, \bar{\eta}_2 = \bar{\zeta}_2 = 0$, where $\mu = \frac{m_2}{m_1+m_2}$ is the mass parameter .

In this system of coordinates the equations of motion of the third massless

particle are (see e.g. Szebehely (1967), p. 594):

$$\begin{cases} \tilde{\xi}'' - 2\tilde{\eta}' = \frac{\partial \omega}{\partial \tilde{\xi}}, \\ \tilde{\eta}'' + 2\tilde{\xi}' = \frac{\partial \omega}{\partial \tilde{\eta}}, \\ \tilde{\zeta}'' = \frac{\partial \omega}{\partial \tilde{\zeta}}, \end{cases} \tag{2}$$

where the derivatives are taken with respect to the true anomaly f, and

$$\omega = (1 + e\cos f)^{-1}\,\Omega,$$

with

$$\Omega = \tfrac{1}{2}\left(\tilde{\xi}^2 + \tilde{\eta}^2 - e\tilde{\zeta}^2\cos f\right) + \frac{1-\mu}{\sqrt{\left(\tilde{\xi}+\mu\right)^2+\tilde{\eta}^2+\tilde{\zeta}^2}} + \tag{3}$$
$$+ \frac{\mu}{\sqrt{\left(\tilde{\xi}-1+\mu\right)^2+\tilde{\eta}^2+\tilde{\zeta}^2}} + \tfrac{1}{2}\mu(1-\mu).$$

Performing the same operations, which in the restricted three-body problem leads to the Jacobi-integral, in the case of the spatial ERTBP Makó and Szenkovits (2004) derived the invariant relation:

$$\left(\frac{d\tilde{\xi}}{df}\right)^2 + \left(\frac{d\tilde{\eta}}{df}\right)^2 + \left(\frac{d\tilde{\zeta}}{df}\right)^2 = 2\omega - e\int_{f_0}^{f} \frac{\tilde{\zeta}^2 \sin h}{1+e\cos h}dh - \tag{4}$$
$$-2e\int_{f_0}^{f} \frac{\Omega \sin h}{(1+e\cos h)^2}dh - C_0,$$

which is the generalization of Szebehely's invariant relation (Szebehely (1967), p. 595) for the spatial ERTBP. Unfortunately (4) is not an integral of motion, because it contains not only functions of the coordinates and velocities (and the true anomaly f) at any point of the orbit, but it depends also on the values of these quantities along the whole arc of the orbit from the initial position up to a given position. The value of the Jacobi constant C_0 can be calculated at the initial moment $t = t_0$, when $f = f_0$ and when the two integral terms in (4) are vanishing:

$$C_0 = 2\omega\left(\tilde{\xi}_0, \tilde{\eta}_0, \tilde{\zeta}_0, f_0\right) - \left[\left(\frac{d\tilde{\xi}}{df}\right)^2 + \left(\frac{d\tilde{\eta}}{df}\right)^2 + \left(\frac{d\tilde{\zeta}}{df}\right)^2\right]_{f=f_0}. \tag{5}$$

In a recent paper Szenkovits and Makó (2005) studied the properties of the pulsating zero velocity surfaces (ZVS) in the ERTBP, given by the equation:

$$\frac{2\Omega}{1+e\cos f} - e\int_{f_0}^{f} \frac{\bar{\zeta}^2 \sin h}{1+e\cos h}dh - 2e\int_{f_0}^{f} \frac{\Omega \sin h}{(1+e\cos h)^2}dh = C_0. \qquad (6)$$

These surfaces delimite the Hill's regions, in which the motion of the third particle is possible.

The expression of Ω in the $\bar{\xi}\bar{\eta}$ plane is

$$\Omega_0 = \frac{1}{2}\left(\bar{\xi}^2+\bar{\eta}^2\right) + \frac{1-\mu}{\sqrt{\left(\bar{\xi}+\mu\right)^2+\bar{\eta}^2}} + \frac{\mu}{\sqrt{\left(\bar{\xi}-1+\mu\right)^2+\bar{\eta}^2}} + \frac{1}{2}\mu(1-\mu), \quad (7)$$

identical with the similar potential used in the case of the circular restricted three-body problem (CRTBP). The critical points of Ω_0 are the so called Lagrange-points, the collinear points:

$$L_1\left(\bar{\xi}_1,0\right), L_2\left(\bar{\xi}_2,0\right), L_3\left(\bar{\xi}_3,0\right),$$

where

$$\bar{\xi}_3 < -\mu < \bar{\xi}_2 < 1-\mu < \bar{\xi}_1,$$

and the triangular points $L_4\left(\frac{1}{2}-\mu, \sqrt{3}/2\right)$ and $L_5\left(\frac{1}{2}-\mu, -\sqrt{3}/2\right)$, with the same critical values:

$$C_4 = C_5 < C_3 = 3 < C_1 < C_2. \qquad (8)$$

These critical points of Ω_0 are also the relative equilibrium points in the restricted three-body problem, and in the planar ERTBP too. The variation of the topological type of the ZVS in the ERTBP pointed aut in Szenkovits and Makó (2005) shows the exixtence of out-of-plane critical points of Ω.

3 Out-of-plane critical points of Ω

The explicit form of the system

$$\frac{\partial\Omega}{\partial\bar{\xi}} = 0, \frac{\partial\Omega}{\partial\bar{\eta}} = 0, \frac{\partial\Omega}{\partial\bar{\zeta}} = 0$$

which gives the critical points of Ω in the $\left(\bar{\xi},\bar{\eta},\bar{\zeta}\right)$ space is:

$$\begin{cases} \tilde{\xi} - \dfrac{(1-\mu)(\tilde{\xi}+\mu)}{\left(\sqrt{(\tilde{\xi}+\mu)^2+\tilde{\eta}^2+\tilde{\zeta}^2}\right)^3} - \dfrac{\mu(\tilde{\xi}-1+\mu)}{\left(\sqrt{(\tilde{\xi}-1+\mu)^2+\tilde{\eta}^2+\tilde{\zeta}^2}\right)^3} = 0, \\ \tilde{\eta}\left(1 - \dfrac{(1-\mu)}{\left(\sqrt{(\tilde{\xi}+\mu)^2+\tilde{\eta}^2+\tilde{\zeta}^2}\right)^3} - \dfrac{\mu}{\left(\sqrt{(\tilde{\xi}-1+\mu)^2+\tilde{\eta}^2+\tilde{\zeta}^2}\right)^3}\right) = 0, \\ \tilde{\zeta}\left(e\cos f + \dfrac{(1-\mu)}{\left(\sqrt{(\tilde{\xi}+\mu)^2+\tilde{\eta}^2+\tilde{\zeta}^2}\right)^3} + \dfrac{\mu}{\left(\sqrt{(\tilde{\xi}-1+\mu)^2+\tilde{\eta}^2+\tilde{\zeta}^2}\right)^3}\right) = 0. \end{cases} \tag{9}$$

If $\tilde{\zeta} = 0$, the potential Ω is reduced to Ω_0, given in (7) the potential used in the planar restricted three-body problem, which leads to the well known Lagrangian equilibrium points.

If $\tilde{\zeta} \neq 0$, the system (9) giving the critical points is:

$$\begin{cases} \tilde{\xi} - \dfrac{(1-\mu)(\tilde{\xi}+\mu)}{\left(\sqrt{(\tilde{\xi}+\mu)^2+\tilde{\eta}^2+\tilde{\zeta}^2}\right)^3} - \dfrac{\mu(\tilde{\xi}-1+\mu)}{\left(\sqrt{(\tilde{\xi}-1+\mu)^2+\tilde{\eta}^2+\tilde{\zeta}^2}\right)^3} = 0, \\ \tilde{\eta}\left(1 - \dfrac{(1-\mu)}{\left(\sqrt{(\tilde{\xi}+\mu)^2+\tilde{\eta}^2+\tilde{\zeta}^2}\right)^3} - \dfrac{\mu}{\left(\sqrt{(\tilde{\xi}-1+\mu)^2+\tilde{\eta}^2+\tilde{\zeta}^2}\right)^3}\right) = 0, \\ e\cos f + \dfrac{(1-\mu)}{\left(\sqrt{(\tilde{\xi}+\mu)^2+\tilde{\eta}^2+\tilde{\zeta}^2}\right)^3} + \dfrac{\mu}{\left(\sqrt{(\tilde{\xi}-1+\mu)^2+\tilde{\eta}^2+\tilde{\zeta}^2}\right)^3} = 0. \end{cases} \tag{10}$$

The main result of our paper can be formulated in the next:

Theorem. *The potential Ω of the ERTBP admits two critical points $L_6\left(\tilde{\xi}_6, 0, \tilde{\zeta}_6\right)$ and $L_7\left(\tilde{\xi}_7, 0, \tilde{\zeta}_7\right)$, $(\tilde{\xi}_6 = \tilde{\xi}_7, \tilde{\zeta}_7 = -\tilde{\zeta}_6)$ in the $\tilde{\xi}\tilde{\zeta}$ plane if and only if $f \in \left(\frac{\pi}{2}, \frac{3\pi}{2}\right)$.*

Proof. i) If $\tilde{\zeta} \neq 0$ and $\tilde{\eta} \neq 0$, the sysem (10) is equivalent with

$$\begin{cases} \tilde{\xi} - \dfrac{(1-\mu)(\tilde{\xi}+\mu)}{\left(\sqrt{(\tilde{\xi}+\mu)^2+\tilde{\eta}^2+\tilde{\zeta}^2}\right)^3} - \dfrac{\mu(\tilde{\xi}-1+\mu)}{\left(\sqrt{(\tilde{\xi}-1+\mu)^2+\tilde{\eta}^2+\tilde{\zeta}^2}\right)^3} = 0, \\ 1 - \dfrac{(1-\mu)}{\left(\sqrt{(\tilde{\xi}+\mu)^2+\tilde{\eta}^2+\tilde{\zeta}^2}\right)^3} - \dfrac{\mu}{\left(\sqrt{(\tilde{\xi}-1+\mu)^2+\tilde{\eta}^2+\tilde{\zeta}^2}\right)^3} = 0, \\ e\cos f + \dfrac{(1-\mu)}{\left(\sqrt{(\tilde{\xi}+\mu)^2+\tilde{\eta}^2+\tilde{\zeta}^2}\right)^3} + \dfrac{\mu}{\left(\sqrt{(\tilde{\xi}-1+\mu)^2+\tilde{\eta}^2+\tilde{\zeta}^2}\right)^3} = 0, \end{cases} \tag{11}$$

from where, by using the second and the third equations, condition $e\cos f = -1$ results, which is impossible, because of $e < 1$. This means that for $\tilde{\zeta} \neq 0$ and $\tilde{\eta} \neq 0$ the potential Ω does not admits critical points.

ii) In the case of $\tilde{\zeta} \neq 0$ and $\tilde{\eta} = 0$, the system (10) is equivalent with

$$\begin{cases} \tilde{\xi} - \dfrac{(1-\mu)(\tilde{\xi}+\mu)}{\left(\sqrt{(\tilde{\xi}+\mu)^2+\tilde{\zeta}^2}\right)^3} - \dfrac{\mu(\tilde{\xi}-1+\mu)}{\left(\sqrt{(\tilde{\xi}-1+\mu)^2+\tilde{\zeta}^2}\right)^3} = 0, \\ e\cos f + \dfrac{(1-\mu)}{\left(\sqrt{(\tilde{\xi}+\mu)^2+\tilde{\zeta}^2}\right)^3} + \dfrac{\mu}{\left(\sqrt{(\tilde{\xi}-1+\mu)^2+\tilde{\zeta}^2}\right)^3} = 0, \end{cases} \tag{12}$$

or

$$\begin{cases} \tilde{\xi}(1+e\cos f) - \dfrac{(1-\mu)\mu}{\left(\sqrt{(\tilde{\xi}+\mu)^2+\tilde{\zeta}^2}\right)^3} + \dfrac{\mu(1-\mu)}{\left(\sqrt{(\tilde{\xi}-1+\mu)^2+\tilde{\zeta}^2}\right)^3} = 0, \\ e\cos f + \dfrac{(1-\mu)}{\left(\sqrt{(\tilde{\xi}+\mu)^2+\tilde{\zeta}^2}\right)^3} + \dfrac{\mu}{\left(\sqrt{(\tilde{\xi}-1+\mu)^2+\tilde{\zeta}^2}\right)^3} = 0. \end{cases} \tag{13}$$

We can observe that the second equation of (13) does not admits solutions for $e\cos f \geq 0$. This means that if $f \in \left[-\frac{\pi}{2}, \frac{\pi}{2}\right]$, there are no critical points out of the coordinate plane $\tilde{\xi}\tilde{\eta}$.

Let now $f \in \left(\frac{\pi}{2}, \frac{3\pi}{2}\right)$ and denote in this case $e\cos f = -\alpha \in (-e, 0), \alpha \in (0, e) \subset (0, 1)$. In this case the system (12) can be transformed equivalently to:

$$\begin{cases} \dfrac{1-\mu}{\left(\sqrt{(\tilde{\xi}+\mu)^2+\tilde{\zeta}^2}\right)^3} = (1-\alpha)\tilde{\xi} + \alpha(1-\mu), \\ \dfrac{\mu}{\left(\sqrt{(\tilde{\xi}+\mu-1)^2+\tilde{\zeta}^2}\right)^3} = (\alpha-1)\tilde{\xi} + \alpha\mu. \end{cases} \tag{14}$$

From the system (14) we can derive the next conditions for the $\tilde{\xi}$ coordinate of the possible critical points:

$$\begin{cases} (1-\alpha)\tilde{\xi} + \alpha(1-\mu) > 0, \\ (\alpha-1)\tilde{\xi} + \alpha\mu > 0, \end{cases} \tag{15}$$

or

$$\frac{\alpha\mu - \alpha}{1-\alpha} < \tilde{\xi} < \frac{\alpha\mu}{1-\alpha}. \tag{16}$$

With respect to the conditions (16), system (14) can be transformed equivalently into:

$$\begin{cases} \left(\tilde{\xi}+\mu\right)^2+\tilde{\zeta}^2=\sqrt[3]{\frac{(1-\mu)^2}{\left[(1-\alpha)\tilde{\xi}+\alpha(1-\mu)\right]^2}}, \\ \left(\tilde{\xi}+\mu-1\right)^2+\tilde{\zeta}^2=\sqrt[3]{\frac{\mu^2}{\left[(\alpha-1)\tilde{\xi}+\alpha\mu\right]^2}}. \end{cases} \tag{17}$$

Eliminating $\tilde{\zeta}^2$ from this system, we obtain the equation

$$2\tilde{\xi}+2\mu-1=\sqrt[3]{\frac{(1-\mu)^2}{\left[(1-\alpha)\tilde{\xi}+\alpha(1-\mu)\right]^2}}-\sqrt[3]{\frac{\mu^2}{\left[(\alpha-1)\tilde{\xi}+\alpha\mu\right]^2}}, \tag{18}$$

which gives the $\tilde{\xi}$ coordinate of the possible out-of-$\tilde{\xi}\tilde{\eta}$-plane critical points of Ω.

Introducing the notations

$$a=\frac{1-\mu}{1-\alpha}, \qquad b=\frac{\mu}{1-\alpha}, \tag{19}$$

for which

$$a+b=\frac{1}{1-\alpha}, \qquad a,b>0,$$

equation (18) is equivalent with

$$2\tilde{\xi}+2\mu-1=\sqrt[3]{\frac{a^2}{\left(\tilde{\xi}+\alpha a\right)^2}}-\sqrt[3]{\frac{b^2}{\left(\tilde{\xi}-\alpha b\right)^2}}, \tag{20}$$

where $\tilde{\xi}$ satisfies the conditions $-\alpha a<\tilde{\xi}<\alpha b$.

Considering the function $f_1:(-\alpha a,\alpha b)\to R$, $f_1\left(\tilde{\xi}\right)=2\tilde{\xi}+2\mu-1$, defined with the left hand side expression of equation (20), a function strictly incrasing and bounded, and at the other side the function $f_2:(-\alpha a,\alpha b)\to R$, $f_2\left(\tilde{\xi}\right)=\sqrt[3]{\frac{a^2}{\left(\tilde{\xi}+\alpha a\right)^2}}-\sqrt[3]{\frac{b^2}{\left(\tilde{\xi}-\alpha b\right)^2}}$, a strictly decreasing function, with infinite limits $f_2\left(-\alpha a+0\right)=+\infty$, $f_2\left(\alpha b-0\right)=-\infty$, we can conclude that equation (20) admits exactly one solution.

This solution can be determinated by using numerical approximations.

If $\tilde{\xi}$ is determined, the corresponding $\tilde{\zeta}$ coordinates of the critical points

resulting from (17) are given by:

$$\tilde{\zeta} = \pm \left(\sqrt[3]{\frac{(1-\mu)^2}{\left[(1-\alpha)\,\tilde{\xi} + \alpha\,(1-\mu)\right]^2}} - \left(\tilde{\xi} + \mu\right)^2 \right)^{\frac{1}{2}}. \tag{21}$$

We can conclude that out of the plane $\tilde{\xi}\tilde{\eta}$ there are exactly two critical points, for every $f \in \left(\frac{\pi}{2}, \frac{3\pi}{2}\right)$. These critical points lie in the $\tilde{\xi}\tilde{\zeta}$ coordinate plane, and they are simmetrically positioned to the $\tilde{\xi}$ axis: $L_6\left(\bar{\xi}_6, 0, \bar{\zeta}_6\right)$ and $L_7\left(\bar{\xi}_7, 0, \bar{\zeta}_7\right)$, where $\bar{\xi}_6 = \bar{\xi}_7$ is the unique solution of the equation (20), $\bar{\zeta}_6 > 0$ and $\bar{\zeta}_7 = -\bar{\zeta}_6$ can be calculated as function of $\bar{\xi}_6 = \bar{\xi}_7$ by using (21).

The $\bar{\xi}$ and $\bar{\zeta}$ coordinates of the critical points L_6 and L_7 are solutions of the system (12). In consequence they depend on the true anomaly f, i.e. they are not (relative) equilibrium points. This is a consequence of the fact that the system (2) is not autonomous.

The variation of $\bar{\xi}_6$ and $\bar{\zeta}_6$ as funtion of $f \in \left(\frac{\pi}{2}, \frac{3\pi}{2}\right)$ is illustrated in Fig. 1. It is clear that because of the dependence of $\bar{\xi}_6$ and $\bar{\zeta}_6$ only on $\cos f$ (see system 12), these coordinates verify the symmetry properties:

$$\bar{\xi}_6\,(\pi - \varphi) = \bar{\xi}_6\,(\pi + \varphi), \quad \bar{\zeta}_6\,(\pi - \varphi) = \bar{\zeta}_6\,(\pi + \varphi), \qquad \forall \varphi \in \left(0, \frac{\pi}{2}\right),$$

where $\bar{\zeta}_6\,(\pi - \varphi)$ denotes the value of $\bar{\zeta}_6$ when $f = \pi - \varphi$.

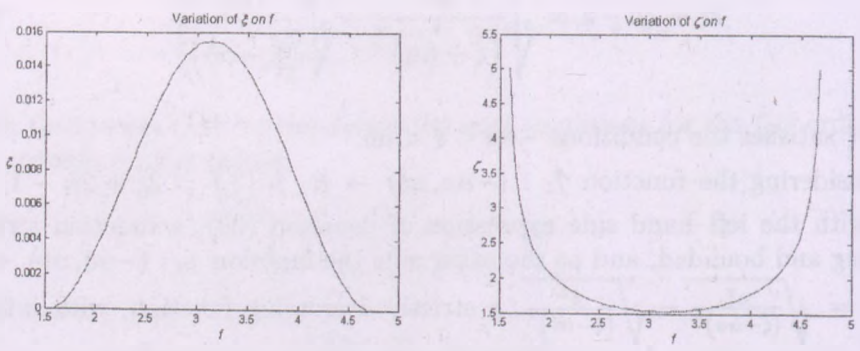

Figure 1: *Variation of* $\bar{\xi}_6$ *and* $\bar{\zeta}_6$ *when* $f \in \left(\frac{\pi}{2}, \frac{3\pi}{2}\right), e = 0.5, \mu = 0.5$

The position of the critical point L_6 in the $\tilde{\xi}\tilde{\zeta}$-plane depending on $f \in \left(\frac{\pi}{2}, \pi\right)$ is plotted in Fig. 2.

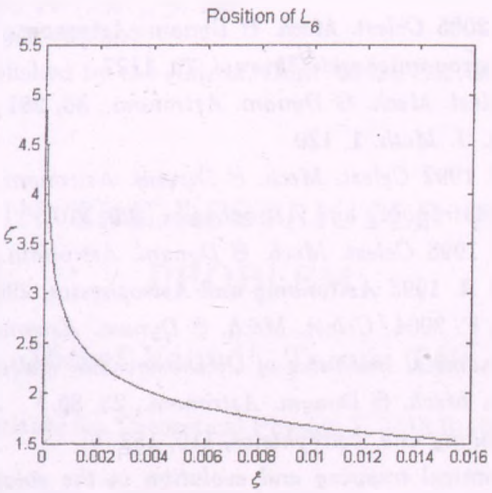

Figure 2: *Position of L_6 in the $\tilde{\xi}\tilde{\zeta}$ plane, when $f \in \left(\frac{\pi}{2}, \pi\right), e = 0.5, \mu = 0.5$*

Acknowledgement

The support of the Hungarian Academy of Science under the grant Bolyai BO/00003/04 is acknowledged.

References

Astakhov, S. A., Farrelly, D. 2004 *MNRAS*, 354, 971

Benest, D. 1988 *Astronomy and Astrophysics,* 206, 143

Benest, D. 1989 *Astronomy and Astrophysics,* 223, 361

Benest, D 1996. *Astronomy and Astrophysics,* 314, 983

Benest, D. 1998 *Astronomy and Astrophysics,* 332, 1147

Benest, D. 2003 *Astronomy and Astrophysics*, 400, 1103

Contopoulos, G. 1967, *The Astronomical Journal*, 72, 669

Danby, J.M.A. 1964, *The Astronomical Journal* 69, 165

Domingos, R. C.; Winter, O. C.; Yokoyama, T. 2006 *Monthly Notices of the Royal Astronomical Society*, 373, 1227

Dvorak, R. 1977 *Astronomische Gesellschaft, Mitteilungen*, 42, 75

Dvorak, R. 1986 *Astronomy and Astrophysics,* 167, 379

Dvorak, R. 1992 *Celest. Mech. & Dynam. Astronom.*, 54, 195

Érdi, B., Sándor, Zs. 2005 *Celest. Mech. & Dynam. Astronom.*, 92, 113

Evteev, V. P. 1993 *Astronomicheskii Zhurnal*, 70, 1127

Györgyey, J. 1985 *Celest. Mech. & Dynam. Astronom.*, 36, 281

Hill, G. W. 1878, *Am. J. Math.* 1, 129

Hadjidemetriou, J. D. 1992 *Celest. Mech. & Dynam. Astronom.*, 53, 151

Kotoulas, T.A. 2005 *Astronomy and Astrophysics*, 429,.1107

Liao, X., Saari, D. G. 1998 *Celest. Mech. & Dynam. Astronom.*, 70, 23

Lohinger, E.; Dvorak, R. 1993 *Astronomy and Astrophysics*, 280, 683

Makó, Z., Szenkovits, F. 2004, *Celest. Mech. & Dynam. Astronom.* 90, 51

Meire, R. 1980 *Astronomical Institutes of Czechoslovakia, Bulletin*, 31, 312

Meire, R. 1981 *Celest. Mech. & Dynam. Astronom.*, 23, 89

Meire, R. 1982 *Astronomy and Astrophisics*, 110, 152

Meire, R. 1983 *Dynamical trapping and evolution in the solar system; Proceedings of the Seventy-fourth Colloquium*, Gerakini, Greece, August 30-September 2, 1982 (A84-34976 16-89). Dordrecht, D. Reidel Publishing Co., p. 289

Ollé, M., Pacha, J. R. 1999 *Astronomy and Astrophysics*, 351, 1149

Ovenden, M. W., Roy, A. E. 1961, *Mon. Not. R. Astron. Soc.*, 123, 1

Pál, Á., Oproiu, T. 1991 *Romanian Astronomical Journal*, 1, 97

Palacián, J. F.; Yanguas, P., Fernández, S, Nicotra, M.A. 2006: *Phys. D* 213, 15

Palacián, J. F.; Yanguas, P. 2006 *Celest. Mech. & Dynam. Astronom.*, 95, 81

Pilat-Lohinger, E.; Funk, B.; Dvorak, R. 2003 *Astronomy and Astrophysics*, 400, 1085

Sándor, Zs., Érdi, B. 2003 *Celest. Mech. & Dynam. Astronom.*, 86, 301

Sidorenko, V. V. 2006 *Cosmic Research*, 44, 440

Simó, C. 1992 *Positional Astronomy and Celestial Mechanics*, Proceedings of the Second International Workshop held 19-22 October, 1992 in Valencia, Spain. Edited by A. Lopez Garcia, A. Ortiz Gil, J. Chernetenko, and V. Yershov. Valencia: Universitat de Valencia Observatorio Astronomico, p.190.

Szebehely, V. and Giacaglia, G. E. O. 1964, *Astronomical Journal* 69, 230

Szebehely, V. 1967, *Theory of orbits*. Academic Press, New-York

Szenkovits, F.; Makó, Z. 2005 *Publications of the Astronomy Department of the Eötvös University (PADEU)*, 15, 221

Vieira, N. E. and Winter, O. C. 2001, *The Astronomical Journal*, 122, 440

Vrcelj, Z., Kiewiet de J., Joost H. 1978, *The Astronomical Journal* 83, 514

Vrcelj, Z., Kiewiet de J., Joost H. 1978a, *The Astronomical Journal* 83, 664

Vrcelj, Z. 1979, *The Astronomical Journal* 84, 1072

PADEU | PADEU **19** (2007), p. 163
ISBN 963 463 557
©Published by the Astron. Dept. of the Eötvös Univ.

Rotation in the restricted three-body problem

József Vanyó[1], Tamás Tél[2]

Eötvös University, Institute for Theoretical Physics, H-1518 Budapest, Pf. 32, Hungary

E-mail: [1]vanyoj@gmail.com, [2]tel@general.elte.hu

Abstract

The rotation of a nonspherical small body is invetigated in the planar restricted three-body problem along periodic, quasi-periodic or chaotic orbits of the small body's center of mass. A systematic overview of the chaotic rotation dynamics via stroboscopic mappings is possible only in the periodic case. We propose to explore the phase space patterns of nonperiodic cases by following a droplet in the phase space. The temporal evolution of the pattern can be characterized by a time-dependent fractal dimension. It is shown to converge exponentially to the dimension of the phase space for long times.

1 Introduction

We investigate (see also (1)) the rotation of a small body in the planar restricted three-body problem. We suppose that this third component is nonspherical and its rotation axis is perpendicular to the plane of the components.

In the Solar System, there are several bodies of irregular shape whose rotation can be observed. A well known example is Hyperion, a moon of Saturn, whose irregular rotation discovered by Voyager 2 provided the first example of chaoticity within the Solar System. On the one hand, our problem is a generalization of the rotation of Hyperion (which is driven by the simple Keplerian orbit of the center of mass) studied by Wisdom (2), and, on the other hand it is a simplification of the rotation of planets in the Solar System (driven by

an N-body problem) investigated by Laskar (3). According to Laskar, chaotic rotation is typical in planetary systems.

Another example is provided by asteroids. Nowadays, their rotation is routinely monitored by radar, like e.g. the rotation of Kleopatra (4). In the case of another asteroid, Toutatis, really strange rotation states were detected (5). These results indicate the relevance of our investigation.

While chaos arising in periodically driven nonlinear systems is fairly well understood (6), little attention has been paid to the study of temporally unperiodic, in particular, to chaotic driving.

Our choice of the system is motivated by finding the simplest form of chaotic driving, and by the unique feature that all the basic types of driving: periodic, quasi-periodic and chaotic, can be found within the same problem for different initial conditions.

The paper is organized as follows. In Section II we derive the the rotation equation of the three-body problem, and identify the center of mass trajectories along which rotation is studied. Section III concentrates on quasi-periodic and chaotic driving, and presents the results of the droplet dynamics. The convergence of the time-dependent fractal dimension towards its asymptotic value of 2 is shown to be exponential in time. Section IV contains our conclusions.

2 Rotation dynamics

A rigid body, B_3, of irregular shape is considered in the gravitational field of a single spherical body of mass m centered at point B. The reference frame (x', y', z') is fixed to B_3, which has a final extension along the z' axis as well, and its axes coincide with the principal axes of B_3 with its origin in the center of mass (see Fig. 1). The reference frame (x'', y'', z'') is chosen so that the x'' axis goes through the gravitational center B, lying at a distance r_0 from the origin, and the z'' axis coincides with the z' axis around which rotation can take place. The angle between the x' and x'' axes is denoted by α.

The gravitational force acting on a volume element of mass m_i of B_3 located at (x_i'', y_i'') has components (see Fig. 1)

$$F_{x''} = \gamma m_i m \frac{r_0 - x_i''}{s_i^3}, \quad F_{y''} = -\gamma m_i m \frac{y_i''}{s_i^3} \tag{1}$$

where $s_i = \sqrt{(r_0 - x_i'')^2 + y_i''^2}$ denotes the distance between the volume element and the center B, and γ is the gravitational constant. The gravitational torque

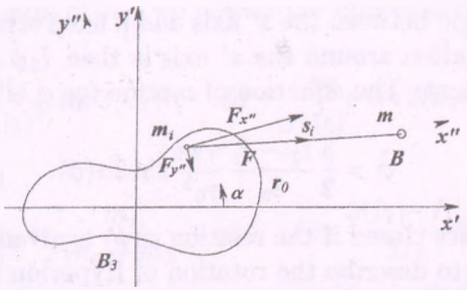

Figure 1: *Configuration of the rigid body B_3 in the gravitational field of a center B at a distance r_0. The frame (x', y', z') is a principal-axis system with its origin in the center of mass. Frame (x'', y'', z'') is chosen so that its x'' axis goes through the gravitational center B. The angle from the x' axis towards the x'' is denoted by α.*

from the volume element around the z'' axis is

$$M_i = -F_{x''} y_i'' + F_{y''} x_i'' = -\gamma m_i m \frac{r_0 y_i''}{{s_i}^3}. \tag{2}$$

Since the size of the rigid body is in reality much smaller than the distance r_0 from the center, we can expand the square root in s_i up to first order to obtain $s_i^{-3} \approx r_0^{-3}(1 + 3x_i''/r_0)$, from which

$$M_i = -\frac{\gamma m_i m}{r_0^3}(r_0 y_i'' + 3x_i'' y_i''). \tag{3}$$

The total gravitational torque M is the integral of these contributions over the volume of the body. The contribution from the term $r_0 y_i''$ vanishes since the origin is the center of mass. The evaluation of the second term is most convenient in the body frame. Using the relations $x'' = x' \cos\alpha + y' \sin\alpha$, $y'' = -x' \sin\alpha + y' \cos\alpha$, we find

$$M = -\frac{3\gamma m}{2{r_0}^3} \int \left[(y'^2 - x'^2) \sin 2\alpha + 2x'y' \cos 2\alpha\right] dx'\, dy'\, dz'. \tag{4}$$

The second term of the integrand is a deviation moment which is zero in the principal-axis system. By writing $y'^2 - x'^2 = y'^2 + z'^2 - (x'^2 + z'^2)$, the principal moments I_1 and I_2 with respect to the x' and y' axis appear, and so

$$M = \frac{3}{2}\frac{\gamma m}{{r_0}^3}(I_2 - I_1) \sin 2\alpha. \tag{5}$$

Let ϕ denote the angle between the x' axis and a fixed straight line in the plane. The equation of rotation around the z' axis is then $I_3\ddot{\phi} = M$, where I_3 is the third principal moment. The equation of motion for ϕ is therefore

$$\ddot{\phi} = \frac{3}{2}\frac{I_2 - I_1}{I_3}\frac{\gamma m}{{r_0}^3}\sin 2\alpha(\phi). \tag{6}$$

The equation becomes closed if the relation $\alpha(\phi)$ is given. This is the equation applied by Wisdom to describe the rotation of Hyperion (2).

In the three-body problem, there are two gravitational centers, the two main bodies B_1 and B_2 (of mass m_1 and m_2) of the three-body problem. Therefore, the total torque will contain two contributions from the two centers from distance r_1 and r_2. Let us use a reference frame (x, y) fixed to the two main bodies as indicated in Fig. 2.

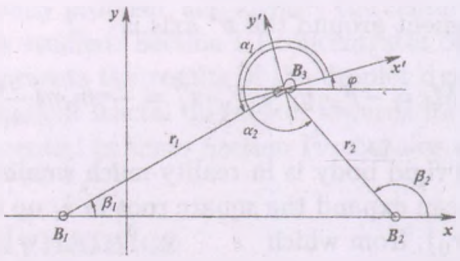

Figure 2: *Configuration of the rigid body B_3 in a reference frame (x, y) co-rotating with the two main bodies B_1, B_2. ϕ denotes the rotation angle with respect to the x axis.*

Since angle α (cf. Fig. 1) is the angle between the direction of the gravitational center and the x' body axis, we have two different angles: $\alpha_i(\phi) = \pi + \beta_i - \phi$, $i = 1, 2$, where β_i is the angle with respect to the x axis under which the center of mass of B_3 is seen from center i. The rotation dynamics is therefore governed by to different torque contributions of the type of (6). In the rotating frame (x, y) inertial forces (centrifugal and Coriolis forces) also act, but their overall torque can be shown to be zero. The rotation equation is thus

$$\ddot{\phi} = \frac{3}{2}\frac{I_2 - I_1}{I_3}\left(\frac{\gamma m_1}{{r_1}^3}\sin 2(\beta_1 - \phi) + \frac{\gamma m_2}{{r_2}^3}\sin 2(\beta_2 - \phi)\right). \tag{7}$$

By measuring time in units of $1/\omega$ where $\omega = (\gamma(m_1 + m_2)/R_0^3)^{1/2}$ is the frequency of rotation of the two main bodies of distance R_0 along their circular

orbit, and length in units of R_0, we obtain the dimensionless rotation equation

$$\ddot{\phi} = \delta \left(\frac{\mu_1}{r_1(t)^3} \sin 2(\beta_1(t) - \phi) + \frac{\mu_2}{r_2(t)^3} \sin 2(\beta_2(t) - \phi) \right), \tag{8}$$

where

$$\mu_i = \frac{m_i}{m_1 + m_2} \quad \text{and} \quad \delta = \frac{3(I_2 - I_1)}{2I_3} \tag{9}$$

represent the mass and principal momentum ratio, respectively. Equation (8) can be rewritten as

$$\ddot{\phi} = B(t) \sin\left(2(\phi - \phi_0(t))\right) \tag{10}$$

to emphasize that the ϕ dynamics is not autonomous, it is driven by the center of mass motion of the small body via the time-dependent quantities $B(t)$ and $\phi_0(t)$.

This driving originates from the planar, circular, restricted three-body problem which specifies the location $(x(t), y(t))$ of the center of mass of the small body according to the well known equations (7)-(10)

$$\ddot{x} = 2\dot{y} + x - \frac{\mu_1 (x + \mu_2)}{{r_1}^3} - \frac{\mu_2 (x - \mu_1)}{{r_2}^3}, \tag{11}$$

$$\ddot{y} = -2\dot{x} + y - \frac{\mu_1 y}{{r_1}^3} - \frac{\mu_2 y}{{r_2}^3}.$$

This dimensionless form is valid in the afore-mentioned units. The center of mass motion preserves the energy E in the co-rotating frame, and can be expressed with the Jacobi constant C as $E = -C/2$, where

$$C = \mu_1 {r_1}^2 + \mu_2 {r_2}^2 + 2\frac{\mu_1}{r_1} + 2\frac{\mu_2}{r_2} - \dot{x}^2 - \dot{y}^2. \tag{12}$$

The coupled set of equation (8) and (11) defines the rotation dynamics. Since ϕ does not appear in (11), the angle dynamics has no feedback on the center of mass. For a given initial condition $(x_0, y_0, \dot{x}_0, \dot{y}_0)$, the orbit $(x(t), y(t))$ uniquely specifies the distances $r_i(t)$ and angles $\beta_i(t)$ which are used as input functions for the angle dynamics with initial conditions $(\phi_0, \dot{\phi}_0)$. The full problem has three independent dimensionless parameters $\mu \equiv \mu_2$, C and δ. In our study we choose them to be

$$\mu = 10^{-3}, \quad C = 3.05, \quad \delta = 0.65. \tag{13}$$

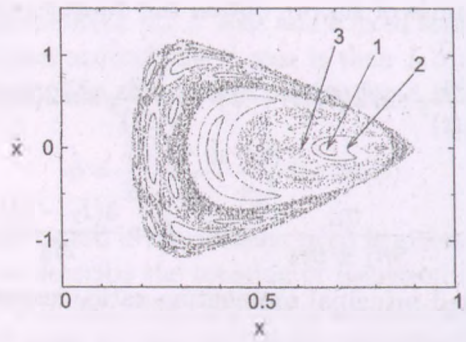

Figure 3: *Poincaré section $y = 0$ of the three body dynamics with $\mu = 10^{-3}$, $C = 3.05$. The arrows point towards the orbits we take as particular driving orbits. They are of different character: 1) periodic, 2) quasi-periodic, 3) chaotic.*

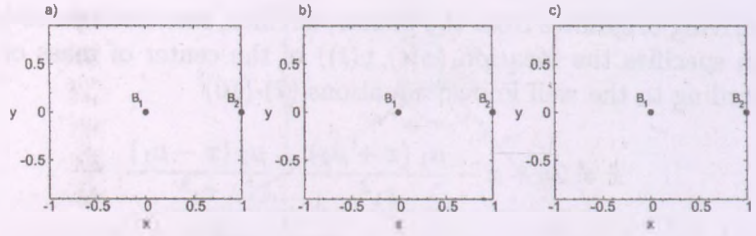

Figure 4: *The center of mass orbits chosen to drive the rotation dynamics. a) The periodic orbit 1) in Table 1. b) The quasi-periodic orbit 2) in Table 1. c) The chaotic orbit 3) in Table 1. The period of the periodic orbit is $T = 12.428596$ dimensionless units. Symbols B_1 and B_2 mark the location of the large bodies.*

The mass ratio corresponds to that of the Sun-Jupiter system, while the principal momentum ratio is about twice that of the Hyperion.

Since the driving dynamics is provided by a chaotic Hamiltonian system, the actual driving effect depends on the initial condition, and, thus, on the actual form of the center of mass orbit. Fig. 3 shows the Poincaré section of the three-body problem on the $y = 0$ hyperplane of the phase space in the co-rotating frame.

We have chosen several trajectories of periodic, quasi-periodic and chaotic type to drive the rotation dynamics. The results will be shown for a representative set whose initial conditions are given in Table 1. The form of these trajectories on the Poincaré map and in real space are shown in Fig. 3 and Fig.

driving	x	y	$\dot{x}$	$\dot{y}$
1) periodic	0.67810202	0	0	0.60014446
2) quasi-periodic	0.72902422	-0.00389250	0	0.47724492
3) chaotic	0.61173708	0.00271398	0	0.76951671

Table 1: *Initial conditions for the three prototypic center of mass orbits in (11) which will be used to drive the rotation dynamics (8).*

4, respectively.

3 Chaotic rotations

The numerical solution of Eq. (8) is shown in Fig. 5, where the temporal evolution of the angular position and the angular velocity of the small body can be seen along the chaotic center of mass orbit. These two data determine the rotational state of the small body.

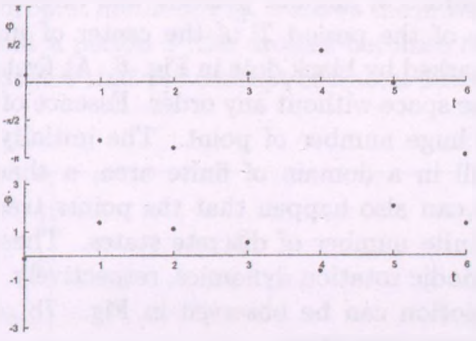

Figure 5: *Temporal evolution of the angle (top panel) and angular velocity (bottom panel) of the third body with chaotic driving (orbit 3). Initial conditions are* $\phi_0 = 0.3$, $\dot{\phi}_0 = -0.1$. *Black dots indicate time instants which are integer multiples of the period T or orbit 1.*

A comparison of this plot with another one, obtained along the periodic orbit does not show a striking difference (see Fig. 6).

It is clear that all the curves are irregular, but no real difference can be observed. Certain characteristic features, in particular those of indicating deterministic order, turn out to remain hidden in this representation.

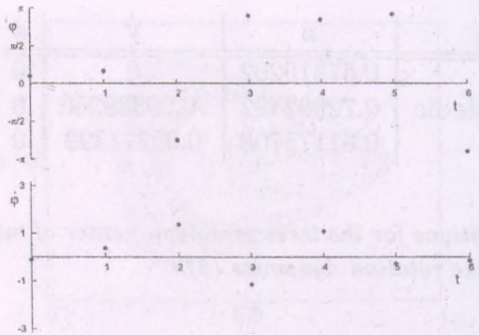

Figure 6: *Temporal evolution of the angle (top panel) and angular velocity (bottom panel) of the third body with periodic driving (orbit 1). Initial conditions are* $\phi_0 = 0.3$, $\dot{\phi}_0 = -0.1$.

For periodic driving, an insight into phase space structures can be obtained by following the dynamics on a stroboscopic map. This leads to a cleanly distinguishable pattern of chaotic and nonchaotic orbits (6).

Fig. 7a helps to understand how a stroboscopic map is constructed. In this figure the coupled values of angular position and angular velocity are plotted at integer multiples of the period T of the center of mass motion. The the plotted states are marked by black dots in Fig. 6. At first sight these points are jumping in the phase space without any order. Essence of this method becomes clear by plotting a huge number of point. The initially randomly appearing points eventually fill in a domain of finite area, a chaotic sea. With other initial conditions it can also happen that the points trace out a closed curve, or jump among a finite number of discrete states. These cases correspond to quasiperiodic or periodic rotation dynamics, respectively. A interwoven pattern of these types of motion can be observed in Fig. 7b, obtained by following several trajectories over long times.

Unfortunately, if the driving is not periodic, stroboscopic maps taken with any fix period of time generates fuzzy, unstructured patterns (Figs. 9a, 10a). To have a better insight into these cases, another method is needed.

This method is suggested by the analogy between phase space dynamics and hydrodynamical flows. In the context of advection by fluid flows, it is natural to follow dye droplets (11) which turn out to have well defined, fractal like shapes even in velocity fields which depend in a chaotic manner on time. As an analog of this, we shall follow an ensemble of trajectories - called a droplet - in the phase space of the dynamical system.

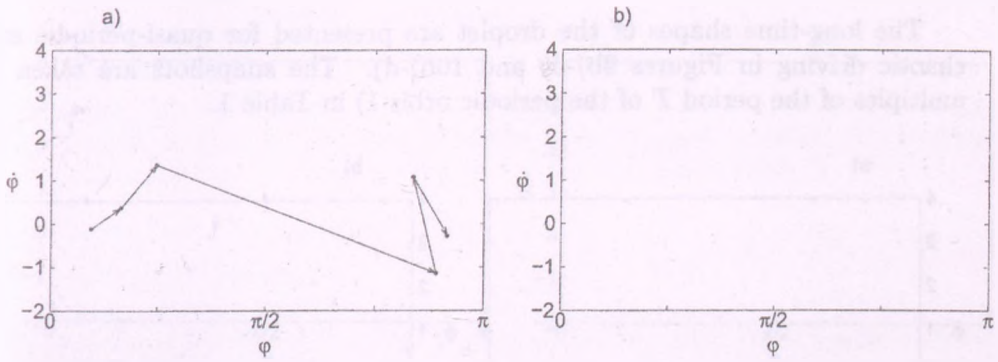

Figure 7: *Stroboscopic map and the way how it is comes about in the case of periodic driving. a) First six points of the stroboscopic map as read off from Fig. 6. b) The stroboscopic map. The sequence started on panel a) is followed up to 1500 points, and traces out a randomly dotted area, the chaotic sea. Furthermore, trajectories with initial conditions e.g.* $\phi_0 = \pi/2$, $\dot{\phi}_0 = 2.9$; $\phi_0 = \pi/2$, $\dot{\phi}_0 = 2.9$; $\phi_0 = \pi/4$, $\dot{\phi}_0 = 3.5$ *and* $\phi_0 = \pi/2$, $\dot{\phi}_0 = -1.6$ *... are also monitored up to the same number of steps. They trace out closed curves and correspond therefore to quasi-periodic rotation.*

To illustrate the droplet method, Fig. 8 shows the initial stages of the droplet dynamics. Well within a period T the droplet becomes not only stretched but aslo folded. This indicates that the concept of fractal dimension might be useful in this context.

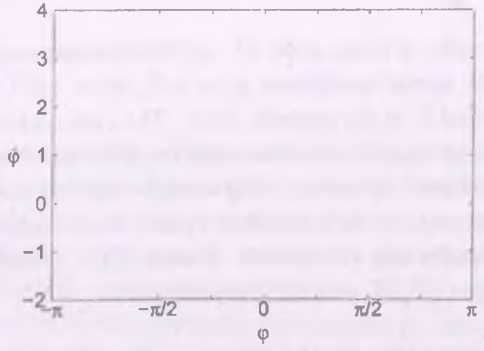

Figure 8: *Typical behavior of a droplet for the chaotic driving. The initial droplet has the shape of a small rectangle. Later stage at time instants* $t = 0$, $t = 1$, $t = 2$, $t = 3$, $t = 4$ *and* $t = 5$ *(dimensionless units) are shown. The stretching and folding of the droplet are well observable in this figure, the latter starts at about the fifth stage.*

The long-time shapes of the droplet are presented for quasi-periodic and chaotic driving in Figures 9b)-d) and 10b)-d). The snapshots are taken at multiples of the period T of the periodic orbit 1) in Table 1.

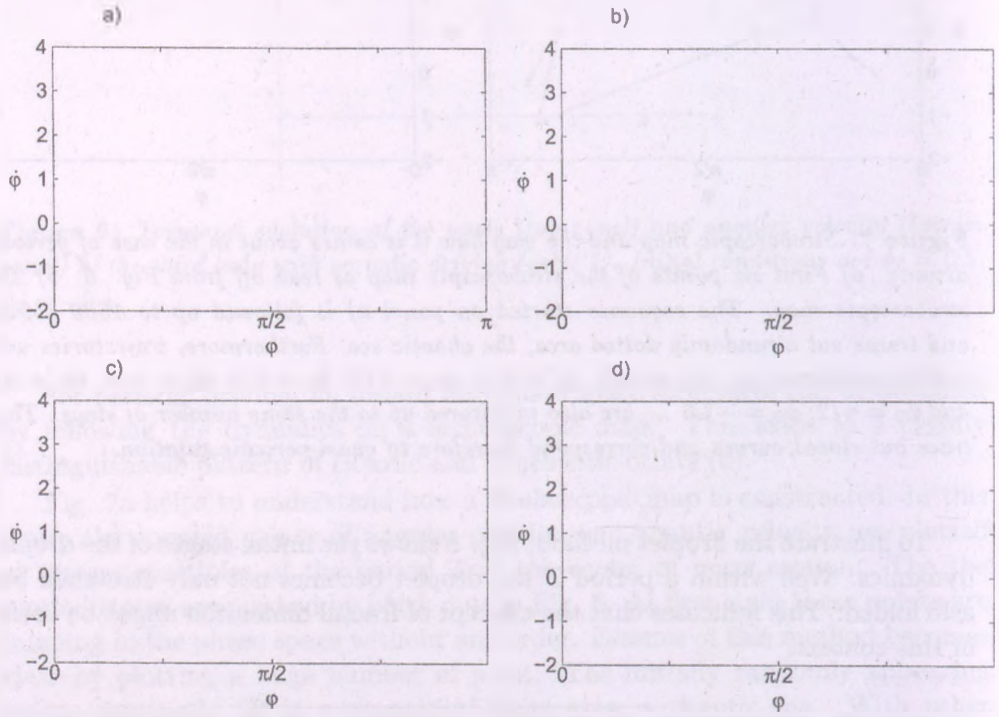

Figure 9: *Quasi-periodic driving, orbit 2). a) Stroboscopic map generated by monitoring 3 trajectories with initial conditions $\phi_0 = \pi/2$, $\dot{\phi}_0 = -0.7, 0.5$ and 3.0. Snapshots are taken with the period T of the periodic orbit. The same set of trajectories would lead for periodic driving to a clear, interwoven pattern of quasiperiodic and chaotic regimes in the map. b)-d) Droplet dynamics: the initial shape of the droplet is a square of size 0.1×0.1 centered at $(\phi = \pi/2, \dot{\phi} = 0.5)$ (small black rectangle in panel (b)) which contains 10^6 points uniformly distributed. Panels (b), (c) and (d) show the shape of the droplet at the times $1T, 2T$ and $6T$, respectively.*

It can be seen that the droplet forms a more and more dense but always sharp, filamentary pattern. It is remarkable that these sharp fractal-like patterns survive over several time units. This is so because the *same* driving is applied to all the points of the droplet at any instant of time. Note that due to the non-periodic driving no invariant sets, and in particular no KAM tori (6),

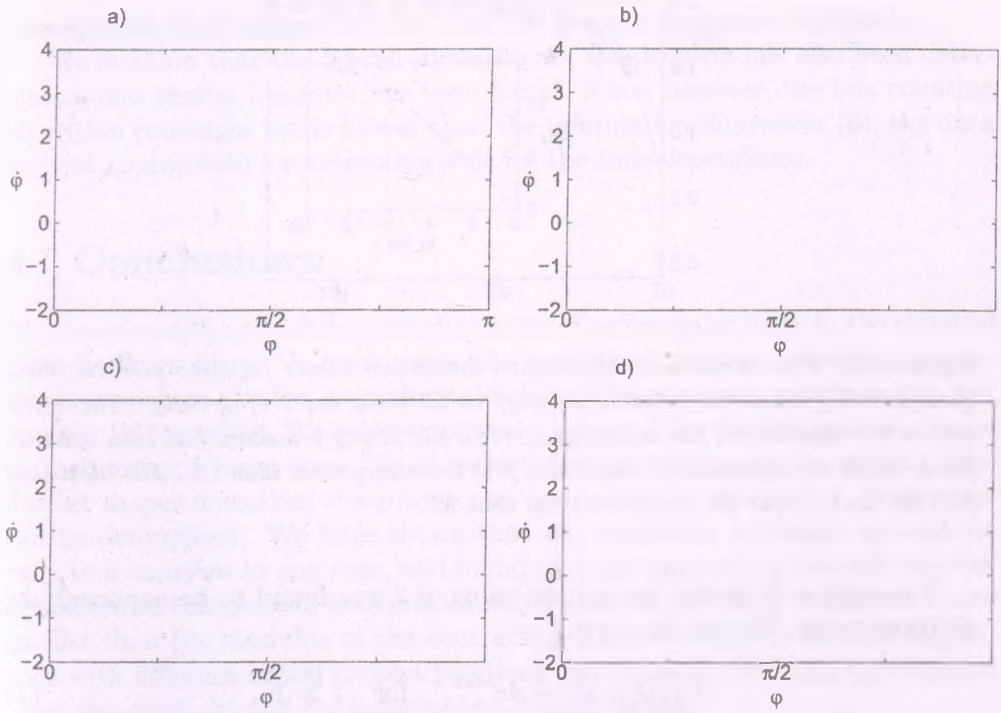

Figure 10: *Chaotic driving, orbit 3). a) Stroboscopic map generated by the same set of trajectories as in the previous figure. The droplet is the same as in Fig. 9. Panels (b), (c), and (d) show the shape of the droplet at the times $1T, 2T$ and $6T$, respectively.*

can exist.

Since the rotation dynamics is Hamiltonian, the asymptotic dimension of all droplets should be 2, as also suggested by panel (d) of Figs. 9, 10. To characterize the approach to this value, we numerically determined the information dimension, D_1 (6), of the distribution defined by the droplets at earlier times. To this end, we evaluated the number of points $P_i(\varepsilon, t)$ (normalized to unity over all boxes) in box i of size ε covering the droplet at time t. The information content $I(\varepsilon) = -\sum_i P_i(\varepsilon, t) \ln P_i(\varepsilon, t)$ was found to behave as $-D_1(t) \ln \varepsilon$. The fact that such a scaling behavior is present even for chaotic drivings over a range of more than a factor of 100 in ε at relatively early times is shown in the inset of Fig. 11. The figure presents the information dimension as a function of time for all the drivings.

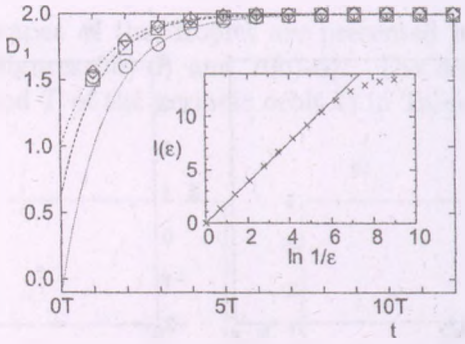

Figure 11: *Time-dependent information dimension values (square: periodic, circle: quasiperiodic, diamond: chaotic driving) in all three cases of driving. The smooth curves are exponential fits according to (14), the fitting procedure has been started at points where the information dimension first becomes greater than* 1.5. *The inset shows* $I(\varepsilon)$ *vs.* $\ln(1/\varepsilon)$ *for the chaotic case at time* $3T$.

The approach to the asymptotic value of 2 was found to be exponential in all three cases. We can thus write

$$D_1(t) = D_1 - Ae^{-\sigma t}, \quad \text{for} \quad t \gg 1, \tag{14}$$

where D_1 is the asymptotic value of the information dimension. In our Hamiltonian problem, $D_1 = 2$. The quantity σ is the convergence rate towards the value of D_1. Table 2 shows the fitted parameters for our three different driving orbits.

driving	σ	A	λ
1) periodic	0.069	2.4	0.26
2) quasi-periodic	0.060	3.7	0.21
3) chaotic	0.064	1.8	0.36

Table 2: *Convergence rates and amplitudes of the exponential convergence of the dimension towards* 2, *and average Lyapunov exponents for different types of driving. The error in these quantities is estimated to be* 5 *percent.*

The investigation of other sets of driving orbits indicates that these data seem to somewhat depend on the choice of the driving orbits, although their order of magnitude is the same as in our representative set. The convergence

rate appears to be always smaller than the average Lyapunov exponent.

We mention that the fractal dimension of the droplets has also been determined, and similar behavior has been found. Since, however, the box counting algorithm converges much slower than the information dimension (6), the data are less appropriate for extracting a fit for the time-dependence.

4 Conclusions

We considered the two-dimensional rotation of an irregular body in the classical three-body problem. In such cases the traditional method of taking stroboscopic snapshots of a few trajectories leads to a fuzzy pattern which washes out any sign of fractality. We suggest instead the use of the droplet method, based on monitoring a large ensemble of trajectories on stroboscopic snapshots. The droplet shapes have then sharp contours, and fractal or information dimensions can be determined. We have shown that the dimension converges asymptotically to a constant in any case, and found that the approach of the information dimension to this plateau is approximately exponential, with a convergence rate smaller than the modulus of the contracting Lyapunov exponent. Our experience with different initial droplet positions and shapes is that the convergence rates at a fixed driving are independent of such factors.

We presented here results for the rotation of the small body around an axis perpendicular to the plane of the three-body problem. We have investigated, however, general spatial rotation, too, and found qualitatively similar features.

Acknowledgement

We are grateful for useful conversations with B. Érdi, G. Károlyi, I. Benczik, Á. Süli, and Á. Horváth. The support of the Hungarian Science Foundation (OTKA no. T047233, TS044839) are acknowledged.

References

[1] J. Vanyó and T. Tél, Dynamics of chaotic driving: rotation in the restricted three-body problem, Phys. Rev. E. submitted, 2006

[2] J. Wisdom, S.J. Peale, F. Mignard, Icarus **58**, 137 (1984); J. Wisdom, Icarus **72**, 241 (1987); J. Wisdom, Astron, J. **413**, 109 (1987).

[3] J. Laskar, P. Robutel, Nature **361** 608-612, (1993);

[4] S.J.Ostro et al., Science **288**, 836 (2000).

[5] R.S.Hudson and S.J.Ostro, Science **270**, 84 (1995).

[6] E. Ott, *Chaotic dynamical systems* (Cambridge Unievrsity Press, Cambridge, 1993, 2002).

[7] V. Szebehely, *Theory of orbits* (Academic Press, London, 1967).

[8] O.C. Winter and C.D. Murray, *Atlas of the planar, circular, restricted three-body problem* QMC Math. Notes **16** (Queen Mary College, London, 1994).

[9] P.H. Richter, Rev. Mod. Astron. **14**, 53 (2001).

[10] J. Nagler, Phys. Rev. **E69**, 066218 (2004); **E71**, 026227 (2005).

[11] J.C. Sommerer and E. Ott, Science **259** 335 (1993); J. Jacobs, E. Ott, T. Antonsen, and J. Yorke, Physica **D110**, 1 (1997); Z. Neufeld and T. Tél, Phys. Rev. **57**, 2832 (1988); G. Károlyi, T. Tél, A. P. S. de Moura, and C. Grebogi, Phys. Rev. Lett. **92**, 174101 (2004).

Part III

Dynamics of Celestial Bodies, Systems and Populations

PADEU | PADEU 19 (2007), p. 179
ISBN 963 463 557
©Published by the Astron. Dept. of the Eötvös Univ.

STABILITY INVESTIGATIONS OF EXOPLANETARY SYSTEMS

Bálint Érdi[1], Zsolt Sándor[1], Áron Süli[1]

[1]Department of Astronomy, Eötvös University, Pázmány Péter sétány 1/A. H-1117 Budapest, Hungary

E-mail: [1]B.Erdi@astro.elte.hu

Abstract
Stability investigations of exoplanetary systems are surveyed. Properties of the dynamical classes of multiple planetary systems are described. In the model of the planar elliptic restricted three-body problem stability maps are computed for single planetary systems.
Keywords: *Exoplanets – Stability*

1 Introduction

The dynamics of exoplanetary systems has been studied in several papers in recent years. The main problems concern the identification of the dynamical processes which determined their evolution, and the stability of the known systems. To date 193 exoplanets have been discovered in 165 extrasolar planetary systems. There are 19 multiple planetary systems in which more than one planet are known. These numbers are rapidly changing owing to the increasing rate of new discoveries.

It is highly improbable that planetary systems are formed with just one planet. Stability investigations of exoplanetary systems with one known planet can indicate places where additional planets might exist.

Multiple planetary systems can be classified according to the level of gravitational interaction between their planets (Barnes and Quinn 2004, Beaugé et al.

2005, Ferraz-Mello et al. 2006). The presently known systems can be grouped into three classes:

- Class Ia. Planets in resonant orbits
- Class Ib. Planets in low eccentricity, near resonant orbits
- Class II. Interacting planets
- Class III. Hierarchical systems

In Class Ia giant planets move in highly eccentric orbits close to the central star. Mutual perturbations are strong, planets can remain stable only in resonant orbits. 6 systems belong to this class with period ratios $P_2/P_1 < 5$: HD 82943 c,b; GJ 876 c,b; HD 128311 b,c; 55 Cnc b,c; HD 202206 b,c; HD 73526 b,c. The first known resonant system was Gliese 876 with a 2:1 orbital or mean motion resonance (Marcy et al. 2001). Beside this there is also an apsidal corotation resonance in this system with aligned apsidal lines. These resonances combined with phase protection ensure the long time stability of the system.

Stability of these systems critically depends on the orbital elements, small changes can lead to instabilities. In the case of the 2:1 resonant system HD 82943 earlier orbital elements were dynamically inconsistent. Ferraz-Mello et al. (2005) derived dynamically consistent orbital elements and showed that the system is near to apsidal corotation, however with large librational amplitudes. Seemingly, capture into resonance took place here without damping of the amplitudes.

In the 2:1 resonant system HD 73526 one of the resonant variables librates with large amplitude, the other circulates and the apsidal lignes are not aligned (Tinney et al. 2006). In another 2:1 resonant system, in HD 128311 the state of the resonance variables has not been determined yet, it might be similar to that of HD 73256 (Tinney et al. 2006).

An important problem is the origin of high eccentricities. This problem is studied in the concept of planetary migration. Several migration mechanisms have been proposed. The most probable comes from the interaction between the planets and the gaseous primordial disk. Hydrodynamical simulations have shown that a proper selection of the parameters of the gaseous disk can cause an inward migration of the planets and trapping into corotation resonance, and also excite the eccentricities (Kley 2001, 2003, Papaloizou 2003). In the case of 55 Cnc b,c Klay (2003) showed with hydrodynamical simulations that tidal migration leads to trapping into 3:1 resonance and also to apsidal corotation. Zhou et al. (2004) also showed the apsidal corotation. It has to be mentioned,

however, that the planet 55 Cnc c is considered not to be confirmed (Naef et al. 2004). Since nearly one third of the known multiple planetary systems are resonant, it is believed that orbital migration plays an important role in the evolution of such systems.

In Class Ib the period ratios are small, $P_2/P_1 < 5$, but either the masses are large and the orbits are relatively far, or the orbits are close but the masses are small and therefore mutual perturbations are not so strong. The orbits have small eccentricities and are close to mean motion resonances. One pulsar planetary system, PSR B 1257+12, and the system 47 UMa b,c belong to this class. The latter shows the most resemblance to our Solar System as to the shape and size of planetary orbits. Our planetary system can also be classified as Class Ib. The planets of 47 UMa are close to a 5:2 (alternatively 7:3 or 8:3) resonance. Psychoyos and Hadjidemetriou (2005) computed 5:2 resonant symmetric periodic solutions for the masses of the system 47 UMa. Zhou and Sun (2003) showed the apsidal secular resonance of the system. However, according to Naef et al. (2004) the planet 47 UMa c is not considered confirmed.

In Class II the period ratios are moderate, $5 < P_2/P_1 < 30$, therefore there are no mean motion resonances between the giant planets. However, the gravitational interactions are substantial manifesting mainly in the secular dynamics of the planets. Since the eccentricities are large, Libert and Henrard (2005) developed the perturbing potential up to 12th order in the eccentricities in order to investigate the secular dynamics. 6 systems belong to this class: mu Ara b,c; 55 Cnc e,b; Ups And b,c,d; HD 12661 b,c; HD 169830 b,c; HD 37124 b,c.

In the system HD 12661 the planets show anti-aligned upsidal libration (with large amplitude), this is the first such exoplanetary system (Libert and Henrard, 2006). In Ups And the two outer planets c and d perform apsidal libration (Libert and Henrard, 2006).

In the system HD 169830 two giants planets of similar size move in close, eccentric orbits. Here the difference of the periastron longitudes is circulating (Libert and Henrard, 2006). The habitable zone (HZ) of the system is situated beyond the orbit of the inner planet and is crossed by the outer planet. The dynamical structure of the HZ was studied by Érdi et al. (2004). It was shown that the HZ is strongly chaotic due to the overlapping of the inner and outer mean motion resonances in this region, and also because of the large masses of the giant planets. (A hypothetical third planet in the HZ can have inner resonances with the outer planet, and outer resonances with the inner planet. Many of these resonances overlap in the HZ.)

In Class III the period ratios are large, $P_2/P_1 > 30$, capture into mean motion resonance is improbable. Planets of these systems interact weakly. 6

systems belong to this class: HD 168443 b,c; HD 74156 b,c; HD 11964 b,c; mu Ara d,b; 55 Cnc c,d; HD 38529 b,c. In the systems HD 74156, HD 168443, HD 38529 the difference of the periastron longitudes of the two planets circulates (Libert and Henrard, 2006). The dynamical sructure of the HZ of the latter two systems were studied by Érdi et al. (2004).

In the system HD 168443 two planets of large masses (the outer possibly a brown dwarf) move in very eccentric orbits close to the star with period ratio $P_2/P_1 = 29.9$. According to Érdi et al. (2004) the HZ of the system is largely chaotic due to the overlapping of inner and outer mean motion resonances.

In the system HD 38529 a small inner planet move in eccentric orbit close to the star, while the outer planet is large orbiting far from the star in eccentric orbit and crossing the HZ. The period ratio is 151.9. According to Érdi et al. (2004) the outer part of the HZ is chaotic. There is a stable region at the inner edge of the HZ, however, this is crossed by high order (7:1, 8:1,...) inner resonances with the outer planet. The stability region persists for a wide range of mass and eccentricity values of the outer planet and not only an Earth-size but also a Jupiter-size additional planet could exist here.

2 Stability investigations in single planetary systems

In most of the so far discovered exoplanetary systems only one planet is known. This is usually a giant planet of the order of or several Jupiter masses. It is very probable that planetary systems consist of more than one planet with terrestrial-like planets among them. It is a great challange for exoplanetary research to discover Earth-like planets. There are space programs in the immediate future, such as COROT in 2006 and Kepler in 2008 aiming at this goal. Stability investigations can contribute to these research indicating places in exoplanetary systems where additional planets could exist beside the already known giant planets.

We made a systematic study to establish the stability properties of planetary systems with one giant planet. We applied the model of the planar elliptic restricted three-body problem corresponding to a system consisting of a star, a giant planet moving in elliptic orbit around the star, and a small terrestrial-like test planet in the orbital plane of the giant planet. This model is a first approach which later will be extended for more general cases such as non-planar motion of the test planet, non-negligible mass of the test planet, and two giant planets

in the system.

We computed stability maps for a large set of initial conditions and mass parameters by using the method of the relative Ljapunov indicators (RLI). This is a very fast and efficient chaos detection method (Sándor et al. 2000, 2004). The stability maps can be used for several purposes:

- If a new planet is discovered in a known exoplanetary system with one giant planet, the dynamical consistency of the orbital elements of the new planet, derived from the observations, can be established at once from the stability maps.

- The stability properties of the HZ of known exoplanetary systems can be seen from the stability maps. This gives an indication where terrestrial-like planets can be expected to exist in the HZ.

- The orbital data of the giant planets of exoplanetary systems are subject to changes and improvements due to the accumulation of observations. The stability properties of the systems with improved orbital data can be established from the stability maps since these are computed for a large set of initial conditions and parameters incomporating those resulting from possible changes of the data of the giant planets.

As examples, in Figs. 1 and 2 we show two stability maps computed for a mass parameter 0.001 (corresponding approximately to a system with a star of one solar mass and a giant planet of one Jupiter mass). The horizontal axis corresponds to the values of the semi-major axis a of the test planet expressed in the unit of the semi-major axis of the giant planet (so values on the horizontal axis are ratios of the two semi-major axes). The vertical axis corresponds to the values of the orbital eccentricity e_1 of the giant planet. The values of the orbital elements along the two axes were changed with a very small stepsize, and for each corresponding orbit (the other initial orbital elements of the test planet were taken zero) the RLI value was computed and visualized in the (a, e_1) parameter plane. Light regions correspond to low values of the RLI (10^{-10}) and ordered, dynamically stable motion of the test planet. Dark regions correspond to large values of the RLI (10^{-5}) and chaotic bahaviour of the test planet.

In Fig. 1 we displayed a case, where the semi-major axis of the orbit of the test planet is larger than that of the giant planet. The dark unstable regions on the left are due to the proximity of the giant planet. The figure is dominated by V-shaped gray stripes corresponding to outer mean motion resonances between the test planet and the giant planet. These resonances, marked at the top

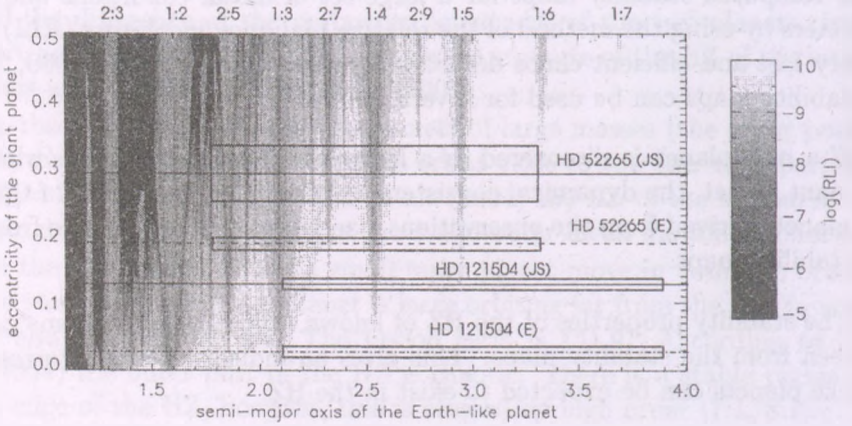

Figure 1: *Stability map for outer orbits of the test planet when the mass parameter is 0.001.*

of the figure, can represent either ordered (stable for infinite time), or weakly chaotic (which may become unstable after very long time) behaviour. With the increase of e_1 many resonances overlap giving raise to strongly chaotic and thus very unstable behaviour. The reason for this is that increasing e_1 the apocenter distance of the giant planet also increases and the giant planet perturbs more strongly the outer test planet.

The figure shows also the position of the HZ of two exoplanetary systems. Sometimes different sources give different orbital data for a given system. This may result in different stability properties of the HZ of the same system. This is shown in Fig. 1 for the case of HD 52265 and HD 121504. The HZ of HD 121504 is stable with the data of the exoplanets catalogue (www.exoplanets.org) (the letter E after the name of the system refers to this catalogue). Using the data of Jean Schneider's catalogue (www.obspm.fr/planets) there are a few resonances in the HZ of HD 121504 and thus it is partly stable. The HZ of the system HD 52265 is either partly stable (with a few resonances, using the data of the cataloge E), or marginally stable (with many resonances, using the data of JS).

In Fig. 2 we displayed a case, where the semi-major axis of the orbit of the test planet is smaller than that of the giant planet. Here again inner mean motion resonances between the test planet and the giant planet dominate the

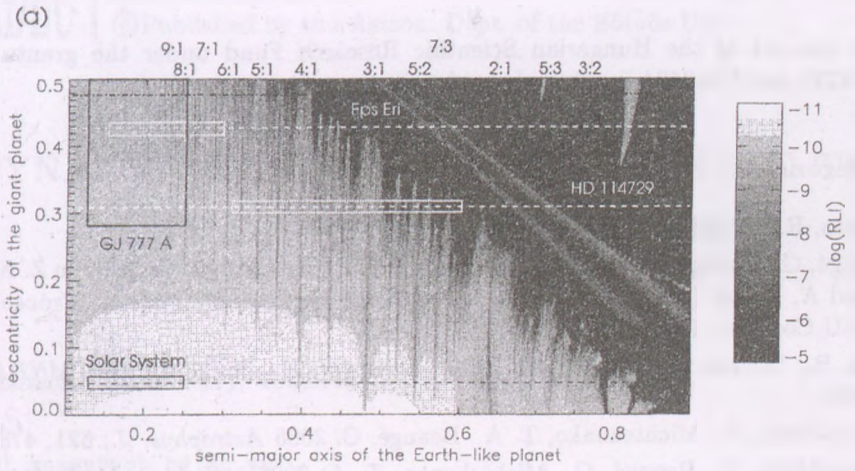

Figure 2: *Stability map for inner orbits of the test planet when the mass parameter is 0.001.*

stability map. Inside the resonances the stable or chaotic behaviour of the test planet depends on the initial angular positions of the two planets. In the strongly chaotic regions on the right, which are due to the proximity of the giant planet, there are two almost parallel light stripes, which correspond to satellite-type orbits around the giant planet. These orbits are less chaotic (or they may be ordered) than those emanating from the surrounding region. Between these stripes the dark gap corresponds to the perihelion distance of the giant planet, therefore in orbits originating from here the test planet suffers close encounters with the giant planet, or they can even collide.

The HZ of our Solar System is shown in Fig. 2, computed with the assumption that there is only one giant planet, Jupiter in the system. It is in the stable region of the figure. The HZ of HD 114729 is unstable, filled completely by overlaping resonances. The orbital data of the giant planet in GJ 777 A are very uncertain resulting in different stability properties of the HZ (changing between stable and marginally stable depending on the orbital eccentricity of the giant planet).

More details of these stability investigations will be given in another paper.

Acknowledgement

The support of the Hungarian Scientific Research Fund under the grants OTKA T043739 and D048424 is acknowledged.

References

Barnes, R., Quinn, T. 2004 *Astrophys. J.*, 611, 494

Beaugé, C., Callegari Jr., N., Ferraz-Mello, S., Michtchenko, T. A. 2005 in Z. Knežević and A. Milani (eds.) *Dynamics of populations of planetary systems*, Proceedings of IAU Coll. No. 197, p. 3

Érdi, B., Dvorak, R., Sándor, Zs., Pilat-Lohinger, E., Funk, B. 2004 *MNRAS*, 351, 1043

Ferraz-Mello, S., Michtchenko, T. A., Beaugé, C. 2005 *Astrophys. J.*, 621, 473

Ferraz-Mello, S., Beaugé, C., Michtchenko, T. A. 2006 in L. Arnold, F. Bouchy, C. Moutou (eds.) *Tenth Anniversary of 51 Peg-b: Status of and prospects for hot Jupiter studies.* Proceedings of a Coll. held at Observatoire de Haute Provence, p. 295

Kley, W, 2001 *MNRAS*, 313, L47

Kley, W. 2003 *Celest. Mech. & Dyn. Astron.*, 87. 85

Libert, A-S., Henrard, J. 2005 *Celest. Mech. & Dyn. Astron.*, 93, 187

Libert, A-S., Henrard, J. 2006 *Icarus*, 183, 186

Marcy, G. W., Butler, R. P., Fischer, D. A., Vogt, S. S., Lissauer, J. J., River, E. J. 2001 *Astrophys. J.*, 556, 296

Naef, D., Mayor, M., Beuzit, J. L., Perrier, C., Queloz, D., Sivan, J. P., Udry, S. 2004 *Astron. & Astrophys.*, 414, 351

Papaloizou, J. C. B. 2003 *Celest. Mech. & Dyn. Astron.*, 87, 53.

Psychoyos, D., Hadjidemetriou, J. 2005 in Z. Knežević and A. Milani (eds.) *Dynamics of populations of planetary systems*, Proceedings of IAU Coll. No. 197, p. 55

Sándor, Zs., Érdi, B., Efthymiopoulos, C. 2000 *Celest. Mech. & Dyn. Astron.*, 78, 113

Sándor, Zs., Érdi, B., Széll, A., Funk, B. 2004 *Celest. Mech. & Dyn. Astron.*, 90, 127

Tinney, C. G., Butler, R. P., Marcy, G. W., Jones, H. R. A., Laughlin, G., Carter, B. D., Bailey, J. A., O'Toole, S. O. 2006 *Astrophys. J.*, 647, 594

Zhou, J. L., Sun, Y. S. 2003 *Astrophys. J.*, 598, 1290

Zhou, L. Y., Lehto, H. J., Sun, Y. S., Zheng, J. Q. 2004 *MNRAS*, 350, 1495

PADEU | PADEU **19** (2007), p. 187
ISBN 963 463 557
©Published by the Astron. Dept. of the Eötvös Univ.

Dynamical Methods to Estimate the Age of Asteroid Families

Zoran Knežević

Astronomical Observatory, Volgina 7, 11160 Belgrade 74, Serbia

E-mail: zoran@aob.bg.ac.yu

Abstract
We present here some new results on the determination of the ages of asteroid families based on the analysis of motion of their members. Two independent methods have been used to assess the age of Veritas family, one making use of dynamical evolution of the stable family members, and the other where we analyze members with chaotic motion. In the former case we look for the refined age estimate by searching for convergence of angular elements to a narrow range of values acquired by the fragments immediately after the family formation event. In the latter case we compute the rate of chaotic diffusion of the resonant family members and estimate the time needed to spread from an initially compact distribution to the presently observed one.
Keywords: *Asteroids: families, resonances, chaotic diffusion*

1 Introduction

The ages of asteroid families, that is the epochs of their formation by collisional breakup of parent bodies, are of utmost importance for the study of dynamical and collisional evolution of asteroids. They serve to constrain the evolutionary models, to better understand physics of collisions and their outcomes, e.g. the initial velocity fields, to reveal the mechanical properties of asteroids, their internal composition and strength, to study the associated dust bands and their interaction with the Earth, etc.

Until quite recently the ages of asteroid families have been essentially unknown. The rough estimates, uncertain even at an order of magnitude level, have been inferred by using the indirect evidence such as cratering records or space weathering. Then Milani and Farinella (1994) invented the method of *chaotic chronology* and applied it to estimate the age of Veritas family. They employed the fact that the two largest members of the family, asteroids (490) Veritas and (3542) Tanjiazhen, chaotically diffuse at a rate that will make them escape the region of the phase space occupied by the family in $\simeq 60$ My. Since both asteroids are at present still located well inside the family region, they concluded that the family cannot be older than 60 My, thus in fact establishing only an upper bound to its age. In the later studies along the same line (Knežević, 1999; Knežević and Pavlović, 2002), a more conservative upper bound to the age of the family of ~ 100 My has been proposed, but in the same time it has been pointed out that the true age might be significantly shorter.

A couple of new methods to estimate the age of asteroid families have been introduced by Nesvorný et al. (2002) and Vokrouhlický et al. (2005). In the case of young families located in a region with no strong resonances, the family can be dated with the use of a method which consists in integrating backwards in time the equations of motion for the family members, until the orientation angles of their perturbed orbits converge to the values they had at the time of break-up. Using this latter method, Nesvorný et al. (2002) determined the age of the Karin family, the most recent break-up discovered so far in the asteroid belt which occurred ~ 5.8 My ago. Subsequently, Nesvorný et al. (2003) applied the same method also to the Veritas family and derived an estimate of the age of ~ 8.3 My. In the case of old families, the use is made of the distribution of the family members on the (H, a_P) plane, where H the absolute magnitude of a body and a_P the proper semi-major axis of its orbit. Due to the size dependent Yarkovsky non gravitational effect the family members drift in the semimajor axis, forming a characteristic V-shape. The age of the family can then be approximately found, by fitting the borders of the family with a theoretically expected curve depending on the physical parameters of the bodies (Vokrouhlický et al., 2005).

In the following we will present some new results of the determination of the age of families, in particular an attempt to refine the existing estimate for Veritas family. These new results have been obtained by using the *modified chaotic chronology method* (Tsiganis et al., 2006). The tools used for this research included numerical integration of orbits of family members and of fictitious asteroids for up to 100 My, computation of the time series of proper elements, of the Lyapunov times, of the coefficients of diffusion, etc.

2 Veritas family example

2.1 Procedures

We performed a large body of different analyzes to assess the distribution of Veritas family members in proper elements space, to identify the main dynamical groups, to analyze their dynamical behaviors and reveal the long-term effects of different resonant multiplets and the corresponding evolutionary time scales, and to study the cases of diffusive and non-diffusive chaos. Eventually we introduced a modified chaotic chronology method to estimate the age of this family. The results of this work are presented in full detail in Tsiganis et al. (2006); here we shall briefly sketch only the most important ones.

We first identified the members of the Veritas family by using the Hierarchical Clustering Method (Zappalà et al., 1995) and finding a total of 180 members for the value of the velocity cut-off $v_c = 40\,\mathrm{m\,s^{-1}}$. For each real family member and for a set of 400 fictitious objects we computed the Lyapunov times T_L by integrating the variational equations. Next we studied the long-term evolution of the proper orbital elements of family members for 100 My. We made two integrations: first, all 180 real objects were integrated for 10 My, then the integration has been extended to 100 My for a sub-group of representative objects. The equations of motion were integrated by means of the public domain *Orbit 9* software package[1]. Using the analytical theory by Milani and Knežević (1994), we subsequently computed the corresponding time series of proper elements for all integrated bodies. A 100 My integration backwards in time, followed also by a computation of the corresponding time series of proper elements, was performed for the members of the family with regular orbits.

For the resonant family members, we also calculated the mean squared displacement, $\langle(\Delta J_k)^2\rangle$, of the two action variables related to e_P and i_P, the average being taken over the corresponding set of family members. In terms of a simple diffusion approximation, the mean squared displacement in action grows linearly with time, at a characteristic rate called *the diffusion coefficient*. The diffusion coefficient in each action, $\mathcal{D}(J_k)$, was computed as the least-squares-fit slope of the $\langle(\Delta J_k)^2\rangle\,(t)$ curve. Finally, a simple random-walk model has been used to describe the evolution of chaotic family members, where, at every Δt, each body undergoes a random 'jump', whose length in J_1 and J_2 is given by a 2-D Gaussian distribution. The values of $\mathcal{D}(J_1)$ and $\mathcal{D}(J_2)$ then correspond to the standard deviation of the projections of the probability density, along the J_1 and J_2 axis, respectively.

[1] Available from the *AstDyS* service at http://hamilton.dm.unipi.it/astdys

2.2 Results

The Veritas family members exhibit a complex distribution in the space of proper elements. In particular, the (a_P, e_P) distribution reveals that the family can be decomposed into at least four dynamically distinct groups, arranged along the a_P values spanned by its members. Bodies clustered around $a_P = 3.168$ AU (group B) and around $a_P = 3.174$ AU (group A) have significantly larger spread in e_P, than the rest of the family. The low a side of the family (group R_1), mostly composed of bodies on regular orbits (Nesvorný et al., 2003), fits well inside the elliptical equivelocity curve computed using the equations of Gauss (Morbidelli et al., 1995), while groups A and B are cutting through this ellipse, producing two 'finger-like' features. If we assume that the family borders immediately after the break-up can be approximated by an equivelocity ellipse, then the initial spread in eccentricity for group-A and group-B objects should have been much smaller than observed at present. We, however, know that these 'finger-like' features are associated with the strong three-body mean motion resonances (Nesvorný and Morbidelli, 1998; Knežević et al., 2002; Nesvorný et al., 2003) among Jupiter, Saturn and the asteroid. The remaining component of the family (group R_2) is located between the two dispersed groups and has again a small spread in e_P.

In order to analyze the dynamical behavior of the main groups we first carried out an analyzis of the chaotic zones and resonances involved. We found that there are two broad chaotic bands cutting through the family, characterized by two different values of T_L: group-A bodies, including (490) Veritas itself, reside in the $T_L \approx 10^4$ yr chaotic band, while most group-B bodies are located in the $T_L \approx 3 \cdot 10^4$ yr band. The rest of group-B asteroids as well as R_2 bodies are located between these two main chaotic bands. Chaotic sidebands are also observed on both sides of the $T_L = 10^4$ yr band, as well as some less important features. While it is well known that the group-A chaotic band is associated with the (5,−2,−2) Jupiter-Saturn-asteroid mean motion resonance (Nesvorný and Morbidelli, 1998), the $T_L = 3 \cdot 10^4$ yr band is associated with the (3,3,−2) resonance (Knežević et al., 2002); also asteroid (37005) moves in the vicinity of the (7,−7,−2) resonance. These two latter resonances are due to frequency combinations of the main (5,−2,−2) resonance and the 2/5 near resonance of Jupiter and Saturn.

Group R_1 consists entirely of asteroids on regular orbits, their proper elements being stable over a 100 My time interval. A somewhat different behavior is observed for the members of the R_2 group, as well as for the members of group B located outside the (3,3,−2) chaotic band. The nearby resonances in-

duce long-periodic, small amplitude perturbations, but these perturbations do not build-up, at least within 100 My. Thus R_2 and non-chaotic asteroids of group-B also have very stable proper elements over a 100 My time span and their long-term behavior is very similar to that of R_1 bodies. In our study of the past evolution of regular family members we, however, considered R_1 bodies only, since they are less affected by the nearby resonances.

By examining more closely the motion inside the two main chaotic bands, we found that the group-A bodies diffuse very efficiently in e_P and $\sin i_P$. As inferred from our integrations, already after 10 My they cover a phase-space region that is about twice as big as the initial one. The behavior of group-B asteroids is quite different as their evolutionary traces cover practically the same region as the one occupied by their present-day distribution, and no macroscopic diffusion is observed. This might appear as somewhat surprising in view of not so very different Lyapunov times for the two groups. However, the instabilities of proper elements are related to the resonances involved, so that different resonances can have similar values of T_L in their chaotic layers, but very different long-term stability properties (hence the notion *stable chaos*; see Milani and Nobili (1992)). We actually found several group-B bodies, whose mean semi-major axis changes in time, the asteroid 'jumping' from one component of the resonance multiplet to another, but this type of chaotic motion does not seem to produce macroscopic diffusion in e_P and $\sin i_P$.

Using the 10 My integrations of the real bodies, we computed the diffusion coefficients in J_1 and J_2 for both chaotic groups. The mean squared displacement in both actions has been found to be a linear function of time and the corresponding values of the diffusion coefficient were $\mathcal{D}(J_1) = 1.1 \cdot 10^{-14}$ yr^{-1} and $\mathcal{D}(J_2) = 1.4 \cdot 10^{-14}$ yr^{-1}. On the contrary, for the chaotic group-B asteroids, we found a much smaller value for $\mathcal{D}(J_1) = 9.6 \cdot 10^{-17}$ yr^{-1} and a much smaller value for $\mathcal{D}(J_2) = 1.9 \cdot 10^{-18}$ yr^{-1}. Thus, chaotic motion is strongly diffusive for group A, while it is almost non-diffusive for group B.

Finally, we derived two independent estimates of the age of Veritas family, one making use of dynamical evolution of the stable family members, and the other based on the members with chaotic motion. In the former case we integrated backwards in time the orbits of the 50 family members of R_1 for 10 My and calculated their proper elements time series. Following Nesvorný et al. (2003), we computed the mean difference of nodal longitudes of all bodies, $\langle \Delta\Omega \rangle$, with respect to the largest member of the family with a stable orbit, asteroid (1086) Nata, as a function of time. A clustering of the nodes within 30° was found at $t = -8.3$ My. Thus, we have confirmed the result obtained by Nesvorný et al. (2003), but our results show a more tight clustering of the nodes

(within 30°) mainly because we excluded from the calculation all non-chaotic B and R_2 family members, and because we made use of proper elements, thus reducing the effects of short periodic variations.

An independent estimate of the age of the family can be obtained, using a modified chaotic chronology method for group A asteroids. A simple random-walk model can be used to describe their evolution, as described in Section 1. Starting from an initial distribution extended as suggested by the equivelocity ellipses, we took a number of snapshots of the evolution of a fictitious initial distribution of 400 (5,−2,−2)-resonant bodies in the $(e_P, \sin i_P)$ space, according to our random-walk model, and we superimpose it on the present-day distribution of group-A family members.

The fictitious objects are spreading diffusively in action space, the variance of the distribution growing linearly with time. The box in a 2-D phase space representing the observed distribution is filled by our random-walkers within less than 10 My; even several particles have leaked out of the box, but still more than 67% of the particles is well contained within the box in both variables. Next we checked the area of the plane covered by the real group-A members, when the latter are propagated for 10 My into the future. At $t = 20$ My, the random-walkers cover an area, which has approximately the same extent as the one covered by the future images of real group-A members. The above results confirm that a simple random-walk approach can be used to obtain an estimate for the age of group A, and, in fact, they indicate that the age of this group must be ~ 10 My.

Of course, the diffusion zone spanned by group-A asteroids does not have the simple elliptical shape of the region covered by the random-walkers. In particular it has three 'tails', two at small and one at high eccentricities, while most of the bodies seem to occupy a more compact region. This suggests that, as the resonant bodies spread, they approach phase-space regions, characterized by different transport properties: the diffusion coefficient may vary significantly, with respect to the region occupied by the present-day distribution of group-A bodies, or transport may deviate significantly from normal diffusion, due to a complex phase-space topology. In either case, the normal diffusion is only an approximation of the real transport process. However, the simple diffusion approximation seems to provide a good estimate for the transport time scale.

In other words, the above results show that, even though the evolution of the distribution function of group-A bodies cannot be assumed to follow Fick's law (see Eq. (1) in Tsiganis et al. (2006)) for all times, their *current* distribution can be viewed as the evolution of a narrow initial distribution in J_1, whose variance grows with time as $\sigma^2(x) = \mathcal{D}/2 \cdot t$. Using the obtained values of

$\mathcal{D}(J_1)$ and of $\sigma(J_1) = 2.2 \cdot 10^{-4}$ taken from the data, we estimate the age of group A to be $\tau_1 = (9.0 \pm 1.3)$ My. This value agrees satisfactorily with the 8.3 My age-estimate of the regular component of the family, taking into account the approximative nature of our assumptions. A similar calculation can be performed for the J_2 distribution. The corresponding values are $\sigma(J_2) = 3.6 \cdot 10^{-4}$ and $\tau_2 = (18.6 \pm 2.7)$ My. The reason for which τ_1 is closer to the value obtained from the analysis of the regular bodies is that the initial J_1 distribution is much closer to a delta function, which is the expected distribution of family members immediately after break-up, than the J_2 distribution.

3 Conclusion

We have shown in this paper that the methods to determine the age of asteroid families improved in the recent years to the point that we can nowadays estimate the age of a number of asteroid families quite accurately, providing they comprise members having either very stable, or strongly (diffusively) chaotic orbits. These dynamical methods have been applied in a number of cases (Veritas, Karin, Eos), of which we have described here the case of Veritas. The results of the application of two independent methods presented here agree fairly well, and this indicates that the family of Veritas has most probably been created as a whole in a single break-up event. It is a very young family, and indeed the youngest known family in the main asteroid belt originated from the parent body as large as 150 km in diameter.

Acknowledgement

This research has been supported by the Ministry of Science and Environmental Protection of Serbia through the project No 146004 "Dynamics of celestial bodies, systems and populations".

References

Knežević, Z. 1999, in: *Evolution and source regions of asteroids and comets. Proc. IAU Coll. 173*, J. Svoren, E.M. Pittich and H. Rickman (eds.), Astron. Inst. Slovak Acad. Sci., Tatranska Lomnica, p. 153

Knežević, Z., Pavlović, R. 2002, Earth, Moon, Planets, 88, 155

Knežević, Z., Tsiganis, K., and Varvoglis, H. 2002. in: *Proceedings of the Conference Asteroids, Comets, Meteors (ACM 2002)*, B. Warmbein (ed.), (Noordwijk: ESA-SP-500), p. 335

Milani, A., and Nobili, A.M. 1992, Nature, **357**, 569

Milani, A., Farinella, P. 1994, Nature, **370**, 40

Milani, A., and Knežević, Z., 1994. Icarus **107**, 219

Morbidelli, A. Zappalà, V., Moons, M., Cellino, A., and Gonczi, R. 1995. Icarus, **118**, 132

Nesvorný, D., and Morbidelli, A., 1998. AJ, **116**, 3029

Nesvorný, D., Bottke, W.F. Jr., Dones, L., Levison, H. F. 2002, Nature, **417**, 720

Nesvorný, D., Bottke, W.F., Levison, H.F., Dones, L., 2003, ApJ, **591**, 486

Tsiganis, K., Knežević, Z. Varvoglis, H. 2006, Icarus, submitted.

Vokrouhlický, D., Brož, M., Bottke, W.F., Nesvorný, D., Morbidelli, A. 2005, in: *Dynamics of Populations of Planetary Systems, Proceedings IAU Coll. 197*, Z. Knežević and A. Milani (eds.) Cambridge University Press, p. 145

Zappalà, V., Bendjoya, Ph., Cellino, A., Farinella, P., and Froeschlé, C., 1995. Icarus, **116**, 291

PADEU | PADEU 19 (2007), p. 195
ISBN 963 463 557
©Published by the Astron. Dept. of the Eötvös Univ.

P–TYPE ORBITS IN THE PLUTO–CHARON SYSTEM

Imre Nagy[1], Áron Süli[2], Bálint Érdi[3]

[1],[2],[3] Eötvös University, Department of Astronomy, H-1518 Budapest, Pf. 32, Hungary

E-mail: [1]I.Nagy@astro.elte.hu, [2]A.Suli@astro.elte.hu,
[3]B.Erdi@astro.elte.hu

Abstract
The dynamical structure of the phase space of the Pluto–Charon system is studied in the model of the spatial circular restricted three-body problem by using numerical methods. With the newly discovered two small satellites Hydra and Nix, the Pluto–Charon system can be considered as the first known binary system in which celestial bodies move in P-type orbits. It is shown that the two satellites are in the stable region of the phase space and their origin by capture is unlikely.
Keywords: *Celestial mechanics – planets and satellites: general – Kuiper Belt – methods: numerical*

1 Introduction

In 1930 C. Tombaugh discovered Pluto, the ninth planet of the Solar system. Pluto's first moon, Charon was found by Christy & Harrington (1978). The Pluto–Charon system is remarkable, since in the Solar system Charon is the largest moon relative to its primary, with the highest mass-ratio 0.130137. Subsequent searches for other satellites around Pluto had been unsuccessful until mid May 2005, when two small satellites designated as Hydra and Nix were discovered (Stern et al., 2005). With this observation Pluto became the first Kuiper Belt object known to have multiple satellites. These new satellites are much smaller than Charon, with diameters 61-167 km (Hydra) and 46-137 km

(Nix) depending on the albedo. Both satellites appear to be moving in nearly circular orbits in the same orbital plane as Charon, with orbital periods 38 days (Hydra) and 25 days (Nix).

From a dynamical point of view the Pluto–Charon system corresponds to such a binary system whose mass parameter is approximately one tenth. The phase space of binaries and the Pluto–Charon system can be studied simultaneously. To survey the phase space of binaries is a fundamental task, since more and more exoplanetary systems are being discovered. The great majority of exoplanets have been observed around single stars, but more than 15 planets are already known to orbit one of the stellar components in binary systems (this type of motion is referred to as satellite or S-type motion).

There are some studies on planetary orbits in binaries. The so far discovered planets in binaries move in S-type orbits. Theoretically there is another possible type of motion, the so-called planetary or P-type, where a planet moves around both stars. There are several studies on S- and P-type motions using the model of the planar elliptic restricted three-body problem see e.g. (Dvorak, 1984, 1986; Holman & Wiegert, 1999; Pilat-Lohinger & Dvorak, 2002) and references therein. The three-dimensional case, that is the effect of the inclination was studied by Pilat-Lohinger, Funk & Dvorak (2003) for P-type orbits in equal-mass binary models.

The main goal of this paper is to investigate the dynamical structure of the phase space of the Pluto–Charon system which can be considered as the first known binary system in which celestial bodies, namely Hydra and Nix move in P-type orbits. In Section 2 we describe the investigated model and give the initial conditions used in the integrations. The applied numerical methods are briefly explained in Section 3. The results are shown in Section 4. Section 5 is devoted to some conclusions.

2 Model and initial conditions

To study the structure of the phase space of the Pluto–Charon system we applied the model of the spatial circular restricted three-body problem. We integrated the equations of motion by using a Bulirsch–Stoer integrator with adaptive stepsize control. The orbits of the primaries were considered circular and their mutual distance A was taken as unit distance. The orbital plane of the primaries was used as reference plane, in which the line connecting the primaries at $t = 0$ defines a reference x-axis. We assume that the line of nodes of the orbital plane of the massless test particle (i.e. Hydra or Nix) coincides with the x-axis at

$t = 0$, thus the ascending node $\Omega = 0°$. The pericenter of the test particle's orbit is also assumed to be on the x-axis at $t = 0$, thus the argument of the pericenter $\omega = 0°$. Though Hydra and Nix are in the orbital plane of Charon, still we study the problem more generally by considering the effect of non-zero inclinations on the orbital stability. Thus our results are applicable to a wider class of satellite or planetary systems around binaries for the mass parameter $\mu = m_2/(m_1 + m_2) = 0.130137$, corresponding to the Pluto–Charon system (m_1 and m_2 being the mass of Pluto and Charon, respectively).

To examine the phase space and the stability properties of P-type orbits, we varied the initial orbital elements of the test particle in the following way (see Table 1):

- the semimajor axis a is measured from the barycentre of Pluto and Charon and it is varied from 1 to 5 A with stepsize $\Delta a = 0.005$ A,
- the eccentricity e is varied from 0 to 0.3 with stepsize $\Delta e = 0.05$ ($\Delta e = 0.002$ in Fig. 2),
- the inclination i is varied from 0° to 180° with stepsize $\Delta i = 1°$,
- the mean anomaly M is given the values: 0°, 45°, 90°, 135°, and 180°.

The above orbital elements refer to a barycentric reference frame, where the mass of the barycentre is $m_1 + m_2$. By the usual procedure we calculated the barycentric coordinates and velocities of the test particle and then transformed them to a reference frame with Pluto in the origin. In the numerical integrations we used the latter coordinates and velocities.

In total almost six million orbits were integrated for 10^3 Charon's period (hereafter T_C) and approximately 500 thousand for 10^5 T_C.

3 Methods

To determine the dynamical character of orbits we used three methods. The method of the relative Lyapunov indicator (RLI) was introduced by Sándor, Érdi & Efthymiopoulos (2000) for a particular problem, and its efficiency was demonstrated in a later paper (Sándor et al., 2004) for 2D and 4D symplectic mappings and for Hamiltonian systems. This method is extremely fast to determine the ordered or chaotic nature of orbits.

For an indication of stability a straightforward check based on the eccentricity was used. This action-like variable shows the probability of orbital crossing

Table 1: *In the first three rows the orbital elements from unrestricted fits (epoch = 2452600.5) are listed (Buie et al., 2005): a, e, i, ω, Ω and M denote the semimajor axis, eccentricity, inclination, argument of the pericenter, longitude of the ascending node, and mean anomaly. In the last column the orbital periods are given in days. The orbital elements for P-type orbits are given with the corresponding stepsizes.*

Object	a [A]	e	i[°]	ω[°]	Ω[°]	M[°]	T [day]
Charon	1.0	0	96.145	–	223.046	257.946	6.387
Nix	2.487	0.0023	96.18	352.86	223.14	267.14	25
Hydra	3.31	0.0052	96.36	336.827	223.173	122.71	38
P-type	0.55–5	0–0.3	0–180	0	0	0–180	
Δ	0.005	0.05	1	–	–	45	

and close encounter of two planets, and therefore its value provides information on the stability of orbits. We examined the behaviour of the eccentricity of the orbit of the test particle along the integration, and used its largest value ME as a stability indicator; in the following we call it the maximum eccentricity method (hereafter MEM). This simple check was already used in several stability investigations, and was found to be a powerful indicator of the stability character of orbits (Dvorak et al., 2003; Süli, Dvorak & Freistetter, 2005).

The maximum difference of the eccentricities method (MDEM). We developed this new method and applied it for the first time in this investigation. Two initially nearby trajectories emanating from a chaotic domain of the phase space will diverge according to the strength of chaos. The divergence manifests itself in the differences between the eccentricities of the orbits and in the angle variables. The more chaotic the system is, the faster the difference in the eccentricities grows. This difference is sensible to the variations around the running average of the eccentricity and depends also on the position along the orbit. Thus if the positions along the two orbits change chaotically, the eccentricities of the two orbits also behave differently and their momentary differences can be large even if the average value of the eccentricity of each orbit remains small. This method characterises the stability in the phase space, whereas the MEM does it in the space of orbital elements. We define the stability indicator MDE as:

$$\mathrm{MDE}(t) = \max|e(t, x_0) - e(t, x_0 + \Delta x)|, \tag{1}$$

where x_0 is the initial condition of the orbit and Δx is the distance of the

nearby orbit in the phase space. The method of the MDE has the advantage with respect to the MEM that in the case of chaotic orbits the MDE grows more rapidly than the ME, and while the difference between the ME for regular and chaotic motions is only 1-2 orders of magnitude, this can be 4-7 orders of magnitude for the MDE and therefore can be detected more easily.

4 Results

We show the results of our investigations in Figs. 1 – 2. These were obtained as follows. By varying the initial orbital elements as described in Section 2, we performed the integration of each orbit for five different initial values of the mean anomaly: $M = 0°, 45°, 90°, 135°$, and $180°$. For each M the indicators $I^{(M)}(a, e, i)$ were determined, where $I^{(M)}$ stands for RLI, ME, and MDE, respectively. Any value, plotted in the figures, is an average over M:

$$\bar{I}(a, e, i) = \frac{1}{5} \sum_{M} I^{(M)}(a, e, i). \tag{2}$$

We note, that this averaging in the case of the RLI and the MDE emphasises the chaotic behaviour of an orbit, while in the case of the ME is not so drastic.

The three methods are not equivalent, however they complete each other. The ME detects macroscopic instability (which may even result in an escape from the system), whereas the RLI and the MDE are capable to indicate microscopic instability.

In most of the simulations the $I^{(M)}$ values were calculated for 10^3 T_C. To decide whether this time interval is enough to map the real structure of the phase space, several test runs were done for a much longer time span, for 10^5 T_C.

We found that the maps obtained from simulations for a time span of 10^5 T_C and 10^3 T_C are in close agreement. Thus we can conclude that the phase space of the Pluto–Charon system can be surveyed in a reliable way by using a time span of 10^3 T_C.

4.1 The phase space of the Pluto–Charon system

We investigated the behaviour of P-type orbits systematically by changing the initial orbital elements of the test particle as described in Section 2 (see also Table 1). Beside direct orbits ($i < 90°$) we studied also retrograd P-type motion ($i > 90°$) of the test particle. All the integrations were made for 10^3 T_C. The

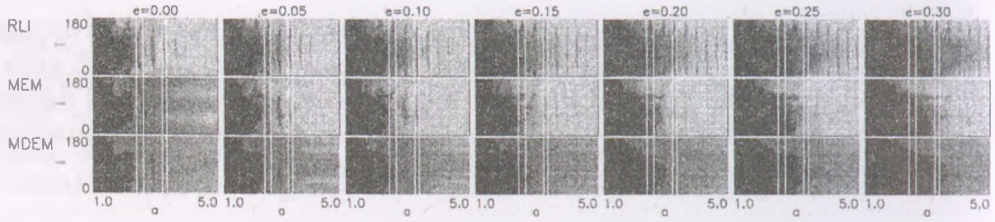

Figure 1: *The results of the 10^3 T_C simulations for $e = 0, \ldots, 0.3$ in the a, i plane. The dark area is unstable, the grey regions are stable. See text for details.*

results are shown in Fig. 1, where the indicators $\bar{I}$ are plotted on the a, i plane for different values of e.

In general, the results show an increase of the chaotic area for higher eccentricities: for $i < 160°$ the chaotic region grows with e. However, the rate of the increase strongly varies with the inclination. The stabile region is more extended for retrograde ($i > 90°$) then for direct ($i < 90°$) orbits. It can also be seen that the resonant islands (4:1 at $a = 2.52$ A, 5:1 at $a = 2.92$ A etc.) merge with the growing chaotic zone. The most striking feature is that the stability of the retrograd P-type motion practically does not depend on e. Inspecting Fig. 1 it is evident that the border of the chaotic zone for $i > 160°$ stay almost constantly at $a \approx 1.7$ A.

4.2 Stability of the satellites Hydra and Nix

We have addressed the problem of stability of the recently discovered satellites of Pluto. The results are shown in Fig. 2, where the values of the MDE (computed for 10^3 T_C and averaged over for the mean anomalies) are plotted on the a, e plane for the planar case ($i = 0°$). Below $a = 2.15$ A the system is unstable for all e, above $a = 2.15$ A there is a stable region depending on e. The two satellites are situated here, in the small rectangles, indicating their dynamically possible most probable places of occurance. These rectangles are defined by the ME, computed in the vicinity of each satellite. This means that we took a grid around the present value of a of each satellite with a stepsize $\Delta a = 0.005$ A, $\Delta i = 1.25°$ in the interval $i = 0 - 180°$, and with initial $e = 0$ we computed the largest ME_{max} during 10^5 T_C (including averaging over the five values of M). We obtained that $\mathrm{ME}_{max} = 0.045$ for Nix and $\mathrm{ME}_{max} = 0.02$ for Hydra. In Fig. 2 these values give the height of the rectangles. We computed the possible

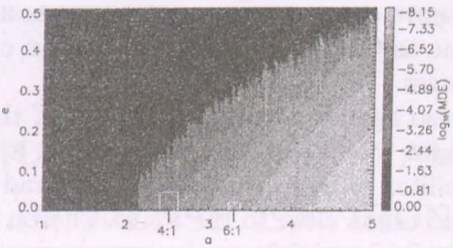

Figure 2: *Stability map in the a, e plane.*

minimal $r_p = a(1-\mathrm{ME}_{max})$ pericenter and maximal $r_a = a(1+\mathrm{ME}_{max})$ apocenter distances of the satellites, these are 2.41 and 2.63 A for Nix and 3.23 and 3.37 A for Hydra. These values define the horizontal limits of the rectangles in Fig. 2, and also the places of the vertical lines in Fig. 1.

From Fig. 2 it can be seen that the determined orbital elements of the two satellites are well in the stable domain of the phase space. If Nix and Hydra move in the orbital plane of Charon, their eccentricities cannot be larger than 0.17 and 0.31, respectively. The present semimajor axis a of Nix is very close to the 4:1 resonance with Charon, whereas that of Hydra is close to 6:1. The locations of the exact resonances are well inside the small rectangles. We presume that these satellites probably move in resonant orbits. This could be confirmed by new observations.

5 Conclusions

Up to now the Pluto–Charon system is the only known binary system which has a relatively large mass-ratio and celestial bodies revolve around it in P-type orbits. This circumstance and the high ratio of binary stellar systems among stars make it important to study the stability properties of P-type orbits in binaries and particularly in the Pluto–Charon system. Our investigations show that the stable region is wider for retrograd than for direct P-type orbits. With the increase of the eccentricity the chaotic region becomes larger, and because of it the eccentricities of the two satellites, at their present semi-major axis, cannot be higher than 0.17 for Nix and 0.31 for Hydra. Below $a = 2.15\ A$ orbits are unstable for all eccentricities, thus no satellite could exist here.

Stern et al. (2005) has shown that Hydra and Nix were very likely formed together with Charon, due to a collision of a large body with Pluto, from mate-

rial ejected from Pluto and/or the Charon progenitor. This is based on the facts that Hydra and Nix move close to Pluto and Charon in nearly circular orbits in the same orbital plane as Charon, and they are also in or close to higher-order mean motion resonances.

Our results are also against the capture origin of these satellites. Firstly, since the stability region for retrograd orbits is wider, it would have been more probable for the satellites to be captured into retrograd than for direct orbits. Secondly, capture into orbits close to the Pluto–Charon binary cannot be with high eccentricity ($e > 0.17$ and 0.31 at the present semimajor axis of Nix and Hydra), since these orbits become unstable on a timescale of $10^3\ T_C$. On the other hand, for eccentric capture orbits the tidal circularisation time for Hydra and Nix is much longer than the age of the Solar System as Stern et al. (2005) pointed out.

Acknowledgement

Most of the numerical integrations were accomplished on the NIIDP (National Information Infrastructure Development Program) cluster grid system in Hungary. The support of the Hungarian NRF, grant no. OTKA T043739 is also acknowledged.

References

Christy, J. W., Harrington, R. S., 1978, AJ, 83, 1005

Dvorak, R., 1984, Celest. Mech., 34, 369

Dvorak, R., 1986, A&A, 167, 379

Dvorak, R., Pilat-Lohinger, E., Funk, B., Freistetter, F., 2003, A&A, 398, L1

Holman, M. J., Wiegert, P. A., 1999, AJ, 367, 943

Pilat-Lohinger, E., Dvorak, R., 2002, Celest. Mech. & Dyn. Astron., 82, 143

Pilat-Lohinger, E., Funk, B., Dvorak, R., 2003, A&A, 400, 1085

Sándor, Zs., Érdi, B., Efthymiopoulos, C., 2000, Celest. Mech. & Dyn. Astron., 78, 113

Sándor, Zs., Érdi, B., Széll, A., Funk, B., 2004, Celest. Mech. & Dyn. Astron., 90, 127

Süli, Á., Dvorak, R., Freistetter, F., 2005, MNRAS 363, 241

Stern, S. A., Weaver, H. A., Steffl, A. J., Mutchler, M. J., Merline, W. J., Buie, M. W., Young, E. F., Young, L. A., et al., 2005, (astro-ph/0512599)

Buie, M. W., Grundy, W. M., Young, E. F., Young, L. A., Stern, S. A., 2005, (astro-ph/0512591)

PADEU | PADEU 19 (2007), p. 203
ISBN 963 463 557
©Published by the Astron. Dept. of the Eötvös Univ.

Morphology and Dynamics of Galaxies in Dense Environments of Radio Galaxies

Nedelia Aantonia Popescu

Astronomical Institute of the Romanian Academy, RO-040557 Bucharest, Romania

E-mail: nedelia@aira.astro.ro

Abstract

The determination of the galaxy interaction rate is obtained by measuring the incidence of strongly-disturbed galaxies or close pairs of galaxies. Photometrical data and HST/WFPC2 morphology of galaxies in dense environments of 3C 220.1 and 3C 34 radio galaxies are used in order to measure the rate of major galaxy merging/ interaction. In our study we determine the photometric redshifts of galaxies and we analyze the frequency of galaxies close pairs in the fields studied.

Keywords: *Galaxies: morphology, dynamics, interactions*

1 Introduction

Radio galaxies are used as efficient tracers of high redshift clustering, because they are usually situated in dense environments. These galaxies configurations represent an opportunity to determine the galaxy interaction rate by measuring the incidence of strongly-disturbed galaxies or close pairs of galaxies.

This paper presents the results of a photometrical, morphological and dynamical study of galaxies in the field of the radio galaxies 3C 220.1 ($z = 0.62$, 64 gal. in a 6.2 arcmin^2 field) and 3C 34 ($z = 0.689$, 89 gal. in a 6.2 arcmin^2 field), using optical and NIR photometrical data (V, I, J, H, K) and HST/WFPC2 morphological data of Stanford et al. 2002.

The primary aims of this paper are:

– to determine the photometric redshifts for the galaxies in the fields studied;

– to search for clustering features of galaxies with similar redshifts in the fields studied;

– to measure the incidence of close pairs of galaxies or strongly-disturbed galaxies.

2 Photometric redshifts determinations

The photometric redshifts technique concentrates on broad features, such as the 4000Å break, and the global shape of a spectrum, redshifts being obtained by comparing the broad band photometry to predictions from galaxy spectral energy distributions (SED's).

Using the Z-PEG software (Le Borgne & Rocca-Volmerange, 2002) we obtain the redshifts for galaxies in the field of 3C 220.1 and 3C 34 radio galaxies. Z-PEG effectuates a χ^2 test, representing the minimization of the distance between the photometric bands observed and synthetic photometry from galaxies simulated by the evolutionary code PEGASE.

In our study the photometrical data are corrected for Galactic reddening. The optical data are calibrated into the Landolt system and the NIR data into the CIT system. The typical rms of these calibration are 0.02 (optical) and 0.03 (NIR).

For our photometric redshifts determinations we consider:

– 5 colors: $(V-I)$, $(J-K)$, $(V-K)$, $(H-K)$, $(I-K)$ (transformed into the Bessel, Brett (1988, 1990) system in order to be in the same system with Z-PEG model);

– the spectral types of template galaxies to be used in the fitting procedure (Starburts - E - S0 - Sa - Sb - Sbc - Sc - Sd - Im);

– the redshift step (0.05);

– the age (2 Myr - 17 Gyr)/redshift range ($0 < z < 5$) of the fitting procedure;

– the cosmological parameters H_0=65 km/s/Mpc, q_0=0.15.

In Figures 1 and 2 we present the histograms of the photometric redshifts determined for galaxies with $K < 19.5$ mag in 3C 220.1 and 3C 34 fields.

For 3C 220.1 field we determined 17 galaxies in the redshift range $0.45 < z < 0.7$ (E/S0) and 26 galaxies in the redshift range $0.75 < z < 1.05$ (15 E/S0, with $z \sim 0.8$). The peak in the redshifts distribution possible represents a galaxies cluster at $z \sim 0.8-0.9$, superposed on the poor cluster of galaxies at the redshift of radio galaxy 3C 220.1 ($z \sim 0.65$).

For 3C 34 field we determined 40 galaxies in the redshift range $0.65 < z < 1$. The peak around $z \sim 0.85$ is conspicuous in the photometric redshifts distribution. Galaxies are mostly E/S0 and constitute a possible cluster of galaxies at $z \sim 0.85$.

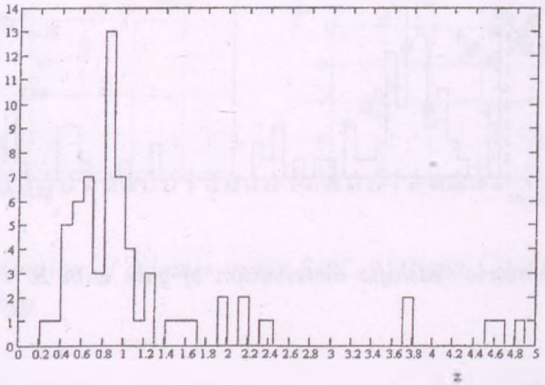

Figure 1: *Photometric redshifts distribution of gal. with $K < 19.5$ mag in 3C 220.1 field*

3 The galaxies distribution function of HST/ WFPC2 morphology

The distribution of the galaxies function of HST/WFPC2 morphology is presented in Figure 3.

For 3C 220.1 field the symbols are as follows: squares - E/S0 galaxies (22 gal.); dots - S galaxies (16 gal.); diamonds - Irr/mergers galaxies (i.e. galaxies in interaction) (20 gal.); + - galaxies outside the WFPC2 field (6 galaxies with undetected morphology).

On the existing symbols the following ones are overlapped: (+) - 17 galaxies with photometric redshifts in the redshift range $0.45 < z < 0.7$; (X) - 26 galaxies with photometric redshifts $0.75 < z < 1.05$ are clustered in three groups, containing 15 E/S0 galaxies. Only 11 galaxies are located in the inner region of the field (50″) close to the brightest cluster galaxy (with K=15.76, $(I-K)$=2.74, $(J-K)$=1.7).

For 3C 34 field there are the following symbols: squares - E/S0 galaxies (19

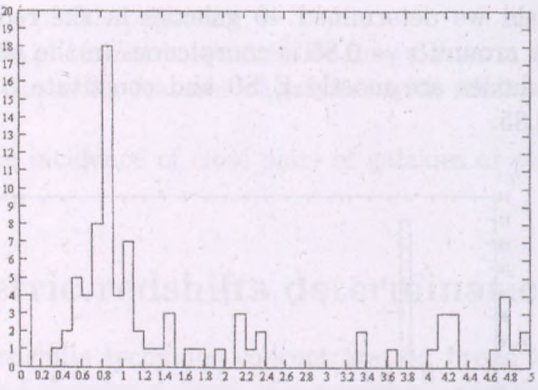

Figure 2: *Photometric redshifts distribution of gal. with $K < 19.5$ mag in 3C 34 fields*

gal.); dots - S galaxies (2 gal.); diamonds - Irr/mergers galaxies (17 gal.); (+) - galaxies outside the WFPC2 field (51 galaxies with undetected morphology).

The symbols (X) are overlapped on the existing ones and represent 40 galaxies with photometric redshifts in the range $0.65 < z < 1$. 30 galaxies with $0.65 < z < 1$ are clustered in the inner region of the field (50″) close to the brightest cluster galaxy (K=15.54, $(I-K)$=2.97, $(J-K)$=1.96), possibly representing a cluster of galaxies at $z \sim 0.85$.

4 Incidence of strongly-disturbed galaxies or close pairs of galaxies

An integrated measure of galaxy clustering on small scales is provided by close pair statistics. These statistics are often assumed to be independent of selection effects such as sampling depth and completeness.

Pairs of galaxies can be uniquely specified by their projected physical separation and rest-frame line-of-sight velocity difference:

$$\begin{gathered} 10h^{-1}kpc < \Delta r_{proj} < r_{max} with r_{max} = 30, 50, 100\ h^{-1}kpc \\ \Delta v < 500 km/s \end{gathered} \tag{1}$$

For a close companion that is likely to merge soon (within 0.5 Gyr), the

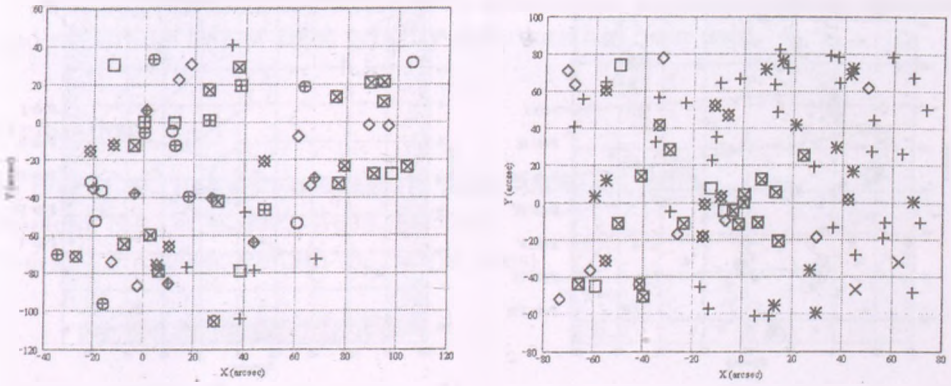

Figure 3: *The distribution of galaxies in the field of 3C 220.1 (left) and 3C 34 (right) function of morphology*

following conditions are considered:

$$\Delta r_{proj} < 20h^{-1}kpc; \Delta v < 500km/s \tag{2}$$

The spatial distribution of galaxies pairs, that meet condition (1), is presented in Figure 4.

In Figure 4 - top (3C 220.1 field), Pairs I and IV consist of galaxies with redshifts in the range $0.45 < z < 0.7$ and projected distances smaller than 50 kpc. The interaction is obvious in the case of Pair I and Pair IV, where a mixed morphology is revealed.

For Pair I, the BCG (E/S0) interacts with an irregular galaxy and a spiral one (see also the distribution of galaxies in the field of 3C 220.1 function of morphology). So, a single galaxy can contribute to two separate dinamically bounded pairs, forming a triplet system in our pair sample. In the field of 3C 220.1, four triplet systems are detected.

Pairs II, III, V, VI and VII consist of galaxies with redshifts in the range $0.75 < z < 1.05$. The mixed morphology can be also observed for Pairs III, V, VI and VII. Pairs III and V contain galaxies that are classified as mergers or galaxies in interaction.

In Figure 4 - bottom (3C 34 field), Pair I is formed by galaxies with redshifts in the range $0.65 < z < 1$ and projected distances smaller than 50 kpc. This is the most interesting region because the BCG (E/S0) interacts especially with other E/S0 galaxies (see also the distribution of galaxies in the field of 3C 34

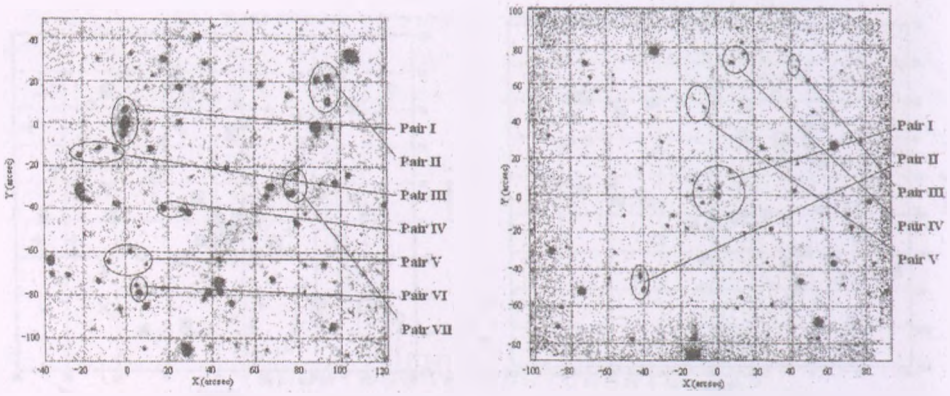

Figure 4: *K-band image of 3C 220.1 (left) and 3C 34 (right) - the distribution of pairs of galaxies*

function of morphology).

Pairs II, III, IV and V contain galaxies with redshifts in the range $0.65 < z < 1$, the mixed morpohology existing only for Pair II.

5 Conclusions

This study belongs to an extended study of search for galaxies clusters and close pairs of galaxies, in the redshift range $0.6 < z < 1.3$ (Popescu, 2006). Our goal is to identify and analyze some morphological, photometric and dynamical properties of disk galaxies and elliptical galaxies at different stages of interaction.

Photometrical data and HST/WFPC2 morphology of galaxies are used in order to obtain the photometric redshifts of galaxies and to analyze the frequency of galaxies close pairs, in dense environments of 3C 220.1 and 3C 34 radio galaxies

Using the Z-PEG software (Le Borgne & Rocca-Volmerange, 2002) we determine the redshifts for galaxies in the field of 3C 220.1 ($z = 0.62$) and 3C 34 ($z = 0.689$) radio galaxies (a total of ~ 150 gal.).

The presence of clustering features of galaxies with similar redshifts is revealed in both fields (especially in the 3C 34 field).

For our study we analyze a sample of 12 pairs of galaxies, observing only 8 mixed pairs (i.e. an elliptical/lenticular galaxy + a spiral or irregular/merger galaxy).

A strong pair isolation criterion in terms of the apparent angular separation and rest-frame line-of-sight velocity difference has been used.

References

Le Borgne, D., Rocca-Volmerange, B. 2002, A&A, 386, 446

Stanford, S.A., et al. 2002, ApJS, 142, 153

Popescu, N.A. 2006, RoAJS, 16, 135 (in press)

Part IV

Chaotic and Regular Motions, Capture, Numerical Methods

PADEU | PADEU **19** (2007), p. 213
ISBN 963 463 557
©Published by the Astron. Dept. of the Eötvös Univ.

On the Long Time Energy Conservation by High Order Geometric Integrators

Călin Ioan Gheorghiu[1], Adrian C. Mureşan[2]

T. Popoviciu Institute of Numerical Analysis, Romanian Academy
P.O. Box 68, 400110 Cluj-Napoca, Romania

E-mail: [1]ghcalin@ictp.acad.ro [2]acmuresan@ictp.acad.ro

Abstract
The main aim of this paper is to investigate the long-time behavior of three high order geometric integrators, namely an implicit Runge-Kutta-Gauss method, the composed Störmer-Verlet method and a high order linear multistep method. All these three families of methods perform fairly accurate, at least qualitatively, when they are used in the integration of the outer Solar system. No spiral outwards or inwards are observed when their orders exceed six. With the long time energy conservation the situation change considerable. A significant improving in the computation of Hamiltonian is observed passing from order two to six but further, in contrast with the trajectories, almost nothing is gain by increasing the order of the method. A partial answer to this intriguing situation is furnished by the analysis of round off errors.
Keywords: *N-body problem, outer Solar system; composed geometric integrators, round-off errors, compensated summation, long time energy conservation*

1 Introduction

It would seem to be an obvious goal for a Hamiltonian integration method both to preserve the symplectic structure of the flow and to conserve the energy, but it has been shown that this is in general impossible (Zhong and Marsden,

1988). Thus a symplectic method which only approximate a Hamiltonian cannot conserve the total energy of the system. Energy conserving algorithms have been designed at the expense of not being symplectic, but for most applications retaining the Hamiltonian structure is more important than energy conservation.

A large number of numerical studies, during the last two decades, confirmed that using symplectic integrators the energy can only undergo bounded oscillations. This is in contrast to integrating the same Hamiltonian system with a nonsymplectic method, where there would be no bound on the energy, which could then increase or decrease without limit, transforming the system into a dissipative one, with completely different long-term behavior. It is well known that the dissipative systems have attractors and Hamiltonian systems do not. This is a major advantage of symplectic methods.

There is a further point about symplectic maps that affects all numerical methods using floating point arithmetic, and that is round-off error. Round-off error is a particular problem for Hamiltonian systems, because it introduces non-Hamiltonian perturbations despite the use of symplectic integrators. In this respect we observe that the Hamiltonian systems are not generic in the set of all dynamic systems, in the sense that they are not structurally stable against non-Hamiltonian perturbations.

Although symplectic methods of integration are undoubtedly to be preferred in dealing with Hamiltonian systems, it should not be supposed that they solve all difficulties of integrating them; they are not perfect. Channell and Scovel (1990) give examples of local structures introduced by using such methods.

The contents of this paper are as follows. In the second section we introduce the governing equations and the numerical methods, in the third section we carry out the numerical experiments and eventually we present some concluding remarks.

2 Governing equations and numerical methods

When we treat each planet as a point of mass m_i with position r_i, $i = 1, 2, \ldots, N$, in a heliocentric frame, the planetary orbits satisfy the following Newtonian system

$$\ddot{r}_i = -\frac{G\left(M_S + m_i\right) r_i}{\left|r_i\right|^3} + \sum_{\substack{j=1 \\ j \neq i}}^{N} \frac{G m_j \left(r_j - r_i\right)}{\left|r_j - r_i\right|^3} - \sum_{\substack{j=1 \\ j \neq i}}^{N} \frac{G m_j}{\left|r_i\right|^3} r_j. \tag{1}$$

Here M_S and G stand for the mass of the Sun and the Gaussian constant respectively. The Hamiltonian corresponding to this system is *separated* and reads

$$H(p,q) = \frac{1}{2}\sum_{i=1}^{N} m_i p_i^2 - 3G\sum_{i=1}^{N}\frac{(M_S+m_i)}{\|q_i\|} - G\sum_{\substack{j=1\\ j\neq i}}^{N} m_j\left(\frac{3}{\|q_i-q_j\|} - \frac{q_i q_j}{\|q_j\|^3}\right). \tag{2}$$

In this expression p and q are vectors of N components p_i and q_i respectively, $q_i := (r_{i,1}\ r_{i,2}\ r_{i,3})^t$ and $\dot{p}_i := q_i$.

The second order differential system (1) is transformed into a first order one and then integrated starting from the initial data $r_i(t_0)$, $\dot{r}_i(t_0)$, $i = 1, 2, \ldots, N$.

The first method used, in order to solve numerically this Cauchy problem, is an implicit Runge-Kutta one. It was introduced mainly in the work of Butcher (1963) and is discussed in details in Chapters V and VI of the monograph of Hairer et al. (2006). The method is symplectic and symmetric, so that it is well suited in the context of geometric integration.

The second method is a partitioned multistep method. It is known that neither explicit nor implicit classical multistep methods have been successful in geometric integration. More than that it is not evident to discuss symplecticity and symmetry of multistep methods because they are not transformations on the phase space. However, Kirchgraber (1986) showed that to every consistent strictly stable multistep method one can associate a so-called *underlying one-step method* which has the same long-time dynamics. In this sense it is natural to call the multistep method symplectic and symmetric if the underlying one-step method has these properties respectively. In our experiments we used a method of order eight which is analyzed in the monograph of Hairer et al. (2006), Chap. XV.

The third method is the so-called Störmer/Verlet method. This method has the following properties: it is of order two, it is symmetric and symplectic, it exactly conserves quadratic first integrals, e.g., the angular momentum in N-body problems and, unlike the methods above, for separable Hamiltonians, it is explicit. As for long time computations in astronomy, where a very high accuracy is demanded, the order two of this method is too low, we will use in our experiments the composed of the method up to order ten. The method is almost exhaustively examined in Hairer et al. (2003).

In order to quantify the importance of round-off errors in long term behavior of Störmer/Verlet method we reported in our paper (Gheorghiu and Muresan, 2006) the following result.

For the second order system

$$\begin{cases} \dot{q} = p, \\ \dot{p} = f(q), \end{cases}$$

the Störmer/Verlet method reads

$$\begin{cases} q_{n+1} = q_n + h\left(p_n + \frac{h}{2} f(q_n)\right), \\ p_{n+1} = p_n + \frac{h}{2}\left(f(q_n) + f(q_{n+1})\right), \ n = 0, 1, 2, \ldots \end{cases} \tag{3}$$

Consider two sequences (p_n, q_n) and $(\bar{p}_n, \bar{q}_n)$ defined respectively by (3) and a similar system perturbed by ε_n^i, $i = 1, 2$ where $|\varepsilon_n^i| < \varepsilon$, ε being the machine rounding-off constant, i.e., $\varepsilon = 10^{-16}$. Suppose that the vector field f is Lipschitzian of constant L and introduce the notations $\alpha_n := \|q_n - \bar{q}_n\|$ and $\beta_n := \|p_n - \bar{p}_n\|$. Then our result reads

$$\max(\alpha_{n+1}, \beta_{n+1}) \leq$$
$$\leq \left(1 + \sqrt{L + \left(\frac{hL}{2}\right)^2}\right) \cdot \left[\max(\alpha_0, \beta_0) + (n+1)\max\left(1, 1 + \frac{hL}{2}\right)\varepsilon\right] e^{T\Lambda},$$
$$n = 0, 1, 2, \ldots,$$

where $\Lambda = \frac{hL}{2} + \sqrt{L + \left(\frac{hL}{2}\right)^2}$ and T is the length of integration interval. This result improves that classical of P. Henrici (1962), p. 332, which refers to a larger class of multistep method for the above system, but contains the power T^2 instead of T in the above estimation. This gain was possible due to the fact that we analyzed the method as a one-step method.

3 Numerical experiments

The Hamiltonian system (1) was solved comparatively by using the above mentioned numerical methods. For the mass of each planet and initial data we used the values from the paper of Quinn et al. (1991), Appendix A. The period of integration was mildly large, up to 2×10^6 days, and $h = 10$ days.

As numerical codes we used the MATLAB codes from (Hairer, E. and Hairer, M.). They effectively implement the so-called *compensated summation* (see for instance (Higham, 1993) for this concept) in order to reduce the round-off errors. The oscillations of the Hamiltonian of the outer Solar system ($N = 5$), as well as its power spectrum, are depicted in Fig. 1. The maximal error in computing the Hamiltonian was equal to $1.4456361257225933e - 01$. The oscillations of

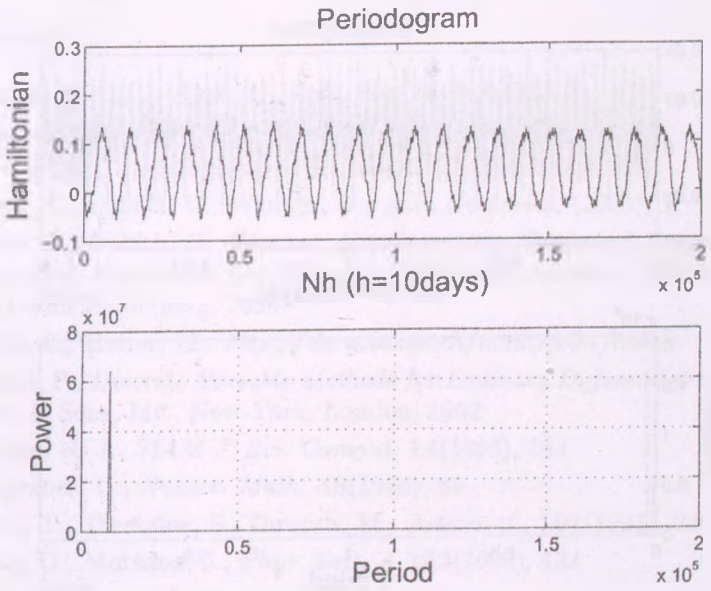

Figure 1: *The variations of the Hamiltonian of the outer Solar system* ($N = 5$)

the Hamiltonian of the reduced outer Solar system ($N = 4$), as well as its power spectrum, are depicted in Fig. 2. The oscillations of the *individual Hamiltonians* of these four planets (from Jupiter to Neptune) follow closely (remain in the same limits) the oscillations of this system. It is important to observe that in this case the maximal error was better, i.e., equal to $3.947533392243384e-02$. The worst approximation for Hamiltonian was encountered for the planet Pluto.

Comparing these two pictures it is a matter of evidence that the presence of the smallest planet in the model, worsen considerable the conservation of the Hamiltonian. It is also worth noting at this point that variations of mass of planet Pluto from $1/1.3e+08$ to $1/(3e+07)$ have no effect on the numerical results. Another important remark refers to the length of the interval of computation. We performed the experiments on various intervals ranging from 2×10^4 to 2×10^6 days. In spite of this quite large scale, no variation of the maximal error in the evaluation of Hamiltonian was noticed.

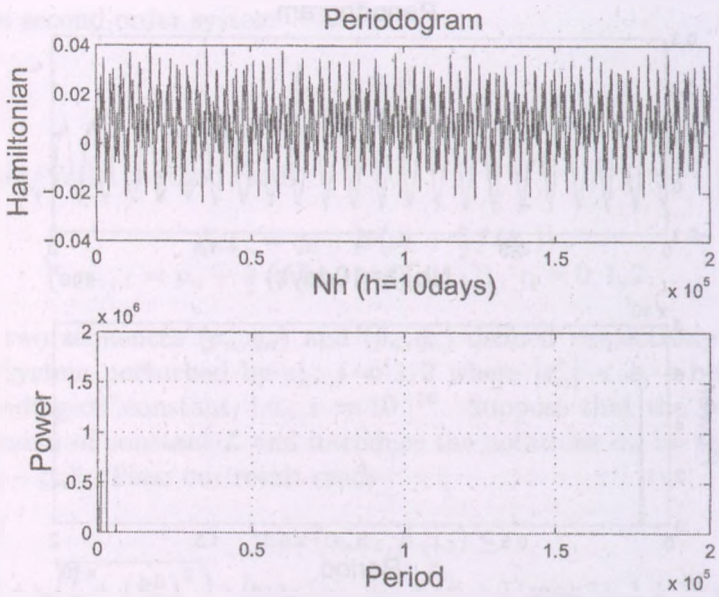

Figure 2: *The variations of the Hamiltonian of the outer Solar system* ($N = 4$)

4 Concluding remarks

The numerical experiments reported above, as well as a lot of others performed on perturbed Kepler's problem (Schwarzchild potential) or Kepler problem with large eccentricity, i.e. *eccentricity* $= 0.9$, confirm the net superiority of high order symplectic and symmetric methods over even higher order, but non symplectic methods such as Runge-Kutta and multistep methods.

The preservation of the total energy still remains an open problem. However it is quite clear that the increasing of order of symplectic and symmetric methods is only a partial solution. It seems that much more sophisticated techniques are needed in order to reduce the numerical noise.

Acknowledgement

The authors express their gratitude to all colleagues for stimulating discussions during the research seminaries of celestial mechanics and astronomy held at the Astronomical Observatory Cluj-Napoca in the winter-spring 2006.

References

[1] Butcher, J. C., *J. Austral. Math. Soc.* **3**(1963), 185

[2] Channell, P.J., Scovel, C., *Nonlinearity* **3**(1990), 231

[3] Gheorghiu, C.I., Muresan, A. C., *RoAJ*, 2006 (submitted),

[4] Hairer, E., Lubich, C., Wanner, G., *Acta Numerica*, (2003), 1

[5] Hairer, E., Lubich, C., Wanner, G., *Geometric Numerical Integration- Structure Preserving Algorithms for Ordinary Differential Systems*, 2nd Ed. Springer Verlag, Berlin Heidelberg, 2006

[6] Hairer, E., Hairer, M., *http://www.unige.ch/math/folks/hairer*

[7] Henrici, P., *Discrete Variable Methods for Ordinary Differential Equations*, John-Wiley & Sons, Inc., New-York, London, 1962

[8] Higham, N. J., *SIAM J. Sci. Comput.* **14**(1993), 783

[9] Kirkgraber, U., *Numer. Math.* **48**(1986), 85

[10] Quinn, T., Tremaine, S., Duncan, M., *Astron. J.*, **101**(1991), 2287

[11] Zhong, G., Marsden, J., *Phys. Lett. A* **133**(1988), 134

PADEU | PADEU 19 (2007), p. 221
ISBN 963 463 557
©Published by the Astron. Dept. of the Eötvös Univ.

About the Efficiency of Fast Lyapunov Indicator Surfaces and Small Alignment Indicator Surfaces

Barna Kovács

Colegiul Naţional "Al. Papiu Ilarian", Tg-Mureş, Romania
Liceul Teoretic "Bolyai Farkas", Tg-Mureş, Romania

E-mail: t_barna_ro@yahoo.com,

Abstract
Chaos detection methods based on calculation of Fast Lyapunov Indicator (FLI) and Small Alignment Index (SALI) are known as fast methods. The celerity of these methods can be improved by the application of a fast and precise, numerical integration method like the conservative integration one. With an integrator, based on the conservative integration algorithm, I constructed SALI and FLI surfaces, to identify chaotic and non-chaotic zones near equilibrium points, and I compared the efficiency of these two chaos-detection methods. Accepting the SALI value as sample, I was interested in finding the value of FLI in the moment of apparition of chaos.
Keywords: *Chaos detection, small alignment index, fast Lyapunov indicator, conservative integration, restricted problem of three bodies*

1 The conservative integrator

The conservative integration method was introduced by *Shadwick, Bowman* and *Morrison* (Bowman et al. 1997, Shadwick et al. 1999, 2001). These authors argued that a faithful evolution of the dynamics is provided by building explicitly the knowledge of the analytical structure of the equations, for example preserving the known first integrals of the motion. They illustrated the method

applied to a three-wave truncation of the Euler equations, the Lotka-Volterra problem and the Kepler problem. *Kotovych et al.* (2002) extended the method to the equations of motion of n bodies in space: to circular restricted three-body problem, then to the general three-body problem and finally to the full n-body case. The equations describing the motion of the solar system form a conservative system: one should consider that in absence of friction no energy is lost, so the whole energy and the angular momentum are conserved. The description of the conservative integration method as it follows is based on the description presented in Froschlé et al. 1997b.

The basis of a conservative integration method is that the dependent variables are transformed in a new space where the energy and other conserved quantities are linear functions of the transformed variables. Then a classical integration algorithm is applied. The new calculated values are retransformed. This transformation is motivated by the following lemma

Lemma 1 Let $\mathbf{x}$ and $\mathbf{c}$ be vectors in $\mathbb{R}^n$. If $\mathbf{f} : \mathbb{R}^{n+1} \to \mathbb{R}^n$ has values orthogonal to $\mathbf{c}$, so that $\mathbf{I} = \mathbf{c} \cdot \mathbf{x}$ is a linear invariant of the first-order differential equation $\frac{d\mathbf{x}}{dt} = \mathbf{f}(\mathbf{x}, t)$, then each stage of the explicit m-stage discretization

$$\mathbf{x}_j = \mathbf{x}_0 + \tau \sum_{k=0}^{j-1} b_{jk} \mathbf{f}(\mathbf{x}_k, t + a_j \tau) \quad j = 1, \ldots, m \tag{1}$$

also conserves I, where τ is the time step and a_j, $b_{jk} \in \mathbb{R}$ (5).

A conservative integration algorithm is constructed by writing any conventional integration algorithm of the form (1), with known specific values of a_j and b_{jk}, in a transformed space. Consider for example the second order predictor-corrector scheme for the system of ordinary differential equations $\frac{d\mathbf{x}}{dt} = \mathbf{f}(\mathbf{x}, t)$,

$$\bar{\mathbf{x}} = \mathbf{x}_0 + \tau \mathbf{f}(\mathbf{x}_0, t), \tag{2a}$$

$$\mathbf{x}(t + \tau) = \mathbf{x}_0 + \frac{\tau}{2}[\mathbf{f}(\mathbf{x}_0, t) + \mathbf{f}(\bar{\mathbf{x}}, t + \tau)]. \tag{2b}$$

In the conservative predictor-corrector algorithm one seeks a transformation $\xi = \mathbf{T}(\mathbf{x})$ of the dependent variable $\mathbf{x}$ such that the quantities to be conserved can be expressed as linear function of the new variables. Then keeping (2b) as the predictor, in the transformed space one applies the corrector

$$\xi(t + \tau) = \xi_0 + \frac{\tau}{2}[\mathbf{T}'(\mathbf{x}_0)\mathbf{f}(\mathbf{x}_0), t) + \mathbf{T}'(\bar{\mathbf{x}}\mathbf{f}(\bar{\mathbf{x}}, t + \tau)]$$

where $\xi_0 = \mathbf{T}(\mathbf{x}_0)$ and $\mathbf{T}'$ is the derivative of $\mathbf{T}$. The new value of $\mathbf{x}$ is obtained by the inverse transformation, $\mathbf{x}(t + \tau) = \mathbf{T}^{-1}(\xi(t + \tau))$.

2 The restricted problem of three bodies (RPTB)

The restricted problem of three bodies can be defined as follows:

Two bodies (of masses m_1 and m_2) revolve around their center of mass in circular orbits under the influence of their mutual gravitational attraction and a third body (m_3, attracted by the previous two but not influencing their motion) moves in the plane defined by the two revolving bodies. The restricted problem of three bodies is to describe the motion of this third body (Szebehely, 1967).

The Hamiltonian of the system is given by:

$$H = \frac{1}{2}(\dot{x}^2 + \dot{y}^2) - \frac{1}{2}(x^2 + y^2) - \frac{1-\mu}{r_1} - \frac{\mu}{r_2},$$

where:

$$r_1 = \sqrt{(x-\mu)^2 + y^2},$$
$$r_2 = \sqrt{(x+1-\mu)^2 + y^2},$$
$$\mu = \frac{m_1}{m_1 + m_2}.$$

Using canonical variables

$$q_1 = x,\ q_2 = y,\ p_1 = \dot{x} - y,\ p_2 = \dot{y} + x,$$

the Hamiltonian becomes:

$$H = \frac{1}{2}(p_1^2 + p_2^2) + p_1 q_2 - p_2 q_1 - \frac{1-\mu}{r_1} - \frac{\mu}{r_2},$$

and the equations of motion are:

$$\dot{q}_1 = \frac{\partial H}{\partial p_1}, \dot{q}_2 = \frac{\partial H}{\partial p_2}, \dot{p}_1 = -\frac{\partial H}{\partial q_1},\ \dot{p}_2 = -\frac{\partial H}{\partial q_2},$$

so the Hamiltonian of the system can be rewritten as follows:

$$H = \frac{1}{2}(\dot{q}_1^2 + \dot{q}_2^2) - \frac{1}{2}(q_1^2 + q_2^2) - \frac{1-\mu}{r_1} - \frac{\mu}{r_2}.$$

In conservative integration this expression of Hamiltonian is transformed in a linear function and integrated as it is described above.

Observing figure 1 one can conclude the importance of the precision of calculations. The left panel shows us a relatively precise integration and an irregular

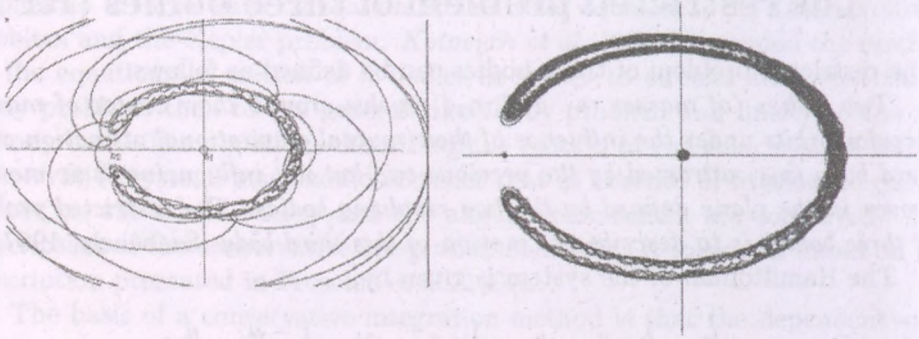

Figure 1: *The trajectory of an infinitesimal body in the Sun-Jupiter system. Left: The initial value of Jacobi constant is C=3.00107500556531351 the final value is C=3.0010750055653078. Integration time: 1461 Earth-years. Integrator: Adams - Moulton multistep integrator.*
Right: The initial and final value of Jacobi constant is the same C=3.00107500556531351 Integration time: 9550 Earth-years. Integrator: conservative integrator.

trajectory. After applying the conservative integrator to the same problem, it can be noticed that, not even after 9000 Earth-years the infinitesimal body leaves the system (right panel). So, in this case not the chaos is the cause of the apparition of irregularities but the imprecise calculus. It is evident the necessity of a highly precise integrator in orbit calculus and determination.

The regions where the motion of the massless particle is possible are the *Hill-regions*. These regions are bounded by the zero velocity surfaces of equation $2\Omega = C$, where

$$\Omega = \frac{1}{2}(x^2 + y^2) + \frac{1-\mu}{r_1} + \frac{\mu}{r_2} + \frac{\mu(1-\mu)}{2}.$$

The shape of the Hill-regions depends on the values of constant C, which is the *Jacobi constant*. The system of primaries is characterized by five critical values $C_i = 2\Omega(L_i)$ $i = 1, \ldots, 5$ where L_i are the Lagrange-points. For these constants we have $3 = C_4 = C_5 \leq C_3 \leq C_1 \leq C - 2 \leq 4,25$. (Szebehely, 1967).

3 Owerview of terms being used

Stable orbits: There are two types of stability, a weaker and a stronger one:

- *Marginal stability*: Every orbit starting in the neighbourhood of a specified orbit will remain in its neighbourhood at the same distance.
- *Asymptotic stability*: Every orbit starting in the neighbourhood of a specified orbit will approach the specified orbit asymptotically.

Unstable orbits: Every orbit starting in the neighbourhood of a specified orbit will leave its neighbourhood exponentially.

Periodic orbits: Orbits with periodic motions that contain one or more frequencies that are rationally related (resonance).

Quasi-periodic orbits: Orbits with periodic motions that contain at least two incommensurable frequencies (the ratio of the frequencies is an irrational number).

Aperiodic orbits: Orbits whose motion cannot be described as a sum of periodic motions.

Regular orbits: An orbit contained in n spatial dimensions can be decomposed into n independent periodic motions. The regular orbit can be described as a path on an invariant n-dimensional torus.

Irregular orbits: Orbits that cannot be decomposed into independent periodic motions: they can move anywhere energetically permitted.

Devaney's definition of Chaos (Devaney, 1987). Let (χ, d) be a metric space. A function $f : \chi \to \chi$ is called chaotic if and only if it satisfies the following three conditions:

(D1) : f is *topological transitive*, that is, for any two sets U and V, there exists k, $k \geq 1$ such $f^{[k]}(U) \cap V \neq \emptyset$, where $f^{[k]} = f^{[k-1]} \circ f$.

(D2) : *The set of periodic points of f is dense.* A point x is called periodic if $f^{[k]}(x) = x$ for some $k \geq 1$

(D3) : *f has sensitive dependence on initial conditions*, that is, $\exists\, \delta > 0$ such that for any open set U and for any point $x \in U$, there exist a point $y \in U$, such that $d(f^{[k]}(x), f^{[k]}(y)) > \delta$ for some k. The positive number δ is called sensitivity constant; it only depends on the space χ and the function f.

Chaotic orbit: – A chaotic orbit is unstable.
– A chaotic orbit is aperiodic.

4 The fast Lyapunov indicator (FLI)

Consider the flow:

$$\dot{\mathbf{x}} = F(\mathbf{x}(t)), \quad \mathbf{x} \in \mathbb{R}^n \quad \text{and} \quad t \in \mathbb{R}$$

and

$$\dot{\mathbf{v}} = \frac{\partial \mathbf{F}}{\partial \mathbf{x}}(x(t))\mathbf{v}.$$

Froeschlé et al. (1997a) used the value of $\log \|\mathbf{v}(t)\|$ at a given time T to discriminate between regular and chaotic motion, even a slow chaotic one. This was the first definition of the *Fast Lyapunov Indicator* (FLI). Another definition of the FLI was introduced in (Froeschlé and Lega, 2000) by averaging the values $\log \|\mathbf{v}(t)\|$ in the interval $[T - \Delta t, T]$. *Froeschlé and Lega* (2001) introduced a third definition of the FLI by considering:

$$FLI(\mathbf{x}(0), \mathbf{v}(0), T) = \sup_{0<k<T} \log \|\mathbf{v}(k)\|.$$

For chaotic orbit the FLI shows an exponential increase with time. In the case of a regular non-resonant orbit the FLI grows linearly with time. As it is shown in (Froeschlé et al. 1997a), the weak chaotic motion is quickly detected by the exponential increase of the FLI. For a periodic orbit, the FLI becomes constant after a while (*Froeschlé and Lega*, 2001).

In other words, given a n-dimensional flow defined by

$$\frac{d\mathbf{x}}{dt} = \mathbf{f}(\mathbf{x}),$$

we are looking at the evolution of a vector $\mathbf{v}$ which is given by the tangent flow, defined by

$$\frac{d\mathbf{v}}{dt} = \mathbf{Df}(\mathbf{x})\mathbf{v},$$

where $\mathbf{Df}$ is the matrix of the variation of the flow given by the velocity field $\mathbf{f}$, i.e.: $[\mathbf{Df}]_{ij} = \dfrac{\partial f_i}{\partial x_j}$. We integrate the above system of equations starting with initial conditions $\mathbf{x}_0$ and $\mathbf{v}_0$. Thus, the evolution of $\mathbf{v}$ is given by $\mathbf{v}(t) = \mathbf{J}(t)\mathbf{v}_0$. Here $\mathbf{J}(t)$ is the $n \times n$ Jacobian matrix, given by

$$\frac{d\mathbf{J}}{dt} = \mathbf{Df}(\mathbf{x})\mathbf{J}.$$

The Lyapunov indicator is based on the computation of the dynamical variable $\phi(t; x_0) = \max_{0 \le t' \le t} \log \|\mathbf{v}(t'; \mathbf{x}_0)\|$, where $\mathbf{v}(t'; \mathbf{x}_0)$ is a tangent vector of the flow at time t (Shchekinova et al. 2004).

5 The small alignment index (SALI)

Let us consider the $2n$-dimensional phase space of a conservative dynamical system, described by a symplectic map $\mathbf{T}$ or a Hamiltonian system defined by the n degrees of freedom Hamiltonian function H. The time evolution of an orbit with initial condition $P(0) = (x_1(0), x_2(0), \ldots x_{2n}(0))$ is defined by the repeated applications of the map $\mathbf{T}$ or by the solution of Hamilton's equations of motion. The time evolution of the deviation vector $\xi(0) = (dx_1(0), dx_2(0), \ldots, dx_n(0))$ is given by the equations of the tangent map:

$$\xi(N+1) = \left(\frac{\partial \mathbf{T}}{\partial P(N)}\right) \xi(N),$$

for maps and by the variational equations

$$\mathbf{J} \cdot \dot{\xi}' = \mathbf{DH} \cdot \xi',$$

for flows, where (') denotes the transpose matrix, and matrices J and DH are defined by

$$\mathbf{J} = \begin{pmatrix} \mathbf{0}_n & -\mathbf{I}_n \\ \mathbf{I}_n & \mathbf{0}_n \end{pmatrix}, \quad DH_{ij} = \frac{\partial^2 H}{\partial x_i \partial x_j} \quad \text{with} \quad i, j = 1, 2, \ldots, 2n,$$

$\mathbf{I}_n$ being the $n \times n$ identity matrix and $\mathbf{0}_n$ the $n \times n$ matrix with all its elements equal to zero. In order to define SALI for the orbit with initial conditions $P(0)$ we follow the time evolution of two initial deviation vectors $\xi_1(0)$ and $\xi_2(0)$. After every time step we normalize each vector to 1 and define the parallel alignment index

$$d_-(t) \equiv \|\xi_1(t) - \xi_2(t)\|,$$

and the antiparallel alignment index

$$d_+(t) \equiv \|\xi_1(t) + \xi_2(t)\|,$$

where $(\|\cdot\|)$ denotes the Euclidean norm of a vector. The smaller alignment index SALI is given by (Skokos, 2001 and Skokos et al. 2003)

$$\text{SALI} = \min(d_-(t), d_+(t)).$$

From the above definitions we can conclude that when two vectors $\xi_1(t)$ and $\xi_2(t)$ tend to coincide we get

$$d_-(t) \to 0, \; d_+(t) \to 2, \; \text{SALI} \to 0$$

while when they tend to become opposite we get

$$d_-(t) \to 2,\ d_+(t) \to 0,\ \text{SALI} \to 0$$

Therefore, it is evident that SALI is a quantity, that clearly informs us if the two deviation vectors tend to have the same direction by coinciding or becoming opposite. In a system of $2n$-dimensional phase space, with $n \geq 2$, the two vectors tend to coincide or become opposite for chaotic orbits. If the tested orbit is ordered, the SALI does not tend to zero, but its values fluctuates around a positive value (Skokos et al. 2003, Voglis et al. 1999).

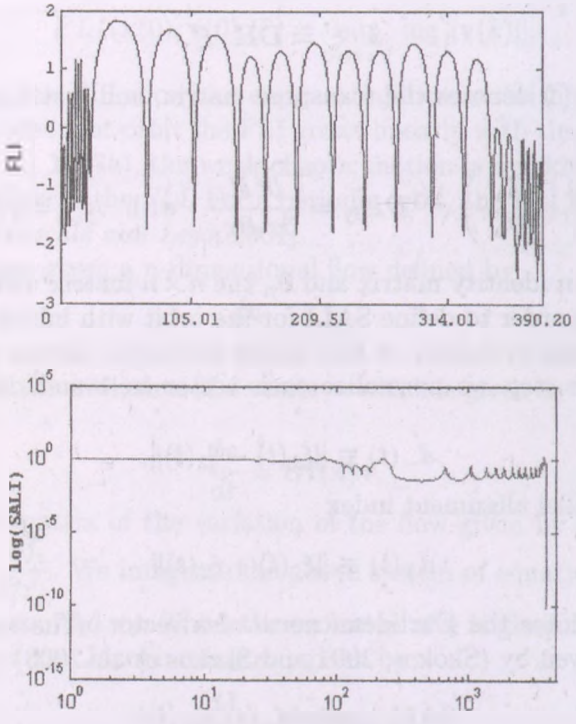

Figure 2: *Variation of FLI (first picture) and SALI (second picture) for a chaotic orbit in the Earth–Moon massless body system, $C = 3.00010914683260$*

6 Results

The *Hill-region* in vicinity of the lagrangean point L_i $i = 1, \ldots, 4$, was represented by an 100×100 matrix. A massless body was launched from every point of the matrix, and the trajectory was calculated numerically with the conservative integrator. The initial conditions, in fact $\dot{y}_0$, was calculated for the given *Jacobi constant*, using the $\dot{x}^2 + \dot{y}^2 = 2\Omega(x, y) - C$ expression of *Jacobi integral*, as $\dot{x}_0$ was considered zero for every starting point. The numerical integration lasted $t = 100$ time units/point. After every integration step FLI and SALI were calculated. If the value of log(SALI) decreased to 10^{-8} or less, the integration was stopped, and FLI and SALI values were registered. These values represented the basis of the FLI and SALI surfaces. It is important to remark that the value of *Jacobi constant*, was constant to the precision of the calculator as well the value of the Hamiltonian.

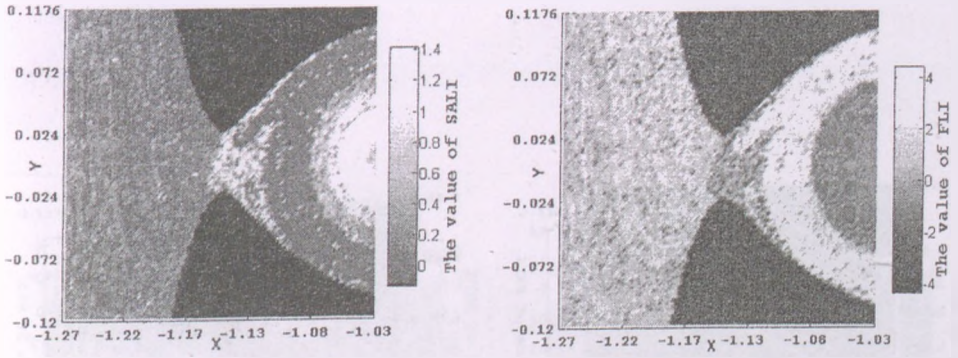

Figure 3: *SALI (left) and FLI (right) sections near L1, it the Earth-Moon infinitesimal body system, $C = 3.184164143174712080$*

On figure 3, 6, and 7 the complete black parts of the SALI and FLI regions are surfaces with $2\Omega - C < 0$. The motion of the infinitesimal body is not possible in these *forbidden regions* (Szebehely, 1967). The Jacobian integral allows the establishment of well-defined regions in the plane, where motion with given initial conditions may take place. It is obvious that the left-hand side of the Jacobi integral is always positive.

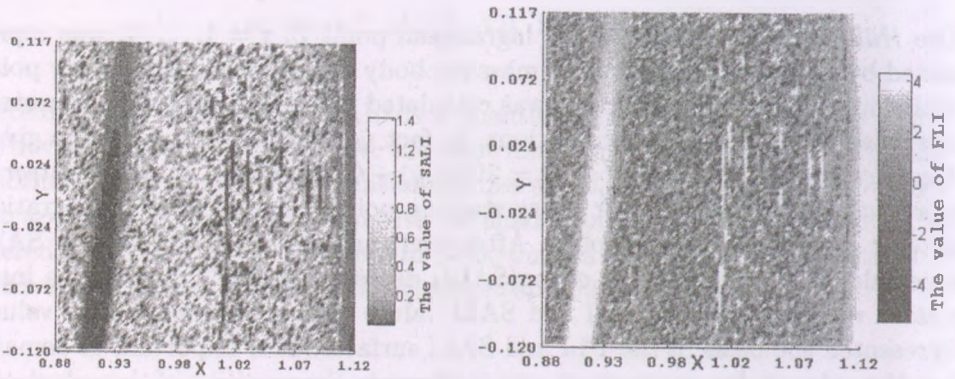

Figure 4: *SALI (left) and FLI (right) sections near L3, it the Earth–Moon infinitesimal body system, C =3.024150262881448730080*

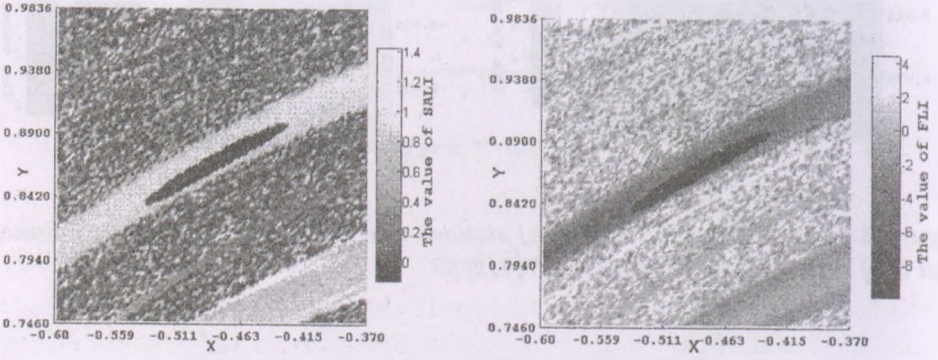

Figure 5: *SALI (left) and FLI (right) sections near L4, it the Earth–Moon infinitesimal body system, C =3.00010914683260*

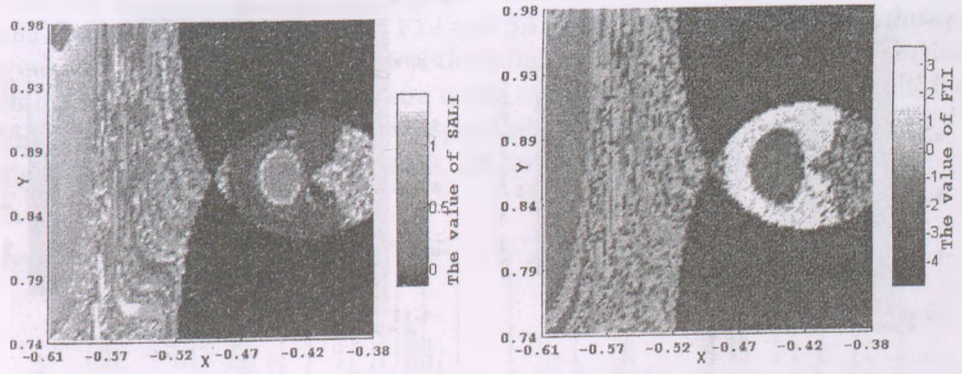

Figure 6: *SALI (left) and FLI (right) section near L1, Sun–Jupiter infinitesimal body system, C =3.706796224087156590*

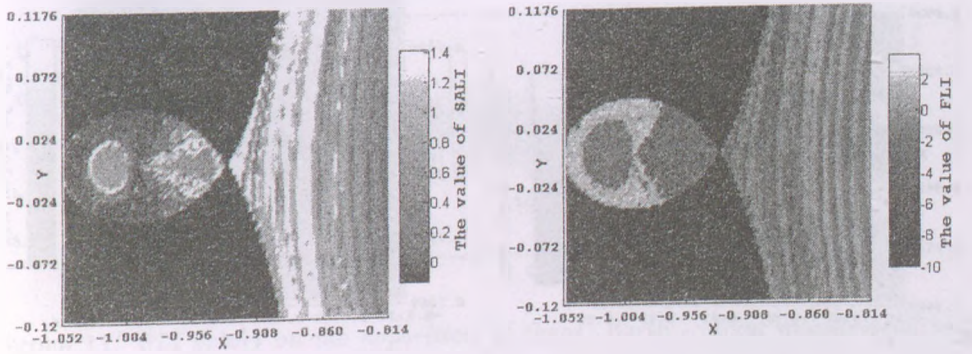

Figure 7: *SALI (left) and FLI (right) section near L2, Sun–Jupiter infinitesimal body system, C =3.039713803336780980*

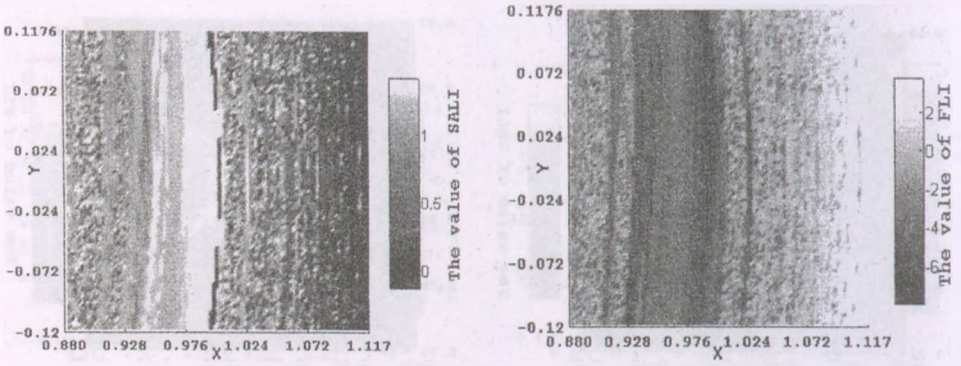

Figure 8: *SALI (left) and FLI (right) section near L3, Sun–Jupiter infinitesimal body system, C = 3.001906821795273570*

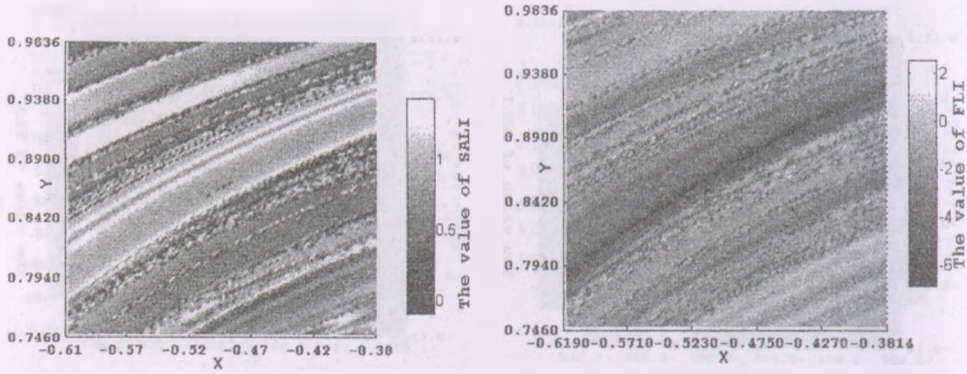

Figure 9: *SALI (left) and FLI (right) section near L4, Sun–Jupiter infinitesimal body system, C =3.000000681648089080*

7 Conclusions

Observing figures 3–9 one can conclude that SALI and FLI surfaces have the same shape and it is obvious that FLI and SALI indicate in a similar way the apparence of chaos in the movement of the infinitesimal body. The chaotic portion existing in the SALI surface appears in the same shape and same position in the FLI surface. A question rises: on apparition of chaos, when $\log(\text{SALI}) \leq 10^{-8}$, what is the value of FLI? Figures 10...13 are to respond to this question.

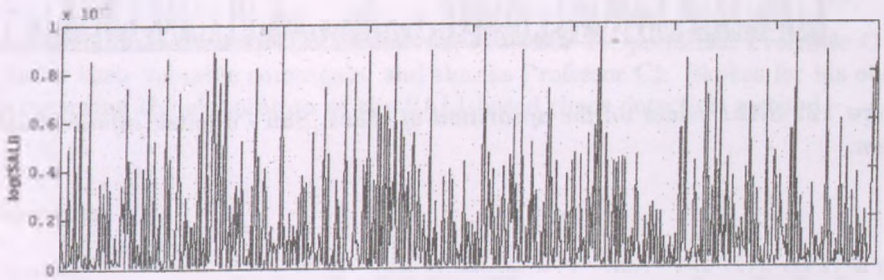

Figure 10: *SALI values on the apparition of chaos.* Earth - Moon *infinitesimal body system.*

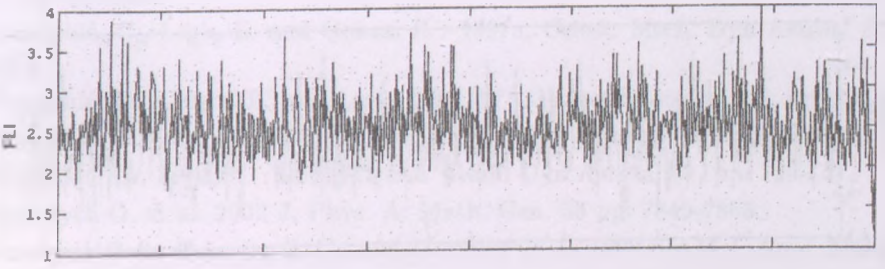

Figure 11: *FLI values on the apparition of chaos.* Earth - Moon *infinitesimal body system.*

The average value of FLI on figure 11 is 2.485473954, the minimal value of the FLI is 1.053644271 and the maximal value is 3.998231636.

The average value of FLI on figure 12 is 1.604314857, the minimal value of the FLI is 0.700365626 and the maximal value is 2.757631229.

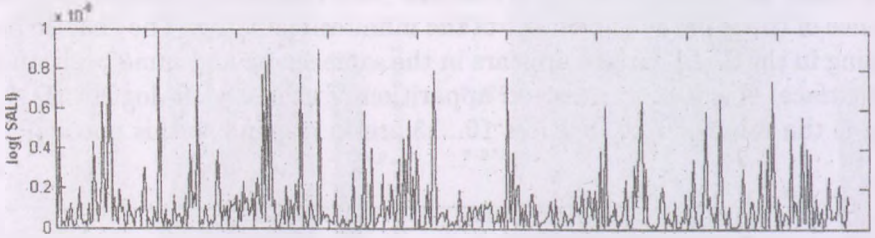

Figure 12: *SALI values on the apparition of chaos.* Sun - Jupiter *infinitesimal body system.*

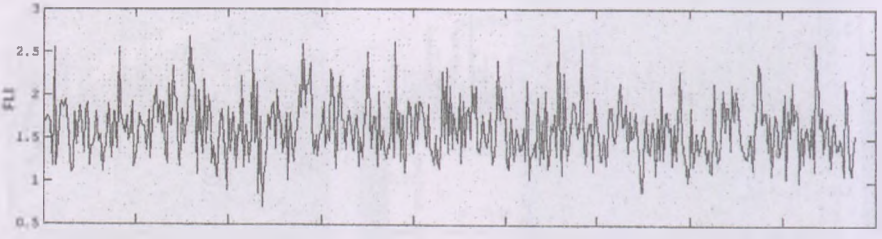

Figure 13: *FLI values on the apparition of chaos.* Sun - Jupiter *infinitesimal body system.*

One can notice that, from case to case the FLI-based chaos detection method or the SALI-based chaos detection method was more effective. It happened, that the FLI-based method indicated chaos before the SALI-based one, see figure 2. The reverse is true as well: on figure 7 (left panel), one can observe a white "stable-ring" and again a "stable-triangle", detected by SALI-based method, and ignored by FLI-based one (fig. 7, right panel).

Acknowledgement

The author thanks Professor F. Szenkovits, Professor T.Oproiu and Professor C. Gheorghiu for their valuable comments, and thanks Professor Ch. Skokos for his observations regarding the elaboration of the SALI-based chaos detection method.

References

[1] Bowman J. C., Shadwick B. A., and Morrison P. J., 1997, The 15th IMACS World Congress on Scientific Computation, Modelling and Applied Mathematics, Berlin, edited by A. Sydow (Wissenschaft & Technik Verlag, Berlin), Vol. 2, pp. 595-600.

[2] Devaney, R. L.: 1987, An introduction to Chaotic Dynamical Systems, Addison -Wesley, New York.

[3] Fouchard M, Lega E., Froeschl CH., Froeschl C.: 2002 Celest. Mech. Dyn Astron. 83, pp. 205-222.

[4] Froeschlé, C., Lega, E. and Gonczi R.: 1997a, Celest. Mech. Dyn Astron. 67, pp. 41-62.

[5] Froeschlé, C., Gonczi R. and Lega, E.: 1997b, Planet Space Sci. 45, pp. 881-886.

[6] Froeschlé, C., Lega, E. : 2000, Celest. Mech. Dyn Astron. 78, pp. 167-192.

[7] Froeschlé, C., Lega, E. : 2001, Celest. Mech. Dyn Astron. 81, pp. 129-147.

[8] Kotovych O. et al. 2002 J. Phys. A: Math. Gen. 35 pp. 7849-7863.

[9] Shadwick B.A., Bowman J. C., and Morrison P. J., 1999 SIAM J. Appl. Math. 59, 1112 .

[10] Shadwick B. A., Buell W. F. and Bowman J. C, 2001, Scientific Computing and Applications, Banff, Vol. 7 of Advances in Computation: Theory and Practice, edited by P. Minev, Y. S. Wong, and Y. Lin (Nova Science Publishers, New York), pp. 247 - 255.

[11] Shchekinova E., Chandre C., Lan Y. and Uzer T.:. 2004 Journ. Chem. Phys vol.121, 8, pp. 3471-3477.

[12] Skokos CH. 2001 J. Phys A: Math. Gen. 34 pp. 10029 -10043.

[13] Skokos CH., Antopoulos CH., Bountis T. and Vrahatis M. N., 2003 Proceedings of the Conference Libration Point Orbits and Applications, edited by G. Gmez, M. W. Lo and J. J. Masdemont, World Scientific, pp. 653 - 664.

[14] Szebehely V.: Theory of Orbits Academic Press, New - York, 1967.

[15] Voglis N., Contopoulos G. and Efthymiopoulos C., 1999, Celest. Mech. Dyn. Astron., 73, pp.211-220.

PADEU | PADEU **19** (2007), p. 237
ISBN 963 463 557
©Published by the Astron. Dept. of the Eötvös Univ.

Chaotic structure of the capture domain

Zoltán Makó

Sapientia University, Department of Mathematics and Informatics, Szabadság tér 1, RO-530104 Miercurea Ciuc, Romania
Babeş-Bolyai University, Department of Applied Mathematics, Str. M. Kogălniceanu Nr. 1, RO-400084 Cluj-Napoca, Romania

E-mail: makozoltan@sapientia.siculorm.ro

Abstract
The ballistic capture is the phenomenon, where a massless particle changes its Kepler-energy around one of the primaries from positive to negative (Belbruno (2004)). Belbruno used the time as measure of the capture. In this paper we study the phenomenon of capture by using the variation of the polar angle of the relative position vector of the small body around the capturing planet. We defined the capture effect of the planet to the captured body, as the variation of this polar angle during the capture. Several zones are determined around the capturing body, in which, for a given velocity, the capture take place. These regions are called capture domains. In this paper we show that the capture domain is a subset of scattering region and chaos in the capture domain is transient.
Keywords: *Ballistic capture, capture effect, capture domain, scattering region*

1 Introduction

Capture of small bodies by major planets is an interesting phenomenon in planetary system, with applications to the study of comets, asteroids, irregular satellites of the giant planets (Astakhov et al., 2004) and different type of low energy lunar transfers (Belbruno, 2004). This phenomenon can be studied by using

different methods. Many authors studied this problem introducing different concepts of capture, like weak capture (Belbruno, 1999); (Belbruno and Marsden, 1997), temporary capture (Brunini, 1996), longest capture (Winter and Vieira, 2001), resonant capture (Yu and Tremaine, 2001), ballistic capture (Belbruno, 2004), etc. The temporary, longest and resonant captures are geometric notions and requires that the motion of massless particle is bounded around a primary body. Ballistic capture is analytically defined for the n-body problem (Belbruno, 2004).

The *ballistic capture* is the phenomenon, where a particle changes its Kepler-energy

$$K_P = \frac{v_P^2}{2} - \frac{k^2 m_P}{r_P} \tag{1}$$

with respect to a primary body, from positive to negative. The region where this capture can occur in the phase space is called the *weak stability boundary*. Ballistic capture occuring on the weak stability boundary is called *weak capture*.

2 The capture effect

In all enumerated studies the time is used as measure of the capture. In this paper we try to study the phenomenon of capture by using the variation of the angle of the small body around the capturing planet. We introduce the capture effect $\triangle\varphi$ of the planet to the captured body, as:

Definition 1 *The capture effect $\triangle\varphi$ of the planet P_2 to the captured body P_3 is the total variation of the angle at centre during the capture, as long as the Kepler-energy*

$$K_{P_3} = \frac{v_{P_3}^2}{2} - k^2 \frac{m_{P_2}}{\|P_2P_3\|} \tag{2}$$

of the small body relative to the planet P_2 is negative, where $v_{P_3}^2$ is the velocity squared of P_3 related to P_2, m_{P_2} is the mass of planet P_2, $\|P_2P_3\|$ is the distance between bodies P_2 and P_3 and k is the Gaussian constant of the gravity. The begining point of the capture is P_3^0 where the Kepler-energy of the captured body, relative to the capturing body P_2, becomes negative. The end of capture is in the point P_3^1 where the Kepler-energy becomes positive (see Figure 1).

Let t_b be the beginning and t_e the end moment of the capture. We assume that $t_b = t_0 < t_1 < ... < t_n = t_e$ is a small partition of the interval $[t_b, t_e]$, such

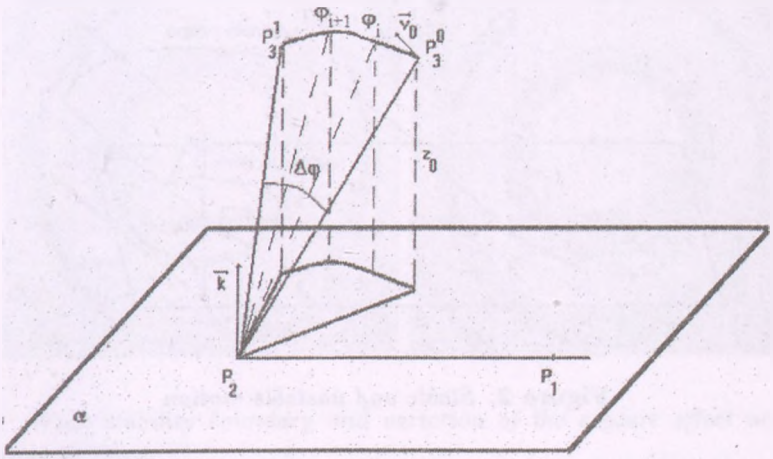

Figure 1: *Capture effect*

that in each subinterval $[t_i, t_{i+1}]$ the $\Delta\varphi_i = \varphi_{i+1} - \varphi_i$ is monotone. The capture effect of P_2 to P_3 with initial conditions $(x_0, y_0, z_0, \dot{x}_0, \dot{y}_0, \dot{z}_0)$ is

$$\Delta\varphi\,(x_0, y_0, z_0, \dot{x}_0, \dot{y}_0, \dot{z}_0) = \sum_{i=0}^{n-1} |\varphi_{i+1} - \varphi_i|\,, \tag{3}$$

where $\varphi_i = \varphi\,(t_i)$. The capture effect gives the total variation of the angle at centre of P_3 during the capture.

The capture effect can be determined by using numerical integrators of the n-body problem. Our algorithm has the following steps:

1. The position and velocity of the small body P_3 are determined at the time t_0.

2. The position and velocity of the capturing planet P_2 and all considered bodies in n-body problem are determined at the time t_0.

3. Using these initial conditions the equations of motion of P_3 are numerically integrated. The Kepler-energy of P_3 relative to the capturing planet is evaluated at each step, with the formla (2).

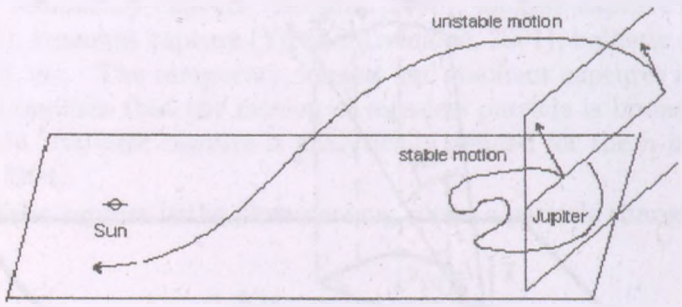

Figure 2: *Stable and unstable motion*

4. The variation of the angle $\Delta\varphi$ is summed, from the beginning to the end of the capture.

Definition 2 *The capture domain of effect $\alpha > 0$ is the following set of initial conditions*

$$S_\alpha = \left\{ \left(x_0, y_0, z_0, \dot{x}_0, \dot{y}_0, \dot{z}_0 \right) : \Delta\varphi \left(x_0, y_0, z_0, \dot{x}_0, \dot{y}_0, \dot{z}_0 \right) \geq \alpha \right\}. \qquad (4)$$

This is a region of the phase space from where starting the test body, the ballistic capture is bound to happen.

The capture domain can be determined by using numerical methods. Our algorithm has the following steps:

1. We consider numerous test particles in a certain region of the phase space with negative or zero Kepler energy relative to the capturing planet P_2.

2. Equations of motion are numerically integrated, and the Kepler-energy (2) relative to the capturing planet is evaluated at each step.

3. The variation of the angle $\Delta\varphi$ is summed, from the beginning to the end of the capture.

4. If the total variation of the angle $\Delta\varphi$ is greater than α, then this starting point is in the capture domain S_α.

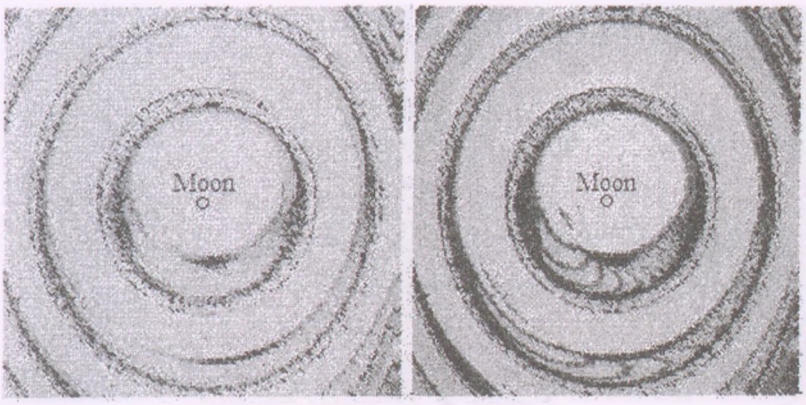

Figure 3: *Weak stability boundary and variation of the capture effect around the Moon, relative to Earth*

Belbruno and Marsden (1997) discussed the motion of ten short-period comets strongly perturbed by Jupiter. In their view the motion of a comet about Jupiter is *stable*, if starting with elliptical initial condition with respect to Jupiter it returns to a reference plan, pssing through its initial condition, without first having moved around the Sun (see Figure 2). It is a difficult unsolved problem to give the necessary conditions of this stability. Our capture domain with capture effect 2π is a subset of that initial conditions, from which arise stable motions.

Mako and Szenkovits (2004) proved that for the real capture phenomenon analysis the model of circular restricted three-body problem is not adequate. Therefore, we studied the variation of capture effect around the Moon, relative to Earth, in the Sun-Earth-Moon and small particle system. The capture effect is calculated by using a fourth order Wisdom-Holman simplectic n-body integrator (Wisdom and Holman (1991); Wisdom and Holman (1992)). We study the variaton of capture effect relative to Earth by taking 32000 test particles in the orbital plane of Moon for 100000 kilometres around. All these test particles have at the initial moment the velocity of the Moon.

In the first picture of Figure 3 the black zone is the subset of initial conditions (x_0, y_0) of the test particles, from which arise stable motions relative to Earth, i.e. the angle at centre described by the test particle around the Earth is greater than 2π. In this picture the color of a started point is growing dark in the same

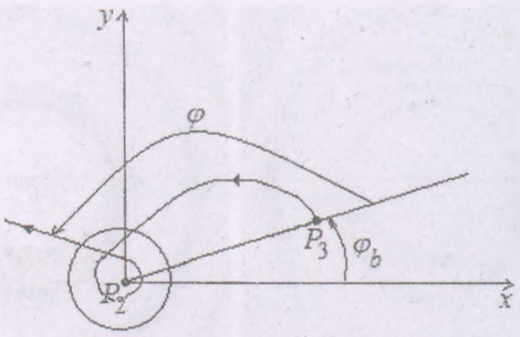

Figure 4: *Scattering function*

way as grows the measure of the angle at the center described the by test particle around the Earth. The second picture of Figure 3 illustrate the variation of the capture effect relative to Earth. The grade of darkness increases the same way as the value of the capture effect. The high-grade similarity of these pictures shows the close relation between stable motion and capture effect notions, i.e. the weak stability boundary and capture domain have similar structure.

3 Transient chaos

If the chaotic process has only finite duration, i.e. the complexity and unpredictability of the motion can be observed over a finite time interval, then this type of chaos is called transient chaos (Tel and Gruiz, 2005).

The chaos in capture phenomenon is transient since, generally the ballistic capture is temporary and, after some time, the Kepler-energy changes back to positive and the massless particle leaves the neighborhood of the primary.

Definition 3 *The scattering function is*

$$S\left(\varphi_b, \|P_2P_3\|\right) = \varphi, \tag{5}$$

where $\varphi_b = \varphi(t_b)$ *is the angle at centre,* $\|P_2P_3\|$ *is the distance between* P_2 *and* P_3 *in the beginning moment of the capture and the output parameter* φ *is the angle of deflection (see figure 4).*

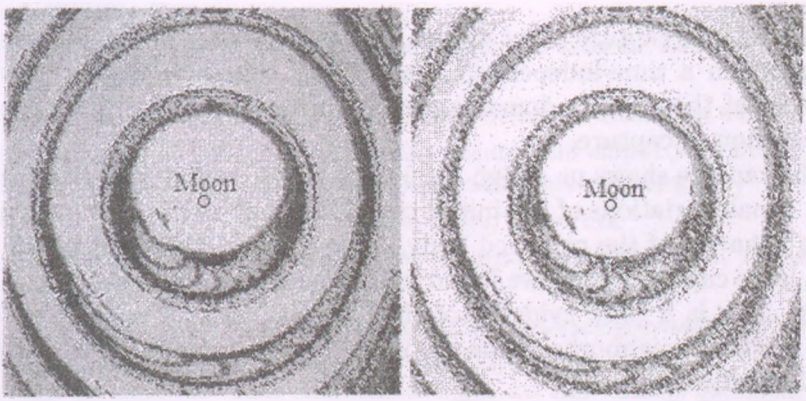

Figure 5: *Variation of the capture effect and graph of the scattering function around the Moon, relative to Earth*

Proposition 1 *In the planar case, for a given velocity, between scattering function and capture effect has the following relation:*

$$S\left(\varphi_b, \|P_2P_3\|\right) = \triangle\varphi\left(\|P_2P_3\|\cos\varphi_b, \|P_2P_3\|\sin\varphi_b\right) \quad mod\,(2\pi)\,. \tag{6}$$

Remark 1 *The scattering region B is the domain where the interaction is significant, i.e. where the capture effect is positive or zero. Consequently*

$$S_\alpha \subseteq B \text{ for all } \alpha > 0. \tag{7}$$

The first picure of Figure 5 illustrate the variation of capture effect around the Moon, relative to Earth and, the second picture contains the graph of scattering function around the Moon, relative to Earth. Inboth of these pictures the dark is growing in the same way as the value of the capture effect $\triangle\varphi$, respectively as the value of deflection angle φ. The high-grade similarity of these pictures shows the close relation between the scattering region B and graph of scattering function.

Proposition 2 (The general properties of chaotic scattering) *Chaotic scattering is the conservative limit of the transient chaos. Inside the scattering region it can be found the hyperbolic structure of chaos.*

4 Conclusions

The introduced capture effect gives a new tool to characterize the phenomenon of capture in a time-independent way. Using this measure and studying the structure of the capture domains we can find new aspects of the complicated phenomenon of capture.

The capture shows us a high sensitivity to the variation of the initial conditions. Small variations of the initial conditions may cause fundamental changes in the behavior of the captured body. Near a "long" captured initial condition (with large capture effect) we found initial conditions that lead to non-captured orbits. This is a good evidence of the fact that there are many initial conditions in whose neighborhood the property of capture depends chaotically on the initial conditions.

Chaos in capture domain is transient since the capture domain is a subset of scattering region and the capture effect satisfy the relation (6).

Using a modified form of the capture effect, measuring only the one-directional variation of the angle at centre, we can determine those initial conditions, which lead to orbits encircling completely the capturing body. We can measure also the number of loops of the captured orbit.

Belbruno (2004) showed that the unstable properties of the weak stability boundary can be used to find a different type of low energy transfer to the Moon using ballistic capture. Since the weak stability boundary is a subset of scattering region it is possible to elaborate a new methodology for the construction of low energy transfers for spacecraft using the scattering region or chapture domain.

Acknowledgments

This work was supported by the Research Programs Institute of Foundation Sapientia under grant 2006-2007.

References

Astakhov, S.,Burbanks A.,Wiggins S., Farrelly D. 2004, Dynamics of Capture in the Restricted Three-Body Problem, Order and Chaos in Stellar and Planetary Systems, ASP Conference Series, 316, p. 80

Belbruno, E. 1999, Hopping in the Kuiper Belt and significance of the 2:3 resonance, *The Dynamics of Small Bodies in the Solar System*, p. 37

Belbruno, E. 2004, Capture Dynamics and Chaotic Motions in Celestial Mechanics, Princeton University Press

Belbruno, E., Marsden, B. G. 1997, Resonance hopping in comets, *The Astronomical Journal*, 113, p. 1433

Brunini, A. 1996, On the satellite capture problem, *Celestial Mechanics*, 64, p. 79

Makó Z. and Szenkovits F. 2004, Capture in the circular and elliptic restricted three-body problem, *Celestial Mechanics and Dynamical Astronomy*,90, p. 51

Szebehely, V. 1967, *Theory of orbits*, Academic Press, New-York

Yu, Q., Tremaine, S. 2001, Resonant capture by inward-migrating planets, *The Astronomical Journal*, 121, p. 1736

Winter, O.C. and Vieira, N.E. 2001, Time analysis for temporary gravitational capture: satellites of Uranus. *The Astronomical Journal*, 122, p. 440

Wisdom, J. and Holman, M. 1991 Symplectic maps for the N-body problem, *The Astronomical Journal*, 102. p. 1528

Wisdom, J. and Holman, M. 1992 Symplectic maps for the N-body problem: Stability analysis. *The Astronomical Journal*, 104, p. 2022

Tél-T., Gruiz M. 2006, Chaotic Dynamics: An Introduction Based on Classical Mechanics, Cambridge University Press

PADEU | PADEU **19** (2007), p. 247
ISBN 963 463 557
©Published by the Astron. Dept. of the Eötvös Univ.

Numerical Integration of the Polygonal n-body Problem in High Precision Arithmetic

Dorina Peter[1], Radu Zapotinschi[2], Albert Tóth Endre[3]

[1,3] Astronomical Institute of the Romanian Academy, Cireşilor 19, RO-400487, Cluj-Napoca, Romania
[2] Department of Applied Mathematics, Babeş-Bolyai University, Astronomical Observatory, Cireşilor 19, RO-400487, Cluj-Napoca, Romania

E-mail: [2]raduz@math.ubbcluj.ro

Abstract
The paper presents a computer algebra program dedicated to the synthesis and generation of numerical code for the integration of the n-body problem using an arbitrary precision arithmetic library. The program is able to apply several numerical methods specified in the high level programming language of the computer algebra system and to generate efficient low level code. The library is tested in the numerical integration of the general n-body problem starting with the initial conditions where the equal mass bodies having equal velocities are placed at the vertices and in the center of a regular polygon. In this case the problem has analytical solution but proves to be hard to integrate numerically in standard double precision due to the instability of the symmetric configuration.
Keywords: *n-body problem, numerical methods, computer algebra, stability*

1 Introduction

The polygonal n-body problem is a particular case of the general n-body problem, where $n-1$ bodies of equal mass m are placed in the vertices of an $n-1$

regular polygon and one body of mass M is placed in the center of the circumscribed circle. If the initial velocities of the $n-1$ bodies make the same angle to the radius from the center and have equal magnitude, while the central body is at rest, the polygonal configuration is preserved during the orbital evolution of the system and the problem has a simple analytical solution.

Indeed, due to symmetry, the resultant gravitational forces that act on each body are oriented towards the center of the polygon, thus the motion of each of the polygon bodies is equivalent to a motion in a central field produced by an equivalent mass $m_\star$, that can be easy computed as:

$$m_\star = M + \frac{m}{4} \sum_{i=1}^{n-2} \frac{1}{\sin \frac{i\pi}{n-1}}$$

Furthermore, if the initial velocities of the bodies are oriented perpendicular to the radius from center and their modules have the value of the circular velocity for the mass $m_\star$:

$$v_{\text{circ}} = \sqrt{\frac{Gm_\star}{R}}$$

the trajectories are circular (figure 1, a) and in a rotating frame all bodies are at rest. If the above conditions are not fulfilled the trajectories are conical sections,

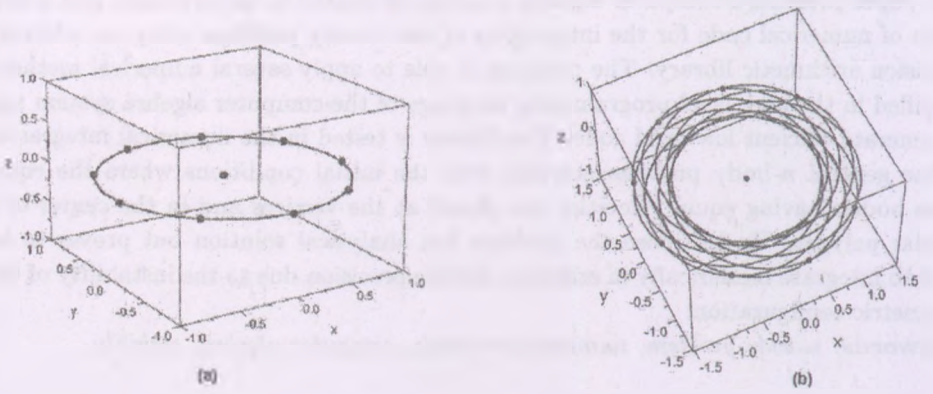

Figure 1: *Trajectories for the polygonal problem a) circular case, b) elliptical*

(e.g., ellipses, figure 1, b) but the polygonal symmetry is kept throughout the evolution of the system.

Since in the polygonal configuration the n-body problem has analytical solution, we attempted to use this particular configuration as a test for our general

n-body integrator, i.e., we have fed the polygonal configuration of positions and velocities as initial data to a general n-body integrator in order to test its accuracy. However, in some cases our attempt to integrate the system for longer time intervals has failed systematically, regardless of the numerical method we had used.

We have used as a test for accuracy the level at which the integrator maintains the polygonal symmetry after a number of orbital periods. The initial data depends on two parameters: the number of bodies n, and the mass ratio M/m. What we have observed is that for certain ranges of these parameters, the integrator is unable to keep the polygonal configuration for more than a few orbital periods. We have used various numerical methods from symplectic methods tailored for hamiltonian systems (Yoshida, 1993) to powerful numerical integrators for general equations (Hairer et al., 1987) and methods specific to stiff problems (Hairer et al., 1991). The list of methods includes:

- explicit and implicit Euler,
- leapfrog,
- embedded Runge-Kutta Prince-Dormand 8(7),
- implicit Runge-Kutta Kuntzmann-Butcher of orders 6 and 8,
- backwards differentiation formula,
- a symplectic method of order 4 based on generating function (Yoshida, 1993).

All these methods failed to keep the symmetry of the polygonal configuration very soon after the start of integration, with very small differences and regardless of the stepsize and other specific parameters such as the stationarity condition for implicit methods.

The explanation for this failure is given by the fact that the physical system is unstable for different values of n and small values of M/m ratio. The stability of the polygonal configuration was studied by Elmabsout (Elmabsout, 1987, 1996). All the cases where we experienced difficulties fall in the range of linear instability theoretically computed by Elmabsout. Since the physical system is unstable, in the numerical simulation of its orbital evolution errors tend to accumulate and throw rapidly the system from its symmetrical configuration.

Although using precise numerical methods may reduce the inherent approximation errors, there remains an important source of errors that cannot be dealt

with by means of improving the numerical accuracy: roundoff errors. Indeed, in our experience, the only method to increase the number of orbital periods for which the symmetry is preserved is to increase the numerical precision of the integrator beyond that of double precision.

This paper describes our approach to integrate multiple precision arithmetic in our symbolic code generation program sydna (Zapotinschi, 1999), and its application to the integration of the polygonal n-body problem.

2 Code generation with sydna

Sydna is a MuPAD package dedicated to code generation of numerical algorithms. Its core libraries are `codeg` that is able to translate a subset of MuPAD language to C and `parteval` a library that supports partial evaluation. Usage of sydna consists in implementing numerical algorithms in an abstract fashion, using computer algebra capabilities of MuPAD, then using the partial evaluator to instantiate the algorithms on concrete algebraic data and perform all symbolic operations, finally generating C program by translation of the resulted code.

The principles of sydna usage can be easily presented by considering a simple example: Newton's tangent method for solving a nonlinear equation $f(x) = 0$. It starts from a "first guess" solution x_0 and improves it by the iteration

$$x_{n+1} = x_n - \frac{f(x_n)}{f'(x_n)}$$

In this example, the symbolic data is the particular form of the function f, while the symbolic operation is computing the derivative; this operation cannot be directly translated to C (unless a symbolic computation library is used, but this option falls out of the scope of this paper). Thus, one has to specify the function f, say $\sin(x)$ and sydna will replace its instances and compute its derivative resulting an iteration of the form:

$$x_{n+1} = x_n - \frac{\sin(x_n)}{\cos(x_n)}$$

that now can be translated to C using `codeg` library.

The computations performed by sydna become more complicated when less trivial examples are considered. For instance, if the nonlinear equation is replaced with a set of nonlinear equations, it becomes apparent that sydna has

to perform a synthesis of the numerical method and the specific problem. For instance, the problem can consist in a set of equations of the form:

$$\{f_1(x_1, x_2) = 0, f_2(x_1, x_2) = 0\}$$

but it can also be an indexed set like:

$$\{f_i(x_j) = 0\}, \quad i, j \in \{1, \ldots n\}$$

or

$$\{f_{ij}(x_{kl}) = 0\}, \quad (i, k), (j, l) \in \{1, \ldots n\} \times \{1, \ldots m\}$$

where the numbers n and m are not statically known, i.e., they will be provided by the user of the generated program. Thus, in the first example, the final code will consist in two iteration formulae, while in the other two cases loops on the index set should be generated, as well as linear algebra function calls to compute the inverse of the Jacobian matrix.

In the case of numerical integration of initial value problems for systems of ordinary differential equations, as the n-body problem, the synthesis calculus is more intricate since several numerical methods should be applied to different variants of the problem, each being specified separately. Consider the system of differential equations:

$$\frac{\mathrm{d}\mathbf{y}}{\mathrm{d}x} = \mathbf{f}(x, \mathbf{y})$$

and the simplest Euler method:

$$\mathbf{y}(x_{i+1}) = \mathbf{y}(x_i) + (x_{i+1} - x_i)\, \mathbf{f}(x_i, \mathbf{y}(x_i))$$

In sydna this method can be specified simply as:

```
for j in Index(y) do
   y[i+1][j]:=y[i][j]+(x[i+1]-x[i])*f[j](x[i], Seq(y[i]))
end_for
```

but its final implementations will vary depending on actual values of **y** and **f**.

If for instance the set of differential equations consists in a fixed number of equations, say two, the Euler method will be implemented by unrolling the for loop:

```
y1[i+1]:=y1[i]+(x[i+1]-x[i])*f1(x[i], y1[i], y2[i]);
y2[i+1]:=y2[i]+(x[i+1]-x[i])*f2(x[i], y1[i], y2[i])
```

Typically, in this case, the functions `f1` and `f2` are known statically and thus they can be inlined, i.e., their actual expression can replace the expressions `f1(x[i], y1[i])` and `f2(x[i], y1[i])`. In some cases however, the computation of these functions (or just for one of them) is too complicated and inlining cannot be performed.

Now, if the number of equations is not known in advance the implementation of the Euler method will certainly contain a loop:

```
for j from 1 to n do
   y[i+1][j]:=y[i][j]+(x[i+1]-x[i])*f[j](x[i], y[i])
end_for
```

Let us complicate things more: consider that the system of differential equations of motion for the n-body problem in two dimensions, i.e., the set of $4n$ equations:

$$\begin{aligned}
\frac{\mathrm{d}x_j}{\mathrm{d}t} &= v_{xj} \\
\frac{\mathrm{d}y_j}{\mathrm{d}t} &= v_{yj} \\
\frac{\mathrm{d}v_{xj}}{\mathrm{d}t} &= \sum_{k=1,\, k\neq i}^{n} G\frac{m_k}{r_{jk}^3}(x_k - x_j) \\
\frac{\mathrm{d}v_{yj}}{\mathrm{d}t} &= \sum_{k=1,\, k\neq i}^{n} G\frac{m_k}{r_{jk}^3}(y_k - y_j)
\end{aligned}$$

If the number of bodies is not statically known, an efficient implementation should only partially unroll the for loop, in fact it should transform it to loop not through the equations, but through the n bodies. Furthermore, the right hand sides of the last two equations are extremely simple and they can be easily inlined, while the first two should be implemented separately:

```
for j from 1 to n do
   x[i+1][j]:=x[i][j]+(t[i+1]-t[i])*vx[i][j];
   y[i+1][j]:=y[i][j]+(t[i+1]-t[i])*vy[i][j];
   vx[i+1][j]:=vx[i][j]+
      (t[i+1]-t[i])*fvx(t[i], x[i], y[i], vx[i], vy[i]);
   vy[i+1][j]:=vy[i][j]+
      (t[i+1]-t[i])*fvy(t[i], x[i], y[i], vx[i], vy[i])
end_for
```

Sydna system is capable of synthesizing efficient code in all these cases, and also for a lot more complicated numerical algorithms, such as Runge-Kutta methods, that are implemented in a generic fashion, i.e., a particular RK method is generated if the corresponding set of RK parameters is provided. All the methods mentioned in the introduction were implemented in this generic fashion.

3 Arbitrary precision arithmetic

There are two ways in which we can make use of arbitrary precision arithmetic (APA): one is to use a computing system that includes in its structure a higher precision arithmetic library, for instance a symbolic computing environment such as Maple, Mathematica or MuPAD. By altering a global parameter (`Digits` in Maple, `DIGITS` in MuPAD or `$MinPrecision` and `$MaxPrecision` in Mathematica) one can simply set the precision of the numerical computations. The main disadvantage of this approach is the fact that a computer algebra system introduces supplemental latencies due to the interpreted nature of its programming language and also to its inherent inefficiency in handling datastructures.

The other method to employ APA is to call functions of an APA library from a compiled program written in a language like C or Fortran. Examples of APA libraries are PARI (`http://pari.math.u-bordeaux.fr/`), GMP (Gnu MP, `http://swox.com/gmp/`), CLN (`http://www.ginac.de/CLN/`) and many others. The major disadvantage of this approach is the fact that programming using these libraries is very cumbersome since all arithmetical operators should be replaced to specific library function calls.

Our goal is to have both the ease of a computer algebra system and the increased efficiency of the compiled program. In our approach, this is achieved by extending sydna code generator such that it is able to transform arithmetical operations into calls to an APA library. For our tests we have used GMP with its extension MPFR (`http://www.mpfr.org`), but targeting the code generator to other APA libraries should be quite simple.

Basically, what the APA code generator does is to separate each arithmetical operation in two operands expressions. For instance

```
x:=a+b*c
```

should be decomposed in

```
V1:=b*c;
x:=a+V1
```

Then, all these operations are translated to MPFR function calls.

The example in figure 2 shows the MPFR translation of the expression:

$$a_x := -\frac{\mu(x_1 - x_2)}{((x_1 - x_2)^2 + (y_1 - y_2)^2)^{3/2}}$$

```
mpfr_init2(fv1, 1024);
mpfr_init2(fv2, 1024);
mpfr_init2(fv3, 1024);
mpfr_init2(fv4, 1024);
mpfr_init2(fv5, 1024);
mpfr_init2(fv6, 1024);
mpfr_init2(fv7, 1024);
mpfr_init2(fv8, 1024);
mpfr_init2(fv9, 1024);
mpfr_init2(fv10, 1024);
mpfr_init2(fv11, 1024);
mpfr_init2(fv12, 1024);
mpfr_init2(fv13, 1024);
mpfr_init2(fv14, 1024);
mpfr_sub(fv1, x1, x2, GMP_RNDN);
mpfr_mul(fv2, G, fv1, GMP_RNDN);
mpfr_sub(fv3, x1, x2, GMP_RNDN);
mpfr_set_i(fv4, 2, GMP_RNDN);
mpfr_pow(fv5, fv3, fv4, GMP_RNDN);
mpfr_sub(fv6, y1, y2, GMP_RNDN);
mpfr_set_i(fv7, 2, GMP_RNDN);
mpfr_pow(fv8, fv6, fv7, GMP_RNDN);
mpfr_add(fv9, fv5, fv8, GMP_RNDN);
mpfr_set_i(fv10, 3, GMP_RNDN);
mpfr_set_i(fv11, 2, GMP_RNDN);
mpfr_div(fv12, fv10, fv11, GMP_RNDN);
mpfr_pow(fv13, fv9, fv12, GMP_RNDN);
mpfr_div(fv14, fv2, fv13, GMP_RNDN);
mpfr_neg(ax, fv14, GMP_RNDN);
mpfr_clear(fv1);
mpfr_clear(fv2);
```

Figure 2: *MPFR/GMP translation of the x component of the gravitational acceleration in the two-body problem (MuPAD output)*

Before starting the code generation process, a preprocessing step is required to eliminate all floating point operations from statements, without changing their semantics. Consider the simple loop statement:

```
while x1-x2>tol do
   .....
end_while
```

Since the loop continuation test `x1-x2>tol` contains two arithmetical operations (subtraction and comparison), a new statement that evaluates the difference should be generated and added before each program point from where the test can be reached:

```
v1:=x1-x2;
while v1>tol do
   .....
   v1:=x1-x2
end_while
```

4 Runtime comparison

As we have stated above, an increase of the precision of the arithmetic computations will improve the quality of the integration. In particular, it will increase the number of orbital periods (np) for which the polygonal symmetry is maintained by the integrator. This fact is shown in figure 3 for the leapfrog integrator.

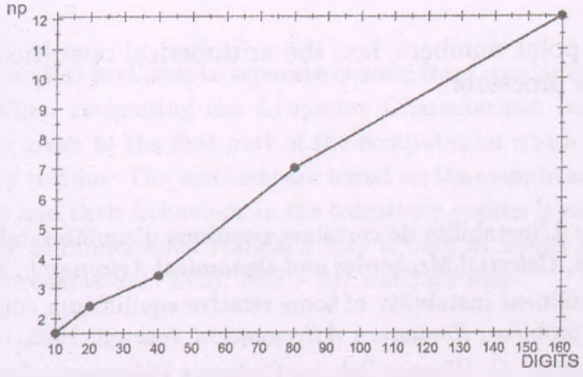

Figure 3: *Number of orbital periods for which the leapfrog scheme keeps the polygonal symmetry, depending on precision*

We are mainly interested whether the generated code is faster than the original MuPAD program. Again for the leapfrog method (shown in figure 4), the generated code is several times faster than the original MuPAD code in simple and double precision; however, when the precision increases, and the floating point operations tend to the dominate the computation, the speedup decreases while still remaining significant.

It is also interesting that our tests performed on the integration of the n-body problem show that setting the computation accuracy of the MPA library such that it provides the same precision as the numerical processor (double precision for instance) make the code up to 100 times slower than the same code that uses

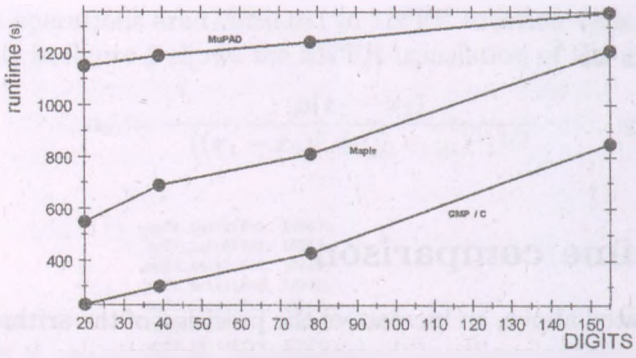

Figure 4: *Runtime dependence on numerical precision for leapfrog integration, n=4, comparison between computer algebra code and generated C/GMP*

built-in floating point numbers, i.e., the arithmetical operations are performed by the numerical processor.

References

Elmabsout B., Sur L'instabilite de certaines positions d'equilibre relatif dans le probleme des n corps, *Celestial Mechanics and Dynamical Astronomy*, 1987, **41**, 131–151.

Elmabsout B., Nonlinear instability of some relative equilibrium configurations in the $(n+1)$ - body problem, *Romanian Astronomical Journal*, 1996, vol **6** no.1, 61–71.

E. Hairer, S.P. Norsett, G. Wanner Solving Ordinary Differential Equations I Nonstiff Problems Springer, 1987.

Hairer, E., Waner, G., Solving Differential Equations II Stiff and Differential-Algebraic Problems Springer, 1991.

Sorgatz, A., Dynamic Modules User's Manual and Programming Guide for MuPAD 1.4, Springer, 1999

Zapotinschi R., Symbolic analysis of computational algorithms with SYDNA, Proc. of the 2nd Workshop on Computer Algebra in Scientific Computing, CASC'99, 499-509.

Yoshida, H., Recent progress in the theory and application of symplectic integrators, *Celestial Mechanics and Dynamical Astronomy*, 1993, **56**, 27-43.

PADEU | PADEU 19 (2007), p. 257
ISBN 963 463 557
©Published by the Astron. Dept. of the Eötvös Univ.

Motion indicators: behaviour in the transitory regime

Áron Süli

Eötvös University, Department of Astronomy, H-1518 Budapest, Pf. 32, Hungary

E-mail: a.suli@astro.elte.hu

Abstract
Two very simple and fast methods to separate chaotic from regular orbits for mappings are presented. When computing the Lyapunov Characteristic Indicator very little attention has been given to the first part of the computation which was considered as a kind of transitory regime. The methods are based on the computation of the norm of the tangent vector and their behaviour in the transitory regime is used as an indicator of the motion. The bi-dimensional standard map is used as model problem.
Keywords: *Chaos indicators: LCE, FLI - 2D standard map*

1 Introduction

The numerous experiments conducted in the last decades show that the chaotic behaviour is typical and already occurs in simple but nonlinear systems. This finding throws completely new light upon these systems and the study of chaotic behaviour became of high concern. A major part of the frontline research focuses on the structure of the phase space, therefore the problem to separate ordered and chaotic motion in systems, which possess only a few degrees of freedom and are described by ordinary differential equations, has become a fundamental task in a wide area of modern research. The phase space of these nonlinear systems can not be described by the known mathematical tools. To map the phase space and study the chaotic behaviour of a given system fast and reliable numerical tools are needed. These tools are extremely useful in those cases,

when the inspected dynamical system has more than two degrees of freedom and accordingly its phase space can't be explored in a direct way, or the classical method of surface of section can not be applied which is widely used in the case of conservative systems with two degrees of freedom. The basic idea of the method of surface of section (SoS) was invented by Poincaré (1899) and its application was renewed by Hénon & Heiles (1964).

In the past decade several research was initiated to develop new numerical methods to characterize the stochasticity of the trajectories in the phase space in short timespan and in arbitrary dimension. The developed methods can be classified in two groups: one group consists of the methods which are based on the analysis of the orbits (e.g. SoS or frequency analysis see Laskar (1990)), the other one is based on the time evolution of the tangent vector i.e. the solution of the linearized equations of motion (e.g. Lyapunov Characteristic Exponents (LCE) see Benettin et al. (1980)). For a detailed list of the methods see Table 1 of Süli (2006).

In this paper two new methods are introduced and compared with the LCE and the Fast Lyapunov Indicator (FLI) (Froeschlé et al., 1997) in the framework of the bi-dimensional standard map. In the literature the above quantities are commonly referred to as chaos indicators. This terminology may be misleading since these quantities indicate not only chaotic motion but also regular one. Already in Froeschlé et al. (2000) new terms such as *indicators of complexity* and *methods of analysis* have been introduced to replace the inappropriate terminology. In the spirit of this effort the motion indicator (MI) is used in this paper. These quantities are inherently connected to the motion itself and indicate whether the phase trajectory lies in the regular or in the chaotic domain of the phase space. This terminology was already used by Nagy et al. (2006).

The paper is organized as follows. In Section 2 the 2D standard map is described and the initial conditions of the orbits are given. In Section 3 the definition of the MIs are given and their behaviour is shortly described. In Section 4 the results, such as the efficiency, the dependence and the confidence of the methods are presented and compared. In Section 5 the results are summarized.

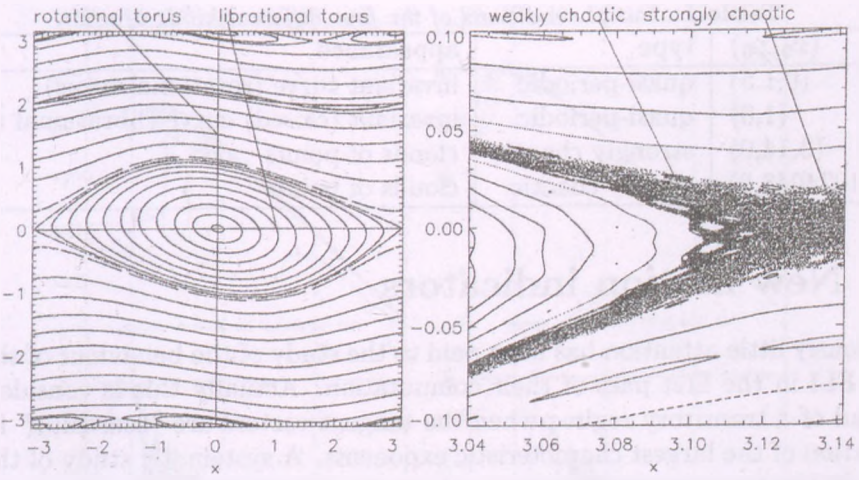

Figure 1: *The phase space of the standard map for $K = 0.3$. The vicinity of the hyperbolic point $(\pi, 0)$ is enlarged to visualise the initial condition of the strongly and weakly chaotic orbit.*

2 Model and initial conditions

The dynamical system used to demonstrate and compare the methods is the area-preserving bi-dimensional standard or Taylor-Chirikov map, defined by

$$\begin{aligned} x_{i+1} &= x_i + y_i, \\ y_{i+1} &= y_i - K \sin(x_i + y_i), \end{aligned} \qquad \text{mod } 2\pi \tag{1}$$

where $K \geq 0$ is the non-linearity parameter.

Throughout the paper the $K = 0.3$ case is considered. For this value of the non-linearity parameter the complete phase space of the system and the vicinity of the hyperbolic point $(\pi,0)$ is depicted in Fig. 1.

In this work the new MIs and the LCI and FLI were calculated for four different kinds of orbits. The initial conditions for the four orbits of the standard map are listed in Table 1 with their type and appearance on the phase space (see Fig. 1).

Table 1: *Initial conditions of the four different kinds of orbit.*

(x_0, y_0)	type	appearance
(0,1.5)	quasi-periodic	invariant curve (rotational torus)
(1,0)	quasi-periodic	invariant (closed) curve (librational torus)
(3.14,0)	strongly chaotic	clouds of points
(3.1024048,0)	weakly chaotic	clouds of points

3 New motion indicators

Curiously little attention has been paid to the study of the behaviour of the LCI and FLI in the first part of their computation. Actually this is considered as a kind of a transitory regime when the tangent vectors are "searching" for the direction of the largest characteristic exponents. A systematic study of the LCI and FLI in the transitory regime leads to the definition of two new quantities.

First let us briefly review the definition of the LCE and the FLI! Given a mapping M from $\Re^n$ to $\Re^n$, an initial condition $\vec{x}_0 \in \Re^n$, and an initial vector $\vec{\xi}_0 \in \Re^n$ of norm 1, the definition of the largest LCE (Benettin et al. (1980)):

$$\mathrm{LCE}\left(\vec{x}_0, \vec{\xi}_0\right) = \lim_{k\to\infty} \frac{1}{k} \log \|\vec{\xi}_k\|, \tag{2}$$

and the definition of the FLI (Froeschlé et al. (1997):

$$\mathrm{FLI}\left(\vec{x}_0, \vec{\xi}_{10}, \ldots, \vec{\xi}_{n0}\right) = \sup_{j=1,\ldots,n} \|\xi_j(t)\|, \tag{3}$$

where the evolution of the vector $\vec{\xi}_i$ is given by the set of coupled equations

$$\begin{aligned} \vec{x}_{k+1} &= M\vec{x}_k, \\ \vec{\xi}_{k+1} &= \frac{\partial M}{\partial \vec{x}}(\vec{x}_k)\vec{\xi}_k. \end{aligned} \tag{4}$$

The second equation of Eq. (4) is the first order variational (i.e. linearized) equation.

In Fig. 2 the LCI curves go to zero in the case of regular orbits (motion on librational and rotational tori), whereas in the case of chaotic or sticky orbits they converge to positive values. In Fig. 3 the FLI tends to infinity both for ordered and for chaotic orbits but on completely different time scales which allows to classify the orbits. The stopping time was set to 10^7 iterations. In the

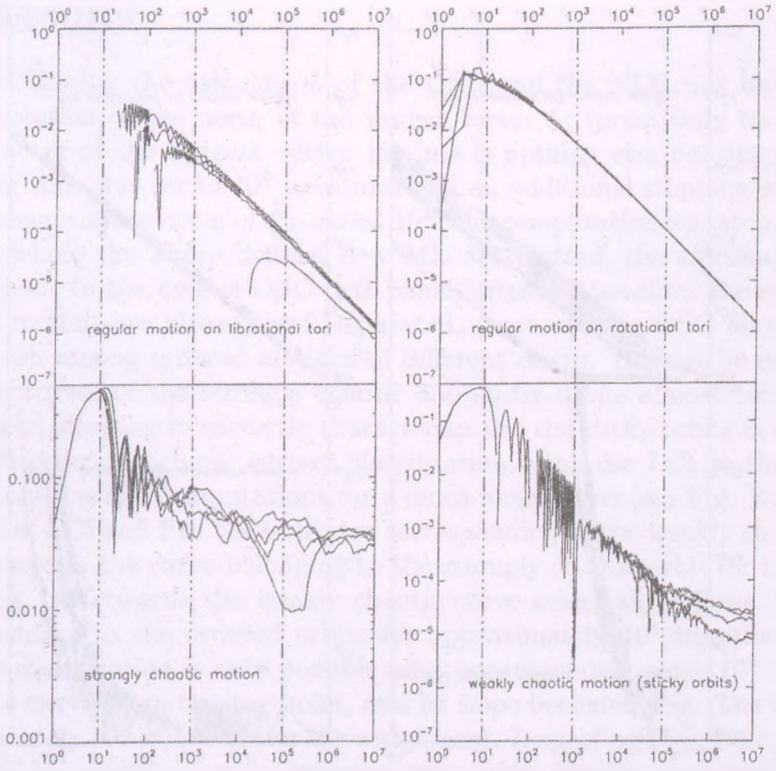

Figure 2: *Variation of LCI with the number of iterations for four kinds of orbits of the standard map. The axes are logarithmic.*

case of FLI an additional stopping criteria was used: whenever the FLI reached 10^{20} the computation was stopped.

Inspecting the curves belonging to all four different types of orbit the LCI and FLI curves can be characterized in terms of the number of peaks and of the amplitudes of the fluctuations. From Figs. 2 and 3 it is clear that the curves evolve completely differently for regular and for chaotic or sticky orbits. This

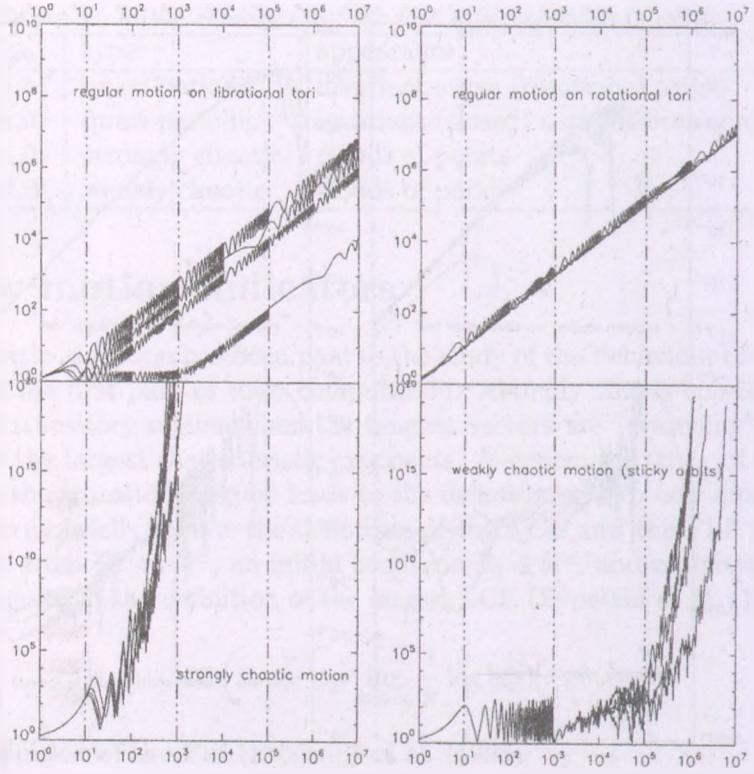

Figure 3: *Variation of FLI with the number of iterations for four kinds of orbits of the standard map. The axes are logarithmic.*

difference is reflected in the following quantities, defined as:

$$\mathtt{OSC}_n = \frac{1}{n}\sum_{k=0}^{n} |\log(MI)_{k+1} - \log(MI)_k|, \tag{5}$$

$$\mathtt{NLE}_n = \sum_{k=0}^{n} \mathtt{Number\ of\ Local\ Extrema}, \tag{6}$$

where n is the number of iterations, the MI can be either the LCI or the FLI, and the local maximum and minimum are based on three consecutive points of the MI curve.

4 Results

In the following the calculation of the OSC and the NLE was based on the time evolution of the norm of the tanget vector $\vec{\xi}_0$ (practically the evolution of the norm of the tangent vector in time is nothing else but the FLI). The stopping time was set to 10^7 iterations and an additional stopping criteria was used: whenever the norm of $\vec{\xi}$ reached 10^{20} the computation was stopped. From Fig. 4 where the above defined new MIs are plotted, the efficiency[1] can be established. In the case of OSC (left panel) after 10 iterations the regular and chaotic motion are already well separated, moreover the OSC allows also to distinguish among ordered motions of different origin. It must be emphasized that the curves of the strongly chaotic and sticky orbits almost coincide with each other, allowing to correctly characterize also the sticky orbits in very short time. In order to achieve correct classification using the LCI or the FLI one has to continue the computations for a much longer time (see Fig. 2 and 3). In the case of LCI and FLI the indicator corresponding to the weakly chaotic orbit follows exactly the curve belonging to the strongly chaotic orbit for the first 10 iterations. Afterwards the weakly chaotic curve essentially follows the curves corresponding to the ordered orbits for approximately 10^6 iterations. Using LCI the classification is only possible after approximately some 10^6 iterations, when the curve has a turning point, and its slope becomes zero. The FLI needs approximately 10^6 iterations for the assignment. Inspecting Fig. 4 it can be seen that after 10^3 all curves reach their maximum value. For the latter computations this number of iterations can be used as the stopping time.

On the right panel of Fig. 4 the NLE is plotted for the same set of orbits. The classification of the orbits is possible after several 10 iterations. Again it is remarkable that the sticky orbits can be detected as soon as the strongly chaotic ones and in addition the NLE definitely discriminates between motion on librational and rotational tori.

Figs. 2 and 3 show the efficiency of LCI and FLI. Between 1 and 10^2 iterations neither the LCI nor the FLI is capable to establish the type of the orbit: both curves are overlapping each other inhibiting the classification. Inspecting the LCI panel of Fig. 2 it is evident that after 10^3 the chaotic and regular curve are well separated. In the case of the FLI the separation is possible after 10^2 iterations.

It is only natural to expect that the methods are sensitive to the initial direction of the tangent vector $\vec{\xi}_0$. To test the dependence of the MIs on the

[1]The efficiency or speed is measured by the minimum number of iterations needed to establish with certainty the nature of an orbit.

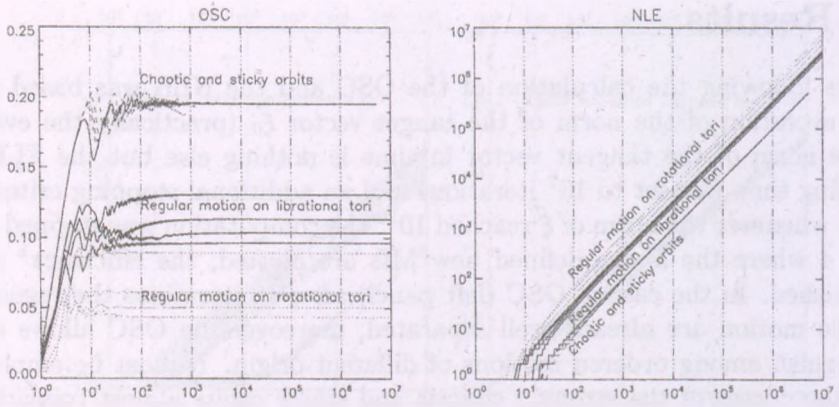

Figure 4: *Variation of OSC and NLE with the number of iterations for four kinds of orbits of the standard map. The x-axis is logarithmic, the y-axis is linear for OSC and logarithmic for NLE*

direction of the tangent vector, $\vec{\xi}_0$ is rotated by $\phi \in [0, 360°]$ with stepsize $0°.5$, and the MIs are calculated. The result is presented in Fig. 5 in which the values of the MIs are plotted against the angle ϕ, for the different kinds of orbits and for different numbers of iterations. The ϕ is the angle between $\vec{\xi}_0$ and the x-axis. The calculations were performed for $N = 10^2 - 10^5$ iterations depending on the MI. From Fig. 5 it is obvious that the LCI and the FLI values are far from being constant when varying the angle ϕ. This is not the case with the OSC or the NLE methods: none of them shows any significant variations with ϕ.

In order to measure the dependence of the methods on the direction of the tangent vector(s) the following quantity is introduced:

$$\Delta_{\mathrm{MI}} = \log_{10}\left(\frac{\max(\mathrm{MI})}{\min(\mathrm{MI})}\right), \tag{7}$$

which measures the order of magnitudes of the dependence (it vanishes for those methods which are completely independent of $\vec{\xi}_0$). The results are listed in Table 2 for different number of iterations (in the case of LCI for 10^2 iterations no calculation was done since it is insufficient, as it was explained above, whereas 10^4 and 10^5 are too many for OSC and NLE). Table 2 contains also the value of ϕ where the MIs reached their maximum and minimum.

It can be seen that Δ_{MI} decreases as N increases except for the FLI where

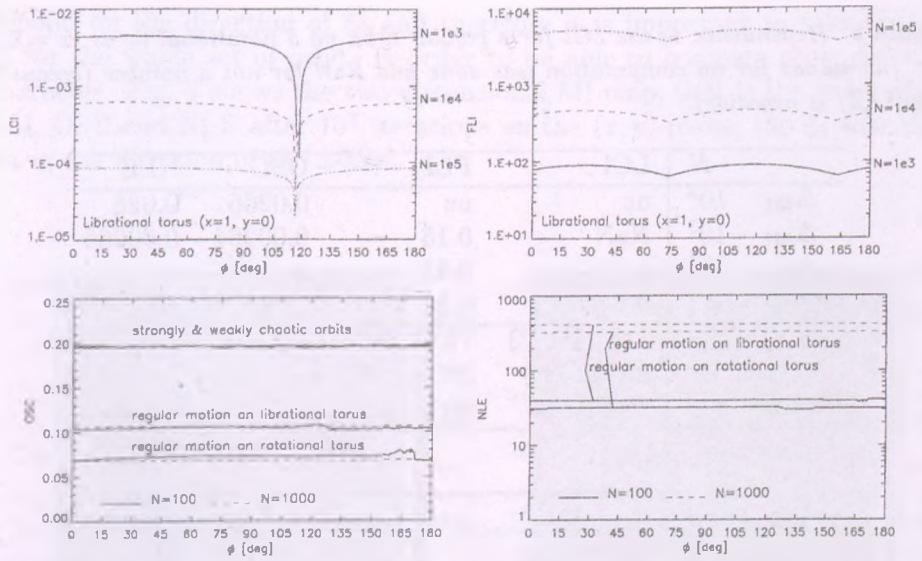

Figure 5: *Variation of the MIs as a function of the initial direction of the tangent vector(s). Upper left the LCI, upper right the FLI is plotted for three different numbers of iteration. In the lower left panel the OSC, in the right the NLE is plotted for two different numbers of iteration.*

it stays constant around 0.15. Clearly the new methods have the smallest dependence with almost the same values (see the 5^{th} and 6^{th} columns), and the LCI has the largest one. The consequences will be very well demonstrated in the confidence test in Fig. 7.

The LCI is periodic with 180° since this method is based on one tangent vector, while the FLI is periodic with 90°, because it is based on two tangent vectors which are initially perpendicular to each other. In Fig. 5 a sharp minimum of the LCI curve is visible at $\phi = 118°$ and its maximum is at $\phi = 28°$ (see also Table 2). From Fig. 6 it can be seen that if the tangent vector is perpendicular to the local tangent of the orbit (i.e. $\phi = 28°$) then the LCI(ϕ) function takes its maximum value. If $\vec{\xi}_0$ is parallel with the local tangent of the orbit (i.e. $\phi = 118°$) then the LCI(ϕ) function takes its minimum value. This follows because in the direction along the flow, $\vec{\xi}_0$ grows only linearly with time. Similar behaviour can be observed for the FLI, but naturally such relationship does not exist in the case of the new MIs.

Table 2: *Dependence of the MIs for a regular orbit on a librational torus ($x = 1, y = 0$). (nc stands for no computation was done and NaN for not a number (because the* min(LCI) *is negative).*

	N	LCI	FLI	OSC	NLE
Δ_{MI}	10^2	nc	nc	0.0266	0.028
Δ_{MI}	10^3	NaN	0.15	0.00264	0.00266
Δ_{MI}	10^4	1.15	0.15	nc	nc
Δ_{MI}	10^5	0.64	0.15	nc	nc
ϕ_{min}		118° (118°)	73° (163°)	–	–
ϕ_{max}		28° (208°)	28° (118°)	–	–
$\Delta\phi$		180°	90°	–	–

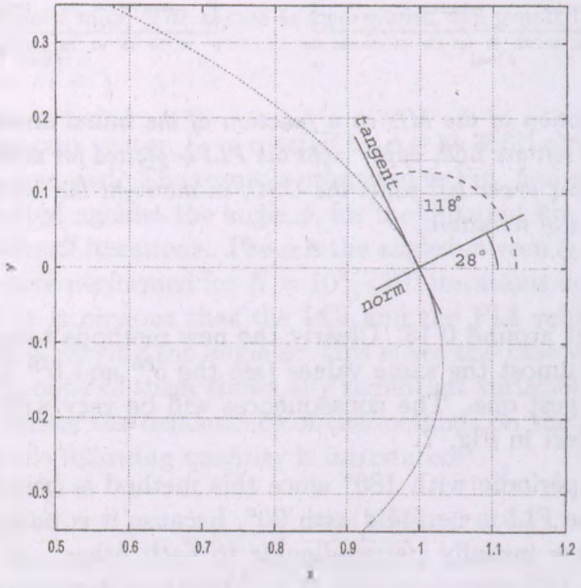

Figure 6: *Regular orbit (librational torus) of the standard map with initial conditions (1,0) and the local tangent and normal of the orbit (see text for details).*

To determine the MIs confidence the MI values for a set of 1001×1001 initial conditions regularly spaced on the (x, y)-plane in the region $[0, \pi] \times [0, \pi]$ was computed. According to the previous results the values of the LCI and FLI

depend on the direction of $\vec{\xi}_0$ and therefore it is important to take the same $\vec{\xi}_0$ for the whole set of orbits in order to be able to compare their dynamical character. Fig. 7 shows the two dimensional MI map, that is the value of LCI, FLI, OSC and NLE after 10^3 iterations on the (x, y)-plane; the $\vec{\xi}_0$ was always set in the direction of the x-axis.

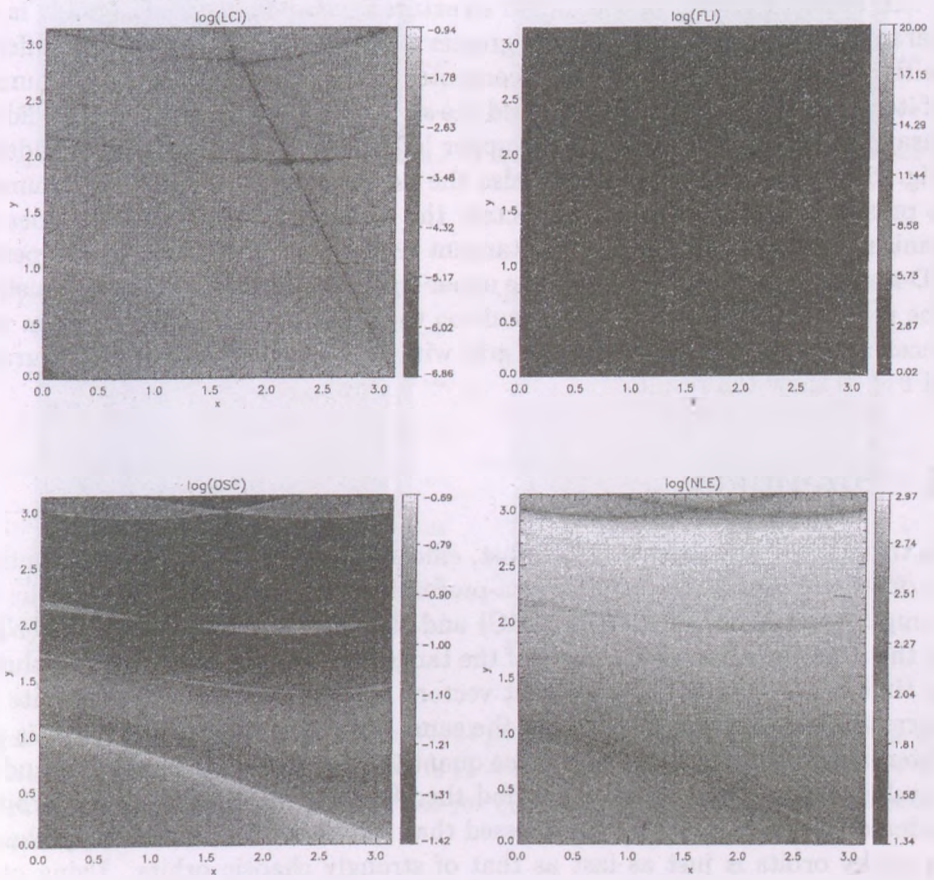

Figure 7: *Values of the MIs on the (x, y)-plane after 10^3 iterations. The tangent vectors were $\vec{\xi}_{10} = (1, 0)$ and $\vec{\xi}_{20} = (0, 1)$. The colour code for the values are given on the right of each panel.*

The most striking feature in Fig. 7 is the structure that appears on the

LCI map but absent on the other maps. This structure is like a thick line that connects the $[\pi, 0]$ and the $[\pi/2, \pi]$ points. Along this line the values of the LCI are significantly smaller than for the adjacent points. The advantage of our simple model is now undeniable: this structure is not real but an artifact of the method LCI. Apart from this significant difference, the maps are in excellent agreement with Fig. 1. Islands are distinct from tori and the chaotic zone i.e. the separatricies between them are well visible.

In order to get rid of the unreal structure several changes were made in the parameters of the computations: greater iteration number (10^4) and different initial tanget vectors were used to compute the 2D maps. Increasing the number of iterations by a factor of 10 reduced the size of the false structure but it did not disappear as it is visible from the upper left panel of Fig. 8. After considering Fig. 5 (upper left panel), where also the dependence on the iteration number is presented this is what one expected: the dependence decreases but does not vanish. An adequate choice of the tangent vector $\vec{\xi}_0 = (0, 1)$ resulted in a perfect 2D map for the LCI as shown in the upper right panel of Fig. 8. To demonstrate the independency of the new methods on the tangent vector both of them were recalculated on the above defined grid with $\vec{\xi}_0 = (0, 1)$. The two lower graphs of Fig. 8 show the results.

5 Summary

In this article we introduced two fast, efficient and easy to compute quantities in order to check if orbits of 2D area-preserving map are ordered or chaotic: the computation of the oscillation (OSC) and the number of local extrema (NLE) of the time evolution of the norm of the tangent vector. We follow the evolution in time of an orbit and the tangent vector. At each time step we compute the norm of the tangent vector and at the same time the OSC and the NLE is also determined. It was shown that these quantities are different for chaotic and for regular orbits. The proposed method therefore classifies definitely an orbit as ordered or chaotic. It must be stressed that the classification of weakly chaotic or sticky orbits is just as fast as that of strongly chaotic orbits. Using other methods the detection of sticky orbits takes several order of magnitudes longer time. A further advantage of using OSC or NLE is that they are practically independent of the initial direction of the tangent vector.

These methods were compared with other well known methods that are developed to determine the ordered or chaotic nature of orbits. First the efficiency was tested and it turned out the these new methods are faster than the LCI

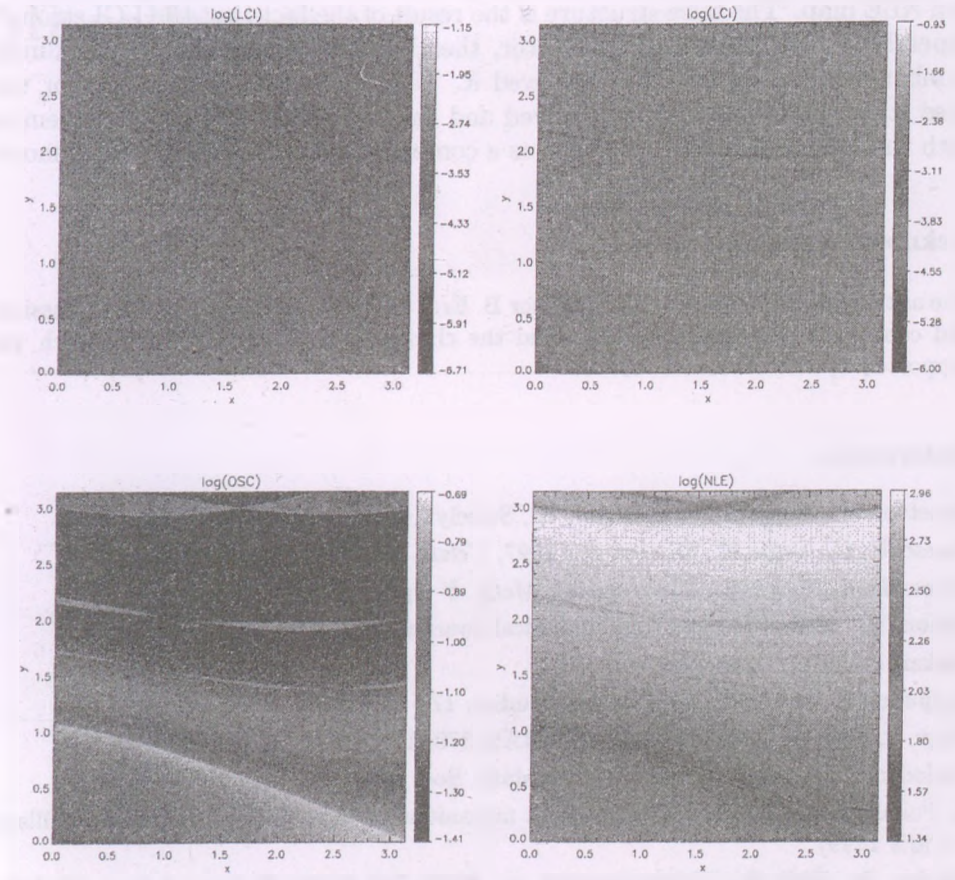

Figure 8: *The tangent vector is* $\vec{\xi}_0 = (1, 0)$ *for the upper left panel and the map was iterated* 10^4 *times. The tangent vector is* $\vec{\xi}_0 = (0, 1)$ *for the upper right panel for* 10^3 *iterations. Values of the OSC and NLE for* $\vec{\xi}_0 = (0, 1)$ *are on the lower two panel, respectively* ($N = 10^3$).

and at least as fast as the FLI. In the dependence test the new methods clearly proved to be better than the other two since they practically are independent of the initial direction of the tangent vector.

The confidence of the LCI, FLI and the new methods were tested on a large portion of the phase space. The most striking feature in Fig. 7 is the appearance

of a false structure on the LCI map. This structure is absent on the FLI, OSC and NLE map. The false structure is the result of the fact that the LCI strongly depends on the initial tangent vector, therefore the increase of the maximum number of iterations did not removed it. Using adequate tangent vector this false structure is completely removed and the results are in perfect agreement with the real phase space structure as a comparison of Fig. 7 with Fig. 1 shows.

Acknowledgement

The author would like to thank Professor B. Érdi and R. Dvorak for fruitful discussions and comments which greatly improved the clarity of the paper. This research was supported by the OTKA T043739.

References

Benettin, G., Galgani, L., Giorgilli, A., Streclyn, J. M., 1980, Meccanica, 15, 2

Froeschlé, C., Lega, E., Gonczi, R., 1997, *Celest. Mech. & Dyn. Astron.*, 67, 41

Froeschlé, C., Lega, E., 2000, *Celest. Mech. & Dyn. Astron.*, 78, 167

Hénon, M., Heiles, C., 1964 Astronomical Journal, 69, 73

Laskar, J., 1990, *Icarus*, 88, 266

Lyapunov A. M., 1907, Ann. Math. Studies, 17

Nagy, I., Süli, Á., Érdi, B., 2006, MNRAS, 370, 19

Oseledec, V. I., 1968, Trans. Moscow Math. Soc. 19, 197

H. Poincaré, Méthodes nouvelles de la mécanique céleste, Tome 3 (Gauthier Villars, Paris 1899)

Sándor, Zs., Érdi, B., Efthymiopoulos, C., 2000, *Cel. Mech. & Dyn. Astron*, 78, 113

Süli. Á., 2006 4th AHW in press

Skokos, Ch., 2001, *Journal of Physics A*, 34, 10029.

Part V
Miscellaneous

PADEU | PADEU 19 (2007), p. 273
ISBN 963 463 557
©Published by the Astron. Dept. of the Eötvös Univ.

From the International Geophysical Year to the International Heliophysical Year

Cristiana Dumitrache

Astronomical Institute of Romanian Academy

E-mail: crisd@aira.astro.ro

Abstract

This presentation summarizes the evolution of solar researches in Romania during these fifty years passed from IGY to IHY. New projects are designed for the new goals of IHY science.

Keywords: *Sun, Heliosphere, IGY, IHY*

1 Introduction

The International Geophysical Year included comprehensive global geophysical activities during one year and half. In this project were involved more than 70 countries that led to the discovery of the Van Allen radiation belts around planets, the theory of tectonic plates, exploration of outer space, construction of artificial Earth satellites, and increased research in the Arctic and Antarctic Polar Regions. The International Council of Scientific Unions, which functioned as an apolitical, global, scientifically oriented entity, oversaw this international scientific endeavor from July 1957 to December 1958. In the National Academy of Sciences (NAS) of USA, IGY Program Report, this 1.5 year program goal was: "...to observe geophysical phenomena and to secure data from all parts of the world; to conduct this effort on a coordinated basis by fields, and in a space and time, so that results could be collated in a meaningful manner."

The IGY advanced our understanding on Earth and atmosphere sciences and had a significant effect on the future of the Antarctic Continent. Solar researches known an important spring and a new era of space researches started.

The IGY idea came from the two previous Polar Years, 1882 – 1883 and 1932 - 1933, where coordinated scientific studies were conducted to understand our planet's natural processes and cycles.

The most significant IGY achievements were:

- Defining the system of mid-ocean ridges that encircle the globe, furthering our understanding of the Earth's crust and the theory of Plate Tectonics.
- Discovery of the Van Allen Radiation Belts. These belts surround the Earth at altitudes of hundreds and at thousands of kilometers above the surface and are significant to present day electronic communications.
- Collection of synoptic data, a comprehensive overview of global physical phenomena.

2 IGY in Romania

The story begun in 1952, when the International Council of Scientific Unions (ICSU) decided to establish July 1, 1957, to December 31, 1958, as the International Geophysical Year (IGY) because the scientists forecasted that the solar activity cycle would be at a high point then. The investigations focused on the following areas: aurora and airglow, cosmic rays, geomagnetism, glaciology, gravity, ionospheric physics, longitude and latitude determination, meteorology, oceanography, rocketry, seismology, and solar activity. In addition, a technical panel was set up to attempt to launch an artificial satellite into orbit around the earth. The International Geophysical Year was proposed by several reasons. The solution to various problems in Earth science and astrophysics requires data synchronously taken worldwide. Such problems include better predictions of events and natural phenomena. The Sputnik launch opened a new era of researches and international cooperation.

Romanian researchers participated at the IGY coordinates activities within the frame organized by Soviet Union and Eastern European countries. A National Committee of Geodesy and Geodynamics, chaired by Academician Gheorghe Demetrescu, director of the Bucharest Observatory at that time, was founded in 1956. Professor Călin Popovici understood the opportunity of the

moment and settled up new areas of research at the Bucharest Observatory, under the aegis of the Romanian Academy.

The systematic solar observations began in Bucharest in 1956, through the setting up of a solar working group in 1955. The solar observations were performed at the Prin-Merz double astrograph: two lunettes Bardou were attached on the equatorial montage. One lunette Bardou was used for the sunspots draw. The other one, equipped with a spectroscope, was used for the prominence observations. Later, a five meters diameter solar dome was built and the equipment was purchased for survey the solar photosphere and chromosphere. The instruments of this dome were two refractors on a unique montage: the lunette for photosphere – a Zeiss equatorial 13/195 cm and the other for chromosphere – 11/16.60 cm.

First results were published in "Analele Universitatii C.I.Parhon" in 1956 (Obs.sol., 1956), where the solar rotations 1363-1368 were surveyed between 28 July 1955 and 7 January 1956. Observationes Solaires nr.1 – Rotations 1374-1381, entitled "Bulletin", containing observations performed between 23 May 1956 and 27 December 1956, was published in 1958, as a lithographed issue. In 1958 a second lithographed volume was issued too (Obs.sol., 1957). These two volumes contain the first Romanian observations of solar prominences, where a special spectroscope was used. Starting with 1961 (Obs.sol., 1961) and till 1997, Observationes Solaires, an annual bulletin of photospheric and chromospheric observations performed at Bucharest Observatory, was published in a continuous series under the aegis of the Romanian Academy. Observations Solaires was nominated after 1990 for the awards of the Romanian Academy. The last issue was published in 1997 (Obs.sol., 1997), containing the observations performed during the year 1994.

Officially, the astrophysics section of the Astronomical Observatory of Romanian Academy exists since 1961, containing three departments: solar physics, stellar photometry and satellites. In a report of Acad. Călin Popovici, published in 1966 (Popovici, 1966) we found precious information on the research activity at the Bucharest Observatory. We will focus on the solar researches in this article. The research was focused on the solar patrol of the photosphere and chromosphere in the frame of the international cooperation to survey the solar activity. Many researches are carried out within international collaboration of the Eastern countries and USSR. The oldest collaborations are with Ondrejov Observatory (now in Czech Republic) – from 1960 and Pulkovo Observatory from USSR – from 1963. Special collaborations were also set up with Zurich Observatory in 1957, with Meudon Observatory in 1961, with "Fraunhofer Institute" (Freiburg, Germany) in 1961. A long collaboration with the world data

centers of the solar activity started in this period: with Moscow Data Center B and Boulder Data Center A (1965).

The solar photosphere observations were focused on the sunspots area and positions determination, using photographic records on plates. The relative sunspot number was found from the daily diagram plot. A special attention was paid to the sunspot groups' evolution. The visual observations of the solar photosphere were communicated regularly to Zurich and were also published in "Quarterly Bulletin on Solar Activity", since 1957. The photographic observations of the photosphere were included in the "Catalogue of the solar activity" of the Pulkovo Observatory (USSR) since 1958.

H alpha observations of solar chromosphere started in 1958, with the acquisition of a Lyot-Ohman filter. This filter was used with the 11/160 cm refractor until 2004. A new H alpha filter (Solar Spectrum) will start to work this year.

Starting with 1958, the chromospheric patrol observations were made daily. Regularly observations of prominences and flares were submitted to the world data centers and were also published in our own bulletin Observations Solaires. At the early stage of this survey activity, the records of the Romanian observations were also sent to:

- Daily maps of the Sun, Fraunhofer Institut, Freiburg, Germany, since 1961
- Quarterly Bulletin on solar activity, Zurich, UAI, since 1961
- Solnechnyie Dannye Bulletin, Pulkovo Observatory, since 1963
- Compilations of solar-geophysical data, NBS, Central Radio Propagation Laboratory, Boulder-Colorado, USA, since 1963
- International Geophysical Year - Intermediate Report of Prominences (Filaments) Activity, since 1964.

The researches were focused mainly on statistics study of various solar and geomagnetic phenomena or to observational topics linked to active regions, prominences and flares (Dumitrache&Popescu , 2005).

3 New topics

After 1995 new area of researches was added: numerical MHD simulations. In this context prominences and coronal streamers formations, flares and CME

phenomena and coronal holes numerical models were obtained (Dumitrache , 2002).

The space new era opened different approach for the observational papers: data from the specialized satellites are now interpreted to obtain information on solar phenomena, CME, solar wind or interplanetary magnetic field. The Romanian researchers worked up data from SOHO and TRACE and new projects are at the beginning or in progress with focus on the next solar and heliospheric satellites.

The obvious next step is to extend global studies into the Heliosphere to incorporate the drivers of geophysical change into the global system - the International Heliophysical Year. The main goals of IHY program are two folds:

- Coordinating some specific scientific activities (observing campaigns, data sharing, meetings) that require cross-disciplinary studies;
- Education of students and large public about the recent progress on these activities through conferences, exhibitions etc.

The International Heliophysical Year (IHY) expands the frontier of the IGY to the boundary of the heliosphere with a focus on fundamental processes. Five themes are of great interest for IHY science:

- Evolution and Generation of Magnetic Structures and Transients
- Energy Transfer and Coupling Processes
- Flows and Circulations
- Boundaries and Interfaces
- Synoptic Studies of the 3-D Coupled Solar-Planetary-Heliospheric System

The Romanian scientists have new projects for the future. Our interest will focus also on the interpretations of data provided by specialized satellites launched by ESA and NASA. Our interest goes now to the study of 3D structure of coronal mass ejections or of Heliosphere itself. The co-rotating system from the solar atmosphere and heliosphere also represents an important question we wish to investigate, as for as the magnetic field distribution into the interplanetary space. In this order we will consider the heliospheric extension of the solar current sheets and the CME disturbance on the IMF boundaries. We intend to use data from STEREO and others future solar missions (Dumitrache , 2006).

Our projects cover also problems linked to the Heliosphere – Galaxy coupling and data provided by Ulysses and Voyager will be used to understand the heliospheric horizons. New challenges wait for us to improve our knowledge on the Sun, solar system and neighborhood. We wish to point out that the solar and heliospheric researches are very important for the direct impact on the Earth life.

References

C.Dumitrache, MHD numerical simulations of solar active phenomena (invited paper), Proceedings of the Regional Meeting "Solar Researches in the South-Eastern European Countries: Present and Perspectives", Bucuresti, 24-28 aprilie 2001, (G. Maris and M. Messerotti, eds.), Observations Solaires, 2002, Ed. Acad. Romane, p.95

C.Dumitrache: 2006, Annual Meeting of the Balkans, Black Sea and Caspian Sea Regional Network on Space Weather Studies, March 30 - April 1, 2006, Manavgat - Antalya, TURKEY

C.Dumitrache, N.A.Popescu, Fifty Years of Romanian Astrophysics, 100 pag., Ed. Cartea Universitara, 2005, ISBN 973-731-236-8

Observatii solare: rotatiile 1363-1368, 28 iulie 1955-7 ianuarie 1956, Analele Universitatii "C.I.Parhon", 11, 81-102, 1956

Observatii solare: rotatiile 1363-1373, 28 iulie 1955-22 mai 1956, St.cerc.asttr.seism., II, 1, 7-37, 1957

Observationes Solaires : Rotations 1409-421 (3 janvier1959- 23 decembre 1959), Ed.Acad.R.P.R., 1961

A.Dimitriu, S.Dinulescu, C.Dumitrache(ed), M.Ghizaru, G.Maris, M.Orzaru, S.Pojoga, Observationes Solaires: Rotations 1864-1890 (24 decembre 1992-31 decembre 1994), Ed. Acad.Rom., 1997

Calin Popovici, Studii si cercetari de astronomie, tom 11, nr.2, p.205, Ed.Acad.Rom, 1966

PADEU | PADEU 19 (2007), p. 279
ISBN 963 463 557
©Published by the Astron. Dept. of the Eötvös Univ.

Contributions to the improvement of NEOs positions by means of CCD Astrometry

A. Nedelcu[1], P. Paraschiv[2], P. Popescu[3], R. Popescu[4], O. Badescu[5]

[1 2 3 4 5] Astronomical Institute of Romanian Academy, Str. Cutitul de Argint 5, RO-040557 Bucharest, Romania

E-mail: [1]octavian@aira.astro.ro, [2]nedelcu@aira.astro.ro, [3]paras@aira.astro.ro, [4]petre@aira.astro.ro [5]pradu@aira.astro.ro

Abstract
For detecting and observing NEOs for astrometrical purposes, we prepared a special observing system. We mean a special equipped instrument and a specific CCD method of identifying the object and data acquisition. Our efforts were concentrated on both subjects: the topic shows the improvements made to the instrument to the pointing device, the observation system CCD camera / accessories and the results obtained.
Keywords: *Astrometry, NEOs*

1 Introduction

We define a NEO as an object having a perihelion distance of ~ 1.3 AU. Dynamical calculations show that lifetime spans for NEOs are typically a few million years, eventually ending by crashing into the Sun, being ejected from the solar system, or impacting a terrestrial world. NEO population must have some source of resupply. Understanding the source and mechanism of their resupply is one of the fundamental scientific goals for NEO studies.

Asteroidal NEOs are traditionally subdivided into groups based on their orbital characteristics a, q, Q (semi-major axis, perihelion distance, aphelion

Table 1:

Major existing NEO Surveys	Telescope	Diameter (m)
Spacewatch	1.8	48054
NEAT	1.2	12803
LONEOS	0.6	12713
LINEAR	1.0	157346
CSS	0.4	4309

distance) with respect to Earth's and are called Amor, Apollo and Atena asteroids. Amor objects are defined as bodies residing just outside the orbit of Earth (a $\sim$ 1 AU), having $1.017 < q < 1.3$ AU. Objects having a semi-major axis = 1 AU and $q < 1.017$ AU are known as Apollos. Relatively equal numbers of Amor and Apollo asteroids are currently known; combined they account for $\sim$90% of all currently known NEOs. Atens have orbits substantially inside that of Earth ($a < 1$ AU, $Q > 0.983$ AU), and represent about 8% of the known NEO population (short-period comets account for the remaining 2%).

The discovery of the potentially hazardous near-Earth asteroid (NEA) component of the minor-planet population has been enhanced by better detecting and computing technology. Improved detector and computing technology has stretched the search volume for 1-km objects to make the NASA goal potentially achievable in the future with the curent smaller aperture telescopes, and discussion is shifting toward extending the inventory to smaller objects that could cause significant regional damage. For example, a catalog 90% complete to the 300-m size is one of the proposed objectives of the Large-aperture Synoptic Survey Telescop (NRC, 2001) recommended by the recent astronomy decadal study. The Spaceguard report estimates that there are between 12,500 and 50,000 NEA larger than 300 m. Below $\sim$ 100 m, the mass that survives entry through the atmosphere is likely too small to create widespread destruction. Table 1 is a description of main NEO surveys in the last years.

2 Observational program

Was based on the detection system CCD camera Apogee AP47P, with the chip that contains 1024 $\times$ 1024 square pixels sized at 13 μm. and quantum efficiency

exceed 90 % at 650 nm. Technical data of instrument system:

- Finder with Mintron CCD camera;
- Field: 6.08 ± .08 arcmin;
- Angular resolution: 0.712 arcsec/pxl in 2 × binning mode.

3 Observational tasks

- To solve the problem of magnitudes. On the images we need magnitudes more than 15^m, in order to be able by adding the images to obtain $18^m - 20^m$. Finder with Mintron CCD camera;
- To solve the problems concerning instrument stability.
- High-speed identification and pointing the observational area.
- Accurate finder CCD image means accurate parallelism of optical axes (telescope, finder) and accurate methods of identification. We used different catalogues with sufficient number of stars in the area with magnitudes more than 15^m and adequate computing methods.
- High speed detection of objects crossing the images.

4 Image processing

The software used for image reduction and analysis was IRAF, both for bias, dark and flat corrections, and for the astrometric computations. Positions of stellar objects in CCD images are extracted using daofind routine. Catalogs data (USNO B1.0, UCAC2, 2MASS) for the selected area are obtained using batch mode scripts from VizieR web service. ccxymatch is used to match stelar positions from catalogs with positions extracted from CCD images by daofind. Finally with the matched star list from ccxymatch, ccmap compute the plate solution and adds WCS information to the FITS headers for each image. Fake matching induced by bright stars near to the image's edge were rejected by choosing a matching tolerance of 0.5 pixels.

5 Conclusions

- The need of technical support consist in contracts for improving the instruments and investments in detection and computing system.
- The need to build a reference system referred to the ICRF sources in order to perform the connection of the dynamical reference system (asteriods) and cinematical reference system (ICRF and catalogue stars)
- The need of accurate star catalogues and zonal catalogues (aronud ICRF sources), for provinding better positions of NEOs.

References

[1] Popescu, P. et al., Proceedings Journees 2005, Warsaw, 2005, in press
[2] Nedelcu, A. et al., Rom. Astron. J., Vol. 15, Supplement, p. 69-75, Bucharest, 2005

ISBN: 963-463-557
(Department of Astronomy
of the Eötvös University)
ISBN: 978-973-610-555-5
(Cluj University Press)